Karlsruhe Institute of Technology

Structure and Composition of PtPd Model Catalysts under Operando Conditions

Zur Erlangung des akademischen Grades eines

DOKTORS DER NATURWISSENSCHAFTEN
(Dr. rer. nat.)

von der KIT-Fakultät für Chemie und Biowissenschaften
des Karlsruher Instituts für Technologie (KIT)

genehmigte
DISSERTATION

von

M.Sc. Jiachen Chen

1. Referent: Prof. Dr. Felix Studt
2. Referent: PD Dr. Philipp N. Plessow

Tag der mündlichen Prüfung: 09.12.2024

Abstract

This dissertation explores the atomic-scale processes that govern the stability, structure, and catalytic properties of Pt/Pd alloy catalysts supported by oxide surfaces, particularly focusing on the hydroxylated surfaces of α-Al_2O_3(0001) and α-Fe_2O_3(0001) surfaces. Through a combination of density functional theory (DFT) and advanced computational modeling techniques, this work provides new insights into the thermodynamic stability of hydroxylated oxide surfaces, the behavior of CO adsorption on alloy nanoparticles, and the effects of surface composition on catalytic performance.

Key findings reveal that hydroxylated surfaces with low concentrations of hydroxyl groups are thermodynamically stable across a wide range of chemical potentials, offering a robust framework for understanding oxide-supported catalysts. The study also uncovers how the local atomic environment within Pt/Pd alloy nanoparticles significantly influences CO adsorption characteristics, with both surface and subsurface compositions playing critical roles. Furthermore, the research highlights the impact of surface hydroxylation on the adsorption and migration behaviors of Pt and Pd species, emphasizing the importance of surface conditions in catalytic applications.

Additionally, the dissertation employs Gaussian process regression (GPR) and Monte Carlo simulations to predict the segregation behavior of Pd/Pt alloys and the influence of CO adsorption, showing how temperature and CO partial pressure can dramatically alter surface composition and catalytic activity.

This work advances our understanding of heterogeneous catalysis at the atomic level, offering valuable insights that can inform the design of more efficient and durable catalysts for applications in emission control and energy conversion.

Zusammenfassung

Diese Dissertation untersucht die atomaren Prozesse, die die Stabilität, Struktur und katalytischen Eigenschaften von Pt/Pd-Legierungskatalysatoren bestimmen, die auf Oxidoberflächen geträgert sind, wobei der Schwerpunkt auf den hydroxylierten Oberflächen von α-Al_2O_3(0001) und α-Fe_2O_3(0001) liegt. Durch eine Kombination aus Dichtefunktionaltheorie (DFT) und fortgeschrittenen rechnergestützten Modellierungstechniken liefert diese Arbeit neue Erkenntnisse zur thermodynamischen Stabilität von hydroxylierten Oxidoberflächen, zum Verhalten der CO-Adsorption auf Legierungsnanopartikeln sowie zu den Auswirkungen der Oberflächenzusammensetzung auf die katalytische Leistung.

Wesentliche Ergebnisse zeigen, dass hydroxylierte Oberflächen mit niedrigen Konzentrationen an Hydroxylgruppen über einen weiten Bereich chemischer Potentiale thermodynamisch stabil sind und somit ein robustes Modell für das Verständnis von oxidgestützten Katalysatoren bieten. Die Studie zeigt außerdem, wie das lokale atomare Umfeld in Pt/Pd-Legierungsnanopartikeln die Eigenschaften der CO-Adsorption erheblich beeinflusst, wobei sowohl die Zusammensetzung der Oberfläche als auch die der zweiten Lage eine entscheidende Rolle spielen. Darüber hinaus werden die Auswirkungen der Oberflächenhydroxylierung auf das Adsorptions- und Diffusionsverhalten von Pt- und Pd-Spezies untersucht, sowie die Bedeutung der Oberflächenbedingungen für katalytische Anwendungen.

Zusätzlich verwendet die Dissertation Gauß-Prozess-Regression und Monte-Carlo-Simulationen, um das Segregationsverhalten von Pd/Pt-Legierungen und den Einfluss der CO-Adsorption vorherzusagen, wobei gezeigt wird, wie Temperatur und CO-Partialdruck die Oberflächenzusammensetzung und die katalytische Aktivität drastisch verändern können.

Diese Arbeit erweitert das Verständnis der heterogenen Katalyse auf atomarer Ebene und liefert wertvolle Erkenntnisse, die die Entwicklung effizienterer und langlebigerer Katalysatoren für Anwendungen in der Emissionskontrolle und Energieumwandlung unterstützen können.

Contents

1. Introduction

1.1. Motivation

The internal combustion engine has been a driving force of modern society, powering vehicles and machinery that facilitate global transportation and industrial processes. However, the combustion of fossil fuels in these engines emits pollutants such as carbon monoxide (CO), unburned hydrocarbons (HC), and nitrogen oxides (NO_x) (compositions shown in Fig. 1.1), which have detrimental effects on air quality and public health. To mitigate these emissions, catalytic converters have become an essential component of automotive exhaust systems, with the three-way catalyst (TWC) being the most prevalent technology for gasoline engines.

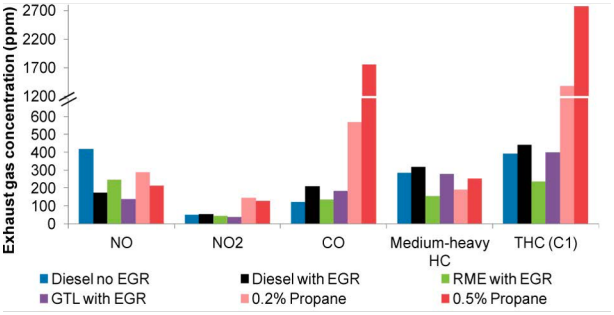

Figure 1.1: Engine exhaust gas compositions obtained by a single-cylinder diesel engine were operated with different diesel fuels (diesel, Rapeseed Methyl Ester (RME), Gas-to-Liquid (GTL)) as well as with propane/diesel in a dual fuel combustion mode. Exhaust gas recirculation (EGR) was also used in most of the cases, as it is a well-known engine calibration strategy currently used to reduce NO_x. Reprinted with permission from *Environ. Sci. Technol.* **2014**, 48, 4, 2361–2367.[1] Copyright© 2014 American Chemical Society.

Three-way catalysts are so named because they simultaneously facilitate three critical reactions: the oxidation of CO to carbon dioxide (CO_2), the oxidation of unburned hydrocarbons to CO_2 and water, and the reduction of NO_x to nitrogen gas (N_2). The active components in TWCs are noble metals from the platinum group metals (PGMs), such as platinum (Pt), palladium (Pd), and rhodium (Rh). [2] These metals are finely dispersed as nanoparticles on high-surface-area oxide supports like alumina (α-Al_2O_3) or ceria (CeO_2), which enhances their catalytic efficiency by increasing the available active sites for reactions.

Despite their effectiveness, the reliance on PGMs presents significant challenges since platinum, palladium and rhodium recorded significant deficits in 2023. These metals are scarce and expensive, with a substantial portion of global production dedicated to automotive—over 80% of rhodium and palladium and 43% of platinum as of 2023. [3] The high cost and finite supply of PGMs necessitate strategies to reduce their usage without compromising the catalytic performance. This need is further intensified by increasingly stringent emission regulations and advancements in engine technology that lower average exhaust temperatures, demanding catalysts that are active under these new conditions. [4]

Efforts to replace PGMs with more abundant, non-noble metals have been explored. Metals like copper[5], nickel[6], and cobalt[7] exhibit some catalytic activity for oxidation reactions. However, they often fall short in meeting all the requirements for automotive catalysts, such as high-temperature stability, resistance to poisoning by fuel impurities, and sufficient low-temperature activity. As a result, the most promising approach lies in enhancing the efficiency and stability of existing PGM catalysts to reduce the amount of noble metal required.

Achieving this goal requires a fundamental understanding of the catalysts at the atomic level. Catalytic activity is governed by the nature of active sites on the nanoparticle surfaces, which are influenced by factors such as particle size, shape, composition, and interactions with the support material. However, real-world catalysts are complex, hierarchically structured materials with significant structural heterogeneity. Nanoparticles vary in size and morphology, and their random orientations and interactions with the support add complexity. [8–12] Moreover, only a fraction of the metal atoms in a catalyst are on the surface and directly participate in the catalytic reactions.

Additionally, catalysts undergo dynamic structural changes during operation, such as sintering, where particles grow larger and reduce surface area, or changes in oxidation state due to varying reaction conditions. [8] These transformations can alter the activity and selectivity of the catalysts over time, posing challenges for maintaining optimal performance and for characterizing the catalysts under realistic conditions.

Addressing these challenges necessitates a multiscale approach that bridges the gap between macroscopic catalytic performance and microscopic structural understanding. By integrating advanced synthesis techniques, in situ and operando characterization methods, and theoretical modeling, we can investigate catalysts across different length scales, from atomic clusters to industrial reactors. This comprehensive understanding is essential for the rational design of next-generation catalysts with reduced noble metal content and enhanced performance.

This dissertation aims to contribute to this endeavor by focusing on several key areas that are critical for advancing the understanding and development of heterogeneous catalysts for emission control:

- Hydroxylated Oxide Surfaces of α-Al_2O_3 and α-Fe_2O_3: The properties of oxide supports significantly influence the dispersion, stability, and activity of supported metal nanoparticles. Hydroxyl groups on oxide surfaces can modify surface reactivity and metal-support interactions. Investigating the atomic structures of hydroxylated surfaces under various conditions enhances our understanding of how these surfaces interact with metal nanoparticles and reactants. This knowledge can inform strategies to optimize the support materials to improve catalyst performance and durability.
- CO as a Probe Molecule on Surfaces: CO is widely used as a probe molecule to study surface properties due to its sensitivity to the electronic and structural characteristics of

metal surfaces. Analyzing CO adsorption on Pt, Pd, and their alloys provides valuable insights into the nature of active sites, surface morphology, and electronic states. This research helps in characterizing catalysts and understanding how modifications at the atomic level.

- Ostwald Ripening of PdPt Nanoparticles on Oxide Surfaces: Catalyst stability during operation is a significant concern, as nanoparticles can grow and agglomerate over time through processes like Ostwald ripening, leading to decreased surface area and activity. Examining the mechanisms of Pd and Pt atom migration and aggregation on oxide supports such as α-Al_2O_3 and CeO_2 provides insights into how support materials and reaction conditions influence nanoparticle stability. Understanding these mechanisms can inform the design of catalysts that are more resistant to sintering, thereby enhancing their longevity.

- Surface Segregation in PdPt Alloys: In bimetallic catalysts, the distribution of different metal atoms on the nanoparticle surface is influenced by the reaction condition and can significantly affect catalytic properties. Surface segregation phenomena, where one type of metal atom preferentially occupies the surface, can alter reactivity and selectivity due to changes in electronic structure and adsorption energies. Studying how Pd and Pt atoms segregate under various reaction conditions enables the tuning of surface composition to optimize catalytic performance. Machine learning methods, such as Gaussian process regression, can model these behaviors and predict the most stable and active surface structures.

1.2. Hydroxylated Oxide Surfaces of α-Al_2O_3 and α-Fe_2O_3

The corundum-type oxides of aluminum and iron, α-Al_2O_3 and α-Fe_2O_3, are currently of great interest, both from a technological and a fundamental scientific point of view.

Like γ-alumina [13], α-alumina is also employed as a support material for metal particles in catalysis [14–26] and for atoms or molecules [27–31]. The α-Al_2O_3(0001) surface is frequently studied, for example, with respect to its interface with solids and liquids [32–45]. The level of hydroxylation has been shown to influence the reactivity of oxide surfaces critically [46–52]. Due to its importance, multiple studies have also focused on the atomic structure of the clean α-Al_2O_3(0001) surface itself [53–55]. However, many aspects remain unclear, specifically how the surface termination changes as a function of external conditions.

In ultra-high vacuum (UHV), the clean (1×1)-α-Al_2O_3(0001) surface is stable until, at temperatures higher than 1000 °C, surface reconstructions take place. Most notably, at above 1350 °C, the oxygen-deficient $(\sqrt{31}\times\sqrt{31})R9°$ surface is formed [56–60]. The hydroxylated state of the α-Al_2O_3(0001) surface, which is caused by exposure to water, has also received considerable attention [61]. Based on temperature-programmed-desorption (TPD) experiments, it has been

concluded that water is completely desorbed at temperatures higher than 600 K [62]. On the other hand, analysis of X-ray photoelectron spectroscopy (XPS) of the O 1s level suggests that hydroxyl groups are present even when the surface is annealed up to 1000 K–1200 K [46, 47]. Different reports, however, propose that characteristic high-temperature XPS features do not stem from OH-groups [63]. Based on ion-scattering experiments, it was concluded that OH-groups are present up 1100 °C [64]. The use of low energy electron diffraction (LEED) for structure-determination is limited because the electron beam has been reported to lead to dehydroxylation [56, 65]. The presence of water was also studied for the α-$Al_2O_3(1\bar{1}02)$ surface [66, 67], the α-$Al_2O_3(11\bar{2}0)$ surface [67–71] and for other modifications of Al_2O_3, such as the γ and θ phases [72–75].

Various theoretical investigations have shown that the Al-terminated, stoichiometric (1×1)-surface is the most stable α-$Al_2O_3(0001)$ surface in the absence of water and that the formation of reduced surfaces is expected only for low chemical potentials of oxygen [76, 77]. Two main types of hydroxylated surfaces have been studied theoretically. The first surface results from water adsorption and dissociation on the clean surface [78–85]. Here, multiple investigations have shown that water adsorption and dissociation is facile up to $\mu_{H_2O} \approx$ -1.5 eV. The barrier for dissociation was shown to be low ($<$ 0.5 eV [79, 82]) and further diffusion of the dissociated proton was also studied [81, 86]. Another termination is the fully hydroxylated surface, which can be derived from the oxygen terminated α-$Al_2O_3(0001)$ surface, where every surface oxygen is saturated with hydrogen. This results in the most stable known hydroxylated surface [76, 79, 80]. At low temperatures, an additional 2D-ice-like layer of water was predicted to form on top of this surface and this has also been investigated in detail [78–80, 87, 88]. Despite being more stable, it is not clear how the fully hydroxylated surface can form from the stoichiometric surface since these surfaces differ in the concentration of Al atoms in the first layer [78, 80].

Iron oxides are abundantly available on Earth and are technologically relevant in many areas.[89] The common oxidation states of Fe are +2 and +3 and this leads to the existence of iron oxides with varying composition, where hematite (α-Fe_2O_3) consists only of Fe^{3+}. In catalysis, hematite was investigated as an electrode material for photocatalytic water-splitting, as a catalyst for H_2S-removal[90–92] and as a precatalyst for CO_2 hydrogenation to hydrocarbons. [93–96] Iron is also discussed as an energy carrier, which can be oxidized to iron oxide using retrofitted coal plants and reduced using green H_2. [97] On an atomic scale, the surface of hematite is one of the central surfaces for oxidation/reduction processes. [98]

The atomic structure of a surface controls its reactivity and properties. Making reliable predictions using first-principles calculations thus requires the determination of the state of the surface, which is given by the thermodynamically most stable termination, if the system is in equilibrium. Hydroxylation is difficult to determine both experimentally and theoretically, but is known to strongly influence the properties of oxide surfaces. [99] For this reason, many studies have been concerned with determining the most stable termination of the 0001-surface

of hematite.[100–107]

Like alumina, hematite crystallizes in the corundum structure, see Fig. 1.2, and particles with different morphologies can be synthesized or found in nature. [108, 109] The stable 0001-facet is found in naturally occurring crystals and has been the subject of many investigations.[110–113] The most stable stoichiometric termination of α-Fe_2O_3(0001) is the single-metal, or O3-M terminated surface,[113] which is analogous to α-Al_2O_3[53, 100]. This is also referred to as the clean or dry surface and we will from here on refer to it as the dry surface.

However, in contrast to α-Al_2O_3, hematite can be more easily reduced at the surface, which is also one of the essential properties in its applications. For theoretical investigations, changes in the oxidation state of Fe pose a considerable challenge. For iron oxides, the local density approximation (LDA) and the generalized gradient approximation (GGA) are generally considered insufficient to obtain qualitatively correct results for properties, such as the band gap, magnetic moments, but also for the stability and reactivity of surfaces. The computationally most efficient way to tackle these challenges is through a Hubbard-U correction [114–117] applied to the d-electron of the transition metal atoms.

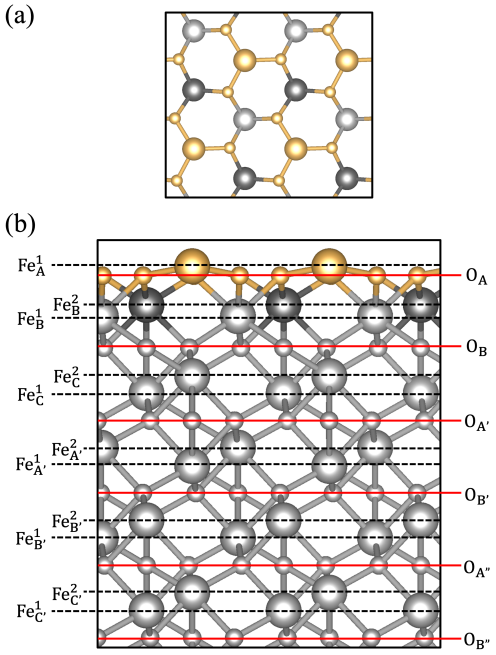

Figure 1.2: Single Fe-terminated surface model (Clean and dry surface). (a) top view (b) side view. Using letters (A, B, C) in the lower corner to indicate atoms at different layers, and use the number (1, 2) of upper corners to distinguish different atoms in the same layer. Large spheres represent metal atoms while small spheres are oxygen atoms.

The α-Fe_2O_3(0001) surface has been studied computationally in 2004 by Rohrbach, Hafner and Kresse using GGA+U calculations.[113] Their study included the stoichiometric single-metal (or O3-M) terminated surface (same as the dry surface), as well as reduced (oxygen deficient) and oxidized (oxygen enriched) surfaces. As in other investigations,[100, 102] their GGA-calculations

predict oxidized surfaces, where the formal oxidation state of Fe exceeds +3, to be relatively stable. However, ref. 113 clearly showed that oxidation of the surface is predicted to be significantly less favorable when using GGA+U with $U_{\text{eff}} = U - J = 4$ eV. Specifically, the chemical potential of oxygen μ_{O} below which the dry surface becomes more stable than any oxidized surface is shifted from $\mu_{\text{O}} \approx$ -1.25 eV to $\mu_{\text{O}} \approx$ -0.1 eV for $Fe_2O_3(0001)$ when $U_{\text{eff}} = 4$ eV is applied. According to the GGA+U calculations, oxidized α-$Fe_2O_3(0001)$ surfaces (formal oxidation state of Fe > +3) are therefore not expected to form at relevant conditions. Recently, Wang and Hellmann have also found, using calculations with the HSE hybrid functional, that oxidation of the hematite surface is only viable at very high chemical potentials of oxygen ($\mu_O >$ -0.25 eV).[118] It is also noteworthy, that the coexistence of surface areas with different terminations was predicted with DFT for α-$Fe_2O_3(0001)$. [101, 119, 120]

The existence of ferryl terminations (Fe=O) has been discussed extensively and was proposed based on infrared (IR) spectroscopy measurements under mildly oxidizing conditions, for example, 973 K and 2 mbar O_2, corresponding to $\mu_{\text{O}} =$ -1.2 eV.[121] However, as indicated above, computational investigations going beyond the GGA level (either GGA+U or hybrid functional) find oxidized structures including ferryl groups to be unfavorable.[104, 118] Surface sensitive X-ray diffraction measurements also indicate the presence of oxygen at the surface of hematite[99], which may, however, also be present in the form of hydroxyl groups.

In addition to oxidation and reduction, the adsorption of water and the formation of hydroxyl groups play an important role in determining the properties of hydroxylated oxide surfaces.[122] Hydroxylation of hematite surfaces has been observed experimentally using XPS[123] and polarization-dependent infrared reflection absorption spectroscopy (IRRAS)[124]. Computationally, the adsorption of water on the dry surface and its dissociation were studied extensively.[103, 104, 124–126] The other main hydroxylated surface that has been studied a lot is the fully hydroxylated surface (Fe-$(OH)_3$ terminated).[118] The interface of hematite with liquid water was also investigated in a number of studies.[127–129] Beyond the well-known dry surface and the fully hydroxylated surface, a vast number of hydroxylated structures have been studied computationally. [103, 104, 118, 124–131] These were typically obtained by cutting the surface at some layer (O_3, Fe, or Fe_2) and adding variable amounts of H or OH groups. Many of the structures generated in this way contain Fe in bonding situations differing from the usual oxidation states (+2 and +3). To our knowledge there is no known stable hydroxylated structure in between fully hydroxylated and dry surfaces, except defective reduced structures that are only stable at the extremely low chemical potential of oxygen μ_O.

1.3. CO as Probe Molecule on Surfaces

Pd/Pt alloy NPs are most prominently used for emission control in applications involving CO and methane oxidation, as well as catalysts in fuel cells.[132, 133] The use of an alloy increases the stability of the NPs against aging: Pure Pt NPs sinter and decrease in their catalytic efficiency

in the catalysis process, but the addition of Pd slows this process down, making the catalysts last longer[134–137] and possibly increases the catalytic activity.[138] In emission control, Pd/Pt NPs are often supported by Al_2O_3 due to its good thermal and mechanical stability as well as the high surface area that is achieved when a porous Al_2O_3 structure is used.[136, 139]

The catalytic activity is controlled by the active surface sites of the NPs.[140]. To study the active sites, model systems with good control over all structural parameters are needed. Here, NPs are grown onto α-Al_2O_3 single-crystal substrates and are probed by CO adsorption. Similar model catalysts were employed in the past to study the pressure and coverage dependence [141] of CO adsorption on Pd NPs. The adsorption of CO molecules on metal surfaces weakens the bond between carbon and oxygen, resulting in a shift in the vibrational frequency that can be probed by Fourier transform infrared reflection absorption spectroscopy (FT-IRRAS).[142, 143] The frequency shift reflects the chemical environments at the catalyst surface, as well as the adsorption site.

CO can adsorb on metal surfaces in different configurations, most of them fall into one of three categories: on-top, bridge or hollow adsorption sites. It is well established that at room temperature Pt surfaces favor on-top adsorption of CO [144, 145], whereas Pd surfaces mostly give rise to bridge- and hollow-site adsorption.[146, 147] At lower temperatures (and higher coverages) on-top adsorption of CO on Pd and bridge site adsorption on Pt is possible. Furthermore, the adsorption configuration may depend on the coverage.[141] As a trend, the wavenumber to excite a vibrational state of the CO adsorbed on a bridge site is larger than on a hollow site, and the wavenumber corresponding to adsorption on-top is larger than the wavenumber corresponding to adsorption on bridge sites.[144, 148–150] In many cases, the vibrational frequency for CO increases with increasing coverage due to dipole-dipole coupling in between adsorbed CO molecules and due to changes in the chemical bond in the presence of several molecules.[151–154] For NPs, the molecular vibration of CO is influenced by the coordination number of the adsorption site, specifically considering adsorption on edges compared to adsorption on facets. [149, 151, 155] From theoretical and experimental investigations it is known that CO adsorption on Pt steps and edges results in lower vibration wavenumbers compared to adsorption on facets.[156, 157] On the contrary, for the adsorption of CO on Pd, the wavenumber of the molecular vibration of CO increases when the molecule adsorbs on a low coordinated site.[141, 147] Moreover, in the case of NPs, CO adsorption on the support may also take place.[158]

In the case of alloy NPs, additional phenomena take place that influence the CO adsorption behavior: DFT calculations predict that the Pd/Pt alloy surface termination depends on the bulk alloy composition and the surrounding atmosphere.[159] Under UHV, for Pd-rich alloys the formation of a Pd shell is energetically favorable, whereas it is favorable to form a Pt shell if the alloy is Pt-rich.[159] If an oxygen adlayer is present, Pd segregation is energetically advantageous due to its high affinity towards oxygen adsorption. Experimental investigations regarding the surface segregation of Pd/Pt alloy NPs report a preference for Pd segregation in UHV, H_2, and

oxygen.[160–162]

Given the great complexity of Al_2O_3 nanomaterials, a thorough understanding remains a challenging task. Consequently, surface science studies based on well-controlled model systems are required to provide reliable and accurate reference data. IR has the advantage of being applied to metal-oxide systems in the form of both macroscopic monocrystals and powder particles. [163] However, studies using IRRAS on oxide single-crystal surfaces face significant inherent experimental challenges due to the dielectric properties of oxidic substrates.

The α-Al_2O_3 surface is known to be the most energetically stable surface of α-Al_2O_3. In addition, the bare, adsorbate-free α-Al_2O_3(0001) has been proposed to be single Al-terminated (shown in Figure 3.1a). Here, our collaborators present the first polarization-resolved IRRAS data on the α-Al_2O_3(0001) single crystal surface using CO as a probe molecule. The CO surface-ligand IR (CO-SLIR) approach has been demonstrated to be extremely sensitive to the surface structure of catalysts and the chemical environments of adsorption sites. [164–169] The IRRAS characterization was complemented by grazing-emission X-ray photoelectron spectroscopy (XPS).

1.4. PdPt Ostwald Ripening on Oxide Surfaces

Ostwald ripening is a critical process in the stability and activity of metal catalysts supported on oxide surfaces. Pd clusters on CeO_2(111) predominantly undergo Ostwald ripening due to the high mobility of Pd atoms compared to clusters. This process is facilitated by adsorbed CO, which lowers the diffusion and detachment barriers for Pd atoms.[170] In oxidizing environments, volatile PtO_2 species on CeO_2 can be trapped at defect sites, forming stable single-atom catalysts, which prevents particle growth and enhances sintering resistance.[171] The interaction of Pd with the α-Al_2O_3(0001) surface, especially under hydroxylation, shows that hydroxylated surfaces reduce the binding energy and hopping rate of Pd atoms, leading to more stable atomistic configurations and impacting cluster formation.[172] DFT studies show that Pd atoms on hydroxylated α-Al_2O_3(0001) surfaces exhibit a significant interaction, which is modulated by the presence of hydroxyl groups, influencing the catalytic properties and stability of the surface.[173] Hydroxylation of α-Al_2O_3(0001) significantly stabilizes the surface and lowers the surface free energy, which influences the morphology and reactivity of Pd clusters.[174] The hydroxylation of surfaces impacts the diffusion pathways and energy barriers for metal atoms, thereby affecting the sintering behavior and stability of catalytic sites.[66]

Computational research indicates that the Ostwald ripening of Pd and Pt on α-Al_2O_3(0001) and CeO_2(111) surfaces is significantly influenced by the surface hydroxylation state. Hydroxylated surfaces stabilize metal atoms, reduce diffusion barriers, and impact the formation and stability of catalytic clusters, enhancing the catalytic efficiency and sintering resistance of supported catalysts.

1.5. Surface Segregation of PdPt Alloys

The structure of a metal catalyst is pivotal in determining its activity. [175–177] Recent in situ experiments have revealed that catalysts undergo significant structural reconstructions when exposed to changing gaseous environments. [178–180] One example is the reshaping of metal NPs under reaction conditions, which has attracted considerable attention because it alters the number of active sites and can generate new ones during structural transformations. [181] Therefore, understanding the nonequilibrium transformations of nanocatalysts under reaction conditions is important because the process may create metastable atomic structures that offer unique activities in reactions.[182]

For a multicomponent alloy system, we are interested in understanding the behavior of a system over a vast configuration space. For instance, in an alloy with two types of atoms (A and B), each site in the lattice can be occupied by either atom A or atom B. The number of possible configurations grows exponentially with the number of sites.

Surface segregation in PdPt alloys is a critical factor influencing their catalytic properties, structural stability, and overall performance in various applications. Computational studies provide detailed insights into the atomic-scale mechanisms and energetics of surface segregation phenomena.

Surface segregation studies using Monte Carlo simulations and DFT reveal that Pd atoms tend to segregate to the surface layers in PdPt alloys. This enrichment is driven by the lower surface energy of Pd compared to Pt.[183] Segregation profiles often show an oscillatory behavior, with alternating layers of Pd enrichment and depletion below the surface.[184] Higher temperatures generally reduce the extent of Pd segregation due to increased atomic mobility and mixing. However, segregation can still be pronounced at elevated temperatures in specific alloy compositions.[185] The segregation behavior is significantly influenced by the overall composition of the alloy. Pd-rich alloys show more pronounced segregation compared to Pt-rich alloys.[186] In PdPt NPs, Pd tends to segregate to the surface, forming Pd-enriched shells with Pt-enriched cores. This segregation is influenced by factors such as particle size, shape, and surface facets.[187] Monte Carlo simulations have shown that both core-shell and random alloy PdPt NPs can be metastable and kinetically trapped, which impacts their segregation behavior and catalytic activity.[187] The presence of gases like hydrogen and oxygen can enhance Pd segregation at lower temperatures. Hydrogen treatment, in particular, has been shown to induce significant Pd segregation, which can be reversed by annealing.[188] The adsorption of gases such as H_2, O_2, and CO influences the segregation dynamics and can alter the surface composition significantly.[189]

The Gaussian process regression (GPR) model is a nonlinear, nonparametric regression tool useful for interpolating between data points scattered in a high-dimensional input space. [190] It is based on Bayesian probability theory and has very close connections to other regression techniques, such as kernel ridge regression (KRR) and linear regression with radial basis functions.

GPR has been applied in computational materials science to predict various properties of materials and alloys, including the study of atomistic properties and the construction of interatomic potentials. This method aids in the understanding of material behaviors at the atomic level, including segregation phenomena.[190] The scalable application of GPR for predicting material properties has demonstrated its efficiency in handling large datasets while maintaining high accuracy. This includes the prediction of segregation tendencies in binary alloys, leveraging batch processing and co-clustering techniques.[191] Multi-fidelity GPR approaches have been developed to enhance the prediction accuracy of random fields in materials science. This method integrates data from various fidelity levels to improve the reliability of predictions regarding alloy segregation and other properties.[192] GPR has been used to accelerate computational processes, such as geometry optimizations in materials modeling. By interpolating potential energy surfaces, GPR reduces the computational cost and enhances the efficiency of studying alloy segregation at the atomic level.[193] Methods have been developed to handle the computational challenges associated with GPR, particularly when dealing with large datasets. These methods involve optimizing the covariance function and reducing the complexity of matrix operations, which are crucial for studying segregation in complex alloy systems.[194]

The study of surface segregation and adsorption phenomena in bimetallic alloys is of paramount importance in heterogeneous catalysis and surface science. Pd/Pt alloys, in particular, have gained significant attention due to their remarkable catalytic properties in various chemical reactions, including hydrogenation, oxidation, and CO oxidation. Understanding the atomic-scale behavior of these alloy surfaces under different environmental conditions is crucial for optimizing their catalytic performance and stability.

1.6. Scope of the Thesis

The aim of this thesis is to gain a deeper understanding of the structure and composition of PtPd model catalysts, which are supported by metal oxides under operando conditions. The contents of this thesis can be summarized by the following:

Chapter 3 presents a detailed DFT study on the thermodynamic stability of hydroxylated α-Al_2O_3 and α-$Fe_2O_3(0001)$ surfaces. For α-$Al_2O_3(0001)$, we report a new termination with low concentrations of hydroxyl groups, shown to be more stable than previously reported structures at low chemical potentials of water, maintaining stability up to around 1000 K at 1 mbar partial pressure. The formation of these surfaces from adsorbed water is thermodynamically favorable with accessible barriers. For α-$Fe_2O_3(0001)$, hydroxylated surfaces with low OH-concentrations are stable within a water chemical potential range of $-0.95\,\text{eV}$ to $-2.22\,\text{eV}$, predicted to be the dominant termination under various experimental conditions. Reduced surfaces with Fe^{2+} are only stable at very low oxygen chemical potentials ($\mu_O <$ -2.44 eV), except for a single OH-group removed surface stable at higher μ_O.

This chapter is based on:

- **Chen, J.**; Sharapa, D.; Plessow, P. N. Stability and formation of hydroxylated α-Al_2O_3(0001) surfaces at high temperatures. *Phys. Rev. Res.* **2022**, *4* (1). DOI: 10.1103/physrevresearch.4.013232
- **Chen, J.**; Sharapa, D. I.; Plessow, P. N. Stability of hydroxylated α-Fe_2O_3(0001) surfaces. *ACS Omega* **2024**, *9* (33). DOI: 10.1021/acsomega.4c02113

Chapter 4 presents a comprehensive study on CO adsorption on Pd/Pt NPs with varying compositions, using FT-IRRAS and DFT calculations. The study reveals that CO adsorption sites and stretching band frequencies are influenced by the Pd/Pt alloy ratio, with distinct behaviors compared to pure Pd and Pt NPs. Additionally, the chapter includes findings on the reactivity and partial hydroxylation of the Al-terminated α-Al_2O_3(0001) surface under UHV conditions, identified through polarization-resolved IRRAS and supported by DFT calculations, showing two distinct CO species with different binding energies.

This chapter is based on:

- Dolling, D. S.; **Chen, J.**; Schober, J.-C.; Creutzburg, M.; Jeromin, A.; Vonk, V.; Sharapa, D. I.; Keller, T. F.; Plessow, P. N.; Noei, H.; Stierle, A. Probing Active Sites on Pd/Pt Alloy Nanoparticles by CO Adsorption. *ACS Nano* **2024**. DOI: 10.1021/acsnano.4c08291
- Gojare, S.*; Chen, S.*; **Chen, J.***; Yu, Z.; Quesada, J. V.; Plessow, P. N.; Fink, K.; Wang, Y. Adsorption of CO on α-Al_2O_3(0001): A combined experimental and computational study. *in Preparation* (* indicates equal contribution)

Chapter 5 presents a detailed DFT investigation of Pd/Pt species adsorbed and migrated on α-Al_2O_3(0001) and CeO_2(100) surfaces and the effect of surface hydroxylation.

Chapter 6 presents advanced predictive modeling of Pd/Pt catalyst behaviors through GPR and Monte Carlo simulations. In this chapter, surface segregation is simulated under different temperatures and CO partial pressure.

This chapter is based on:

- **Chen, J.**; Sharapa, D.; Plessow, P. N. Advanced Predictive Modeling of Bimetallic Catalyst Behaviors through Gaussian Process Regression and Monte Carlo Simulations. *in Preparation*

2. Computational Theory and Methods

2.1. Introduction

Computational modeling and simulation of materials have greatly benefited from advancements in computer technology, leading to the development of sophisticated software that facilitates the refinement of materials and their applications. Understanding the definitions of 'model' and 'simulation' is essential: a 'model' idealizes the real behavior of a system by approximately describing it based on empirical or theoretical principles, using mathematical relations to represent physical quantities or behaviors. In contrast, a 'simulation' applies this model to study the influences of external forces and constraints on the system, with the accuracy of the simulation depending on various factors, including the chosen methods and underlying assumptions.

Computational Materials Science (CMS), which combines modeling and simulation, is invaluable for understanding and predicting material behavior. This discipline enables more profound insights into systems by examining phenomena that might not be accessible experimentally, thus strengthening the relationship between theoretical predictions and real-world observations. For systems on the length scale of 1 Å (10^{-10} m) to 100 microns (10^{-4} m), where atomic bonding governs behavior, quantum mechanics provides the framework to study the electronic structure of atomic bonds and electron distributions within materials.

In this chapter, we introduce the theoretical basis of the methods employed in this dissertation. For investigating multi-atomic systems, DFT serves as a primary tool to compute electronic ground-state energy and optimize atomic configurations at 0 K. By applying the Born-Oppenheimer approximation, which separates the fast motion of electrons from the relatively slow motion of nuclei, DFT enables accurate calculation of electronic properties while treating nuclei as fixed. Additionally, through the harmonic approximation for atomic vibrations, DFT calculations allow us to compute thermodynamic properties such as the Gibbs free energy, enabling predictions of stability and equilibrium constants. To explore reaction kinetics, transition states can be identified using the nudged elastic band or dimer methods, with the resulting energy barriers used to calculate rate constants and bridge static DFT calculations to kinetic simulations.

Quantum mechanics thus forms the foundation for these calculations, while the Born-Oppenheimer approximation simplifies the quantum mechanical problem by decoupling electronic and nuclear motion. Thermodynamics, particularly through Gibbs free energy, provides a framework for understanding equilibrium and stability, while statistical methods extend these results to account for more complex material behavior.

Markov Chain Monte Carlo (MCMC) methods are also employed to sample complex probability distributions, offering insights into systems with many degrees of freedom. By constructing a

Markov chain that converges to the desired equilibrium distribution, MCMC enables the approximation of properties such as means and variances, bridging static calculations to dynamic simulations. Furthermore, GPR is utilized as a non-parametric, probabilistic model for regression, allowing us to flexibly model data without a predefined functional form. GPR's capacity to quantify uncertainty provides an additional layer of insight, particularly useful for modeling non-linear relationships in materials systems.

Together, these methods—DFT, thermodynamics, statistical sampling with MCMC, and GPR—constitute a powerful computational toolkit. This toolkit enables a comprehensive approach to investigating material properties, from electronic structure and stability to reaction kinetics and dynamic behavior, thus allowing theoretical predictions to translate into meaningful insights about materials' real-world performance. In the sections that follow, each method will be discussed in greater detail, highlighting its relevance and application within this research.

2.2. Quantum Mechanics

In non-relativistic quantum mechanics, the core concept for describing the state of a system is the wave function. The Schrödinger equation is used to describe the evolution of the wave function and is one of the fundamental assumptions of quantum mechanics, stating that the state of a microscopic particle is represented by its wave function. The single-particle time-dependent Schrödinger equation is:

$$\mathrm{i}\hbar\frac{\partial\Psi(r,t)}{\partial t} = \left(-\frac{\hbar^2}{2m}\nabla^2 + V(r,t)\right)\Psi(r,t) \tag{2.1}$$

Here, $\Psi(r,t)$ is the wave function of the quantum system. It is a complex-valued function that depends on both position r (which can be a vector in three-dimensional space, i.e., $r = (x,y,z)$) and time t. The wave function contains all the information about the system. The probability density of finding a particle at a position r at time t is given by $|\Psi(r,t)|^2$. $\hbar$ is the reduced Planck constant, defined as $\hbar = \frac{h}{2\pi}$, where h is Planck's constant. Its value is approximately 6.582×10^{-16} eV $\cdot$ s. ∇^2 is also called the Laplacian) which is a differential operator that acts on the wave function $\Psi(r,t)$. In three dimensions, it is given by:

$$\nabla^2 = \frac{\partial^2}{\partial x^2} + \frac{\partial^2}{\partial y^2} + \frac{\partial^2}{\partial z^2} \tag{2.2}$$

The operator $-\frac{\hbar^2}{2m}\nabla^2$ represents the kinetic energy part of the Hamiltonian (the total energy operator) for a particle of mass m. The term $\frac{\hbar^2}{2m}$ has units of energy times length squared, making the whole term have the correct units of energy. $V(r,t)$ is the potential energy function of the system. It can depend on both the position r and time t. The potential energy term

accounts for the forces acting on the particle due to external fields or other particles. The expression inside the parentheses is the Hamiltonian operator ($\hat{H}$) acting on the wave function $\Psi(r,t)$:

$$\hat{H}\Psi(r,t) = \left(-\frac{\hbar^2}{2m}\nabla^2 + V(r,t)\right)\Psi(r,t) \tag{2.3}$$

The Hamiltonian operator represents the total energy (kinetic + potential) of the system. The term on the left side of the equation 2.1 represents the time evolution of the wave function. The equation shows that the time evolution of the quantum state (left-hand side) is determined by the total energy (right-hand side).

Many problems can be approximated as being time-independent so than the potential energy term V does not explicitly depend on time t, but is only a function of the spatial coordinates r. In this case, the total energy of particles moving in the potential field is a conserved quantity. Therefore, the time-independent Schrödinger equation can be written as:

$$\Psi(r,t) = \psi(r)e^{-\mathrm{i}Et/\hbar} \tag{2.4}$$

$$\left(-\frac{\hbar^2}{2m}\nabla^2 + V(r)\right)\psi(r) = E\psi(r) \tag{2.5}$$

2.2.1. Born-Oppenheimer Approximation

Most electronic structure first-principles methods, including but not limited to DFT, are based on the time-independent Schrödinger equation. These methods aim to solve the electronic Schrödinger equation from fundamental physical principles, without relying on empirical parameters. Aside from DFT, other widely used first-principles approaches include Hartree-Fock (HF), which approximates the wave function as a single Slater determinant, and Quantum Monte Carlo (QMC) methods, which use stochastic processes to solve the Schrödinger equation more accurately but at a higher computational cost. Essentially, these computational methods can be viewed as different approximate solutions to the Schrödinger equation, each with its own advantages and limitations depending on the specific system. Here, we assume:

$$\hat{H}\Psi(\{\boldsymbol{r}_i\},\{\boldsymbol{R}_A\}) = E\Psi(\{\boldsymbol{r}_i\},\{\boldsymbol{R}_A\}) \tag{2.6}$$

Considering the kinetic energy of the nuclei, the kinetic energy of the electrons, and the Coulomb interactions between nuclei, between nuclei and electrons, and between electrons, the Hamiltonian in the International System of Units (SI) can be expressed as:

$$\begin{aligned}\hat{H} = &-\sum_{i=1}^{M}\frac{\hbar^2}{2m_A}\nabla_A^2 - \sum_{i=1}^{N}\frac{\hbar^2}{2m_e}\nabla_i^2 + \sum_{A=1}^{M}\sum_{B>A}^{M}\frac{Z_A Z_B e^2}{4\pi\varepsilon_0 R_{AB}} \\ &+ \sum_{i=1}^{N}\sum_{j>i}^{N}\frac{e^2}{4\pi\varepsilon_0 r_{ij}} - \sum_{i=1}^{N}\sum_{A=1}^{N}\frac{Z_A e^2}{4\pi\varepsilon_0 r_{iA}}\end{aligned} \tag{2.7}$$

where:
A and B are the index of nuclei,
i and j are the index of electrons,
m_A and m_i are the mass of nuclei and electrons,
Z_A and Z_B are the positive charges carried by each nucleus,
R_{AB}, r_{ij} and r_{iA} are the nucleus-nucleus, electron-electron and nucleus-electron distance,
e is the elementary charge, $e = 1.6022 \times 10^{-19}$ C,
ε_0 is the vacuum permittivity, $\varepsilon_0 = 8.854\,19 \times 10^{-12}$ $\mathrm{C^2\,J^{-1}\,m^{-1}}$.

The first two terms of this equation represent the kinetic energy of the nuclei and electrons, respectively. The last three terms represent the Coulomb interactions: between the nuclei, between electrons, and between the nuclei and electrons. The greatest difficulty in solving the many-body Schrödinger equation lies in the presence of electron-electron interaction terms, which prevent the use of the separation of variables method to solve the equation. Therefore, the key to solving this problem is appropriately introducing approximations that transform a many-body problem into a single-body problem.

Since the presence of $\frac{Z_A}{r_{iA}}$ prevents the straightforward separation of variables for the electron and nuclear motion equations, one key approximation method to further simplify this Schrödinger equation is the Born-Oppenheimer approximation. Given that the mass of a nucleus is typically thousands of times greater than that of an electron, the slow motion of the nuclei and the fast motion of the electrons can be effectively separated and solved independently, without introducing significant errors. Theoretically, we can explicitly separate the nuclear motion part from the total wave function. In the Born-Oppenheimer approximation, the total wave function $\Psi(\boldsymbol{r}, \boldsymbol{R})$ is expressed approximated as a product of the electronic wave function $\psi(r; R)$ and the nuclear wave function $\chi(R)$:

$$\Psi(\{\boldsymbol{r}_i\}, \{\boldsymbol{R}_A\}) = \psi(\{\boldsymbol{r}_i\}; \{\boldsymbol{R}_A\})\chi(\{\boldsymbol{R}_A\}) \tag{2.8}$$

Here, $\psi(\{\boldsymbol{r}_i\}; \{\boldsymbol{R}_A\})$ represents the electronic wave function under the configuration $\{\boldsymbol{R}_A\}$, $\chi(\{\boldsymbol{R}_A\})$ represents the corresponding nuclear wave function.

2.2.2. Density Functional Theory

In the framework of DFT, the task is to determine the electronic ground state energy and electron density of a multi-electron system for a fixed nuclear configuration, as dictated by

the Born-Oppenheimer approximation. Instead of directly solving the many-body Schrödinger equation for the full electronic wave function, DFT transforms this problem into a single-particle one by emphasizing the electron density, $\rho(\boldsymbol{r})$, as the central variable. This transformation simplifies the complex interactions among electrons while still capturing the essential physics.

2.2.2.1. Thomas-Fermi-Dirac Approximation

The first attempt at density functional theory was made independently by Thomas and Fermi in 1927, who each proposed a method to express the system's energy as a function of electron density. This approach is known as the Thomas-Fermi theory. The main idea is to use the analytical results of a uniform electron gas (UEG) to express the total energy of the system, including kinetic energy and Hartree terms, in the following form:

$$E_i = \int \varepsilon_i[\rho(\boldsymbol{r})]\rho(\boldsymbol{r})\mathrm{d}\boldsymbol{r} \tag{2.9}$$

In the expression, $\rho(\boldsymbol{r})$ represents the energy "density" of each term under the UEG model, corresponding to the electron density $\rho(\boldsymbol{r})$ at point $\boldsymbol{r}$. Furthermore, the equation indicates that the system's energy depends only on the electron density $\rho(\boldsymbol{r})$ at that specific point.

The Thomas-Fermi theory neglected the exchange-correlation effects of the many-body system. Dirac extended the Thomas-Fermi theory by proposing that the exchange energy density of electrons should satisfy $\varepsilon_x \propto \rho^{1/3}$. Therefore, the total energy of the system can be expressed as:

$$E_{\mathrm{TFD}} = 2.871 \int \rho(\boldsymbol{r})^{5/3}\ \mathrm{d}\boldsymbol{r} + \frac{1}{2}\iint \frac{\rho(\boldsymbol{r})\rho\left(\boldsymbol{r}'\right)}{|\boldsymbol{r}-\boldsymbol{r}'|}\mathrm{d}\boldsymbol{r}\mathrm{d}\boldsymbol{r}' + \int V_{\mathrm{ext}}\left(\boldsymbol{r}\right)\rho(\boldsymbol{r})\mathrm{d}\boldsymbol{r} - 0.739\int \rho(\boldsymbol{r})^{4/3}\ \mathrm{d}\boldsymbol{r} \tag{2.10}$$

Equation 2.10 is referred to as the Thomas-Fermi-Dirac (TFD) approximation. TFD depends solely on the system's electron density distribution $\rho(\boldsymbol{r})$ and can be expressed as a functional of $\rho(\boldsymbol{r})$.

Based on the constraint condition:

$$\int \rho(\boldsymbol{r})\mathrm{d}\boldsymbol{r} = N \tag{2.11}$$

The ground state energy and the corresponding electron density distribution can be obtained using the method of Lagrange multipliers:

$$\frac{\delta\left[E_{\mathrm{TFD}}[\rho] - \mu\left(\int \rho(\boldsymbol{r})\mathrm{d}\boldsymbol{r} - N\right)\right]}{\delta\rho(\boldsymbol{r})} = 0 \tag{2.12}$$

One then receives the TFD equation:

$$\mu - \frac{5}{3}C_1\rho(\boldsymbol{r})^{2/3} + V_{\text{ext}}(\boldsymbol{r}) + \int \frac{\rho(\boldsymbol{r}')}{|\boldsymbol{r}-\boldsymbol{r}'|}\mathrm{d}\boldsymbol{r} + C_2\rho(\boldsymbol{r})^{1/3} = 0 \tag{2.13}$$

The Lagrange multiplier μ is the chemical potential of the electrons, also known as the Fermi energy. Given μ and $V_{\text{ext}}(\boldsymbol{r})$, this equation can be solved inversely to obtain the ground-state electron density distribution.

According to the TFD approximation, the ground state energy of the system can, in principle, be obtained from a single function $\rho(\boldsymbol{r})$. Compared to the Hartree-Fock method, which requires solving N coupled equations, the TFD approximation is much simpler and has yielded satisfactory results in calculations involving alkali metal systems. However, since Equation 2.10 is derived from the uniform electron gas model and does not consider electron correlation effects, the TFD approximation is less effective for systems with strong bonding directionality, such as ionic or covalent bond systems. The rigorous DFT and its practical algorithms were introduced by Hohenberg, Kohn, and Sham over thirty years after the TFD approximation was proposed.

To overcome these limitations, DFT was developed based on the Hohenberg-Kohn theorems and the Kohn-Sham equations, which extend and improve upon the TFD approximation. The Hohenberg-Kohn theorems establish that the ground state density of a multi-electron system uniquely determines its ground state properties, creating a one-to-one correspondence between the electron density and the many-electron Hamiltonian. The Kohn-Sham equations further simplify the problem by converting the interactions between electrons into a set of single-electron equations. These equations include an effective external potential for electron-nucleus attraction, Coulomb repulsion, and exchange-correlation effects. Solving the Kohn-Sham equations provides the Kohn-Sham orbitals, which yield the electron density and allow for calculating the system's ground state energy.

2.2.2.2. Hohenberg-Kohn Theorem

The Hohenberg-Kohn theorem establishes the functional relationship between the system's energy and the electron density distribution, allowing the many-body problem to be rigorously transformed into a single-body problem. Therefore, it is the foundation of modern density functional theory. The theorem consists of two main parts.

Hohenberg-Kohn Theorem 2.1: The external potential $V_{\text{ext}}(\boldsymbol{r})$ experienced by any system of interacting particles is uniquely determined, except for a constant factor, by the ground state electron density distribution $\rho^0(\boldsymbol{r})$.

Corollary 2.1: Since $V_{\text{ext}}(\boldsymbol{r})$ determines the system's Hamiltonian $H(\boldsymbol{r})$, and $V_{\text{ext}}(\boldsymbol{r})$ is determined by $\rho^0(\boldsymbol{r})$, the many-electron ground state wave function Ψ^0 is completely determined by $\rho^0(\boldsymbol{r})$ and is a functional of $\rho^0(\boldsymbol{r})$.

Hohenberg-Kohn Theorem 2.2: For any electron density distribution $\tilde{\rho}(\boldsymbol{r})$, the system's energy can be defined as a functional of $\tilde{\rho}(\boldsymbol{r})$, denoted as $E[\tilde{\rho}(\boldsymbol{r})]$, which is valid for all external potential fields. Given $V_{\text{ext}}(\boldsymbol{r})$, the functional $E[\tilde{\rho}(\boldsymbol{r})]$ reaches its minimum and gives the ground state energy of the system only when the electron density distribution $\rho(\boldsymbol{r})$ is the system's ground state electron density distribution $\rho^0(\boldsymbol{r})$.

The many-body wave function is a functional of the electron density distribution $\rho^0(\boldsymbol{r})$, and determining the wave function means that all properties of the system, such as kinetic energy and electron-electron interactions, can be determined. Therefore, the system's kinetic energy and electron-electron interactions can also be expressed as functionals of $\rho^0(\boldsymbol{r})$, denoted as $T[\rho(\boldsymbol{r})]$ and $E_{\text{ee}}[\rho(\boldsymbol{r})]$, respectively. We can define the functional $F[\rho(\boldsymbol{r})]$ as:

$$F[\rho(\boldsymbol{r})] = T[\rho(\boldsymbol{r})] + E_{\text{ee}}[\rho(\boldsymbol{r})] = \left\langle \psi \left| \hat{T} + \hat{V}_{\text{ee}} \right| \psi \right\rangle \tag{2.14}$$

This is the general form of the functional. This functional depends only on $\rho(\boldsymbol{r})$ and is independent of the external potential V_{ext} $(\boldsymbol{r})$. For any $V_{\text{ext}}(\boldsymbol{r})$, the Hohenberg-Kohn energy functional $E^{\text{HK}}\left[\rho(\boldsymbol{r}), V_{\text{ext}}(\boldsymbol{r})\right]$ can be defined as:

$$E^{\text{HK}}\left[\rho(\boldsymbol{r}), V_{\text{ext}}(\boldsymbol{r})\right] = T[\rho(\boldsymbol{r})] + E_{\text{ee}}[\rho(\boldsymbol{r})] + \int V_{\text{ext}}(\boldsymbol{r})\rho(\boldsymbol{r})\mathrm{d}\boldsymbol{r} + E_{\text{II}}\left(\{\boldsymbol{R}_{\text{I}}\}\right) \tag{2.15}$$

If a given V_{ext}^0 $(\boldsymbol{r})$ has a corresponding ground state electron density $\rho^0(\boldsymbol{r})$, then the ground state energy of the system is equal to the expectation value of the Hamiltonian H^0 with respect to the ground state many-body wave function $\psi^0(\boldsymbol{r})$, which is:

$$E^{\text{HK}}\left[\rho^0, V_{\text{ext}}^0\right] = \left\langle \psi^0 \left| H^0 \right| \psi^0 \right\rangle \tag{2.16}$$

2.2.2.3. Kohn-Sham Equation

To make DFT practically usable, Kohn and Sham proposed an approach that replaces the complex many-electron problem with an equivalent set of single-electron equations. In this approach, the real, interacting system is mapped onto a hypothetical system of non-interacting electrons that move in an effective potential, $V_{\text{eff}}(\boldsymbol{r})$. This effective potential includes contributions from the external potential (due to the nuclei), the Coulomb interaction among the electron densities (Hartree term), and the exchange-correlation interactions between electrons.

The Kohn-Sham formalism simplifies the DFT framework by defining a set of single-electron equations that each electron interacts with the effective potential. This allows the complex many-body Schrödinger equation to be rewritten in terms of a set of independent particle equations:

$$\left[\sum_{i=1}^{N}\left(-\frac{1}{2}\nabla_i^2+V_{\text{eff}}\right)\right]\psi(\{\boldsymbol{r}_i\})=E_{\text{elec}}\psi(\{\boldsymbol{r}_i\}) \tag{2.17}$$

Here, V_{eff} is the effective potential experienced by each electron, defined as:

$$\left(-\frac{\nabla^2}{2}+V_{\text{eff}}(\boldsymbol{r})\right)\psi_j(\boldsymbol{r})=\varepsilon_j\psi_j(\boldsymbol{r}) \tag{2.18}$$

$$V_{\text{eff}}(\boldsymbol{r})=V_{\text{ext}}(\boldsymbol{r})+V_{\text{H}}(\boldsymbol{r})+V_{\text{xc}}(\boldsymbol{r}) \tag{2.19}$$

where: $V_{\text{ext}}(\boldsymbol{r})$ represents the potential from the nuclei, $V_{\text{H}}(\boldsymbol{r})$ is the Hartree term accounting for the Coulomb interaction among electron densities, $V_{\text{xc}}(\boldsymbol{r})$ is the exchange-correlation potential, capturing the quantum mechanical exchange and correlation effects among electrons.

The electron density $\rho(\boldsymbol{r})$ is computed from the Kohn-Sham orbitals $\{\psi_j(\boldsymbol{r})\}$ as follows:

$$\rho(\boldsymbol{r})=\sum_{i=0}^{N}\psi_j^*(\boldsymbol{r})\psi_j(\boldsymbol{r}) \tag{2.20}$$

Where the set $\{\psi_j(\boldsymbol{r})\}$ represents an orthogonal set of (N) wave functions. Additionally, this equation introduces two known functionals: the kinetic energy functional of a non-interacting electron gas $T_0[\rho]$ and the Coulomb interaction between the electron densities (also known as the Hartree term) $E_{\text{H}}[\rho]$. Using atomic units $\hbar=m=e=4\pi/\varepsilon_0=1$, we have:

$$T_0[\rho]=\sum_j\left\langle\psi_j\left|-\frac{\nabla^2}{2}\right|\psi_j\right\rangle \tag{2.21}$$

$$E_H[\rho]=\int\frac{\rho(\boldsymbol{r})\rho\left(\boldsymbol{r}'\right)}{|\boldsymbol{r}-\boldsymbol{r}'|}\mathrm{d}\boldsymbol{r}\mathrm{d}\boldsymbol{r}'=\frac{1}{2}\sum_{ij}\left\langle\psi_i\psi_j\left|\frac{1}{\boldsymbol{r}}\right|\psi_i\psi_j\right\rangle \tag{2.22}$$

The difference between $T_0[\rho]+E_{\text{H}}[\rho]$ and Equation 2.14 can be attributed to the exchange-correlation functional $E_{\text{xc}}[\rho]$.

$$E_{\text{xc}}[\rho]=T[\rho]-T_0[\rho]+E_{\text{ee}}\left[\rho\right]-E_{\text{H}}[\rho] \tag{2.23}$$

Thus, using Equations 2.22 and 2.23, Equation 2.14 can be rewritten as:

$$\begin{aligned}E^{\text{HK}}\left[\rho(\boldsymbol{r}),V_{\text{ext}}(\boldsymbol{r})\right]=&\sum_j\left\langle\psi_j\left|-\frac{\boldsymbol{\nabla}^2}{2}+V_{\text{ext}}\right|\psi_j\right\rangle+\frac{1}{2}\sum_{ij}\left\langle\psi_i\psi_j\left|\frac{1}{\boldsymbol{r}}\right|\psi_i\psi_j\right\rangle\\&+E_{\text{xc}}[\rho]+E_{\text{II}}\left(\{\boldsymbol{R}_{\text{I}}\}\right)\end{aligned} \tag{2.24}$$

The so-called exchange-correlation potential V_{xc} is:

$$V_{\mathrm{xc}} = \frac{\delta E_{\mathrm{xc}}}{\delta \rho} \tag{2.25}$$

Assuming a set of eigenvalues $\{\varepsilon_j\}$ of the Kohn-Sham equations has been obtained, the total ground state energy of the system can be expressed as:

$$E_0 = \sum_j \varepsilon_j - \frac{1}{2} \iint \frac{\rho(\boldsymbol{r}')\,\rho(\boldsymbol{r})}{|\boldsymbol{r} - \boldsymbol{r}'|} \mathrm{d}\boldsymbol{r}\mathrm{d}\boldsymbol{r}' + E_{\mathrm{xc}}[\rho(\boldsymbol{r})] - \int V_{\mathrm{xc}}(\boldsymbol{r})\rho(\boldsymbol{r})\mathrm{d}\boldsymbol{r} \tag{2.26}$$

The first term on the right-hand side of Equation 2.26, $\sum_j \varepsilon_j$, is referred to as the band structure energy, while the last three terms are called the double counting terms (d.c.).

2.2.2.4. Exchange-Correlation Functional

The core idea of DFT is to derive a result that is easy to compute but not entirely accurate by making approximations. All the unknown and difficult-to-calculate contributions are included in the exchange-correlation energy. Therefore, this term's accuracy directly determines the computational accuracy of the Kohn-Sham equations. Researchers typically seek suitable approximation methods to handle the exchange-correlation energy in practical applications.

In real systems, the charge distribution often exhibits significant fluctuations and anisotropy. To utilize the results of the uniform electron gas, the simplest approach is to treat the calculation of $E_{\mathrm{xc}}[\rho]$ as a weighted sum of the exchange-correlation energy density $\varepsilon_{\mathrm{xc}}[\rho(\boldsymbol{r})]$, determined only by the local charge density $\rho(\boldsymbol{r})$ at each discrete point $\boldsymbol{r}$, with the weight being $\rho(\boldsymbol{r})$. That is,

$$E_{\mathrm{xc}}[\rho] = \int \varepsilon_{\mathrm{xc}}[\rho(\boldsymbol{r}), \boldsymbol{r}]\rho(\boldsymbol{r})\mathrm{d}\boldsymbol{r} \tag{2.27}$$

This approach is known as the local density approximation (LDA). In LDA, $\varepsilon_{\mathrm{xc}}[\rho]$ is divided into the exchange energy density $\varepsilon_x[\rho]$ and the correlation energy density $\varepsilon_c[\rho]$. $\varepsilon_x[\rho]$ is generally given by the results for a uniform electron gas (see equation (3.109)). However, $\varepsilon_c[\rho]$ typically does not have a strict analytical solution, and its expression is mainly based on the quantum Monte Carlo (QMC) simulations of the uniform electron gas by Ceperley and Alder. [195] In practical applications, to avoid extensive computations, a fitted functional form is often used to approximate ε_{c}.

In actual solid systems, the distribution of electron clouds within the crystal is not uniform. Therefore, a natural improvement to the LDA is to introduce the gradient of the electron density and higher-order derivative terms into the exchange-correlation term. This approach is

collectively known as the generalized gradient approximation (GGA). To include the correction of the gradient of the electron density, $E_{\mathrm{xc}}[\rho]$ can be expressed as:

$$E_{\mathrm{xc}}[\rho] = \int \varepsilon_{\mathrm{xc}}[\rho(\boldsymbol{r}), \nabla\rho(\boldsymbol{r})]\rho(\boldsymbol{r})\mathrm{d}\boldsymbol{r} \tag{2.28}$$

The most commonly used GGA functionals are Becke-Lee-Yang-Parr(BLYP)[196, 197], Perdew-Wang (PW91)[198], and Perdew-Burke-Ernzerhof (PBE)[199]. In this thesis, most calculations use PBE and BEEF-vdW[200, 201].

Typically, due to the consideration of corrections to the electron density gradient, the computational results of GGA (Generalized Gradient Approximation) functionals are more accurate than those of LDA (Local Density Approximation) functionals. This is mainly reflected in the fact that values for atomic energies, crystal binding energies, bond lengths, bond angles, and other properties in GGA are closer to experimental results.

The PW91 and PBE functionals are widely used to calculate various crystal properties. When calculating the adsorption energy of various molecules on noble metal surfaces, both forms of GGA functionals tend to overestimate the adsorption energy. To accurately calculate the adsorption energy of molecules on noble metal surfaces, it is necessary to introduce self-energy corrections or Van-der-Waals (vdW) interaction.

In DFT calculations, the self-interaction terms and exchange terms do not cancel each other out, leading to significant errors. To address this issue, hybrid functional methods incorporate a portion of the exact Hartree-Fock exchange into the exchange-correlation potential expression. Examples of such functionals include B3LYP[202], HSE03[203–205], and HSE06[206].

These hybrid functionals have been widely used in quantum chemistry calculations based on localized basis sets. However, in plane-wave-based programs, the application is somewhat limited due to the computational difficulty of non-local exchange terms. Recently developed hybrid functionals like HSE06 mitigate this by decomposing the exchange term into long-range and short-range components, incorporating the exact exchange potential only for the short-range part. This reduces the computational load and facilitates the application of hybrid functionals in plane-wave-based density functional programs.

In hybrid functionals, the exchange-correlation energy of the system is often expressed as:

$$E_{\mathrm{xc}}^{\mathrm{HF}} = \alpha E_{\mathrm{x}}^{\mathrm{HF}} + (1-\alpha)E_{\mathrm{x}}^{\mathrm{DFT}} + E_{\mathrm{c}}^{\mathrm{DFT}} \tag{2.29}$$

where α is an adjustable parameter, in HSE03 and HSE06, α is typically set to 0.25.

2.2.2.5. vdW-Dispersion Energy Correction

Many traditional exchange-correlation functionals, such as B3LYP, completely fail to describe dispersion interactions due to the incorrect long-range behavior of the correlation potential.

Similarly, commonly used functionals like PBE and PW91 perform very poorly in describing dispersion interactions. Consequently, their application to problems dominated by dispersion interactions yields highly inaccurate results, such as in the cases of physisorption, the conformations of large molecules like long-chain alkanes, and weakly polar molecular clusters. The most effective method to address the poor performance of these functionals in describing dispersion interactions is to introduce empirical dispersion correction terms. Various dispersion correction methods have been proposed, including TS[207], XDM[208], VV10[209], and others. Among these, the most successful and currently the most popular method is DFT-D[210–213], proposed by Grimme. In this thesis, Grimme's D3 dispersion correction (zero damping) has been used.

DFT-D3 has two versions, Zero-damping (D3(0)) and Becke-Johnson Damping (D3(BJ)), differing in the form of the damping function. The damping function is used to adjust the behavior of dispersion corrections at short and intermediate ranges to avoid double-counting issues. Traditional DFT functionals can describe short-range interactions well, so if the correction energy remains significant at short distances, it will result in double-counting.

In this thesis, the D3(0) variant has been used. This version uses a zero-damping function, which does not modify the dispersion energy at short distances. It ensures that the dispersion correction does not overlap significantly with the interactions already accounted for by the DFT functional at close range.

The DFT-D3 corrected energy added to the originally generalized calculated system energy is the corrected energy. The DFT-D3 corrected energy based on zero damping is written as:

$$E_{\text{disp}}^{\text{DFT-D3}} = -\frac{1}{2}\sum_{A\neq B}\sum_{n=6,8} s_n \frac{C_n^{AB}}{R_{AB}^n} f_{\text{damp},n}\left(R_{AB}\right) \tag{2.30}$$

Where R_{AB} represents the distance between AB atoms, and the superscript n represents the nth power of the distance. c is the interatomic dispersion correction factor, and s_n is the scale factor. The expression for the zero damping function f is:

$$f_{\text{damp},n}\left(R_{AB}\right) = \frac{1}{1+6\left[R_{AB}/\left(s_{r,n}A_0^{AB}\right)\right]^{-\gamma}} \tag{2.31}$$

Where R_{AB}^0 is the truncation radius of the atom pair, $s_{r,n}$ is the scale factor, and γ is a preset constant. It is called zero damping because the damping function smoothly reduces the dispersion correction at short interatomic distances, preventing an overestimation of dispersion effects in the DFT calculations. This approach ensures that the DFT-D3 correction is negligible for short distances, where electronic interactions are already well-represented by the underlying DFT method.

This damping function is crucial for accurately incorporating dispersion interactions without

interfering with the inherent capabilities of the DFT functional to describe short-range correlations.

2.2.2.6. Strong Correlation and DFT+U Method

For strongly correlated systems, such as transition metal oxides or rare earth element compounds, the LDA and GGA methods encounter significant issues. These systems typically have partially filled d or f orbitals, and due to the complexity and itinerancy of the electron cloud in these orbitals, the many-body effects are difficult to describe with LDA or GGA functionals accurately. To address this, DFT+U was proposed to improve the description of systems with strongly correlated d or f electrons, like antiferromagnetic NiO, which are usually inaccurately described with the standard LDA and GGA functionals. [214]

In this thesis, the simplified (rotationally invariant) approach to the DFT+U, introduced by Dudarev et al.[115] is of the following form:

$$E_{\mathrm{DFT+U}} = E_{\mathrm{LSDA}} + \frac{(U-J)}{2} \sum_{\sigma} \left[\left(\sum_{m_1} n^{\sigma}_{m_1,m_1} \right) - \left(\sum_{m_1,m_2} \hat{n}^{\sigma}_{m_1,m_2} \hat{n}^{\sigma}_{m_2,m_1} \right) \right] \tag{2.32}$$

This can be understood as adding a penalty functional to the semilocal total energy expression that drives the on-site occupancy matrix toward idempotency, expressed as $\hat{n}^{\sigma} = \hat{n}^{\sigma}\hat{n}^{\sigma}$. In Dudarev's approach, the parameters U and J are not entered separately; only the difference $U - J$ is meaningful.

2.3. Transition State Search

In the process of a system transitioning from one state to another, it needs to overcome some form of energy barrier. Suppose a system has N degrees of freedom; then the position of the system is described by an N-dimensional vector, meaning the system exists in an N-dimensional space. The coordinates of two adjacent stable states of the system are $\boldsymbol{R}_1^N$ and $\boldsymbol{R}_2^N$, respectively. There are infinitely many pathways connecting these two stable states. Therefore, the transition pathway refers to the minimum energy path (MEP). By moving along this path, the system only needs to cross the lowest energy barrier to complete the transition. The highest point on the MEP is a first-order saddle point of the system. At this point, the energy reaches a maximum along the direction of the MEP, while in any other direction, it is a minimum. This means that the phonon spectrum at this point contains only one vibrational mode with an imaginary frequency. In this mode, atoms vibrate along the direction of the minimum energy path. Accordingly, the transition state (TS) refers to this first-order saddle point on the MEP. In this thesis, the nudged elastic band (NEB) and dimer methods are used to search for the transition states.

2.3.1. Nudged Elastic Band Method

The Nudged Elastic Band (NEB) method, proposed by Mills, Jónsson, and others, can provide the MEP containing multiple saddle points. [215–218]Suppose a system moves between the initial and final states, with each position referred to as an image. Imagine these images simultaneously appearing on the reaction pathway, connected by springs with a stiffness constant k. The initial and final states at the two endpoints remain fixed, while the intermediate images are allowed to relax with all degrees of freedom. Unlike the drag method, the images in the NEB method are coupled to each other by springs, and the images participating in the relaxation do not slip back to the endpoints due to the spring resistance. In this context, the force on image i is given by:

$$\mathbf{F}_i = \mathbf{F}_i^{\perp} + \mathbf{F}_i^{\parallel} \tag{2.33}$$

where:
$\mathbf{F}_i^{\perp}$ is the component of the true force perpendicular to the path, which drives the images to the MEP.
$\mathbf{F}_i^{\parallel}$ is the component of the spring force parallel to the path, which maintains even spacing between images.

The total force on image i can be expressed as:

$$\mathbf{F}_i = -\nabla V(\mathbf{R}_i)^{\perp} + k\left(|\mathbf{R}_{i+1} - \mathbf{R}_i| - |\mathbf{R}_i - \mathbf{R}_{i-1}|\right)\hat{\tau} \tag{2.34}$$

where:
$\nabla V(\mathbf{R}_i)^{\perp}$ is the gradient of the potential energy at image i, projected perpendicular to the path.
k is the spring constant.
$\mathbf{R}_{i+1}$ and $\mathbf{R}_{i-1}$ are the positions of the neighboring images.
$\hat{\tau}$ is the unit tangent vector to the path at image i.

This force ensures the images relax to the MEP without slipping back to the endpoints, effectively finding the transition states along the path.

2.3.2. Dimer Method

The dimer method is a means of finding a saddle point on a potential energy surface starting from a known initial state. It automatically searches for all possible transition pathways using a specific algorithm. [219]

Figure 2.1(a) illustrates a dimer. The positions, energies, and forces of the two images are $\mathbf{R}_1$, E_1, $\boldsymbol{F}_1$ and $\mathbf{R}_2$, E_2, $\boldsymbol{F}_2$, respectively. The unit vector $\hat{\boldsymbol{N}}$ points from $\boldsymbol{R}_2$ to $\boldsymbol{R}_1$. The midpoint of this dimer is $\mathbf{R}$. Therefore, we have:

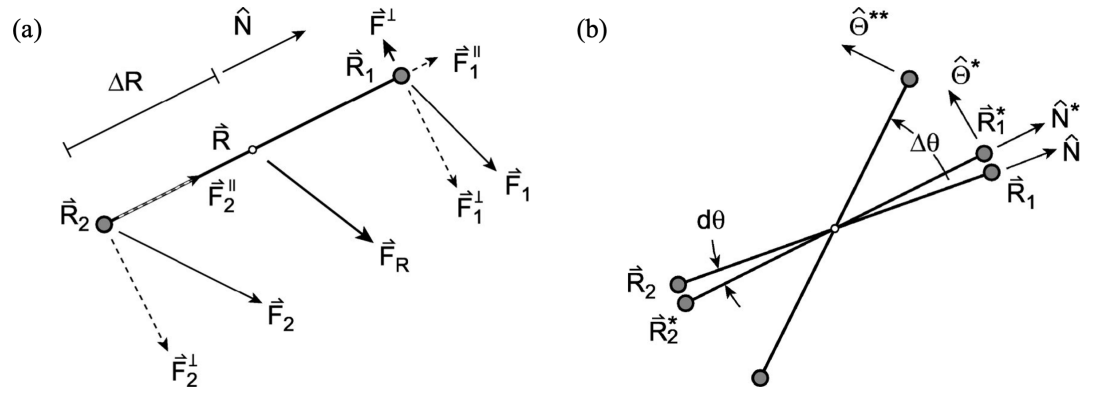

Figure 2.1: The application of the Dimer method. (a) Definition of the various position and force vectors of the dimer. The rotational force on the dimer, $\mathbf{F}^{\perp}$, is the net force acting on image 1 perpendicular to the direction of the dimer. (b) Definition of the various quantities involved in rotating the dimer. All vectors are in the plane of rotation. Obtained from Ref.[219] with permission.

$$\boldsymbol{R}_1 = \boldsymbol{R} + \Delta R\hat{\mathbf{N}}, \quad \boldsymbol{R}_2 = \boldsymbol{R} - \Delta R\hat{\mathbf{N}}, \quad \Delta R = \frac{1}{2}\left(\boldsymbol{R}_1 - \boldsymbol{R}_2\right) \cdot \hat{\boldsymbol{N}} \tag{2.35}$$

The dimer is defined in a $3N$-dimensional space rather than just by two points in a three-dimensional space, as shown in Figure 2.1. The total energy of the system is $E = E_1 + E_2$. The energy at the center of the dipole moment is E_0, and the force is $\boldsymbol{F}_{\mathrm{R}}$, defined as $\boldsymbol{F}_{\mathrm{R}} = \left(\boldsymbol{F}_1 + \boldsymbol{F}_2\right)/2$. Thus, the curvature of the potential energy surface at this point can be calculated using finite differences and the definition:

$$C = \frac{\left(\boldsymbol{F}_2 - \boldsymbol{F}_1\right) \cdot \hat{\mathbf{N}}}{2\Delta R} = \frac{E - 2E_0}{(\Delta R)^2} \tag{2.36}$$

In the Dimer method, each step is divided into two parts: first, the dipole moment is rotated to align with the path of the lowest energy barrier transition; then, it is translated along the transition path to reach the saddle point.

2.4. Harmonic Approximation in Vibrational Analysis

The purpose of the vibrational analysis is to calculate the vibrational frequencies of various vibrational modes of a system, primarily for two key applications: comparison with experimental IR spectra and thermodynamic calculations. Understanding the vibrational frequencies allows for a detailed comparison of theoretical IR spectra with experimental results, providing insights into the accuracy of the model and the atomic interactions within the system. Additionally, vibrational frequencies are essential for thermodynamic analyses, as they contribute to calculations of properties like entropy.

Calculating vibrational frequencies requires solving the Schrödinger equation for the nuclei on the actual potential energy surface, which is time-consuming and complex. Typically, vibra-

tional analysis is performed based on harmonic approximation, which simplifies the solution by approximating the vibrations of the chemical system to those of a harmonic oscillator system. The force constants of the oscillators are obtained from the curvature of the potential energy surface at the minimum point where the vibrational analysis is conducted. Vibrational analysis under the harmonic approximation is usually sufficient for general research needs. One must consider anharmonic effects and the coupling between different vibrational modes to perform vibrational analysis more rigorously than the harmonic approximation.

Normal mode analysis is a method that calculates the vibrational frequencies and modes of a molecule by modeling atoms as masses connected by springs. For a molecule with N atoms, the number of vibrational modes is $3N-6$ for non-linear molecules or $3N-5$ for linear molecules. Near the equilibrium geometry, the potential energy surface can be approximated as a quadratic function of atomic displacements, leading to the harmonic approximation, which simplifies the vibrations to those of a harmonic oscillator.

In this approximation, the potential energy V around the equilibrium configuration is expanded as:

$$V = V_0 + \frac{1}{2}\sum_{i,j}\left(\frac{\partial^2 V}{\partial x_i \partial x_j}\right)_0 \Delta x_i \Delta x_j \tag{2.37}$$

where V_0 is the potential energy at equilibrium, and Δx_i are the displacements of atoms from equilibrium. The Hessian matrix is the matrix of second derivatives of the system's potential energy with respect to atomic coordinates, and it is $3N$-dimensional (where N is the number of atoms). The matrix elements are expressed as:

$$\boldsymbol{H}_{i,j} = \frac{\partial^2 E}{\partial \xi_i \partial \xi_j} \tag{2.38}$$

where ξ represents the Cartesian coordinates.

The Hessian matrix is essential because its eigenvalues correspond to the squares of the vibrational frequencies, while its eigenvectors describe the vibrational modes of the system. Therefore, the Hessian matrix allows us to determine both the frequencies and the specific patterns of atomic motion associated with each vibrational mode.

To accurately reflect the vibrational modes in terms of the actual atomic masses, the Hessian matrix needs to be transformed into mass-weighted Cartesian coordinates $\{q\}$, resulting in the force constant matrix, $\boldsymbol{F}$. This transformation from non-mass-weighted coordinates $\{\xi\}$ to mass-weighted coordinates $\{q\}$ is achieved using the relation:

$$\boldsymbol{F} = \boldsymbol{M}^{-1/2}\boldsymbol{H}\boldsymbol{M}^{-1/2} \tag{2.39}$$

where $\boldsymbol{M}$ is the mass matrix. The elements of the force constant matrix are given by:

$$\boldsymbol{F}_{i,j} = \frac{\boldsymbol{H}_{i,j}}{\sqrt{\boldsymbol{M}_{i,i}\boldsymbol{M}_{j,j}}} = \frac{\partial^2 E}{\partial q_i \partial q_j} \tag{2.40}$$

Here, $q_i = \sqrt{m_A}\xi_i$, with m_A being the mass of the atom associated with the i-th Cartesian coordinate. This mass-weighting step decouples the motion of the nuclei, allowing each vibrational mode to be treated as an independent 1D harmonic oscillator.

After diagonalizing $\boldsymbol{F}$, we obtain $3N$ eigenvalues $\{\lambda\}$ and $3N$ eigenvectors $\{\mathbf{d}\}$:

$$\boldsymbol{F}\mathbf{d}_i = \lambda_i \mathbf{d}_i \tag{2.41}$$

Here, $\mathbf{d}_i$ is the (mass-weighted) normal coordinate or vibrational vector of the i-th vibrational mode, which describes the atomic motions corresponding to the vibrational mode using mass-weighted Cartesian coordinates. λ_i is the force constant of the corresponding vibrational mode.

Using the harmonic oscillator formula, the vibrational frequency ν and wavenumber $\tilde{\nu}$ can be determined from the force constant:

$$\nu_i = \frac{\sqrt{\lambda_i}}{2\pi} \quad \tilde{\nu}_i = \frac{\nu_i}{c} \tag{2.42}$$

where c is the speed of light. When λ is negative, the calculated vibrational frequency is imaginary, indicating that the curvature of the potential energy surface is negative in the direction of the normal coordinate at the current position. At the minimum point of the potential energy surface, all frequencies are real.

2.5. Thermodynamics

The thermodynamic model for catalytic reactions is constructed using the partition function, which includes contributions from translational, rotational, and vibrational modes. These contributions help compute thermodynamic properties like entropy (S), enthalpy (H), and Gibbs free energy (G). G and H of a system are given by the fundamental thermodynamic relations:

$$\Delta G = \Delta H - T\Delta S \tag{2.43}$$

$$\Delta H = \Delta U + P\Delta V \tag{2.44}$$

where T is temperature, P is pressure, and U is internal energy. Following statistical mechanics, U and S can be defined using the partition function Q:

$$U = k_B T^2 (\frac{\partial \ln Q}{\partial T})_{N,V} \tag{2.45}$$

$$S = k_B T \ln Q + k_B T (\frac{\partial \ln Q}{\partial T})_{N,V} \tag{2.46}$$

where k_B is the Boltzmann constant, N represents the number of particles in the system, and V represents the volume of the system. The total partition function is given by:

$$q_{\text{total}} = q_{\text{translation}} \times q_{\text{rotation}} \times q_{\text{vibration}} \times q_{\text{elec}} \tag{2.47}$$

Similarly, the entropy of a system also consists of these four different contributions:

$$S_{\text{total}} = S_{\text{translation}} + S_{\text{rotation}} + S_{\text{vibration}} + S_{\text{elec}} \tag{2.48}$$

This section describes how each of these partition functions contributes to the overall thermodynamic properties of the system.

2.5.1. Ideal Gas Approximation

The translational partition function accounts for the motion of molecules in three-dimensional space and is given by:

$$q_{\text{translation}} = \left(\frac{2\pi m k_B T}{h^2} \right)^{3/2} V \tag{2.49}$$

where m represents the mass. The corresponding entropy contribution due to translational motion is:

$$S_{\text{trans}} = k_B (\ln(\frac{k_B T}{P} (\frac{2\pi m k_B T}{h^2})^{3/2}) + \frac{5}{2}) \tag{2.50}$$

The rotational partition function depends on the type of molecule (linear or nonlinear). For nonlinear polyatomic molecules, it is expressed as:

$$q_{\text{rotation}} = \frac{\sqrt{\pi}}{\sigma} (\frac{8\pi^2 k_B T}{h^2})^{3/2} \sqrt{I_x I_y I_z} \tag{2.51}$$

where $I_{x,y,z}$ are the moments of inertia. The entropy contribution from rotational motion varies depending on the molecular geometry:

- linear molecules:

$$S_{\text{rot}} = k_B [1 + \ln(\frac{8\pi^2 I k_B T}{\sigma h^2})] \tag{2.52}$$

- nonlinear molecules

$$S_{\text{rot}} = \frac{1}{2}k_B[3 + \ln(\frac{\pi}{\sqrt{\sigma}}(\frac{8\pi^2 k_B T}{h^2})^3 I_x I_y I_z)] \tag{2.53}$$

where σ is the symmetry number. The harmonic vibrational partition function is important for describing the contribution of vibrational modes to the thermodynamic properties:

$$q_{\text{vibration}} = \prod_{i=1}^{3N-6} \frac{1}{1 - \exp(-\hbar\omega_i k_b T)} \tag{2.54}$$

where ω_i is the vibrational frequency. The entropy contribution from vibrational motion is given by:

$$S_{\text{vib}} = k_B \sum_{i=1}^{3N-6} [\frac{\hbar\omega_i}{k_B T(\exp(\hbar\omega_i/k_B T) - 1)} - \ln(1 - \exp(-\hbar\omega_i/k_B T))] \tag{2.55}$$

For many systems, only the electronic ground state is considered, resulting in a simple electronic partition function:

$$q_{\text{elec}} = 1 \tag{2.56}$$

The entropy contribution from electronic states is:

$$S_{\text{elec}} = k_B \ln(2s + 1) \tag{2.57}$$

where s is the spin of the system.

The enthalpy of an ideal gas was calculated by extrapolating the energy from 0 K to the real temperature:

$$H(T) = E_{\text{elec}} + E_{\text{ZPE}} + \int_0^T C_p \, dT \tag{2.58}$$

E_{elec} represents the electronic energy. $\int_0^T C_p \, dT$ is the integral of the heat capacity C_p with respect to temperature from 0 to T. It represents the energy required to heat the system from 0 K to the temperature T, where C_p is the heat capacity at constant pressure. E_{ZPE} stands for the Zero Point Energy (ZPE), which is the lowest possible energy that a quantum mechanical system may have, even at absolute zero temperature. It's the energy that remains when the system is at its ground state.

$$E_{\mathrm{ZPE}} = \sum_{i=1}^{N_{\mathrm{modes}}} \frac{1}{2} h\omega_i \tag{2.59}$$

2.5.2. Harmonic Oscillator Approximation

For adsorbed molecules on catalytic surfaces, the translational and rotational modes are restricted, making vibrational modes the primary contributors to thermodynamic properties. These vibrational modes are modeled using the harmonic oscillator approximation.

The internal energy for the harmonic oscillator model is:

$$U(T) = E_{\mathrm{electronic}} + E_{\mathrm{ZPE}} + \sum_i \frac{\hbar\omega_i}{e^{\hbar\omega_i/k_BT} - 1} \tag{2.60}$$

The entropy contribution from vibrational modes is:

$$S = k_B \sum_i [\frac{\hbar\omega_i}{k_BT(e^{\hbar\omega_i/k_BT} - 1)} - \ln(1 - e^{-\hbar\omega_i/k_BT})] \tag{2.61}$$

2.5.3. Surface Free Energy

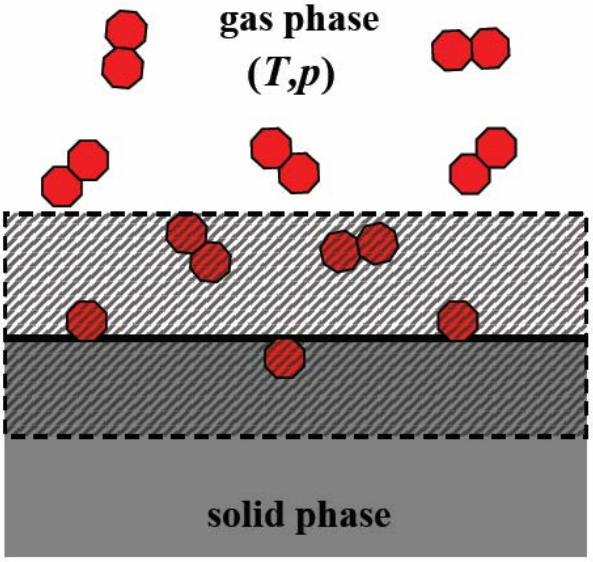

Figure 2.2: Schematic representation of the system discussed here, a single-crystal metal surface in contact with a surrounding gas phase characterized by defined temperature T and pressure p. The shaded area represents the finite part of the system that is affected by the presence of the surface. Reprinted with permission from *NATO Research and Technology Organization (RTO)* **2007**, RTO-EN-AVT-142.[220].

Figure 2.2 shows a schematic representation of the system discussed here, a solid phase in contact with a surrounding gas phase. The Gibbs free energy for the entire system can be described as:

$$G = G_{\text{solid}} + G_{\text{gas}} + \Delta G_{\text{surf}} \tag{2.62}$$

where G_{solid}, G_{gas} and ΔG_{surf} is the Gibbs free energy contribution from the bulk of the solid phase, homogeneous gas phase and an additional term introduced through the surface respectively.

The surface energy, ΔG_{surf}, accounts for the energy required to create a surface by cleaving the bulk material. This process exposes atoms at the surface, leaving them with unsaturated bonds. These surface atoms may then interact with gas-phase molecules to achieve a stable configuration, such as by bond formation or adsorption. As a result, surface energy includes both the energetic cost of creating the surface and the contribution from any reactions or interactions with the gas phase that stabilize the surface atoms. For example, $RuO_2(110)$ surface stability depends on oxygen pressure, with stoichiometric termination only favorable at low oxygen chemical potentials.[221]

If the surface is homogeneous as in the case of an ideal single-crystal surface, ΔG_{surf} will scale linearly with the surface area A, and the surface free energy per unit, γ can be described as:

$$\gamma = \frac{1}{A}(G - G_{\text{solid}} - G_{\text{gas}}) \tag{2.63}$$

Here, we assume the system is a metal oxide(M_zO_y) surface slab in an oxygen atmosphere. The Gibbs free energy can be written as $G(T, p, N_{\text{M}}, N_{\text{O}})$, which depends on the number of metals, N_{M} and O, N_{O} atoms in the slab. The most stable surface composition and geometry is the one that minimizes the $\gamma(T, p)$:

$$\gamma(T, p) = \frac{1}{A}[G(T, p, N_{\text{M}}, N_{\text{O}}) - N_{\text{M}}\mu_{\text{M}}(T, p) - N_{\text{O}}\mu_{\text{O}}(T, p)] \tag{2.64}$$

where μ_{M} and μ_{O} are the chemical potentials of a metal atom and an O atom, respectively. Since:

$$g^{\text{bulk}}_{\text{M}_z\text{O}_y}(T, p) = x\mu_{\text{M}}(T, p) + y\mu_{\text{O}}(T, p) \tag{2.65}$$

where g is the Gibbs free energy per formula unit for M_zO_y. The Eq. 2.64 can be rewritten as:

$$\gamma(T, p) = \frac{1}{A}[G^{\text{slab}}(T, p, N_{\text{M}}, N_{\text{O}}) - N_{\text{M}}g^{\text{bulk}}_{\text{M}_z\text{O}_y}(T, p) + (yN_{\text{M}} - xN_{\text{O}})\mu_{\text{O}}(T, p)] \tag{2.66}$$

It is important to note that, experimentally, assuming thermodynamic equilibrium, μ_{O} cannot be varied indefinitely. If μ_{O} becomes too low, all oxygen would leave the sample, leading to the

decomposition of the oxide into solid metal and oxygen gas. This process would start with the formation of metal crystallites at the surface.

$$\max[\mu_{\mathrm{M}}(T,p)] = g_{\mathrm{M}}^{\mathrm{bulk}}(T,p) \tag{2.67}$$

Together with Eq. 2.65 and $T = 0$ K and $p = 0$ atm limit for the bulk energies, we can get:

$$\min[\mu_{\mathrm{O}}(T,p)] = \frac{1}{y}[g_{\mathrm{M_zO_y}}^{\mathrm{bulk}}(0,0) - xg_{\mathrm{M}}^{\mathrm{bulk}}(0,0)] \tag{2.68}$$

On the other hand, the most oxygen-rich conditions can be defined as the point beyond which gas phase O would start to condense on the sample. Thus, the upper limit of the oxygen chemical potential is:

$$\max[\mu_{\mathrm{O}}(T,p)] = 1/2E_{\mathrm{O_2}^{\mathrm{total}}} \tag{2.69}$$

where $E_{\mathrm{O_2}^{\mathrm{total}}}$ is the total energy of a single O_2 molecule in vacuum at $T = 0$ K.

Since the Gibbs free energy of formation, $\Delta G_f(T,p)$ of the oxide can be described as:

$$\Delta G_f(T,p) = g_{\mathrm{M_zO_y}}^{\mathrm{bulk}}(T,p) - xg_{\mathrm{M}}^{\mathrm{bulk}}(T,p) - \frac{y}{2}g_{\mathrm{O_2}}^{\mathrm{gas}}(T,p) \tag{2.70}$$

So, the range of oxygen chemical potentials between the theoretical boundaries is:

$$\frac{y}{2}\Delta G_f(0,0) < \mu_{\mathrm{O}}(T,p) - \frac{1}{2}E_{\mathrm{O_2}}^{\mathrm{total}} < 0. \tag{2.71}$$

Which can be also written as:

$$\begin{aligned}&\frac{1}{y}[g_{\mathrm{M_zO_y}}^{\mathrm{bulk}}(0,0) - xg_{\mathrm{M}}^{\mathrm{bulk}}(0,0)] < \mu_{\mathrm{O}}(T,p)\\ &< \frac{1}{y}[g_{\mathrm{M_zO_y}}^{\mathrm{bulk}}(0,0) - xg_{\mathrm{M}}^{\mathrm{bulk}}(0,0)] + \frac{y}{2}\Delta G_f(0,0)\end{aligned} \tag{2.72}$$

The expression of $\mu_{\mathrm{O}}(T,p)$ is:

$$\mu_{\mathrm{O}}(T,p) = \mu_{\mathrm{O}}(T,p^\circ) + \frac{1}{2}kT\ln(\frac{p}{p^\circ}) \tag{2.73}$$

Which depends on the temperature and pressure. If we only know the temperature dependence of $\mu_{\mathrm{O}}(T,p^\circ)$ at one particular pressure, p°. We choose the zero reference state of $\mu_{\mathrm{O}}(T,p)$ to be the total energy of oxygen in an isolated molecule, i.e., $\mu_{\mathrm{O}}(0\,\mathrm{K},p) = \frac{1}{2}E_{\mathrm{O_2}}^{\mathrm{total}} \equiv 0$. $\mu_{\mathrm{O}}(T,p^\circ)$ is then given by

$$\begin{aligned}\mu_{\mathrm{O}}(T, p^{\circ}) &= \mu_{\mathrm{O}}^{\text{O-rich}}(0\,\mathrm{K}, p^{\circ}) + \frac{1}{2}\Delta G(\Delta T, p^{\circ}, \mathrm{O}_2) \\ &= \frac{1}{2}[H(T, p^{\circ}, \mathrm{O}_2) - H(0\,\mathrm{K}, p^{\circ}, \mathrm{O}_2)] \\ &- \frac{1}{2}T[S(T, p^{\circ}, \mathrm{O}_2) - S(0\,\mathrm{K}, p^{\circ}, \mathrm{O}_2)],\end{aligned} \tag{2.74}$$

2.6. Markov Chain Monte-Carlo Method

A Markov process is a typical stochastic process. Let $x(t)$ be a stochastic process. When the state of the process at time t_0 is known, the state at time t (where $t > t_0$) is independent of the states of the process before t_0. This property is known as the Markov property, or memorylessness. A stochastic process with the Markov property is called a Markov process. In a Markov process, both time and state can be either continuous or discrete. The Markov chain is a sequence of random variables where the probability of each state depends only on the previous state. Markov Chain is described by a transition matrix P where P_{ij} is the probability of moving from state i to state j. The stationary distribution π is defined as a distribution that remains unchanged when the transition matrix P is applied, meaning it satisfies the condition $\pi P = \pi$. The MCMC methods aim to construct a Markov chain whose stationary distribution is the target distribution we wish to sample.

The Metropolis-Hastings algorithm is one of the most widely used MCMC methods. It provides a way to construct a Markov chain that converges to a target distribution π. The steps of the Metropolis-Hastings Algorithm can be described as:

1. Initialization: Start with an initial state x_0.
2. Proposal Step: Generate a candidate state y from a proposal distribution $q(x, y)$ based on the current state x.
3. Acceptance Probability: Calculate the acceptance probability $\alpha(x, y)$ using:

$$\alpha(x, y) = \min\left(1, \frac{\pi(y)q(y, x)}{\pi(x)q(x, y)}\right) \tag{2.75}$$

   Here, π is the target distribution, and q is the proposal distribution.
4. Acceptance/Rejection Step: Generate a random number u from the uniform distribution $U(0, 1)$.
   If $u \leq \alpha(x, y)$, accept y as the next state; otherwise, retain x as the next state.
5. Iteration: Repeat the proposal and acceptance steps for a large number of iterations to obtain a representative sample from the target distribution.

2.7. Gaussian Process Regression

A Gaussian Process (GP) is a stochastic process defined over a continuous domain, where any finite subset of random variables follows a multivariate Gaussian distribution. A Gaussian process can be seen as an infinite-dimensional Gaussian distribution over the input space. It is defined through a mean function and a covariance function. For any finite set of input points $X = \{x_1, x_2, ..., x_n\}$, the Gaussian process assumes that the corresponding outputs $\mathbf{f} = [f(x_1), f(x_2), ..., f(x_n)]$ follow a multivariate Gaussian distribution.

Here, we define the mean vector as:

$$\mathbf{m} = [m(x_1), m(x_2), ..., m(x_n)] \tag{2.76}$$

where $m(x_i)$ is the value of the mean function at point x_i.

The covariance matrix is as:

$$K = \begin{bmatrix} k(x_1, x_1) & k(x_1, x_2) & \cdots & k(x_1, x_n) \\ k(x_2, x_1) & k(x_2, x_2) & \cdots & k(x_2, x_n) \\ \vdots & \vdots & \ddots & \vdots \\ k(x_n, x_1) & k(x_n, x_2) & \cdots & k(x_n, x_n) \end{bmatrix} \tag{2.77}$$

where $k(x_i, x_j)$ is the value of the covariance function (also known as the kernel function) at points x_i and x_j.

Thus, the output $\mathbf{f}$ can be represented as:

$$\mathbf{f} \sim \mathcal{N}(\mathbf{m}, K) \tag{2.78}$$

In Gaussian process regression, we have the input points and the corresponding observed output values. The goal is to predict the outputs for new input points given the observed data.

Assume we have training data $D = \{(x_i, y_i)\}_{i=1}^n$, where $y_i = f(x_i) + \epsilon_i$ and $\epsilon_i \sim \mathcal{N}(0, \sigma_n^2)$ is the observation noise.

The covariance matrix of observed outputs can be written as:

$$K_y = K + \sigma_n^2 I \tag{2.79}$$

where K is the covariance matrix constructed from the training data, σ_n^2 is the variance of the observation noise, and I is the identity matrix.

Then, for a new input point x_*, we want to predict the corresponding output f_*. The joint distribution of the training data and the new data is:

$$\begin{bmatrix} \mathbf{y} \\ f_* \end{bmatrix} \sim \mathcal{N}\left(\begin{bmatrix} \mathbf{m} \\ m_* \end{bmatrix}, \begin{bmatrix} K_y & k_* \\ k_*^\top & k_{**} \end{bmatrix} \right) \tag{2.80}$$

where,

$$\mathbf{m} = [m(x_1), m(x_2), ..., m(x_n)] \tag{2.81}$$

$$k_* = [k(x_1, x_*), k(x_2, x_*), ..., k(x_n, x_*)] \tag{2.82}$$

$$k_{**} = k(x_*, x_*) \tag{2.83}$$

$$m_* = m(x_*) \tag{2.84}$$

The predictive distribution (posterior distribution) for the new point x_* can be derived from the properties of the joint Gaussian distribution:

$$f_* | X, \mathbf{y}, x_* \sim \mathcal{N}(\mu_*, \sigma_*^2) \tag{2.85}$$

where,

$$\mu_* = m_* + k_*^\top K_y^{-1}(\mathbf{y} - \mathbf{m}) \tag{2.86}$$

$$\sigma_*^2 = k_{**} - k_*^\top K_y^{-1} k_* \tag{2.87}$$

The kernel function is a critical component in Gaussian Process Regression (GPR). It defines the structure and properties of the Gaussian process by determining how input points are correlated with each other. The kernel function $k(x, x')$ measures the similarity between two input points x and x'. Points that are more similar (closer in the input space) will have higher kernel values, indicating stronger correlations between their corresponding output values. The kernel function is used to construct the covariance matrix K for the training data points X. Each element of the covariance matrix is given by:

$$K_{ij} = k(x_i, x_j) \tag{2.88}$$

This covariance matrix encapsulates the pairwise relationships between all training points.

Also, different choices of kernel functions lead to different properties of the GP model. The kernel function used in this thesis is the Squared Exponential (Radial Basis Function, RBF) Kernel. This kernel produces very smooth functions and is controlled by parameters such as the length scale ℓ (which determines how quickly correlations decay with distance) and the signal variance σ_f^2.

$$k(x, x') = \sigma_f^2 \exp\left(-\frac{(x - x')^2}{2\ell^2} \right) \tag{2.89}$$

3. Stability of Hydroxylated Oxide Surfaces at High Temperatures

This Chapter is based on [**Chen, J.**; Sharapa, D.; Plessow, P. N. Stability and formation of hydroxylated α-Al_2O_3(0001) surfaces at high temperatures. *Phys. Rev. Res.* **2022**, *4* (1). DOI: 10.1103/physrevresearch.4.013232] [**Chen, J.**; Sharapa, D. I.; Plessow, P. N. Stability of hydroxylated α-Fe_2O_3(0001) surfaces. *ACS Omega* **2024**, *9* (33). DOI: 10.1021/acsomega.4c02113].

In this chapter, we employ density functional theory (DFT) calculations to study the stability of hydroxylated α-Al_2O_3(0001) [222]and α-Fe_2O_3(0001) [223] surfaces. First, we show that more stable structures than previously predicted exist, which can be described as $Al(OH)_3$ and $Fe(OH)_3$ adsorbed with low coverage on the stoichiometric surface. After that, we study the mechanism for the formation of hydroxylated α-Al_2O_3(0001) surfaces starting from the well-known water adsorption and dissociation on the dry surface. Additionally, we also studied reduced surfaces (Fe in oxidation state +2) with and without hydroxyl groups.

3.1. Computational Details

All DFT calculations were performed using the Vienna Ab initio Simulation Package (VASP), primarily in version 5.4.1 [224, 225], with the calculations using the SCAN functional [226] done in version 5.4.4. The projector-augmented wave (PAW) method was employed using standard PAW potentials. A kinetic energy cutoff of 400 eV was used for the wave function expansion in plane waves for the calculations involving α-Al_2O_3, with an increased cutoff of 600 eV applied for the calculations involving α-Fe_2O_3. Real-space projectors were used (LREAL=AUTO in VASP), and a plane wave basis set for the electronic density was employed, which included reciprocal lattice vectors with a norm up to 3/2 times larger than those used for the wave function, $|\mathbf{G}_{\mathrm{cut}}|$ (PREC=Normal in VASP).

The main results of this study were obtained using the PBE functional [199] along with Grimme's D3 dispersion correction [212]. Other density functionals such as BEEF-vdW [201], SCAN [226], and HSE-06 [203, 206] were also tested. For the α-Fe_2O_3 surfaces, PBE+U calculations [114–117, 199] were performed with $U = 4$ eV and $J = 0$ eV [227] along with Grimme's D3 dispersion correction (zero damping) [212]. The DFT+U method was used in the form proposed by Liechtenstein and Dudarev *et al.*, [114–117] and applied to the d-orbitals of Fe.

The value of the U-parameter can be motivated by empirical fitting to reproduce properties of interest, such as lattice constants, band gaps or reaction energies. Alternatively, it can be deduced from a linear response calculation according to the underlying theory of DFT+U as a means to correct for the self-interaction error and to achieve the correct behavior of the slope of energy vs. number of electrons.[228] Linear response calculations for bulk hematite gave $U =$

3.81 eV and for most surfaces and Fe atoms a value of U in the range between 4 and 5 eV. [229] In a study, where the U-values were systematically tested for 3, 4 and 5 eV, it was concluded that 3 eV is best for the overall thermodynamic properties of iron oxides, while 4 eV gives improved band gaps and structures.[230] Our choice of $U = 4$ eV is therefore a good compromise between an empirical choice of U based on computed properties and results from the linear response approach aiming to fix fundamental shortcomings of the GGA in treating electron-correlation. Furthermore, a value of $U = 4$ eV was used in many previous studies[101, 104, 113, 126, 231] and 4.3 eV was used by Hellman and co-workers.[118, 232] In addition to the calculations with $U = 4$ eV, which are the basis for the results provided in the main text, single point calculations with $U = 3$ and 5 eV were performed and are analyzed in more detail in Section 3.2.3.1.

In addition to the value of U, using a different reference for oxygen is another approach that will change the obtained results. Alternatives to using O_2 as a reference are for example using the O-atom or (H_2O - H_2) and employing the known experimental formation energies[233] of the O-atom (2.558 eV) and H_2O (-2.476 eV). We decided to use the energy of O_2 in its triplet ground state, first and foremost, because this is the common choice of reference state in computational studies on iron oxides[76, 102, 113, 126, 229, 230, 232] and it thus facilitates the comparison with the literature. Second, we do not believe that shifting the oxygen reference provides a general solution (see discussion in the Appendix B.5). Lastly, based on the results presented here, it is easy to read off what the results would be with a different oxygen reference. In particular, using the O-atom as a reference will shift μ_O by +0.43 eV and using H_2O will shift μ_O by +0.20 eV. In both cases, this will make oxygen more reactive, i.e. it will make the formation of reduced α-Fe_2O_3 surfaces less favorable.

α-Al_2O_3 and α-Fe_2O_3 both crystallize in the corundum bulk structure, where the oxygen atoms form a hexagonal closed-packed structure (AB-stacking) in which two-thirds of the octahedral voids are filled with metal ions. In the 0001 direction, each layer contains three O^{2-} ions and two Al^{3+}/Fe^{3+} ions. The two metal ions in one layer are not identical and occupy the three possible octahedral positions alternately and can, therefore, be described as ABC stacking. Therefore, the unit cell consists of six $O_3 - Al_2/O_3 - Fe_2$ layers. The antiferromagnetic order for Fe in α-Fe_2O_3 is "++, −−" by layers along the 0001 direction[113, 234].

For α-Al_2O_3, lattice constants were optimized using an increased energy cutoff of 800 eV, and the obtained values ($a = b = 4.787$ Å, $c = 13.045$ Å). These values agree well with experimental data ($a = b = 4.763$ Å, $c = 13.003$ Å) [16]. Similarly, the lattice constants of α-Fe_2O_3 were optimized, obtaining values ($a = b = 5.053$ Å and $c = 13.824$ Å), which are in good agreement with experimental results [235], ($a = b = 5.035$ Å and $c = 13.747$ Å), as well as previous GGA+U computational results [113], $a = b = 5.067$ Å, $c = 13.882$ Å. An SCF-convergence criterion of $< 10^{-8}$ eV was used for the total energy, and a geometry convergence criterion of < 0.01 eV/Å for α-Al_2O_3 or < 0.005 eV/Å for α-Fe_2O_3 was applied for the maximum norm of individual atomic forces.

Surfaces of α-Al_2O_3 were modeled as slabs with seven formula units of Al_2O_3 per stoichiometric (1×1)-surface, and corresponding slab thicknesses for other terminations. The lower part of the slabs was terminated by a single Al-layer (stoichiometric termination), with the bottom 3.5 formula units of Al_2O_3 per (1×1)-surface frozen at their bulk positions. Slabs were separated by at least 16 Å of vacuum to prevent artificial interactions between periodic images. Similarly, α-Fe_2O_3 surfaces were modeled with symmetric slabs containing nine formula units of Fe_2O_3 per dry (1×1)-surface (approximately 19 Å thick) along with slabs of equivalent thickness for other terminations. These slabs were separated by a minimum of 24 Å of vacuum to reduce artificial interactions among periodic structures.

The Brillouin zone for α-Al_2O_3 surfaces was sampled using a Γ-centered k-point grid with a density corresponding to at least $(3 \times 3 \times 1)$ per (1×1)-α-Al_2O_3(0001) cell. For α-Fe_2O_3, a Γ-centered grid with $(4 \times 4 \times 1)$ k-points for a (1×1)-α-Fe_2O_3(0001) cell and $(2 \times 2 \times 1)$ k-points for (2×2)-cells was used. Gaussian smearing with $\sigma = 0.1$ eV was employed for all calculations.

Reaction paths were optimized using a (3×3) cell with (1×1) k-point sampling, which is smaller than the (2×2) k-point sampling used to compute the thermodynamic stability of (3×3)-surfaces. This simplification is justified because formation energies per (3×3) cell computed with the smaller k-point sampling differ by less than 0.01 eV, while total energies differ by 0.03 eV. The highest barriers of each pathway were determined explicitly, i.e. the transition states were obtained as stationary points with a maximum atomic force component of 0.01 eV/Å and it was furthermore verified that they are first-order saddle points through calculation of a partial Hessian matrix, which gives a single imaginary frequency in normal mode analysis. The connectivity of the transition state was additionally verified through small displacements along the transition mode followed by optimization to the endpoints. Transition states were optimized either using constraints [236] or using the dimer method [219]. Lower barriers were in some cases only estimated through nudged elastic band (NEB) calculations [218], which typically use 10 to 15 images. Additional images were added through linear interpolation in Cartesian space, so that the norm of the distance between the images in Cartesian coordinates is always < 0.1 Å. This results in a dense reaction path with typically 50 to 150 images, providing a rigorous upper limit to the exact barrier. Energies and optimized structures are provided in the Appendix.

3.2. Results and Discussion

3.2.1. Calculation of Stability of Metal Oxide Surfaces

The stability of all α-Al_2O_3 and α-Fe_2O_3 surfaces was assessed by computing the surface free energy γ, which represents the Gibbs free energy of formation relative to the dry surface per unit surface area A.

For α-Al_2O_3 surfaces, the surface free energy $\gamma_{Al_2O_3}$ is given by:

$$\gamma_{Al_2O_3} = \frac{E^{slab} - E^{slab}_{dry} - \frac{x}{2}E^{bulk}_{Al_2O_3} - \frac{m}{2}[E^{gas}_{H_2O} + \mu_{H_2O}]}{A} \tag{3.1}$$

where:

- E^{slab} and E^{slab}_{dry} are the energies of the slab models of the considered surface and of the dry surface with identical surface area A
- $E^{bulk}_{Al_2O_3}$ is the energy per formula unit of bulk α-Al_2O_3, determined as the energy difference between two clean (1×1) slabs differing by one Al_2O_3-layer, which remains consistent across different unit cells or terminations with negligible differences on the order of 0.001 eV.
- $A_{1\times1}$ is the surface area per (1×1) cell, calculated as 19.845 Å^2.
- The chemical potential of water μ_{H_2O} is given relative to the energy of water $E^{gas}_{H_2O}$ and is generally a function of temperature and partial pressure.
- The stoichiometry coefficients x and m are determined by the amount of additional Al and H atoms on the surface with respect to the dry surface.

For α-Fe_2O_3 surfaces, the surface free energy $\gamma_{Fe_2O_3}$ is similarly calculated, but it also accounts for oxygen gas involvement:

$$\gamma_{Fe_2O_3} = \frac{E^{slab} - E^{slab}_{dry} - xE^{bulk}_{Fe_2O_3} - m[E^{gas}_{H_2O} + \mu_{H_2O}] + n[E^{gas}_{O_2}/2 + \mu_O]}{2A} \tag{3.2}$$

where:

- The reaction for the formation of the surface from the dry surface is given by:

$$\text{slab}_{dry} + xFe_2O_3 + mH_2O \longrightarrow \text{slab} + \frac{n}{2}O_2. \tag{3.3}$$

- The stoichiometry coefficients x, m and n are determined by the amount of additional Fe, H and O atoms on the surface with respect to the dry surface are provided in Table 3.1.
- $E^{bulk}_{Fe_2O_3}$ is the energy per formula unit of bulk α-Fe_2O_3, determined in the same manner as for α-Al_2O_3, with negligible variations, approximately around 0.001 eV, across different unit cells or terminations.
- A is the surface area per (1×1) cell, calculated as 22.110 Å^2.
- The chemical potential of oxygen μ_O is given relative to half of the energy of the O_2 molecule in its triplet ground state $E^{gas}_{O_2}/2$.

Table 3.1.: For the studied surfaces, cell-size and stoichiometry coefficients x, m, n and a according to Eq. 3.3 are given.

label	x	m	n	cell-size
θ[$Fe(OH)_3$]=0 (dry/clean)	0	0	0	1×1
θ[$Fe(OH)_3$]=1/4	1	3	0	2×2
θ[$Fe(OH)_3$]=1	1	3	0	1×1
θ[H_2O]=1	0	2	0	1×1
θ[$Fe(OH)_2$]=1/4	1	2	1	2×2
θ[$Fe(OH)_2$]=1	1	2	1	1×1
θ[FeOH]=1	1	1	2	1×1
θ[FeO]=1	1	0	1	1×1

3.2.2. Thermodynamic Stability of Hydroxylated α-Al_2O_3(0001) Surfaces

Understanding the thermodynamic stability of hydroxylated α-Al_2O_3(0001) surfaces is essential for predicting their behavior under various conditions. The bulk structure of α-Al_2O_3 can be described as a hexagonal AB stacking of close-packed O^{2-} ions in the 0001-direction, with Al^{3+} occupying two-thirds of the available octahedral positions. The unit-cell consists of three O^{2-} per layer and two Al^{3+} in between (see Fig. 3.1). The Al^{3+} ions form ABC-layers, in which the unoccupied octahedral position alternates between the three possible locations. This means that the two Al^{3+} per layer are not equivalent and are slightly distorted in 0001-direction. The Al-layering can be described as an (-O_3-Al_2-) stacking and because of the AB stacking of O^{2-} and the ABC-stacking of Al^{3+}, a total of six (O_3-Al_2) layers make up the unit cell, see Fig. 3.1. In agreement with previous work [53, 174, 237], we find that the most stable stoichiometric surface is a (1×1)-surface that is terminated by a single Al-layer (O_3-Al), which is relaxed inwards considerably: -88% predicted by DFT, -63% determined by LEED [64] and -51% determined by X-ray diffraction (XRD) [238, 239].

Figure 3.1 shows the most important known hydroxylated structure, the Al_2-$(OH)_3$-terminated (gibbsite like) surface [76, 79, 80]. This surface is terminated by a full layer of oxygen that is saturated with one hydrogen per oxygen giving an OH-concentration of 3 per (1×1)-cell or 15.1 per nm^2. Based on XRD, the structure of α-Al_2O_3(0001) at room temperature and ambient pressure has been assigned to this fully hydroxylated structure with an additional adsorbed water overlayer [54], in agreement with our and previous calculations [78–80]. If one compares the terminations of the stoichiometric surface (O_3-Al) and that of the fully hydroxylated surface (Al_2-$(OH)_3$), it is clear that these two surfaces always differ by $\frac{3}{2}$ H_2O and $\pm\frac{1}{2}$ Al_2O_3. Therefore, the fully hydroxylated surface can be described as $Al(OH)_3$ adsorbed on the stoichiometric surface with a coverage of $\theta[Al(OH)_3] = 1$.

Figure 3.1 also shows a new type of surface revolving around the structural motif of an isolated $Al(OH)_3$ fragment adsorbed on the stoichiometric surface. By isolated we mean that a surface Al of the underlying stoichiometric surface (shown in gold in Fig. 3.1) binds at most to one of the surface OH groups, which bridge to the adsorbed $Al(OH)_3$ (shown in blue in Fig. 3.1). This

can be contrasted to the known, fully hydroxylated surface with $\theta[Al(OH)_3] = 1$, where each surface Al binds to three OH groups. Importantly, the adsorbed $Al(OH)_3$ binds in the position expected from the bulk structure of α-Al_2O_3 and binding in the other available octahedral site is significantly weaker by 0.78 eV. The most stable orientation of the hydroxyl groups in the $Al(OH)_3$ groups (clock-wise or counter clock-wise) depends on the relative orientation of oxygens in the lower layer. The difference in stability between the two different orientations is relatively large with 0.52 eV. This can be compared to the orientation of the hydroxyl groups in the fully hydroxlated surface ($\theta[Al(OH)_3] = 1$), where it is has been shown that different configurations exist [87, 240–243], in which individual hydroxyl groups can be orientated parallel to the surface to form hydrogen bonds, or point away from the surface. Here we found very small differences of less than 0.01 eV per (1×1) unit cell.

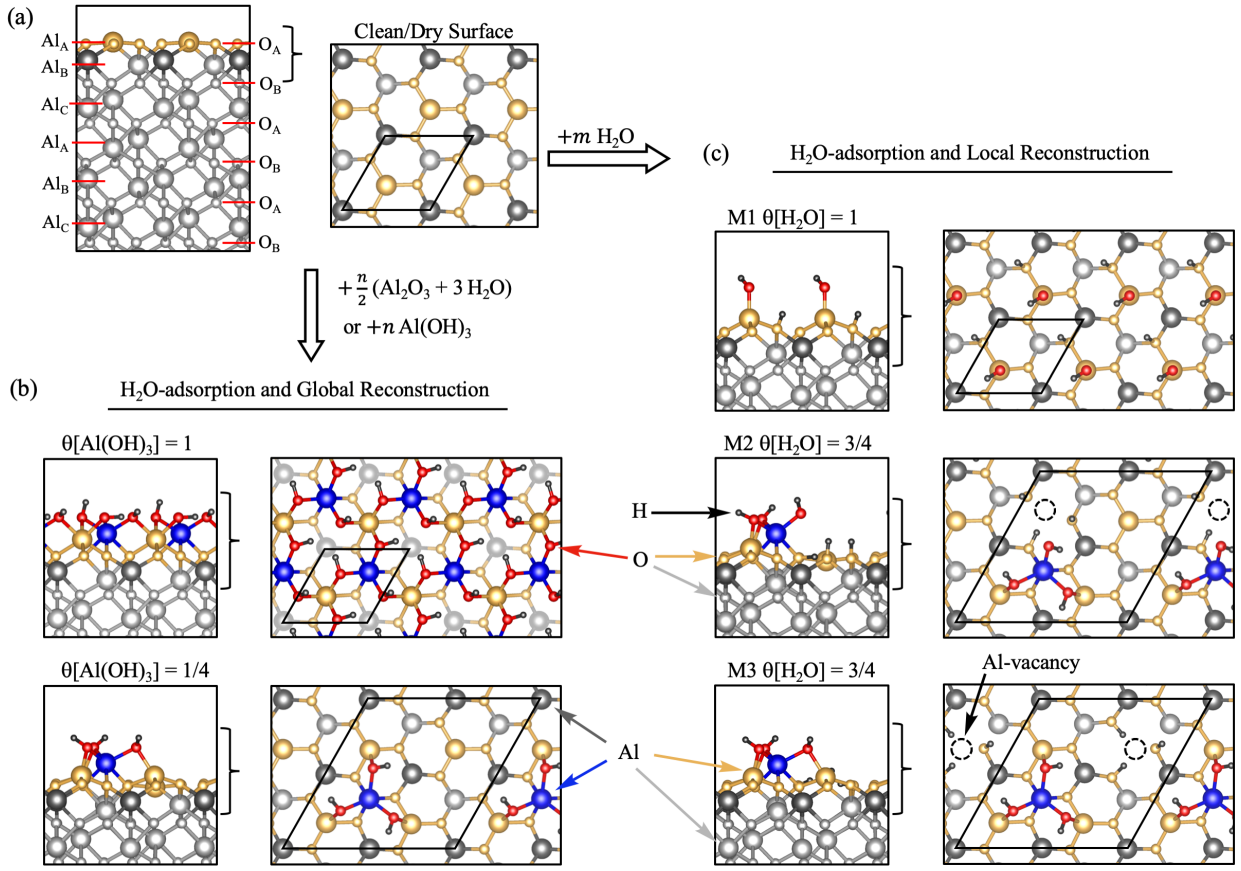

Figure 3.1: Atomic structure of the most relevant surface terminations of α-$Al_2O_3(0001)$. (a) Clean/dry surface. (b) Surfaces with $\theta[Al(OH)_3] = 1$ and $\frac{1}{4}$, which require diffusion of additional Al^{3+} ions onto the clean 0001-surface. (c) Metastable surfaces M1-M3 that can be obtained by adsorption of water and local reconstruction. The unit cell is indicated in the top views. The number of layers visible in the top-views is indicated with braces in the respective side-views.

Figure 3.2a shows the stability of the investigated surfaces as a function of the chemical potential of water, μ_{H_2O}. At high values of μ_{H_2O}, the fully hydroxylated surface $\theta[Al(OH)_3] = 1$ is most stable, for $\mu_{H_2O} \geq$ -0.76 with an additional 2D ice-like overlayer of water (labeled H_2O^* in Fig. 3.2). Isolated $Al(OH)_3$ groups can be formed up to a maximum coverage of $\theta[Al(OH)_3]$

$= \frac{1}{3}$, as illustrated in Fig. 3.2b. Figure 3.2a shows that these surfaces become more stable than the fully hydroxylated surface already for $\mu_{H_2O} \leq -1.25\,eV$, for example at 500 K and 1 mbar H_2O pressure. Importantly, de-hydroxylation and formation of the clean stoichiometric surface is predicted only at $\mu_{H_2O} \leq -2.8\,eV$, which is realized, for example at around 1000 K and 1 mbar H_2O pressure or at 850 K and 0.001 mbar H_2O pressure, see Fig. 3.2c. Complete de-hydroxylation is therefore expected only for temperatures that are about 400 K higher than previously expected for the fully hydroxylated surface.

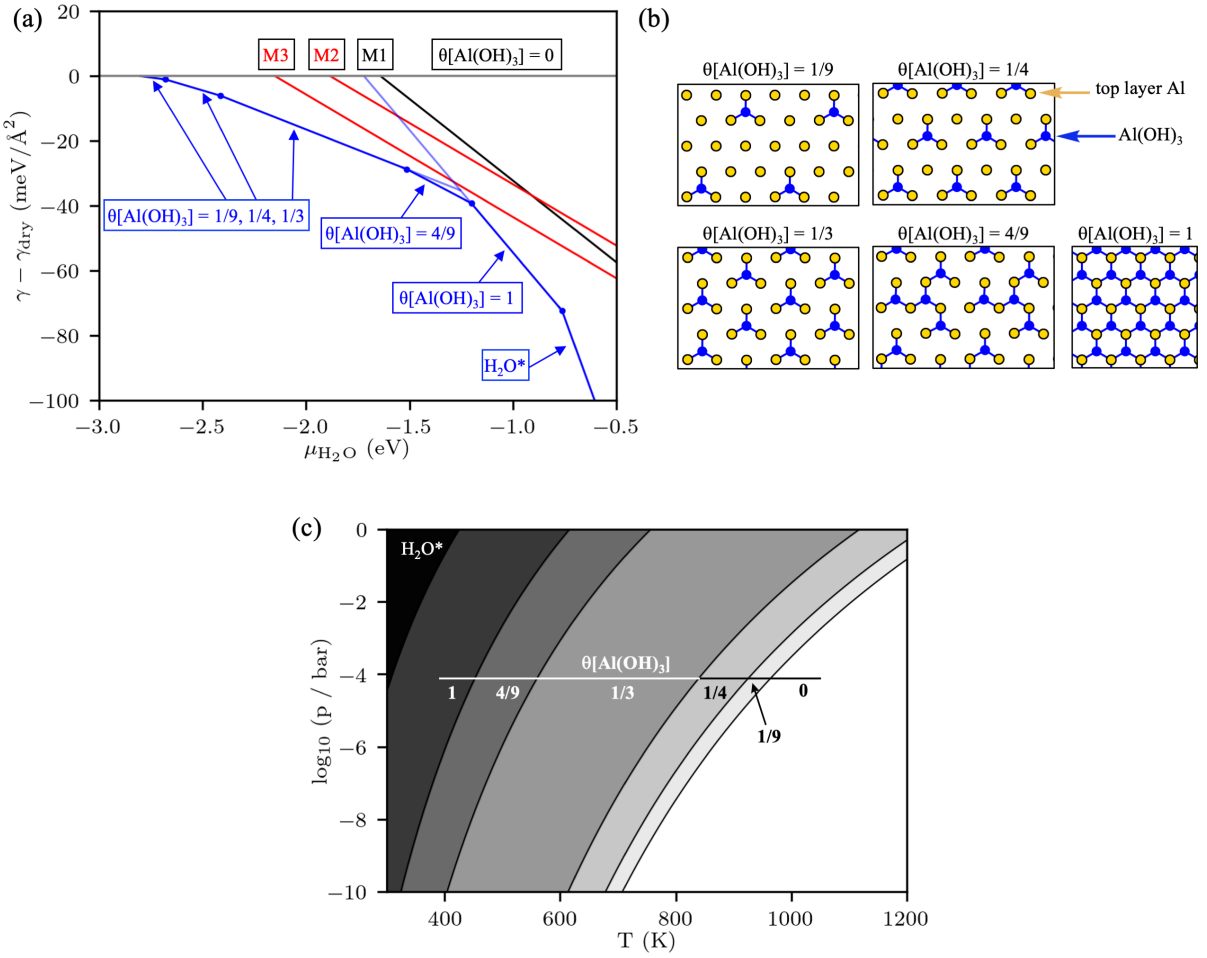

Figure 3.2: Stability of α-Al_2O_3(0001) surfaces. (a) Surface free energies, given relative to the dry surface as a function of the chemical potential of water μ_{H_2O}. The most stable surfaces are shown in blue for various coverages $\theta[Al(OH)_3]$. The metastable structures M1-M3 are shown in red and black. (b) Schematic representation of the surface Al-configurations for the various coverages $\theta[Al(OH)_3]$. (c) Phase diagram, showing only the most stable structures according to Eq. 3.1, where μ_{H_2O} was calculated using the rigid rotor and free translator approximation. At high chemical potentials of water, the most stable structure is a 2D-ice layer adsorbed on $\theta[Al(OH)_3] = 1$, which is labeled H_2O*.

Isolated $Al(OH)_3$ fragments show weakly repulsive adsorbate-adsorbate interaction for $\theta[Al(OH)_3] \leq \frac{1}{3}$, leading to a systematic decrease of $\theta[Al(OH)_3]$ from its maximum value of $\frac{1}{3}$ to zero with increasing temperature and decreasing pressure, as shown in Fig. 3.2c. As shown in Table 3.2, the formation energy per water molecule increases only by 0.07 eV, when going from $\frac{1}{3}$

to $\frac{1}{4}$ and then to $\frac{1}{9}$ coverage, illustrating the weak interaction. The difference in formation energy between $\frac{1}{9}$ and $\frac{1}{16}$ coverage is < 0.01 eV at the PBE-D3 level of theory, showing that adsorbate-adsorbate interaction is already negligible at $\theta[\mathrm{Al(OH)_3}] = \frac{1}{9}$. Table 3.2 also lists results obtained with other functional as single-point energies based on the structure obtained with PBE-D3. These results show that the overall trends are the same, however, there is a general difference in the predicted stability of the hydroxylated surfaces with respect to the dry surface, where formation energies increase in the order SCAN < PBE-D3 < BEEF-vdW $\lesssim$ HSE06, i.e. SCAN predicts hydroxylated surfaces to be most stable (see also Fig. A.4 in the Appendix).

The stability of the surfaces with $\theta[\mathrm{Al(OH)_3}] = \frac{1}{3}$, $\frac{1}{4}$ and $\frac{1}{9}$ shown in Fig. 3.2 were computed for $(\sqrt{3} \times \sqrt{3})R30°$, (2×2) and (3×3) surfaces, see Fig. 3.2b. However, due to the weak interaction, different configurations with the same coverages were found to show only negligible differences in stability. For example, different configurations for $\theta[\mathrm{Al(OH)_3}] = \frac{1}{4}$ differ by less than 1 meV/Å^2, or equivalently by less than 0.05 eV per $\mathrm{Al(OH)_3}$ fragment (see Appendix). In the range of -1.5 eV $< \mu_{\mathrm{H_2O}} <$ -1.2 eV, there is a large variety of structures with similar stability with $\frac{1}{3} < \theta[\mathrm{Al(OH)_3}] < 1$. The most stable of these surfaces with $\theta[\mathrm{Al(OH)_3}] = \frac{4}{9}$ is included in Fig. 3.2. As is shown in Fig. 3.2b, this surface is intermediate between having isolated $\mathrm{Al(OH)_3}$ groups and being fully hydroxylated.

Table 3.2.: Overview over computed terminations of the α-Al_2O_3(0001) surface. The composition is specified in terms of the coverage of H_2O and $Al(OH)_3$ adsorbates relative to the dry surface. The formation energy is given per two OH groups in eV relative to the dry surface and ΔE_{form} is thus equal to the chemical potential μ_{H_2O} at which the surface free energy is identical to that of the stoichiometric surface, see Eq. 1. Additionally, the concentration of hydroxyl groups per surface area, the unit cell and the employed k-point sampling are specified

	coverage (θ)		ΔE_{form} per 2OH (eV)				n(OH)		
Surface	$Al(OH)_3$	H_2O	PBE-D3	BEEF-vDW[a]	SCAN[a]	HSE06[a]	(1/nm^2)	unit cell	k-points
dry/clean	0	0	0	0	0	0	0	[b]	[b]
$\theta[Al(OH)_3]$=1/16	1/16	0	-2.80	-2.75	-2.98	-2.76	0.9	(4×4)	1×1
$\theta[Al(OH)_3]$=1/9	1/9	0	-2.80	-2.75	-2.96	-2.74	1.7	(3×3)	2×2[c]
$\theta[Al(OH)_3]$=1/4	1/4	0	-2.73	-2.70	-2.89	-2.67	3.8	(2×2)	2×2
$\theta[Al(OH)_3]$=1/3	1/3	0	-2.66	-2.66	-2.81	-2.58	5.0	$(\sqrt{3}\times\sqrt{3})R30°$	4×4[c]
$\theta[Al(OH)_3]$=4/9	4/9	0	-2.37	-2.30	-2.51	-2.28	6.7	(3×3)	2×2[c]
$\theta[Al(OH)_3]$=1	1	0	-1.72	-1.44	-1.87	-1.56	15.1	(1×1)	4×4
$\theta[Al(OH)_3]$=1; $\theta[H_2O]$=2	1	2	-1.17	-0.93	-1.21	-0.99	35.3	(1×2)	4×2
M1	0	1	-1.64	-1.57	-1.71	-1.52	10.1	(1×1)	4×4
M2	0	3/4	-1.88	-1.73	-2.00	-1.77	7.6	(2×2)	2×2
M3	0	3/4	-2.15	-2.01	-2.31	-2.04	7.6	(2×2)	2×2

[a] Single point calculation with the PBE-D3 structure. [b] The dry surface serves as the reference and was always computed with the same unit cell and k-point sampling as the hydroxylated surfaces. [c] For HSE06, the k-point sampling in each dimension was reduced by a factor of 2.

Our results suggest that hydroxylated surfaces with $\theta[Al(OH)_3] < 1$ may exhibit no ordered structure, because different configurations at the same coverage $\theta[Al(OH)_3]$, show only very small differences in energy and because of the slow diffusion of $Al(OH)_3$ (vide infra). For this reason, we discuss the state of these surfaces in terms of the coverage $\theta[Al(OH)_3]$ rather than a specific surface reconstruction such as (2×2). The lack of an ordered hydroxylated structure for $\theta[Al(OH)_3] < 1$ may explain why in LEED experiments below 900 °C generally only a (1×1) pattern is observed, which, however, improves with increasing temperatures, concomitantly with the desorption of water [244].

Then we now discuss the limitations of our investigation of the thermodynamic stability of these surfaces. Most importantly, it is of course possible that more stable terminations, for example with different compositions, exist. Secondly, our study is limited by the choice of unit cell, which allows only a finite number of configurations. However, for isolated $Al(OH)_3$ groups, our investigation showed that adsorbate-adsorbate interaction is negligible already at $\theta[Al(OH)_3] = 1/9$, since the formation energy changes by less than 0.01 eV when going from $\theta[Al(OH)_3] = 1/16$ to 1/9. Additionally, we have found that, for a given coverage $\theta[Al(OH)_3]$, the stability does not depend strongly on the relative spatial positions of the $Al(OH)_3$ groups. Consequently, we do not expect that an energetically particularly stable configuration of isolated $Al(OH)_3$ groups was missed due to the limited number of studied unit cells. Our study did not account for vibrational and configurational entropy on the surface and only considered the loss of entropy upon adsorption of water. This approximation is expected to generally underestimate the stabilty of the hydroxylated surfaces with respect to the clean surface, especially at higher temperatures. We have studied four different density functionals, including a hybrid functional, which all support the main conclusion that the type of termination proposed herein is stable at low chemical potentials of water and that $\theta[Al(OH)_3]$ is expected to decrease gradually with increasing temperature. However, the functionals differ in the prediction of the total stability of these surfaces and in the precise values of μ_{H_2O} at which the transitions between these terminations occur. The level of electronic structure theory could be improved, for example with wave function methods that have already been applied to similar problems [81, 86].

3.2.3. Thermodynamic Stability of Hydroxylated α-Fe_2O_3(0001) Surfaces

The most stable dry surface we found for α-Fe_2O_3 is a (1×1) surface that is terminated by a single Fe, i.e. (O_3-Fe), similar to the α-Al_2O_3 we have discussed in the previous section [53, 174, 222, 237, 245] and in agreement with previous work [89, 99, 100, 103, 246, 247]. Figure 1.2 shows both a top-view and a side-on view of this surface. Additionally, the labeling of both Fe- and O-layers is introduced in Fig. 1.2, which will be used to refer to individual layers. Table 3.3 shows how the computed interlayer spacings obtained after relaxation with DFT deviate from the bulk limit. The topmost Fe atom in the first layer strongly relaxes downward, which reduces the distance between the Fe-layer and the lower oxygen layer by -65.3% of the corresponding interlayer spacing of the bulk, so that the interlayer spacing at the surface is 34.7 % of that of

Table 3.3.: Percent change (d%Δ) in layer spacing from the α-Fe_2O_3 relative to the bulk limit.

		θ[$Fe(OH)_3$]		
d%Δ	Dry	$\theta = 1/4$	$\theta = 1$	$\theta[H_2O] = 1$
$O_B - Fe^2_A$	–	7.6	7.7	–
$Fe^2_A - Fe^1_A$	–	73.1	-26.8	–
$Fe^1_A - O_A$	-65.3	-55.2	9.6	-17.3
$O_A - Fe^2_B$	7.8	4.0	0.2	10.1
$Fe^2_B - Fe^1_B$	-37.3	-30.4	2.8	-28.9
$Fe^1_B - O_B$	16.2	14.2	-1.0	10.6
$O_B - Fe^2_C$	4.2	4.7	-0.5	0.7
$Fe^2_C - Fe^1_C$	-5.1	-5.3	1.1	1.4
$Fe^1_C - O_{A'}$	1.6	1.8	-0.2	-0.5
$O_{A'} - Fe^2_{A'}$	-0.9	-0.6	0.2	-0.5
$Fe^2_{A'} - Fe^1_{A'}$	2.7	2.1	-0.2	1.2
$Fe^1_{A'} - O_{B'}$	-0.5	-0.3	0.2	-0.2
$O_{B'} - Fe^2_{B'}$	0.3	0.2	0.0	0.2
$Fe^2_{B'} - Fe^1_{B'}$	-0.5	-0.2	0.2	0.0
$Fe^1_{B'} - O_{A''}$	0.4	0.3	0.1	0.3

the bulk value. This is somewhat more than reported in previous work (-57%)[113]. We note that the corresponding relaxation of the first layer is even stronger for α-Al_2O_3(0001), where computed values range from -82% to -88% [53, 76, 222].

The magnetic moments of the Fe atoms in the near-surface layers are compiled in Table 3.4. The magnetic moments in the first (-4.00 μ_B) and second (+4.14 and +4.17 μ_B) layer differ slightly from the bulk value (± 4.16 μ_B), to which the magnetic moments converge in the third layer (labeled layer "C" in Table 3.3). This is in good agreement with the literature (GGA+U)[113], where the magnetic moment of Fe is ± 4.11 μ_B in the bulk, ± 3.94 μ_B in the first surface layer, and ± 4.10 μ_B in the second surface layer. The experimental value is ± 4.6-4.9 μ_B [248, 249] for Fe in the bulk.

We will now discuss the hydroxylated surfaces of α-Fe_2O_3(0001). As for α-Al_2O_3 [76, 79, 80], the hydroxylated structures have been investigated for α-Fe_2O_3 [118, 123–126, 130, 229, 246, 250–252] both computationally and experimentally. One of the simplest hydroxylated structures results from the dissociative adsorption of water on the dry surface ($\theta[H_2O] = 1$), see Fig. 3.3a. As for α-Al_2O_3[53], the barrier for this dissociation was found to be very low (< 0.1 eV) also for α-Fe_2O_3.[103]

The fully hydroxylated surface is terminated by a complete layer of oxygen that is saturated with one hydrogen per oxygen giving an OH-concentration of 3 per (1×1)-cell or 13.6 per nm^2. We find that there are structures with one or two of the three hydrogens pointing in a direction parallel to the surface and engaging in hydrogen bonding. As in previous work on α-Fe_2O_3(0001) [131] and α-Al_2O_3(0001) [253], we find the difference in stability to be negligible (≤ 0.05 eV) and only show in Fig. 3.3b the structure with one in-plane hydrogen bond. As one

Table 3.4.: Mean magnetic moments (in μ_B) of the upper half layers from the slabs for the relevant α-Fe_2O_3 surface terminations. The magnetic moment is averaged over all Fe-atoms belonging to the respective layer. The computed magnetic value of the bulk is $\mu = \pm 4.16$

		$\theta[Fe(OH)_3]$		
	Dry	$\theta = 1/4$	$\theta = 1$	$\theta[H_2O] = 1$
Fe^2_A	–	-4.24	-4.24	–
Fe^1_A	-4.00	-4.07	-4.21	-4.01
Fe^2_B	+4.14	+4.16	+4.16	+4.16
Fe^1_B	+4.17	+4.17	+4.15	+4.16
Fe^2_C	-4.16	-4.15	-4.16	-4.16
Fe^1_C	-4.16	-4.16	-4.16	-4.16
$Fe^2_{A'}$	+4.16	+4.16	+4.16	+4.16
$Fe^1_{A'}$	+4.16	+4.16	+4.16	+4.16
$Fe^2_{B'}$	-4.16	-4.16	-4.16	-4.16
$Fe^1_{B'}$	-4.16	-4.16	-4.16	-4.16

may expect, MD-simulations on α-$Al_2O_3(0001)$ show that OH-groups are not confined to these rigid positions. [82]

Comparing the termination of the dry surface ($O_3 - Fe$) and that of the fully hydroxylated surface ($Fe_2 - (OH)_3$), these two surfaces always differ by $\frac{3}{2}H_2O$ and $\pm Fe_2O_3$. So, one can think of it as one $Fe(OH)_3$ group adsorbed per (1×1)-cell of the dry surface. Importantly, these $Fe(OH)_3$ groups are most stable, when adsorbed in the positions corresponding to a continuation of the bulk positions expected for Fe. Therefore, as in our previous work on α-$Al_2O_3(0001)$[222], we use the coverage of $Fe(OH)_3$ to describe the degree of hydroxylation of the surface. Here, $\theta[Fe(OH)_3] = 1$ corresponds to the fully hydroxylated surface. The computed structures for $\theta[Fe(OH)_3] = 1$ and 1/4 surfaces are shown in Fig. 3.3.

The surface characterized by $\theta[Fe(OH)_3] = 1/4$ contains an isolated $Fe(OH)_3$ fragment adsorbed on the dry surface. By isolated, we mean that Fe atoms in the layer below the top $Fe(OH)_3$ groups bind at most to one hydroxyl group (Fig. 3.3c).[222]

Figure 3.4 shows the stability of the investigated surfaces as a function of the chemical potential of water, μ_{H_2O}. The surface resulting from dissociative water adsorption on the dry surface ($\theta[H_2O] = 1$) is at no point the most stable structure. At high values of μ_{H_2O}, the fully hydroxylated surface $\theta[Fe(OH)_3] = 1$ is most stable, while at low values of μ_{H_2O}, the dry surface $\theta[Fe(OH)_3] = 0$ is most stable. Fig. 3.4a shows that the $\theta[Fe(OH)_3] = \frac{1}{4}$ surface becomes more stable than the fully hydroxylated surface for $\mu_{H_2O} \leq -0.95\,eV$, for example, at around 400 K and 1 mbar H_2O pressure. Dehydroxylation and the formation of the clean surface are only predicted to appear at $\mu_{H_2O} \leq -2.22\,eV$, for example, at 850 K and 1 mbar H_2O pressure or at 700 K and 0.001 mbar H_2O pressure, see Fig. 3.4b. Figure 3.4b has been obtained by considering only the loss of translational and rotational entropy associated with the reaction of $H_2O(g)$, which is the leading contribution for adsorption at high temperatures.

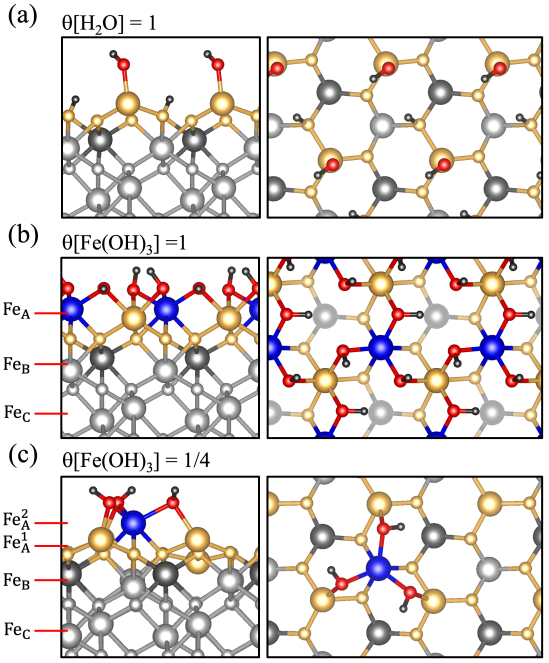

Figure 3.3: Atomic structure of hydroxylated surfaces. (a) Surface configuration with one H_2O molecule dissociated on top of the Fe-terminated $Fe_2O_3(0001)$ (dry) surface. (b) Surface with $\theta[Fe(OH)_3] = 1$. (c) Surface with $\theta[Fe(OH)_3] = \frac{1}{4}$. H, O, and Fe atoms are shown as small, medium, and large spheres, respectively. H atoms are shown in black, while a different color code is used to differentiate between the different layers for Fe (blue, gold, dark gray, light gray) and O (red, gold, light gray).

Tables 3.3 and 3.4 list the surface relaxation and magnetic moments, respectively. The deviation of the interlayer-spacing from the bulk is comparable for most hydroxylated surfaces, but is clearly the smallest for the fully hydroxylated surface, $\theta[Fe(OH)_3] = 1$. This can be explained by the fact the termination by OH-groups is most similar to a bulk-like layer of oxygens. The magnetic moment converges in all cases quickly to the bulk limit with comparable deviations in the first two layers ($< 0.2\ \mu_B$). To investigate how the reactivity of the partially hydroxylated surface with $\theta[Fe(OH)_3] = 1/4$ differs from the dry and the fully hydroxylated surfaces, we considered CO and H_2O as probe molecules, absorbed at a low coverage of $\theta = 1/4$. We find that the binding energy on the partially hydroxylated surface is intermediate between dry and fully hydroxylated surface (see Appendix B.7 for details).

We will now briefly discuss how the stability of the α-$Fe_2O_3(0001)$ surface compares with the results obtained for α-$Al_2O_3(0001)$. This is of interest because the two are iso-structural and the results obtained for α-$Fe_2O_3(0001)$ are significantly different. In both cases, surfaces with low hydroxyl group concentration are stable, but for α-$Al_2O_3(0001)$ this stability extends to much lower values of μ_{H_2O} and it is not obvious why. In Fig. 3.4, we have, as in previous work, given the surface energy relative to the dry surface ($\gamma_{dry} = 0$). This choice is motivated by the fact that the absolute stability of the dry surface is irrelevant to determine which termination is most stable under certain conditions. However, to compare the 0001-surface of the α-Fe_2O_3 and α-Al_2O_3, we found it useful to employ the absolute surface energies. For the comparison,

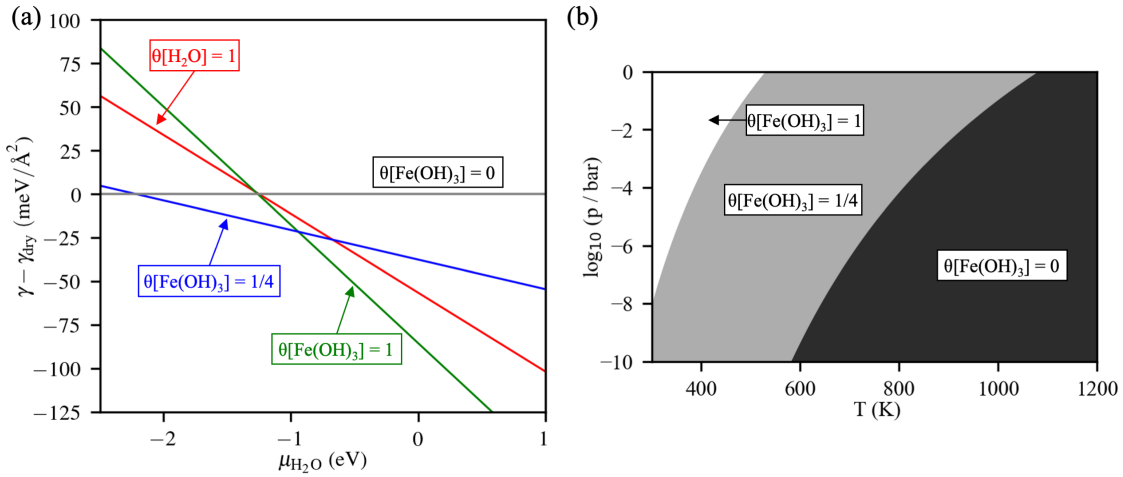

Figure 3.4: Stability of α-Fe_2O_3(0001) surfaces. (a) Surface free energies are given relative to the dry surface as a function of the chemical potential of water μ_{H_2O} (b) Phase diagram as a function of temperature and the partial pressure of water.

it is additionally useful to give the surface energy not per area, but per (1×1)-unit cell, because this leads to the same concentration of hydroxyl groups

$$\gamma = \frac{E^{\text{slab}} - \frac{x}{2}E^{\text{bulk}}_{M_2O_3} - m[E^{\text{gas}}_{H_2O} + \mu_{H_2O}] + n[E^{\text{gas}}_{O_2}/2 + \mu_O]}{2A} \times A_{1\times1} \tag{3.4}$$

As opposed to Eq. 3.2, in Eq. 3.4 all Fe is referenced to bulk α-Fe_2O_3 and x therefore simply equals the number of metal ions in the slab. The absolute surface energies per unit cell are given in Fig. 3.5.

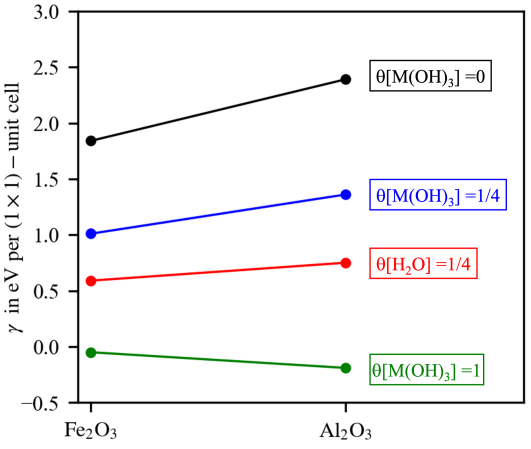

Figure 3.5: Absolute surface energies per unit cell computed according to Eq. 3.4 with data for α-Al_2O_3(0001) taken from previous work.[222]

It can be seen in Fig. 3.5 that the total surface energies of the fully hydroxylated surface, θ[M(OH)$_3$]=1, varies only slightly, with values of -0.05 and -0.19 per unit cell for Fe_2O_3 and

Al_2O_3 respectively. Note that this corresponds to the 0 K ($\mu(H_2O) = 0$) surface energies. Negative surface energies for hydroxylated surfaces at 0 K have been computed before, for α-$Al_2O_3(0001)$[76], θ-$Al_2O_3(110)$ [75, 254] and α-quartz(0001) [254, 255]. The small absolute value and small variation of these surface energies can be explained by the fact that all metal atoms retain their octahedral coordination, when the fully hydroxylated surface is formed from the bulk. Furthermore, the number of hydroxyl groups also stays constant when the hydroxylated surface is created through the reaction with H_2O.

The stability of the dry surface, $\theta[M(OH)_3]$=0 varies strongly from α-Fe_2O_3 to α-Al_2O_3, from 1.84 to 2.39 eV per unit cell. The dry surface and fully hydroxylated surface have the same stability for α-$Al_2O_3(0001)$ when the chemical potential of water is $\mu(H_2O)$ = -1.72 eV [222]. The much more stable dry surface of α-$Fe_2O_3(0001)$ leads to an earlier crossover at $\mu(H_2O)$ = -1.26 eV (Fig. 3.4). Consequently, the lower stability of fully hydroxylated surface $\theta[M(OH)_3]$=1 observed in Fig. 3.4 for α-$Fe_2O_3(0001)$ is mainly due to the more stable dry surface.

For the partially hydroxylated surface with $\theta[M(OH)_3]$=1/4, Fig. 3.5 shows an increase in surface energy from 1.03 to 1.36 eV per unit cell when going from Fe_2O_3 to Al_2O_3. Compared to the stability of α-$Al_2O_3(0001)$ surfaces, both $\theta[Fe(OH)_3] = \frac{1}{4}$ and $\theta[Fe(OH)_3] = 1$ surfaces are relatively less stable than their corresponding alumina-structures. Similar to α-$Al_2O_3(0001)$ surfaces[222], it is possible that there is a large variety of structures between $\theta[Fe(OH)_3] = \frac{1}{4}$ and $\theta[Fe(OH)_3] = 1$, such as $\theta[Fe(OH)_3] = \frac{4}{9}$.

We will now discuss reduced structures, which contain Fe in the oxidation state +2. The motivation for considering surface reduction is that we believe reduction of hematite to magnetite begins at the surface, in this case α-$Fe_2O_3(0001)$. One interesting question is, if surface reduction is more or less favorable than bulk reduction. As above, we will describe the structures in terms of the group that is adsorbed on the dry surface and its respective coverage. The most stable obtained structures can be derived from the hydroxylated structures discussed above (Fe in oxidation state +3) by removing an OH group. Removing an OH-group from $\theta[Fe(OH)_3] = \frac{1}{4}$ and $\theta[Fe(OH)_3] = 1$, results in the structures labeled $\theta[Fe(OH)_2] = \frac{1}{4}$ and $\theta[Fe(OH)_2] = 1$. Here, the topmost Fe is in oxidation state +2 as evidenced by the magnetic moment, see Table 3.5. Further removal of an OH group gives $\theta[Fe(OH)] = 1$, in which both top Fe ions are in oxidation state +2. The reduced surface $\theta[FeO] = 1$ can be obtained by removing H_2O from $\theta[Fe(OH)_2] = 1$.

The atomic structure of the reduced surfaces is shown in Fig. 3.6 and the phase diagram in Fig. 3.7 summarizes all relevant structures. Fig. 3.7a shows the phase diagram as the function of the chemical potentials of oxygen and water. At the top of the phase diagram, for chemical potentials of oxygen μ_O < -1.5 eV, only nonreduced surfaces without Fe^{+2} (also displayed in Fig. 3.4) are stable. The stability of the reduced surfaces is generally a function of the chemical potentials of both water and oxygen. The reduced structures with low hydroxyl concentration ($\theta[FeO] = 1$ and $\theta[Fe(OH)] = 1$) are only stable in a range of chemical potentials μ_O < -2.44 eV,

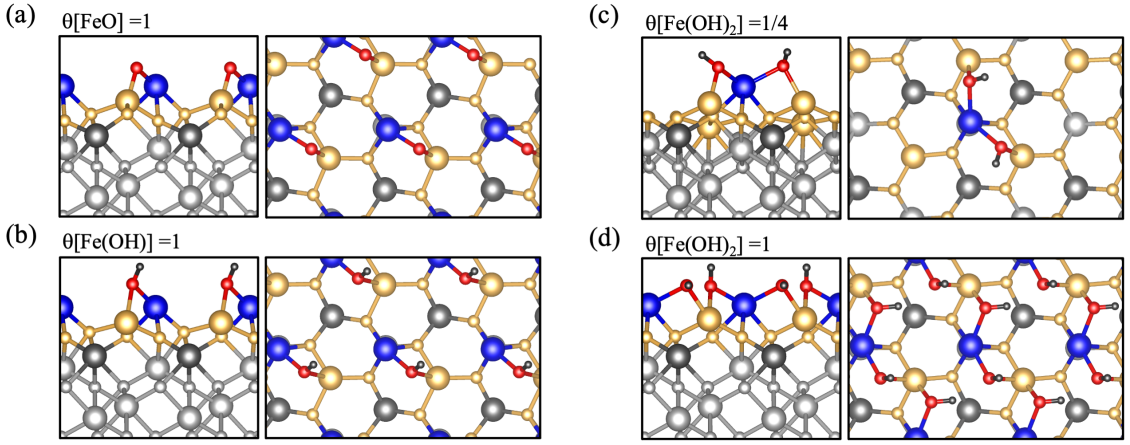

Figure 3.6: Atomic structure of reduced surfaces of α-$Fe_2O_3(0001)$ with the same color code as in Fig. 3.3 for surfaces with (a) $\theta[\mathrm{FeO}] = 1$, (b) $\theta[\mathrm{Fe(OH)}] = 1$, (c) $\theta[\mathrm{Fe(OH)_2}] = \frac{1}{4}$, and (d) $\theta[\mathrm{Fe(OH)_2}] = 1$.

where bulk hematite is less stable than bulk magnetite, according to experimental data.[256] The only reduced surfaces in the phase diagram that extend to higher values of μ_O are $\theta[\mathrm{Fe(OH)_3}] = 1$ and $\theta[\mathrm{Fe(OH)_2}] = \frac{1}{4}$. We also note that the chemical potential of oxygen at which calculations predict this transition is usually lower, ranging from $-1.60\,\mathrm{eV}$ to $-1.73\,\mathrm{eV}$ for PBE+U with $0 < U < 5\,\mathrm{eV}$, as opposed to the experimental value of $\mu_O <$ -2.44 eV.[230] Consequently, the first formation of reduced surfaces is predicted by our calculations at a similar potential at which DFT+U also predicts (erroneously) the transition from bulk hematite to bulk magnetite[230]. From this, we conclude that the formation of reduced α-$Fe_2O_3(0001)$ surface occurs in a similar range of the chemical potential of μ_O as the reduction of bulk hematite to bulk magnetite. This is of course only a thermodynamic analysis and one can speculate that surface reduction of hematite is kinetically more facile than complete reduction of bulk hematite to magnetite.

In Fig. 3.7b, we show the stability of the same phases as a function of the chemical potential of hydrogen and water. The transformation is achieved simply by using the experimental formation energy of water and setting μ_O = -2.476 eV + μ_{H_2O} - μ_{H_2}. Under oxidizing conditions, Fig. 3.7a is a more useful representation, while Fig. 3.7b is more convenient to analyze the stability under reducing conditions. Both of these situations are relevant for a potential process[97], in which iron is used as a solid fuel, that is burned (with O_2) to yield hematite and is then reduced (using H_2) to again give iron.

3.2.3.1. Stability of α-$Fe_2O_3(0001)$ Surfaces under Different U Settings

To validate the effect of U on the prediction of surface stability, we tested the surface stability using different values of U. Compared to the calculations with $U = 4$ eV, the results with $U =$ 3 and 5 eV are similar, with more (less) favorable hydroxylation predicted for 5 (3) eV, see Fig. 3.8. Figure 3.8 is the same as Fig. 3.4 but with the results of single point calculations for $U =$ 3 and 5 eV added. The chemical potential of H_2O, where the transitions that occur are shifted

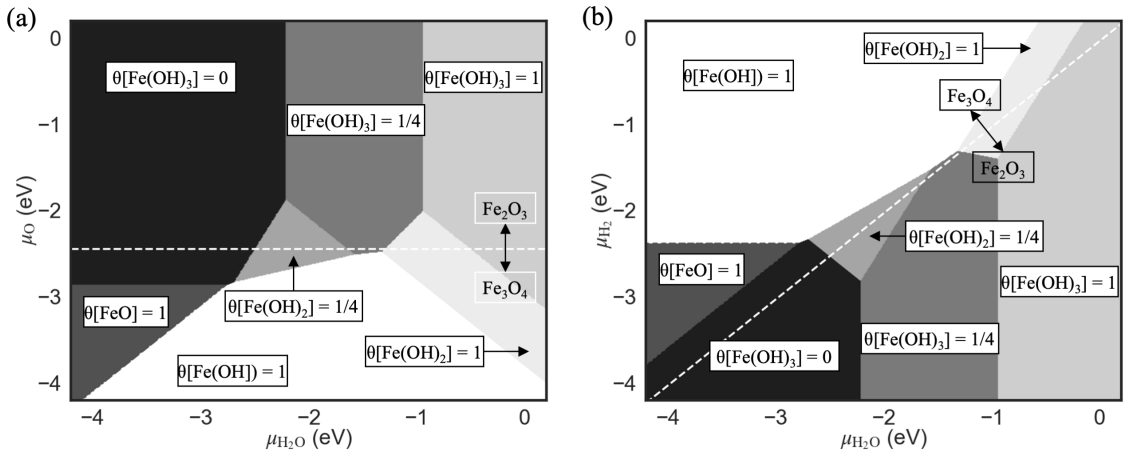

Figure 3.7: Phase diagram for α-$Fe_2O_3(0001)$ surface terminations. (a) as a function of the chemical potential of water μ_{H_2O} and oxygen μ_O. The range of stability of bulk hematite and bulk magnetite is indicated based on experimental values.[256] The horizontal dashed line indicates the chemical potential at which the transition occurs. (b) as a function of μ_{H_2O} and chemical potential of hydrogen μ_{H_2}.

Table 3.5.: Mean magnetic moments (in μ_B) of the upper half layers from the slabs for the relevant reduced α-$Fe_2O_3(0001)$ surface terminations. The magnetic moment is averaged over all Fe-atoms belonging to the respective layer. The computed magnetic value of the bulk is $\mu = \pm 4.16$

			$\theta[Fe(OH)_2]$	
	θ[FeO]=1	θ[FeOH]=1	$\theta = 1/4$	$\theta = 1$
Fe^2_A	-3.67	-3.62	-3.73	-3.71
Fe^1_A	-4.06	-3.64	-4.07	-4.13
Fe^2_B	+4.15	+4.16	+4.14	+4.15
Fe^1_B	+4.15	+4.16	+4.17	+4.16
Fe^2_C	-4.16	-4.16	-4.15	-4.16
Fe^1_C	-4.16	-4.16	-4.16	-4.16
$Fe^2_{A'}$	+4.16	+4.16	+4.16	+4.16
$Fe^1_{A'}$	+4.16	+4.16	+4.16	+4.16
$Fe^2_{B'}$	-4.16	-4.16	-4.16	-4.16
$Fe^1_{B'}$	-4.16	-4.16	-4.16	-4.16

at most by 0.1 eV. We thus concluded that the predicted stability of nonreduced hydroxylated and clean surfaces depends only weakly on the value of U. Fig. 3.9 shows the results obtained for $U = 3$ and 5 eV in addition to those depicted in Fig. 3.7. For these values, the transition between the phases, which is at $\mu_{H_2O} = -0.95\,\text{eV}$ and $\mu_{H_2O} = -2.22\,\text{eV}$ for $U = 4$ eV is shifted to $\mu_{H_2O} = -0.85\,\text{eV}$ and $\mu_{H_2O} = -2.14\,\text{eV}$ for $U = 3$ eV and $\mu_{H_2O} = -1.06\,\text{eV}$ and $\mu_{H_2O} = -2.29\,\text{eV}$ for $U = 5$ eV. A higher U-value (5 eV) generally leads to easier reduction and vice versa for a lower U-value (3 eV). This shifts the phase boundaries systematically by about 0.2 eV (see Fig. 3.9).

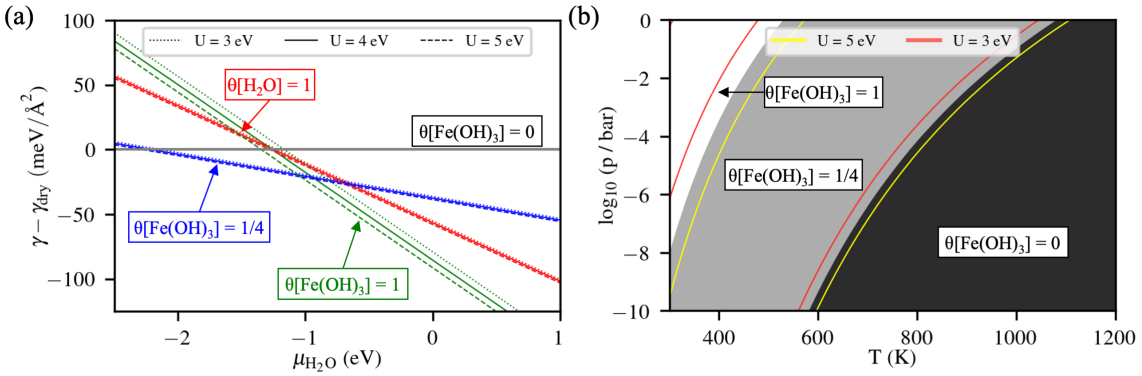

Figure 3.8: (a) Comparative stability plots for α-Fe_2O_3(0001) surface energies under different Hubbard U corrections are given relative to the dry surface as a function of the chemical potential of water μ_{H_2O}. (b) Comparative phase stability plots for α-Fe_2O_3(0001) surface energies under different Hubbard U corrections based on temperature and partial pressure variations ($p(H_2O)$). The background shading indicates the phase region calculated at U=4 eV, and the overlapping boundaries in the white solid line indicate the phase transition. Deviations from phase stability at U=5 eV and U=3 eV are highlighted with red and yellow lines, respectively.

3.2.3.2. Vibrational Contributions to Gibbs Free Energy

To quantify the contribution of surface atomic vibrations to the Gibbs free energy and thus the change in surface stability, normal mode analysis was performed based on a finite difference approximation of the Hessian matrix with a displacement of 0.01 Å. The systems considered are the same symmetric slabs used to compute the energies, however, vibrations were computed only on one surface. For H_2O(g), Gibbs free energies were computed using the rigid rotator and free translator approximation with symmetry number σ=2 in addition to the harmonic vibrations. The contribution to the stability of the different slabs relative to the θ[$Fe(OH)_3$]=0 surface resulting from vibrational, rotational and translational degrees of freedom was calculated analogously to the reaction energies:

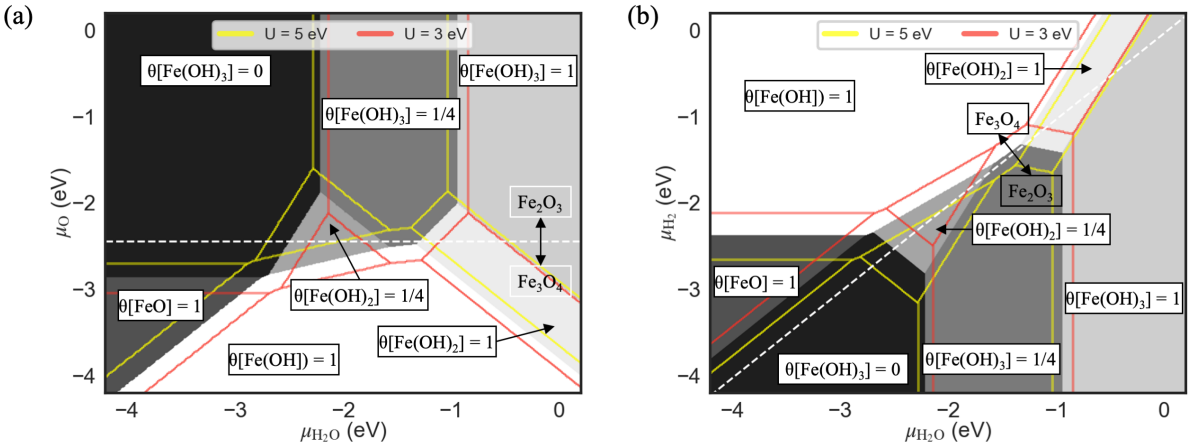

Figure 3.9: Comparative phase stability diagrams for α-Fe_2O_3(0001) surface energies under varying Hubbard U corrections. The background shading delineates phase regions calculated with U=4 eV, while the overlaid boundaries in white dashed lines represent phase transitions. Deviations in phase stability are distinctly highlighted with a yellow line for U=5 eV and a red line for U=3 eV. (a) Surface stability depends on μ_{H_2O} and μ_O. (b) Surface stability depends on μ_{H_2O} and μ_{H_2}.

$$G_{Fe_2O_3} = G_2 - G_1 \tag{3.5}$$

$$\gamma_{vib}(\theta[Fe(OH)_3] = 1) = G_5 - G_1 - \frac{1}{2}G_{Fe_2O_3} - \frac{3}{2}G_{H_2O} \tag{3.6}$$

$$\gamma_{vib}(\theta[Fe(OH)_3] = 1/4) = G_7 - 4 \times G_1 - \frac{1}{2}G_{Fe_2O_3} - \frac{3}{2}G_{H_2O} \tag{3.7}$$

The labeling used, and the zero-point vibrational energy (ZPVE) is given in Table 3.6. The vibration data is shown in Table B.10.

Table 3.6.: Details of the systems considered for vibrational analysis and labeling used. The ZPVE is given in eV.

Structure	Label	Atoms included in partial Hessian	ZPVE	Composition
$\theta[Fe(OH)_3]$=0 (dry/clean)	1	Fe_3O_6	0.607	$Fe_{18}O_{27}$
$\theta[Fe(OH)_3]$=0 (dry/clean)	2	$Fe_3O_6 + Fe_2O_3$	0.932	$Fe_{18}O_{27}$
$\theta[Fe(OH)_3]$=1	5	$Fe_3O_6 + Fe(OH)_3$	1.760	$Fe_{20}O_{33}H_6$
$\theta[Fe(OH)_3]$=1/4	7	$Fe_3O_6 \times 4 + Fe(OH)_3$	3.575	$Fe_{74}O_{114}H_6$
H_2O	H_2O	H_2O	0.574	H_2O

When vibrations are included, similar results are obtained (shown in Fig. 3.10). As one may expect, the main effect of considering the vibrational entropy of the surface is a stabilization of the hydroxyl groups at higher temperatures. The effect is largest for the transition from $\theta[Fe(OH)_3] = \frac{1}{4}$ to the dry surface in the temperature range of 600 to 1200 K. However, it is unclear how good the harmonic approximation is at these elevated temperatures since it cannot

describe the full motion of hydroxyl groups. The main effect of zero-point vibrational energies is to disfavor hydroxylation by approximately 0.13 eV per $Fe(OH)_3$-group.

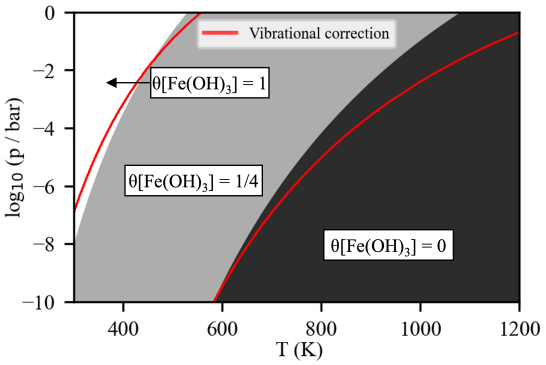

Figure 3.10: Comparative phase stability diagrams for α-$Fe_2O_3(0001)$ surface energies including the vibrational contributions to the Gibbs free energy.

3.2.4. Kinetics and Mechanism of Local Surface Reconstruction in the Hydroxylation of α-Al_2O_3(0001) Surfaces

All previously discussed hydroxylated structures of the α-$Al_2O_3(0001)$ surface require global reconstruction involving the diffusion of Al^{3+} ions, however, in this section, we explore the kinetics and mechanisms by which hydroxylation can occur through local surface reconstruction starting from the clean surface. This has already been discussed for the fully hydroxylated surface $\theta[Al(OH)_3] = 1$ [78, 80]. Apart from the most stable, fully hydroxylated structure, previous theoretical investigations also studied hydroxylation starting from the initial adsorption of water on the clean surface, which dissociates with low barriers, < 0.5 eV [79, 82]. At a coverage of $\theta[H_2O] = 1$, this leads to structure M1 in Fig. 3.1, which is metastable since it is always less stable than a structure with adsorbed $Al(OH)_3$. Figure 3.1 shows that the structural motif of an isolated $Al(OH)_3$ group can also be formed through local reconstruction. In structure M3, an Al-vacancy is formed, saturated with three OH-groups and the removed Al^{3+} ion is placed on the surface as an adsorbed $Al(OH)_3$ group in the same manner as for the structure with $\theta[Al(OH)_3] = 1/4$. Importantly, formation of M3 from the clean surface involves only local reconstruction of the surface and the reaction with three H_2O-molecules. Structure M3 can be described as a local coexistence of 25% of the $\theta[Al(OH)_3] = 1$ structure and 75% of the $\theta[Al(OH)_3] = 1/3$ structure and its stability is in fact almost identical to that of the linear combination of these surfaces. This is apparent from Fig. 3.2a, which shows that the surface free energies of M3, $\theta[Al(OH)_3] = 1/3$ and $\theta[Al(OH)_3] = 1$ cross almost in one point, at μ_{H_2O} = -1.25 eV. At $\mu_{H_2O} <$ -1.25 eV, M3 is actually more stable than the fully hydroxylated surface, $\theta[Al(OH)_3] = 1$.

We investigated the formation of structure M3 from the clean surface via water adsorption and dissociation to M1 followed by diffusion of Al^{3+} ions over the surface to form M3, see Fig.

3.11. A complete reaction pathway was obtained, for which all minima and transition states along the reaction pathway were computed [218, 219, 236]. Although M1 and M3 are (2×2)-surface structures, the path was computed for a (3×3) cell on which only four water molecules were adsorbed in the (2×2) area, where the reaction takes place. This approach was taken to avoid artificial interaction between periodic images of the surface reactions taking place, which would necessarily occur, when using a (2×2)-cell. We decided to start from only four adsorbed water molecules and leave the remaining five sites clean, mainly because this results in a less complex model and because we do not expect a large effect from additional coadsorbed water.

The most favorable pathway for the formation of structure M3 from M1 was found to proceed via two distinct Al-migrations. In a first step, the $Al(OH)_3$ moiety is formed through migration of the closest surface-Al(OH) out of its initial position in the first layer (shown in gold) into the adsorbed position (shown in blue). After a few reaction steps, this gives the intermediate M2, also shown in Fig. 3.1. In a second Al-migration, the Al-vacancy is then moved further away to give M3. In addition to water adsorption and dissociation, the reaction path involves 14 elementary reactions that include both H- and Al-diffusion steps. For one of the proton transfer steps, an adsorbed H_2O molecule was found to facilitate this process as a proton shuttle, which leads to the visible dependence of the corresponding barrier on the chemical potential of water. For all other proton transfers, where this was tested, additional water was not found to lower the barrier at relevant values of μ_{H_2O} for entropic reasons.

Figure 3.11 shows the free energy diagram for the transformation from M1 to M3 for different chemical potentials of water. The chosen values of μ_{H_2O} = -1.80, -1.67 and -1.50 eV where selected to illustrate the effect of μ_{H_2O} on the Gibbs free energy profile. At μ_{H_2O} = -1.67 eV, the initial adsorption of the four H_2O molecules is thermoneutral, while it is uphill in free energy for smaller values of μ_{H_2O}. The kinetics for the initial steps of reconstruction therefore depend on μ_{H_2O} and will become slower with decreasing μ_{H_2O} < -1.67 eV, even if the formation of M3 is still favorable. We note that the value of μ_{H_2O} = -1.67 eV, at which the adsorption of the four water molecules on the (3×3)-surface ($\theta[H_2O]=\frac{4}{9}$) is thermoneutral, is slightly lower than the corresponding value of -1.64 eV given in Table 3.2 for $\theta[H_2O]=1$, which we attribute to adsorbate-adsorbate interaction.

Starting from dissociatively adsorbed water, formation of M2 occurs with moderate barriers of up to 1.02 eV, which are accessible already at ambient temperatures. Importantly, M2 is already more stable than M1 for $\mu_{H_2O} < -0.90$ eV. We note that the type of reconstruction shown for M2 can also occur with a coverage of 1/3, which is slightly more favorable (see Appendix). Due to the relatively high stability of M2, both the reaction backwards to M1 or forwards to M3 is associated with barriers on the order of 2 eV. This becomes feasible approximately at temperatures higher than 700 K, where a first-order rate constant with a barrier of 2.00 eV is 0.07/s. Figure 3.11 shows that the decomposition of M3 to M1 is associated with a large barrier of 3.02 eV. It is important to note that the decomposition of M3 back to M1 and eventually to

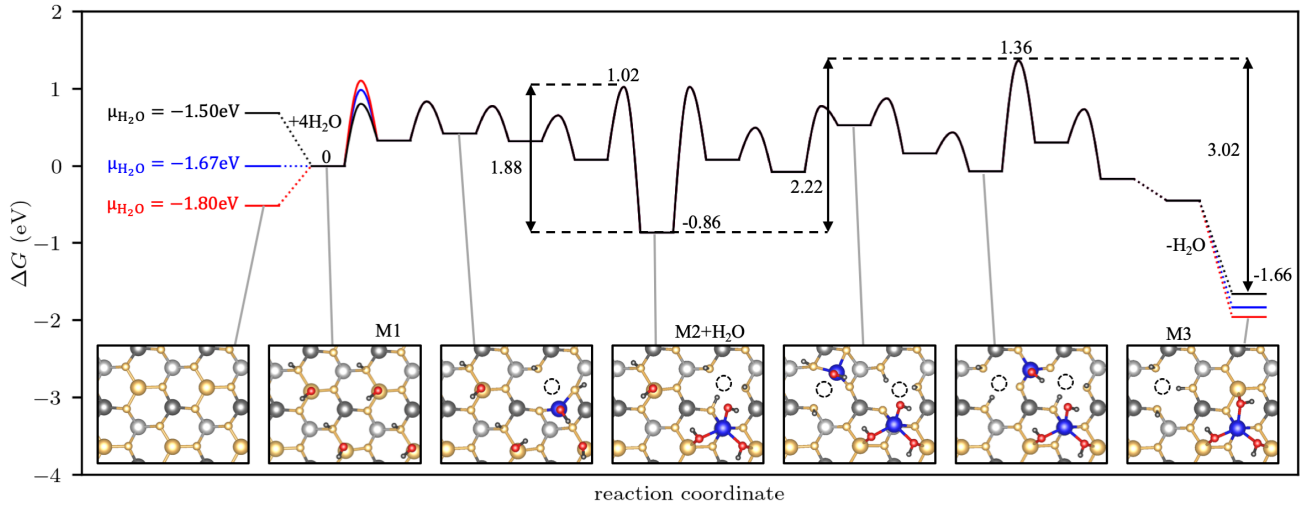

Figure 3.11: Gibbs free energy diagram at μ_{H_2O} = -1.80, -1.67 and -1.50 eV for the reconstruction of structure M1 via M2 to M3. Calculations were performed for a (3×3) unit cell. Selected structures are shown as inset, with the same color code as in Fig. 3.1.

the clean surface also requires an additional water molecule, which facilitates the migration of the Al-species. This results in a high kinetic stability of this surface, especially if water pressure is low, such as in experiments where these surfaces were annealed in UHV and hydroxyl groups were still present [46, 47].

3.2.5. Diffusion Mechanisms for the Formation of Extended Hydroxylated α-Al_2O_3(0001) Surfaces

To further understand the development of hydroxylated surfaces on α-Al_2O_3(0001), we explore how extended hydroxylated structures can form through diffusion mechanisms involving aluminum species. The formation of the extended surfaces listed in Figs. 3.1 and 3.2 with $\theta[Al(OH)_3] = 1, \frac{4}{9}, \frac{1}{3}, \frac{1}{4}, \frac{1}{9}$ and $\frac{1}{16}$ requires the diffusion of additional Al onto the dry surface. The simplest mechanism for this is through direct diffusion of adsorbed $Al(OH)_3$ over the stoichiometric surface, see Fig. 3.12. This is associated with a high barrier of 3.22 eV, which becomes feasible at temperatures around 1100 K, where a first-order rate constant with a barrier of 3.22 eV is 0.05/s.

An alternative to the diffusion of $Al(OH)_3$ is a water-mediated Al-vacancy migration mechanism shown in Fig. 3.13. In this mechanism, an OH-saturated Al-vacancy is assumed to be present on the surface. As discussed above and shown in Fig. 3.11, these vacancies can be formed concomitantly with the $Al(OH)_3$ groups through local reconstruction. Migration of the Al-vacancy occurs through the diffusion of a surface-Al out of its initial position onto the surface and then into the vacancy position. This is facile when a mobile Al(OH) species is created through dissociative H_2O-adsorption. The mechanism for water-mediated Al-vacancy migration is thus similar to the transformation of M2 to M3 (Fig. 3.11), where an additional $Al(OH)_3$

group is coadsorbed. The overall barriers are in both cases on the order of 2.2 eV. In contrast to migration of $Al(OH)_3$, this mechanism requires the presence of an additional molecule of water and will become increasingly unfavorable, for μ_{H_2O} < -1.67 eV. Similar to Fig. 3.11, Fig. 3.12 shows the Gibbs free energy diagram for different values of the chemical potential of water. The values of μ_{H_2O} = -2.20, -1.67 and -1.25 eV were chosen to illustrate how the Gibbs free energy surface changes when water adsorption becomes unfavorable thermodynamically.

Based on the reconstruction and diffusion mechanisms described above, one can now envision how the formation of extended hydroxylated α-$Al_2O_3(0001)$ surfaces can take place. We have shown that, after adsorption and dissociation of water, local reconstruction can lead to a structure as M3, which contains equal amounts of Al-vacancies and adsorbed $Al(OH)_3$. Redistribution of these species through diffusion allows the creation of extended facets of hydroxylated surfaces. Redistribution of adsorbed $Al(OH)_3$ adsorbed on the clean surface allows the formation of surfaces with $\theta[Al(OH)_3] \leq 1$. Agglomeration of the corresponding OH-saturated Al-vacancies exposes the underlying Al-layer and thus leads to the formation of a lower lying, fully hydroxylated surface with $\theta[Al(OH)_3] = 1$. This lower layer with $\theta[Al(OH)_3] = 1$ could further rearrange to a structure with $\theta[Al(OH)_3] < 1$ only through diffusion of Al^{3+} away from this facet. This would be possible via diffusion across a step edge, which was not investigated in this work.

3.3. Conclusion and Outlook

We have investigated the hydroxylated terminations of both the α-$Al_2O_3(0001)$ and α-$Fe_2O_3(0001)$ surfaces, revealing new insights into their stability and structural properties.

For the α-$Al_2O_3(0001)$ surface, we identified a novel termination featuring isolated $Al(OH)_3$ groups adsorbed on the dry surface. This structure is predicted to be stable at higher temperatures compared to previously proposed models for hydroxylated surfaces. Our findings indicate that the interaction between adsorbed $Al(OH)_3$ groups is weakly repulsive at coverages

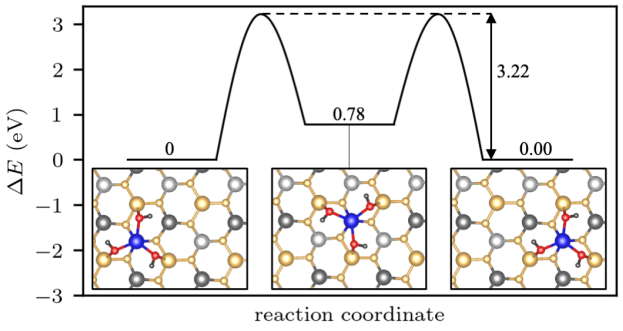

Figure 3.12: Energy diagram for the diffusion of an adsorbed $Al(OH)_3$ group. Calculations were performed for a (3×3) unit cell.

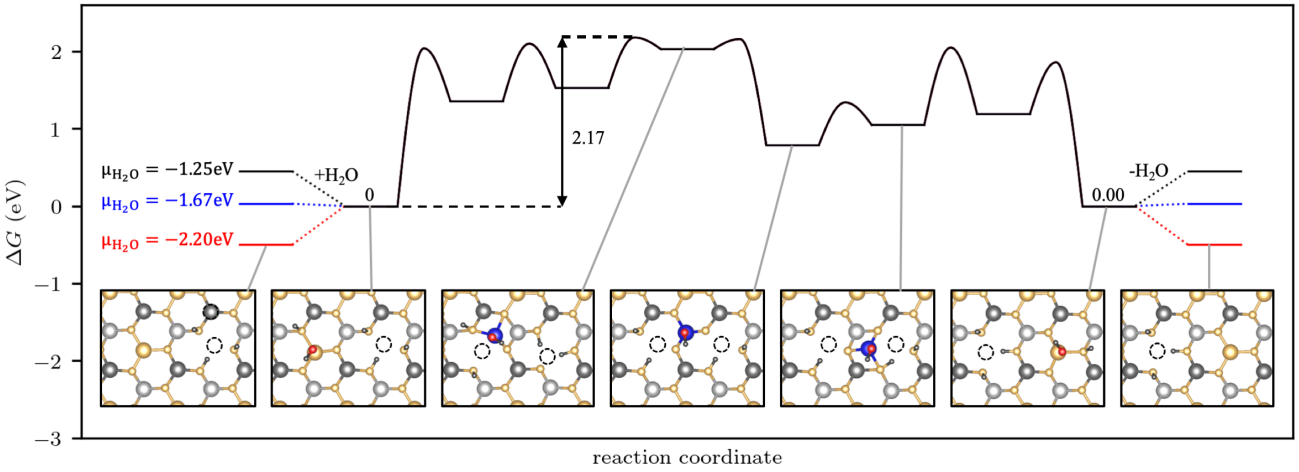

Figure 3.13: Free energy diagram for the diffusion of an OH-saturated Al-vacancy on the stoichiometric surface. The final state is in both cases equivalent to the initial state, with the $Al(OH)_3$ group (Al vacancy) shifted right (left). Calculations were performed for a (3×3) unit cell. Selected structures are shown as inset, with the same color code as in Fig. 3.1.

up to $\theta[Al(OH)_3] \leq \frac{1}{3}$, and the stability shows little dependence on the precise positions of the adsorbates. This leads to multiple stable configurations.

Similarly, for the α-$Fe_2O_3(0001)$ surface, we found that structures with a low concentration of hydroxyl groups, described as isolated $Fe(OH)_3$ groups, are stable at relatively low chemical potentials of water. These structures are identical in form to the hydroxylated terminations observed on α-$Al_2O_3(0001)$. Additionally, we explored oxidized and reduced terminations, finding that while oxidized surfaces are not stable under relevant conditions, certain reduced surfaces become stable only at low chemical potentials of oxygen, where bulk hematite is less stable than bulk magnetite.

The formation and decomposition processes of these hydroxylated surfaces were also studied. For α-$Al_2O_3(0001)$, we observed that local reconstruction via adsorption and dissociation of water leads to the formation of $Al(OH)_3$ groups and OH-saturated Al-vacancies, requiring modest energy barriers (∼1 eV). Further reconstruction, essential for forming the thermodynamically most stable surfaces, demands higher barriers (>2 eV). The kinetics of these processes are influenced significantly by the partial pressure of water, which also facilitates the migration of Al atoms on the surface and the dehydroxylation process.

For α-$Fe_2O_3(0001)$, the predicted stability of hydroxylated surfaces with low OH-concentration remains robust across different computational methodologies. However, the oxidation and reduction behaviors show a strong dependence on the chosen value of U in the PBE+U calculations, indicating a need for higher-level theories for more accurate predictions.

Overall, both studies highlight the thermodynamic stability of hydroxylated surfaces with low hydroxyl group concentrations over a wide range of water chemical potentials. This stability makes them suitable starting points for future research into surface properties and reactivity

under various conditions. Our results suggest that these hydroxylated terminations could be relevant for other phases of Al_2O_3 and Fe_2O_3, as well as other oxides crystallizing in the corundum structure, such as Cr_2O_3 and V_2O_3. Future studies, potentially employing kinetic Monte Carlo simulations, could provide more detailed predictions on the evolution of these surfaces under specific experimental conditions.

4. CO as Probe Molecule on Surfaces

4.1. CO Adsorption on PdPt alloy (111) Surfaces

This chapter is based on [Dolling, D. S.; **Chen, J.**; Schober, J.-C.; Creutzburg, M.; Jeromin, A.; Vonk, V.; Sharapa, D. I.; Keller, T. F.; Plessow, P. N.; Noei, H.; Stierle, A. Probing Active Sites on Pd/Pt Alloy Nanoparticles by CO Adsorption. *ACS Nano* **2024**. DOI: 10.1021/acsnano.4c08291] [Gojare, S.*; Chen, S.*; **Chen, J.***; Yu, Z.; Quesada, J. V.; Plessow, P. N.; Fink, K.; Wang, Y. Adsorption of CO on α-Al_2O_3(0001): A combined experimental and computational study. *in Preparation* (* indicates equal contribution)].

In this section, the relationship between active surface sites and CO vibrational frequencies as a function of nanoparticle composition has been systematically studied using DFT. To support the theoretical framework and discussions, I have integrated experimental data provided by collaborators at the **Centre for X-ray and Nano Science CXNS, Deutsches Elektronen-Synchrotron DESY, Hamburg, Germany**. The experimental procedures and analyses were conducted by the group of **Prof. Dr. Andreas Stierle**. I did not participate in the experiments but have included the data here, with permission, to enhance the comparison between theory and experiment. The experiments involved polarization-modulated Fourier transform infrared reflection absorption spectroscopy (FT-IRRAS) to investigate the interaction of CO molecules with different adsorption sites on model catalysts consisting of Pd/Pt alloy nanoparticles grown on α-Al_2O_3 which shown as Fig. 4.5.

4.1.1. Computational Details

All DFT calculations were performed with the VASP version 5.4.1[225, 257] and the ASE [258] using the BEEF–vdW functional[200, 201] and the PAW method.[224, 259] The lattice constants of Pd/Pt alloys were optimized using an energy cutoff of 600 eV, while slabs calculations were performed with a cutoff of 400 eV and Γ-centered k-point grid with a $6 \times 6 \times 1$ mesh for (2×2) surface unit cell. Surfaces were modeled with a four-layer slab, with two bottom layers frozen. The slabs are separated by 28 Å of vacuum to eliminate artificial interactions due to periodic boundary conditions. The unit cells of the alloys and their calculated lattice constant are shown in Fig. 4.1. CO-adsorption was studied in the low-coverage limit (θ=1/16). The vibrational frequencies of adsorbed CO were calculated using finite differences within the harmonic approximation.

The expansion of the density includes reciprocal lattice vectors up to 3/2 times the norm used for the wave function, $|\mathbf{G}_{\mathrm{cut}}|$ (PREC=Normal in VASP). The calculations were performed with real-space projectors (LREAL=AUTO) and the self-consistent field (SCF) procedure was converged to a threshold of 10^{-8} eV for the total energy. A criterion of 0.01 eV/Å for the maximum forces on individual atoms was used for geometry convergence. Gaussian smearing with a 0.1 eV width was applied.

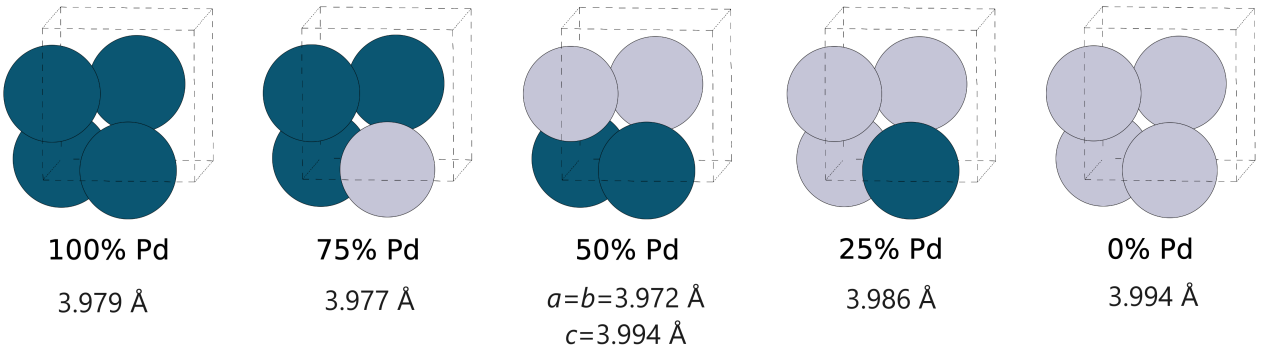

Figure 4.1: The unit cells of Pd/Pt alloy bulk with different compositions and their lattice parameters.

Table 4.1.: DFT value for CO-vibrational frequency in the gas phase. δ is the displacement used in the calculation of the numerical Hessian. NFREE corresponds to the number of force calculations performed per Cartesian component of an atom. The shift is defined as $\nu^{\mathrm{CO}}_{\mathrm{DFT}} - \nu^{\mathrm{CO}}_{\mathrm{exp.}}$.

PREC	NFREE	δ / Å	ν / cm^{-1}	Shift / cm^{-1}
normal	2	0.01	2124.4	-18.6
normal	4	0.02	2122.7	-20.3
accurate	4	0.02	2122.3	-20.7

Due to anharmonicity and the systematic DFT error, it should not be expected that the absolute value of the computed frequency of CO would fit well with the experimental data. Thus, to eliminate systematic errors and to compare with experiment, we followed the common approach to shift the computed vibrational frequencies by a constant value (shown in Table 4.1) so that the computed gas phase vibration matches the experimental value (2143.0 cm^{-1}).[260] The theoretical CO-vibrational frequency is obtained by Eq. 4.1, and the same shift is applied to all computed vibrations of adsorbed species calculated by the same setting.

$$\nu_{\mathrm{theory}} = \nu_{\mathrm{DFT}} + (\nu^{\mathrm{CO}}_{\mathrm{DFT}} - \nu^{\mathrm{CO}}_{\mathrm{exp.}}) \tag{4.1}$$

Only CO was included in the numerical Hessian, with a displacement of 0.02 Å. The DFT value of the CO vibrational frequency in the vacuum varies slightly with the setting, as shown in Table 4.1. For the calculation of the shift of adsorbed CO, the vibration of adsorbed CO, as well as CO in the gas phase have always been computed with a consistent setting. The vibration data are shown in Table C.12, which is calculated by setting PREC = Normal and NFREE = 2, except for the top site on 100 Pd surfaces, which is PREC = Accurate and NFREE = 4. The vibration data are shown in Table C.13, which is calculated by setting PREC = Normal and NFREE = 4.

4.1.2. Results and Discussion

We studied adsorption on the fcc(111) facets and systematically varied the composition of the binding site and the next-nearest neighbors in the sublayer, as shown in Fig. 4.2a. Adsorption was considered at on-top, bridge and hollow sites. In contrast to the experiment, here a distinction was made between fcc and hcp hollow sites. Both sites are threefold coordinated, but the sublayers are different due to the fcc stacking. As illustrated in Fig. 4.2a, we define the site as consisting of the binding metal atoms, i.e. one/two/three atoms for top/bridge/fcc+hcp sites. The atoms, which were varied in the sublayer are also indicated.

Table 4.2.: The studied compositions for the different sites, atoms in the sublayer and for the bulk composition, see also Fig. 4.2 and 4.4.

Category	% Pd
Site: Top	0, 100
Site: Bridge	0, 50, 100
Site: Hollow (fcc, hcp)	0, 33.3, 66.7, 100
Sublayer	0, 33.3, 66.7, 100
Bulk	0, 25, 50, 75, 100

As a first step, we have studied the fcc(111) surfaces that result from stoichiometric terminations of pure metals (Pd and Pt) and bulk alloys ($L1_0$ and $L1_2$) with the composition ($PtPd_3$, Pt_2Pd_2, Pt_3Pd, see Fig. 4.1). These surfaces already give rise to many possible compositions of active sites and sublayers, as shown in Fig. 4.2b. Figure 4.2b shows the computed harmonic frequency of adsorbed CO as a function of the bulk composition of the slab. Additionally, the composition of the binding site is illustrated with a color code. The general observation is that - for a constant composition of the active site - the vibrational frequencies decrease with an increasing amount of Pd in the bulk. One can furthermore see that the trend with respect to active site composition is opposite to that of bulk composition: the frequency generally increases with increasing amounts of Pd in the nearby atoms. The frequencies for on-top binding are in the range of 2040 to 2060 cm^{-1} and are lower for increasing Pd-content in the bulk. The frequencies for CO binding on top of Pt or Pd are similar, although we note that our DFT calculations predict CO-binding on top of Pd not to be favorable (see Fig. 4.3), in agreement with the experimental observations. Frequencies for binding at hcp and fcc sites are very similar (1740 cm^{-1} to 1800 cm^{-1}), although our calculation also shows the well-known preference for binding at the fcc-site(see Fig. 4.3). Bridge-sites were generally not found to be particularly stable, but the predicted frequencies agree with the observed experimental trend, i.e. they are found at higher frequencies than fcc, at around 1850 cm^{-1}.

For adsorption at the fcc site, the influence of the closest atoms was further analyzed through variation of the three binding atoms and the three sublayer atoms in the possible compositions (Pt_3, Pt_2Pd, $PtPd_2$, Pd_3). These sites were created by substituting the three atoms in the fcc site as well as the three subsurface atoms in the stoichiometric surfaces mentioned above (bulk

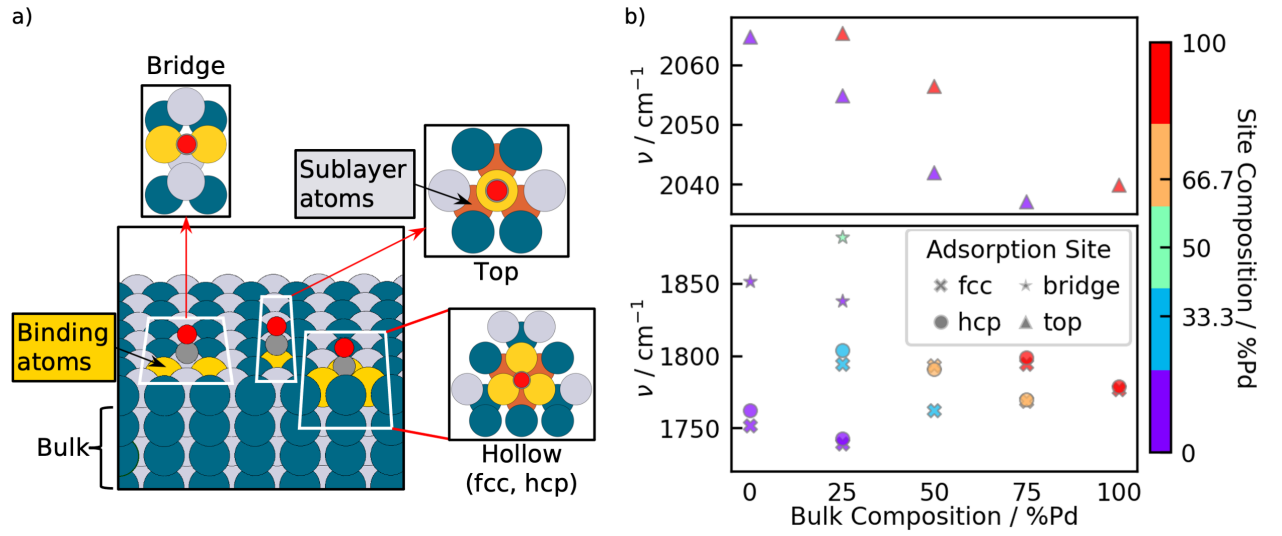

Figure 4.2: (a) Illustration of the CO adsorption sites on the fcc(111) surface based on a bulk alloy with 50% Pd in the Pd/Pt alloy system. The binding atom at the active site are highlighted in yellow and the subsurface layer is indicated in red. Pd and Pt are shown in blue and light gray, C and O in dark gray and red. (b) CO vibrational frequencies adsorbed on different sites on (111) surfaces with varying compositions. All surfaces are assumed to have a stoichiometric termination of ordered bulk alloys.

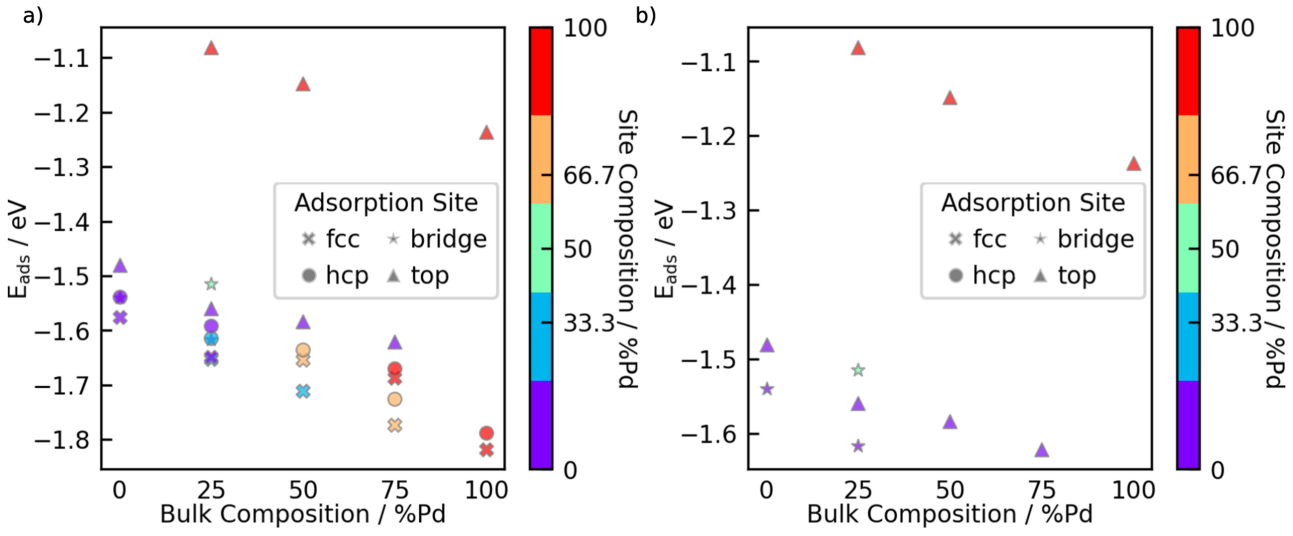

Figure 4.3: (a) The adsorption energy of the same structures shown in Fig. 4.2. (b) Only shows the top site and bridge site

compositions Pd, $PtPd_3$, Pt_2Pd_2, Pt_3Pd and Pt). Figure 4.4 shows the computed data as a function of three parameters: bulk composition, site composition and sublayer composition. In agreement with trends observed for the stoichiometric, ordered surfaces, CO-frequencies generally increase with Pd-content in the fcc site. On the other hand, frequencies decrease with increasing Pd content in the bulk. The sublayer composition causes a variation of approximately 10 cm^{-1} in the vibrational frequency.

In contrast to the theory, in the FT-IRRAS experiment, only the overall composition of the particles is known, and not how it relates to the exact composition of the binding site. The trend observable in Fig. 4.5a for CO bound on top of Pt atoms is in agreement with the trend we find in Fig. 4.2b. For the other binding sites (Fig. 4.5b-c), there is no clear trend in the experimentally observed frequencies with particle composition. Based on our calculations, this can be explained by the competing influences of changes in the composition of both the surface site and the bulk.

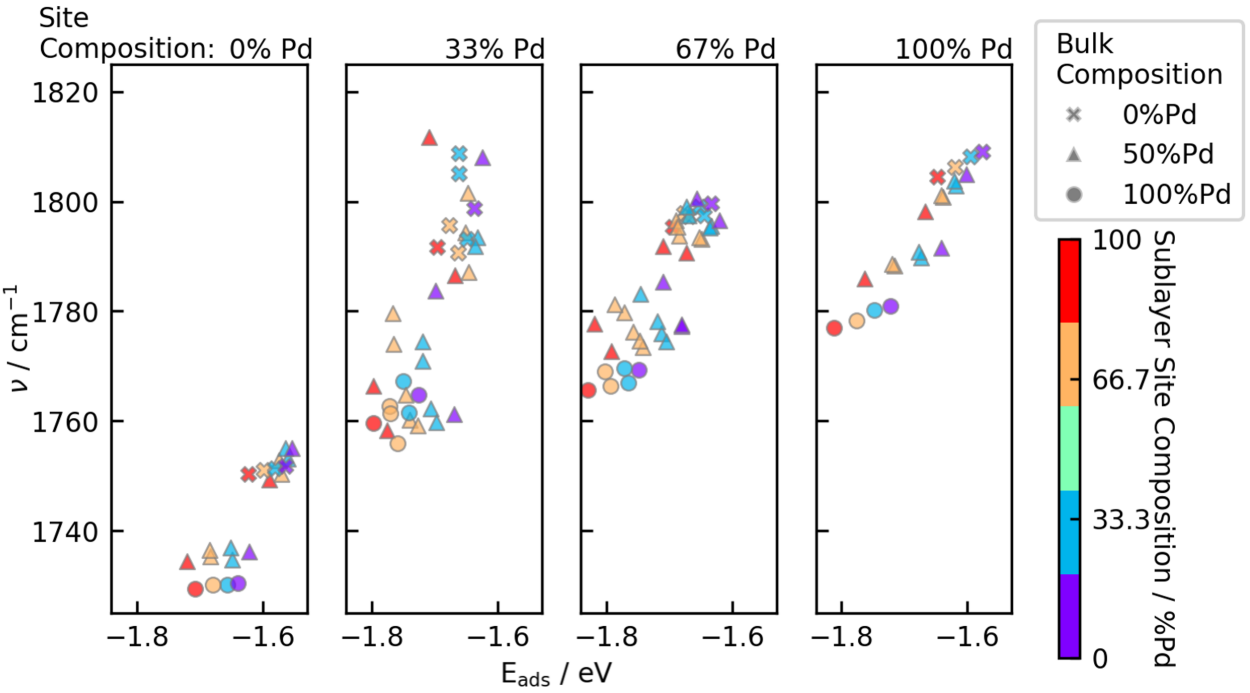

Figure 4.4: CO vibrational frequencies on fcc sites are shown as a function of the adsorption energies. Each panel contains structures with one site composition. The bulk composition is indicated with different symbols and the composition of the sublayer can be identified from the color of the symbols.

The DFT calculations offer insights into the dependence of the vibrational bands on the specific local alloy composition, whereas the FT-IRRAS results yield information on the sum of the wavenumbers of all adsorption sites. The DFT calculations for hollow site adsorption of CO show a red shift for increasing amounts of nearby Pt atoms. A similar trend can be seen in the FT-IRRAS measurement for the adsorption of CO on bridge sites, see Fig. 4.5. For on-top adsorption sites, however, the experimental results show the opposite behavior, see Fig.

4.5. The very broad IR bands measured for the alloy samples can be related to the different specific adsorption configurations, as the DFT calculations showed that IR band wavenumber shifts several 10 cm^{-1} for different sublayer and nearby atom configurations. This can best be seen for on-top adsorption of CO on Pt on side facets (2078 cm^{-1} for pure Pt NPs): The band is strongly broadened for alloy nanoparticles, featuring a long shoulder towards the lower wavenumber.

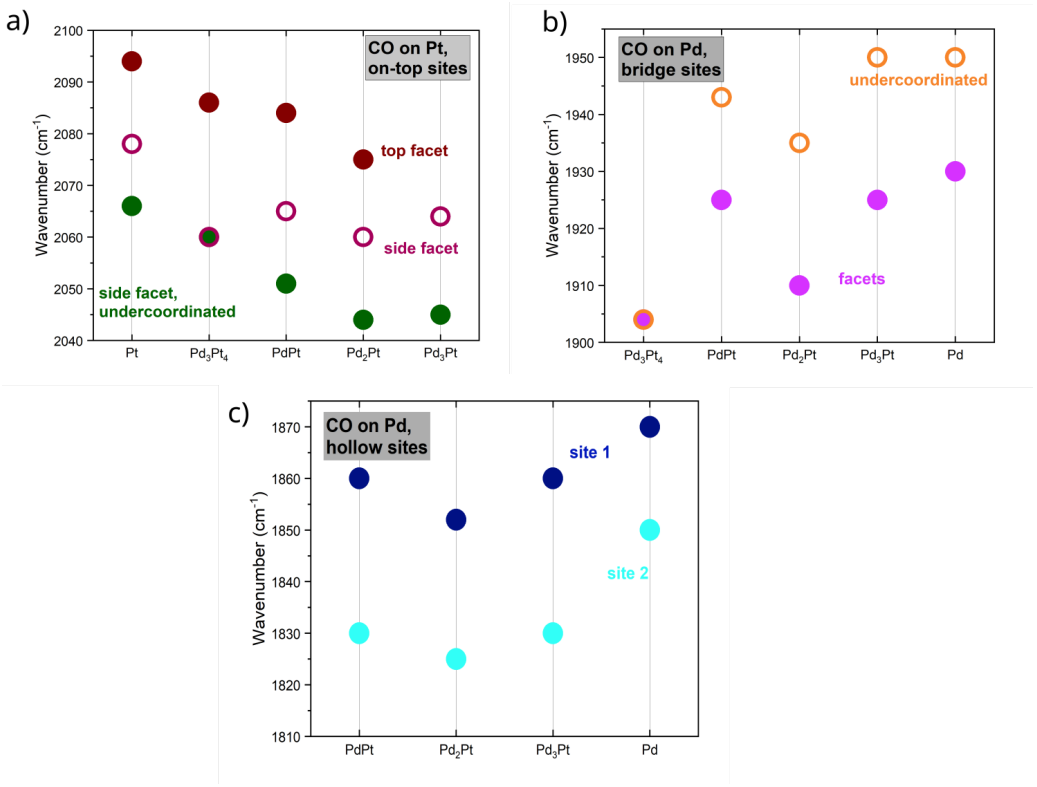

Figure 4.5: Comparison of the wavenumbers assigned to CO on a) on-top sites on Pt, b) bridge sites on Pd and c) hollow sites on Pd. The data is taken from measurements at room temperature at p-polarization after exposure to 5 L CO (dosed at 10^{-8} mbar partial pressure). Reprinted with permission from *ACS Nano* **2024**.[261] Copyright© 2024 American Chemical Society.

4.1.3. Conclusion

In this work, we systematically investigated the relationship between the composition of Pd/Pt alloy nanoparticles and the vibrational frequencies of adsorbed CO using DFT and polarization-dependent FT-IRRAS experiments. We compared the theoretical results with the experimental result and provided a detailed understanding of how the local atomic environment within the nanoparticles influences CO adsorption at various active sites.

DFT calculations revealed that the vibrational frequencies of CO adsorbed on different sites, such as on-top, bridge, and hollow sites, are highly dependent on the local composition of the alloy. Specifically, a general trend was observed where increasing Pd content in the bulk led to a decrease in vibrational frequency, while increasing Pd content at the active site resulted

in an increase in frequency. These findings indicate that both the surface composition and the underlying sublayers play crucial roles in determining the CO adsorption properties, although the sublayer composition has a comparatively minor influence.

The experimental FT-IRRAS data supported the theoretical predictions, particularly for CO adsorption on top of Pt atoms, where a clear trend was observed with varying nanoparticle composition. However, the experimental data for bridge and hollow sites showed less distinct trends, likely due to the complex interplay of surface and bulk composition effects. The broad IR bands observed in the experiments can be attributed to the heterogeneous nature of the alloy surface, where varying local configurations lead to a range of CO vibrational frequencies.

The integration of DFT calculations with experimental FT-IRRAS measurements enabled a comprehensive analysis of the active sites on Pd/Pt alloy nanoparticles, offering valuable insights into the composition-dependent behavior of these catalysts. This study underscores the importance of local atomic composition in dictating the catalytic properties of alloy nanoparticles and highlights the utility of CO as a probe molecule for characterizing surface sites under reaction conditions. These findings contribute to the broader understanding of alloy catalysts and pave the way for the development of more efficient catalysts for applications in emission control and energy conversion.

4.2. CO Adsorption on $\alpha-Al_2O_3(0001)$ Surfaces

In this section, we thoroughly investigate the adsorption of CO on various surfaces reported in Chapter 3, including dry surfaces, surfaces with different degrees of hydroxylation, and metastable water-dissociated surfaces under different water coverage by integrating experimental data provided by collaborators at **Institute of Functional Interfaces IFG, KIT**. The experimental procedures and analyses were conducted by **Dr. Shuang Chen** and **Dr. Yuemin Wang**. Although I did not participate in the experimental work, I have included their data here, with permission, to support the theoretical discussions. The combined experimental and theoretical results consistently reveal that the α-$Al_2O_3(0001)$ surface is stabilized by partial hydroxylation, as evidenced by two distinct CO bands at 2163 cm^{-1} (CO-OH) and 2172 cm^{-1} ($CO-Al^{3+}$) with characteristic binding energies.

4.2.1. Computational Details

All periodic DFT calculations were performed with the VASP version 5.4.1[225, 257] and the ASE [258] using the PBE functional[199] with Grimme's D3 dispersion correction [212] and the PAW method [224, 259]. The lattice constants of α-Al_2O_3 were taken from a previous study on the hydroxylation of α-$Al_2O_3(0001)$ in Chapter 3.[222] Slabs calculations were performed with a cutoff of 400 eV and Γ-centered k-point grid with a $4 \times 4 \times 1$ mesh for (1×1) surface slab unit.

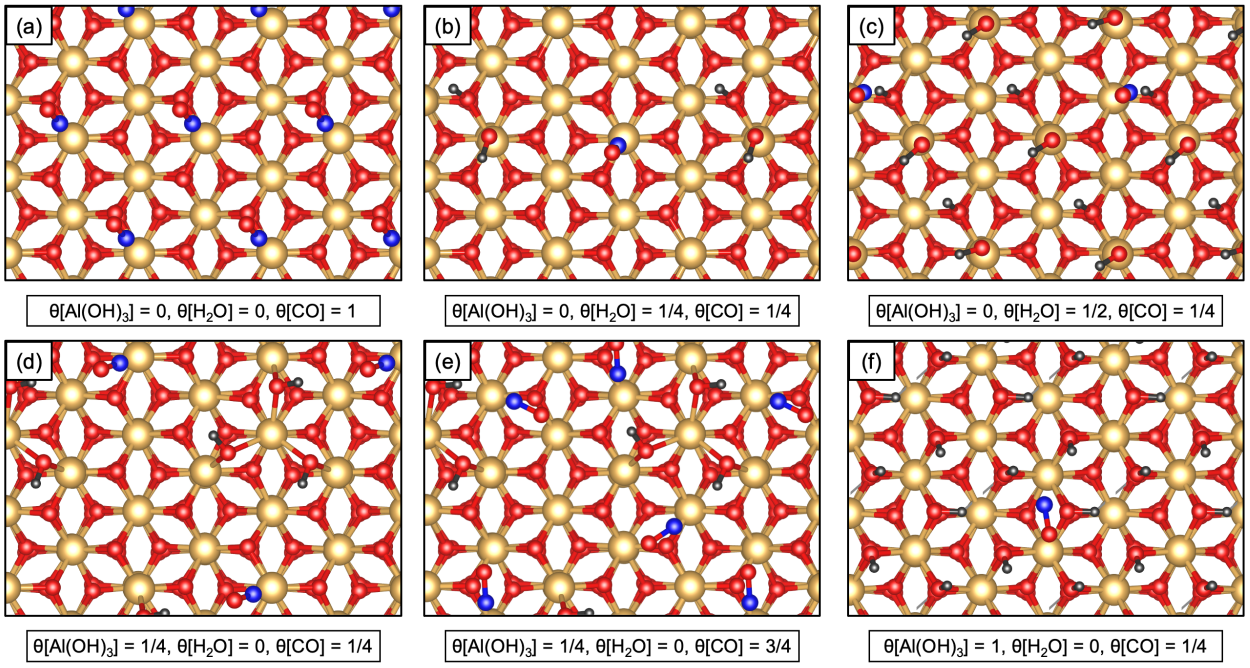

Figure 4.6: The typical configurations of CO adsorption on different α-$Al_2O_3(0001)$ surfaces. Each structure is described by the coverage rate of $Al(OH)_3$, H_2O, and CO. The gold sphere represents the Al atom, red represents O, black represents H, and blue represents C. All configurations are displayed in top views.

Surfaces were modeled as slabs with seven formula units of Al_2O_3 per stoichiometric (1×1)-surface and slabs of corresponding thickness for other terminations. The lower part of the slabs was terminated by a single Al-layer (stoichiometric termination) and the bottom 3.5 formula units of Al_2O_3 per (1×1)-surface were kept frozen at their bulk positions. The slabs were separated by at least 16 Å of vacuum to prevent artificial interaction between periodic images. In the CO adsorption calculations, a plane wave basis set for the electronic density, which includes reciprocal lattice vectors with a norm up to 3/2 or 2 times larger than for the wave function, $|\mathbf{G}_{\text{cut}}|$ (PREC=Normal or Accurate in VASP). CO and binding atoms (Al or OH) were included in the numerical Hessian, with a displacement of 0.01 Å or 0.02 Å. The settings are listed in Table D.14 in the Appendix. The calculations were performed with real-space projectors (LREAL=AUTO) and the self-consistent field (SCF) procedure was converged to a threshold of 10^{-8} eV for the total energy. A criterion of 0.005 eV/Å for the maximum forces on individual atoms was used for geometry convergence. Gaussian smearing with a 0.1 eV width was applied.

4.2.2. Results and Discussion

Different adsorption configurations for various CO coverages on different α-$Al_2O_3(0001)$ surfaces, including dry (stoichiometric), water-dissociated, and partial and fully hydroxylated surfaces were investigated. The typical configurations are shown in Fig. 4.6. Here, each adsorption

configuration is described by the degree of surface hydroxylation ($\theta[Al(OH)_3]$), the water coverage ($\theta[H_2O]$), and the CO coverage ($\theta[CO]$).

The result of CO vibrational frequency is shown in Fig. 4.7a. All the vibrational frequencies are shifted by subtracting the computed vibrational frequency of CO in vacuum (2124.3 cm^{-1}). The most important factor affecting the vibrational frequency is the adsorption site; CO adsorbed on Al usually has a higher frequency, while CO adsorbed on H has a lower vibrational frequency.

Multiple vibrational frequencies are observed when a surface slab adsorbs more than one CO when simulating a higher coverage rate of CO. The vibrational band for the C-O stretch can split into multiple peaks. Each peak corresponds to CO molecules adsorbed at different sites with slightly different interaction strengths. Although we placed each CO in a consistent environment to study the effect of CO coverage, multiple similar vibration frequencies are still generated because of subtle differences caused by computational accuracy, and here we only record the frequency with the highest vibration intensity. On the same surface, at higher coverage levels, interactions between adjacent CO molecules can also influence the stretching frequency.

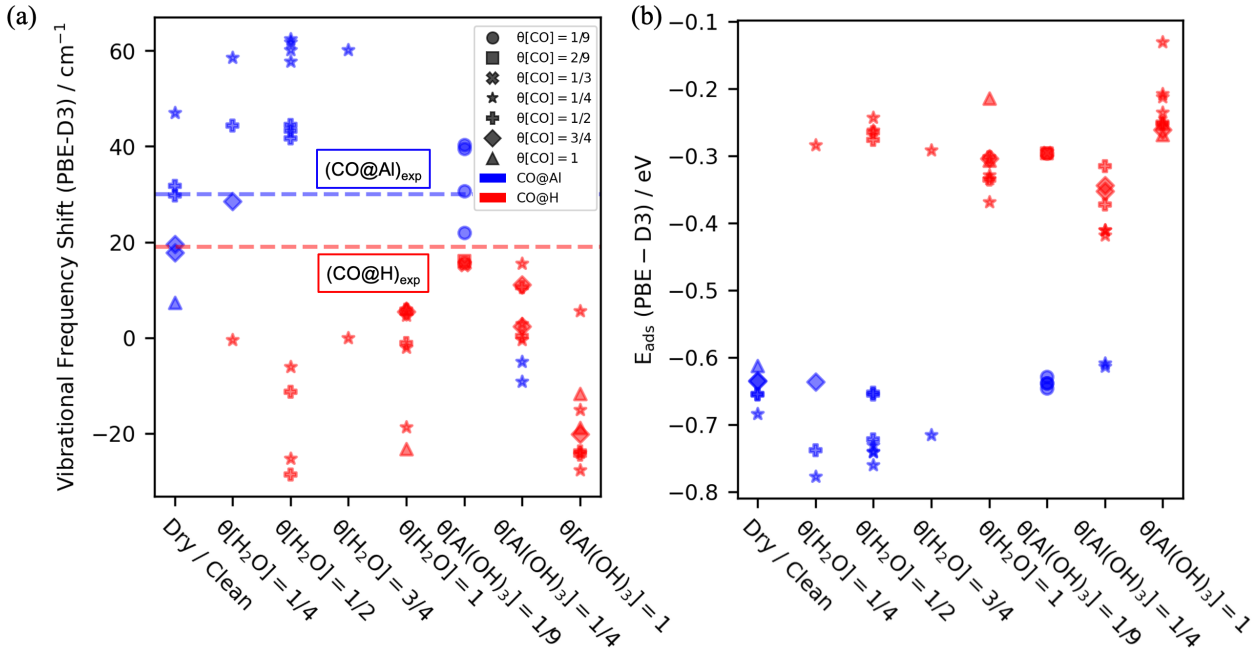

Figure 4.7: The calculated shifted vibrational frequency and adsorption energy of various CO adsorption rates on different α-$Al_2O_3(0001)$ surfaces. The different markers represent different CO coverages and the colors represent the adsorption sites. The blue and red dashed lines are the vibrational frequency of CO adsorbed on Al and H obtained from the experiments. (a) CO vibrational frequency versus different surfaces. (b) CO adsorption energy versus different surfaces.

When CO approaches a surface atom with an empty orbital (like aluminum on an α-$Al_2O_3(0001)$ surface), the carbon atom's lone pair of electrons in its sp-hybridized orbital can donate electron density to the surface atom. This σ-donation forms a σ-bond between the carbon and the surface

atom, slightly increasing the electron density around the C–O bond. As a result, the C–O bond strength increases slightly, causing a blue shift in the C–O stretching frequency.

CO can form a hydrogen bond with the hydrogen atom of the surface OH group. The carbon end of the CO molecule, which has a partial negative charge, interacts with the partially positive hydrogen atom of the OH group. The formation of the hydrogen bond leads to a redistribution of electron density within the CO molecule. The hydrogen bond effectively pulls electron density towards the hydrogen atom of the OH group, away from the C-O bond. The hydrogen bonding interaction with the OH group results in a withdrawal of electron density from the CO molecule. This reduces the electron density in the C-O bond, weakening it. A weaker C-O bond has a lower bond force constant, which causes a lower vibrational frequency and longer bond distance. Figure 4.8a clearly shows the linear relationship between bond length and vibrational frequency, i.e., the longer the bond length, the lower the vibrational frequency.

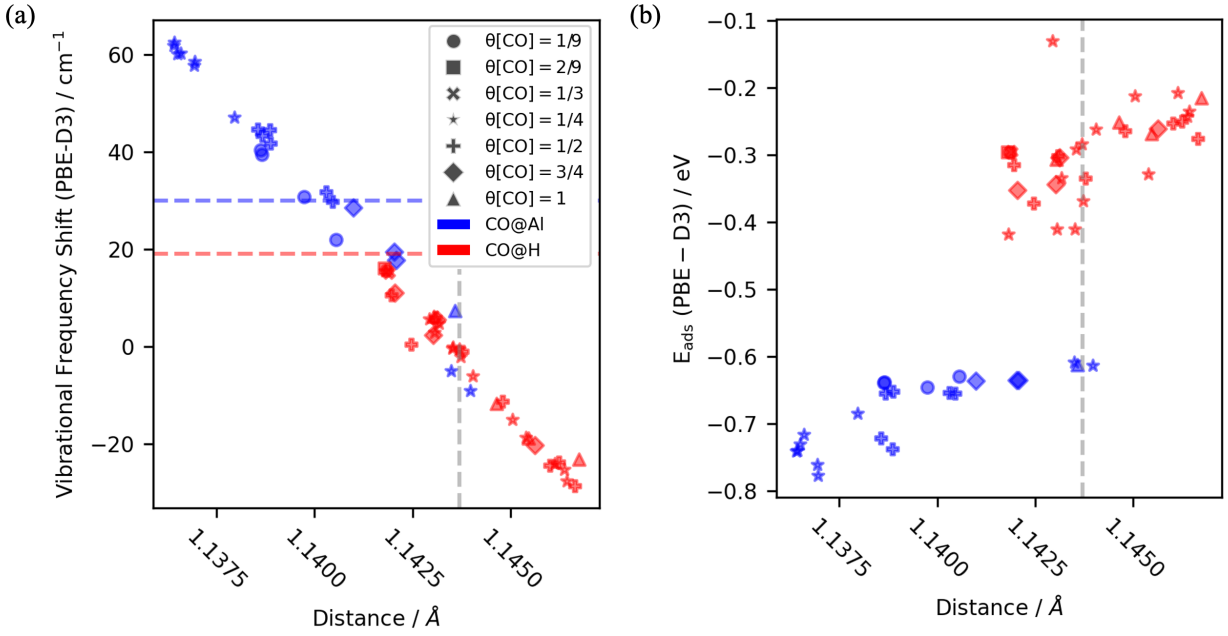

Figure 4.8: (a) Vibrational frequency versus CO bond length. The vertical grey dashed line represents the computational value of the bond length of free CO. (b) Adsorption energy versus CO bond length.

The result of adsorption energy is shown in Fig. 4.7b, the CO adsorption energy for adsorption on Al is at least about 0.2 eV greater than that for adsorption on H. For low CO coverage, such as 1/4, the presence of H_2O will enhance CO adsorption on Al sites relative to the dry surface. However, this enhancement is gradually weakened with the increase of H_2O coverage. The presence of $Al(OH)_3$ will undermine the CO adsorption on the Al site. The relation between CO bond length and adsorption is shown in Fig. 4.8b. Unlike the clear linear relationship between vibrational frequency and bond length, the adsorption energy roughly follows the relationship in that the larger the bond length, the weaker the adsorption. The same bond

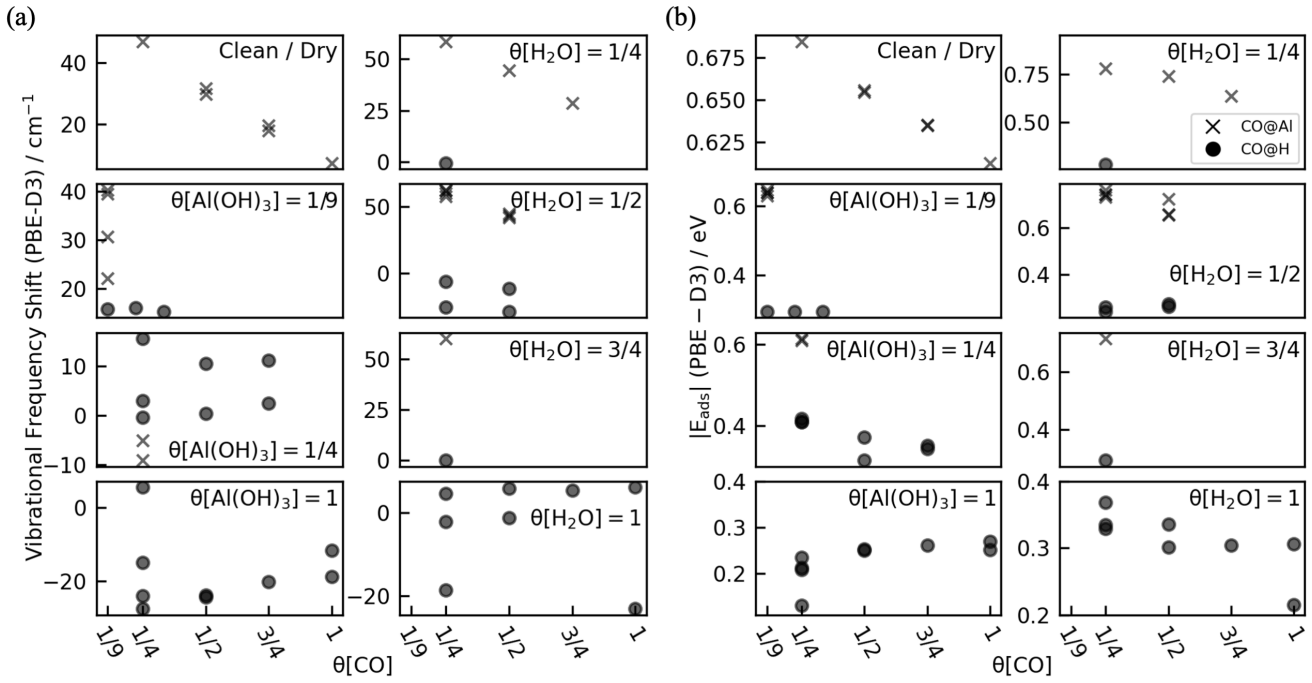

Figure 4.9: (a) Vibrational frequency versus CO coverage on different surfaces. (b) Adsorption energy versus CO coverage on different surfaces.

length can produce an adsorption energy gap of 0.2-0.5 eV at different adsorption sites.

The effect of CO coverage on vibrational frequency is shown in Fig. 4.9a. On the dry surface, Al is the only available site, and all the vibrational frequencies are blue-shifted. As CO coverage increases, the vibrational frequency decreases linearly. On $\theta[Al(OH)_3] = 1/9$ surface, the vibrational frequencies of CO on both Al and H sites are blue-shifted. For CO adsorption on Al, the adsorption site (position relative to $Al(OH)_3$) and angle determine the vibration frequency. For the H site, CO is adsorbed on the hydroxyl group of $Al(OH)_3$, and the number of CO does not affect the vibrational frequency. For surfaces with a higher degree of hydroxylation, $\theta[Al(OH)_3] = 1/4$, the vibrational frequency of CO adsorption on H decreases with increasing CO coverage. There is only one available Al site on this surface, which is the surface Al farthest from $\theta[Al(OH)_3]$. We found two stable adsorption configurations with different adsorption angles but similar adsorption energies (∼0.61 eV) for this adsorption site. For the fully hydroxylated surface, $\theta[Al(OH)_3] = 1$, there is no exposed Al site. Therefore, all CO can only be adsorbed on H. Due to the effect of hydrogen bonds, the H on the surface is not identical, so when a single CO is adsorbed on a unit slab, there will be different adsorption configurations. In an extremely weakly adsorbed configuration (E_{ads} = 0.13 eV), the vibrational frequency will be blue-shifted. The vibrational frequencies will be red-shifted for other relatively more stable adsorption configurations (E_{ads} = 0.20 - 0.25 eV). For the stable adsorption configuration, the vibrational frequency increases with the CO coverage. For surfaces with water molecules dissociated, as the water coverage increases, the available H sites increase while the Al sites decrease. For $\theta[H_2O] = 1/4$ surface, adsorption on H hardly changes the vibrational frequency of CO.

However, when CO is adsorbed on Al, the vibrational frequency increases further compared to when it is adsorbed on Al on a dry surface. A similar phenomenon also occurs on $\theta[H_2O] = 1/2$ surfaces. On this surface, CO adsorption on H produces a red shift, but is insensitive to CO coverage. Since each CO is not identical when more CO is adsorbed on the $\theta[H_2O] = 3/4$ surface, we only list the results of 1 CO adsorption here. For $\theta[H_2O] = 1$, the vibrational frequencies at different adsorption positions are quite different, with CO adsorbed on lower positions of OH having lower vibrational frequencies. At the same time, the vibrational frequency is almost unaffected by the CO coverage.

The effect of CO coverage on adsorption energy is shown in Fig. 4.9b. On the dry surface, the adsorption energy becomes weaker as the CO coverage increases. For surfaces with different degrees of hydroxylation, the adsorption energy of CO is almost unaffected by the CO coverage. For water-dissociated surfaces, the adsorption energy of CO becomes weaker with increasing CO coverage. Meanwhile, the presence of water enhances the adsorption of CO on Al sites.

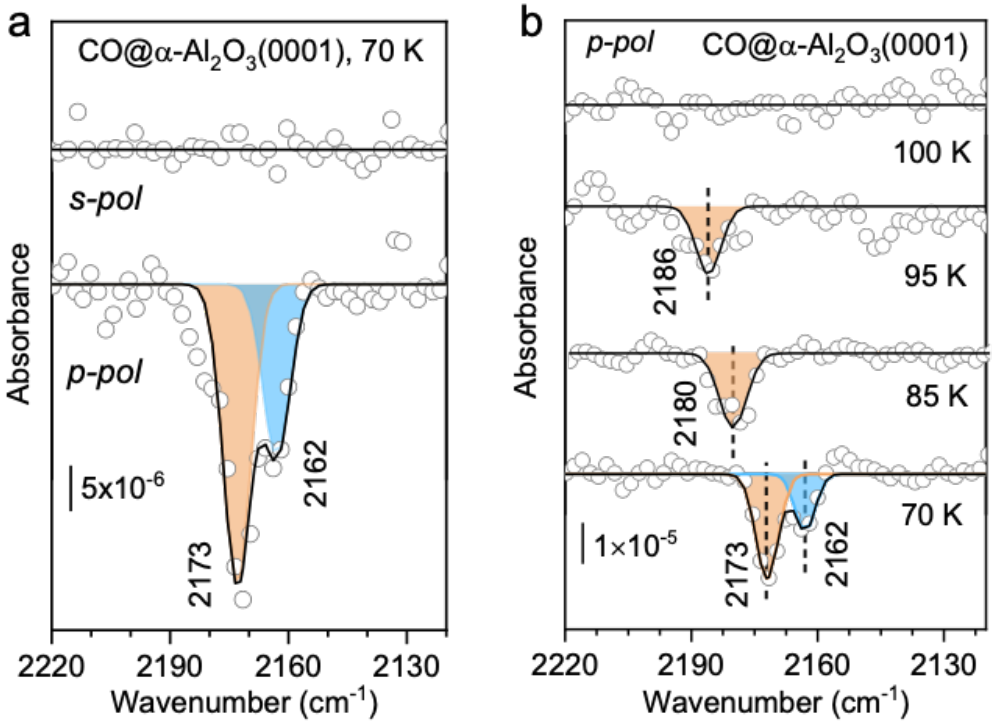

Figure 4.10: (a) polarization-resolved IRRAS data recorded after 5 L CO adsorption on α-$Al_2O_3(0001)$ at 70 K at a grazing incidence angle of 80°. (b) Temperature-dependent IRRAS data obtained after saturation adsorption of CO at 70 K on the α-$Al_2O_3(0001)$ surface, then subsequently annealing to indicated temperatures.

The DFT results give an identical trend to the experimental IRRAS results shown in Fig. 4.10. The experimental result indicates that the pristine α-$Al_2O_3(0001)$ surface, prepared according to the well-established preparation procedures in UHV outlined in the experimental section, is not free of adsorbates but rather partially hydroxylated.

Partial hydroxylation of the α-Al_2O_3(0001) surface is further confirmed by the corresponding IRRAS data. Fig. 4.10a displays the deconvoluted, polarization-resolved IRRAS results obtained from α-Al_2O_3(0001) surface with CO saturation adsorption at 70 K. In the p-polarized spectrum, two distinct CO vibrations are clearly discernible at 2162 and 2173 cm^{-1}. The dominant band at 2173 cm^{-1} can be attributed to CO adsorbed on surface Al^{3+} cations. The weaker signal at 2162 cm^{-1} can be attributed to CO adsorbed on surface hydroxyl groups. These two signals are identical with the DFT prediction shown in Fig. 4.7a. If we look at the lowest hydroxylation surface, $\theta[Al(OH)_3] = 1/9$, the vibrational frequency of CO on the Al site is distributed between 2155-2065 cm^{-1}, and on the OH site is between 2138-2140 cm^{-1}. The temperature-dependent IRRAS data provide solid evidence of two distinct CO species with differentbinding energies. As shown in Fig. 4.10b, the IR band at 2162 cm^{-1} disappears entirely upon increasing the sample temperature slightly to 85 K, revealing a weakly bound CO species, consistent with the assignment to CO-OH species via hydrogen bonding. In contrast, the 2173 cm^{-1} band decreases gradually in intensity with further heating and vanishes at about 100 K (Fig. 4.10b), demonstrating relatively higher thermal stability, which aligns with CO species chemisorbed to surface Al3+ cations. The CO-Al related IR signal is accompanied by a significant blue shift in frequency as it decreases in coverage, from 2173 cm^{-1} at 70 K to 2186 cm^{-1} at 95 K (Fig. 4.10b), which is also identical with our DFT results.

Overall, the polarization-resolved IRRAS results reveal that the stoichiometric, Al-terminated α-Al_2O_3(0001) surface exhibits high reactivity and is stabilized by partial hydroxylation with surface OH groups present even under UHV conditions, consistent with our previous DFT predictions.

4.2.3. Conclusion

In this section, we conducted a detailed theoretical investigation of CO adsorption on the α-Al_2O_3(0001) surface, considering various surface conditions, including dry, partially hydroxylated, and water-dissociated surfaces with different CO coverage. Our results demonstrate that the α-Al_2O_3(0001) surface exhibits distinct reactivity towards CO depending on its hydroxylation state, which directly influences CO adsorption behavior.

DFT calculations revealed that CO adsorption on Al sites leads to higher vibrational frequencies, while adsorption on OH groups results in lower frequencies. This finding is consistent with the experimental observation of two distinct CO vibrational bands at 2172 cm^{-1} (attributed to CO on Al^{3+}) and 2163 cm^{-1} (attributed to CO interacting with surface hydroxyl groups). The vibrational frequencies and binding energies of CO were found to be strongly dependent on the local adsorption environment and CO coverage. Specifically, we observed that increasing CO coverage generally leads to a decrease in vibrational frequency due to interactions between adjacent CO molecules, whereas the adsorption energy tends to weaken as coverage increases, particularly on the dry surface.

The study also highlighted the significance of hydrogen bonding interactions on hydroxylated surfaces, where the formation of hydrogen bonds between CO and surface OH groups leads to red shifts in vibrational frequencies. This behavior is indicative of a weakening of the C-O bond, as confirmed by the correlation between bond length and vibrational frequency.

Overall, this work provides a comprehensive understanding of the adsorption characteristics of CO on α-$Al_2O_3(0001)$ surfaces, offering valuable insights into the influence of water dissociation and surface hydroxylation. These findings contribute to the broader field of surface science, particularly in the context of catalyst design for applications involving alumina-supported metal catalysts.

5. PdPt Ostwald Ripening on Oxide Surfaces

In this chapter, we explore the adsorption and migration behaviors of Pt and Pd species on two distinct surfaces: $\alpha{-}Al_2O_3(0001)$ and $CeO_2(100)$. These materials are relevant in catalysis due to their widespread use as support materials in heterogeneous catalytic processes. [15, 26, 174, 262] The stability, adsorption energies, and diffusion barriers of various Pt and Pd species on these surfaces are crucial factors influencing their deactivation through sintering and therefore eventually their catalytic performance. We investigated the adsorption energies and formation energies of metal, metal oxide, metal carbonyl, and metal hydroxide species by using the DFT+U method. Additionally, we analyze the diffusion barriers for Pt and Pd species to understand their mobility on these surfaces, which is essential for predicting their behavior under catalytic conditions. The findings from these computational studies offer insights into the comparative stability and mobility of Pt and Pd species on $\alpha{-}Al_2O_3(0001)$ and $CeO_2(100)$ surfaces, aiding in the design and optimization of catalytic systems.

5.1. Computational Details

The computational details for calculations on $\alpha{-}Al_2O_3$ are identical to those described in Section 3.1. The DFT calculation settings for CeO_2 are the same as $\alpha{-}Al_2O_3$ regarding the energy cutoff, real-space projectors, and convergence criteria.

For the $CeO_2(100)$, PBE+U calculations[114–117, 199] were carried out with a value of $U = 5$ eV and $J = 0$ eV applied to f-orbitals [263] along with Grimme's D3 dispersion correction (zero damping) [212].

The lattice constants of CeO_2 were optimized, obtaining values ($a = b = c = 5.477\,\text{Å}$) that agree well with experimental results ($a = b = c = 5.411\,\text{Å}$) [264]. The values also agree with the PBE+U computational results from prior studies: $a = b = 5.48\,\text{Å}$. [263]

Surfaces were modeled with symmetric slabs containing eight formula units of $CeO_2(100)$ per dry (1×1)-surface (approximately 8.3 Å thick) with two bottom frozen layers. The dry (1×1)-surface is terminated with $-O_4{-}Ce_2{-}O_2$. These slabs were separated by a minimum of 24 Å of vacuum to reduce artificial interactions among periodic structures. A Γ-centered k-point grid with $(4 \times 4 \times 1)$ k-points for a (1×1)-$CeO_2(111)$ cell and $(2 \times 2 \times 1)$ k-points for (2×2)-cells was used to sample the Brillouin-zone of surfaces using a Gaussian smearing with $\sigma = 0.1$ eV. Fig. 5.1 shows the relevant $CeO_2(100)$ surface configurations that have been considered in this chapter. The configuration is described by the water coverage $\theta[H_2O]$. The dry surface is labeled as $\theta[H_2O] = 0$, the surface with one H_2O molecule dissociated on 1×1 dry surface slab is labeled as $\theta[H_2O] = 1/2$, the surface with two H_2O molecules dissociated on 1×1 dry surface slab is described as $\theta[H_2O] = 1$.

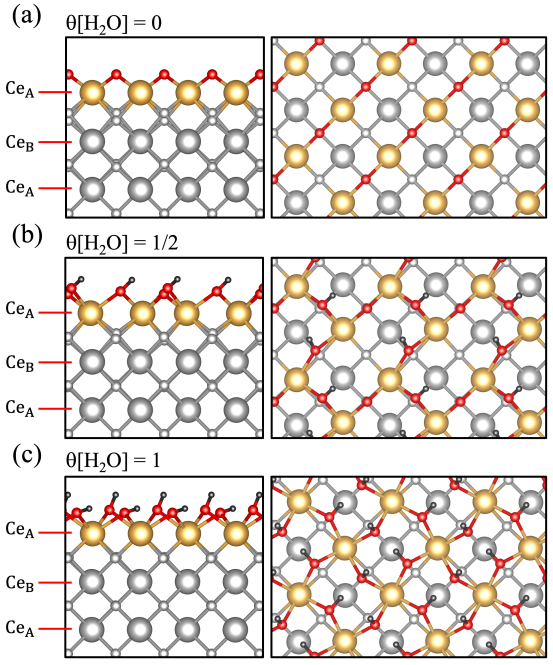

Figure 5.1: Atomic structure of $CeO_2(100)$ surfaces. (a) Dry surface. (b) Surface with $\theta[H_2O]$ = 1/2. (c) Surface with $\theta[H_2O]$ = 1. H, O, and Ce atoms are shown as small, medium, and large spheres, respectively. H atoms are shown in black, while a different color code is used to differentiate between the different layers for Ce (gold, gray) and O (red, gray).

5.2. Results and Discussion

The stability of different adsorbate species has been investigated. The formation energy of different adsorbate species is shown in Fig. 5.2. The formation energy is calculated as follows:

$$\Delta E_{\text{form}}^{\text{M(gas)}} = E_{\text{M}}^{\text{gas}} - E_{\text{M}}^{\text{bulk}} \tag{5.1}$$

$$\Delta E_{\text{form}}^{\text{MO}} = E_{\text{MO}} - E_{\text{M}}^{\text{bulk/gas}} - E_{\text{O}_2}/2 \tag{5.2}$$

$$\Delta E_{\text{form}}^{\text{MO}_2} = E_{\text{MO}_2} - E_{\text{M}}^{\text{bulk/gas}} - E_{\text{O}_2} \tag{5.3}$$

$$\Delta E_{\text{form}}^{\text{MCO}} = E_{\text{MCO}} - E_{\text{M}}^{\text{bulk/gas}} - E_{\text{CO}} \tag{5.4}$$

$$\Delta E_{\text{form}}^{\text{MOH}} = E_{\text{MOH}} - E_{\text{M}}^{\text{bulk/gas}} - E_{\text{H}_2\text{O}}/2 - E_{\text{O}_2}/4 \tag{5.5}$$

$$\Delta E_{\text{form}}^{\text{M(OH)}_2} = E_{\text{M(OH)}_2} - E_{\text{M}}^{\text{bulk/gas}} - E_{\text{H}_2\text{O}} - E_{\text{O}_2}/2 \tag{5.6}$$

Fig. 5.2a presents the formation energies (ΔE_{form}) of different adsorbate species relative to bulk and gas phases. The reference point for the bulk phase is set at $\Delta E_{\text{form}} = 0$ for both Pt and Pd compounds. For the gas form (M_{gas}), the formation energy for Pt is significantly higher than that for Pd, indicating that gaseous Pt is less stable relative to its bulk form compared to Pd, which is identical with the experimental results (the standard enthalpy of formation: $\Delta_f H^\circ$(Pd) = 3.92 eV, $\Delta_f H^\circ$(Pt) = 5.86 eV). [256] When examining the metal oxides (MO

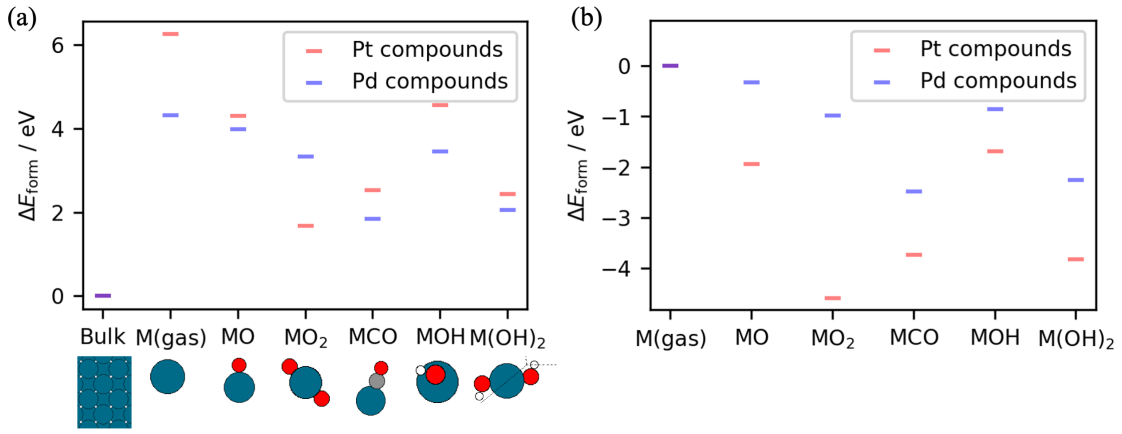

Figure 5.2: Formation energy of different adsorbate species relative to (a) bulk, (b) gas. The red line represents the Pt compounds, and the blue line represents the Pd compounds. The configuration of each adsorbate species is shown at the bottom of (a).

and MO_2), PtO exhibits higher formation energies than PdO, however, PdO_2 exhibits higher formation energies than PtO_2 when relative to their respective bulk phases. Both Pt and Pd carbonyl compounds (MCO) show intermediate formation energies, with PdCO being slightly more stable than PtCO. Similarly, hydroxide compounds (MOH and $M(OH)_2$) follow this trend, where Pd-based hydroxides have lower formation energies, indicating greater stability compared to Pt-based hydroxides.

The formation energies relative to the gas phase (shown in Fig. 5.2b) give insights into the stability of Pt and Pd compounds. The formation energy for both Pt and Pd in their gas forms (M_{gas}) is set to zero as a reference point. For all the compounds, the formation energies are negative, indicating that they are more stable than their respective gas states. All Pt compounds show higher stability compared to Pd compounds across various adsorbate species when referenced to the gas phase.

5.2.1. PdPt Migration on $\alpha-Al_2O_3(0001)$ Surfaces

Fig. 5.3a illustrates the adsorption energies (E_{ads}) of various Pt and Pd species on $\alpha-Al_2O_3(0001)$ surfaces. The adsorption is defined as: $E_{ads} = E_{total} - E_{slab} - E_{adsorbate}$. The $E_{adsorbate}$ is the energy for the single adsorbate species in a vacuum. The adsorption energies are evaluated for both dry and fully hydroxylated (marked as $\theta = 1$) surfaces. The adsorption energies of Pt and Pd species on $\alpha-Al_2O_3(0001)$ surfaces vary depending on the surface condition and adsorbate configuration. For metal adsorption, Pt exhibits stronger adsorption on dry surfaces with a more negative energy of -2.47 eV compared to Pd's -1.80 eV. On fully hydroxylated surfaces, the adsorption strength decreases for both metals, with Pt still showing stronger adsorption (-1.80 eV for Pt and -1.38 eV for Pd). In the case of metal oxides (MO), Pt also shows stronger adsorption than Pd on dry surfaces (-2.68 eV for Pt and -2.23 eV for Pd), with reduced adsorption strength on hydroxylated surfaces (-2.31 eV for Pt and -1.89 eV for Pd). Metal carbonyls

follow a similar trend, with Pt exhibiting stronger adsorption than Pd on both dry and hydroxylated surfaces, although the difference in adsorption strength decreases on the hydroxylated surfaces. For metal hydroxides, Pt hydroxide demonstrates significantly stronger adsorption on dry surfaces (-3.02 eV for Pt and -2.28 eV for Pd), with a decrease in adsorption strength on hydroxylated surfaces. Interestingly, for metal dihydroxides, Pd shows stronger adsorption on dry surfaces (-4.16 eV for Pd and -3.62 eV for Pt), while on hydroxylated surfaces, both metals exhibit reduced adsorption strength, with Pd still showing slightly stronger adsorption. These observations highlight that adsorption energies are generally more negative on dry surfaces, indicating stronger adsorption, particularly for Pt species. However, in the case of $M(OH)_2$, Pd shows stronger adsorption on dry surfaces. The type of adsorbate significantly influences the adsorption energy, with metal hydroxides and dihydroxides displaying stronger adsorption compared to other configurations.

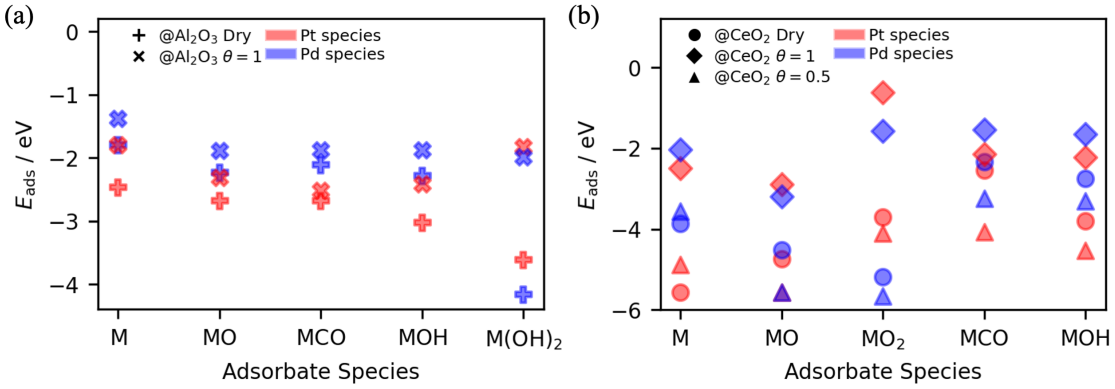

Figure 5.3: The adsorption energy for different Pd/Pt species on different surfaces. (a) Adsorption on $\alpha-Al_2O_3(0001)$ surfaces, '+' represents the dry surfaces, '×' represents the fully hydroxylated surfaces ($\theta = 1$). (b) Adsorption on $CeO_2(100)$ surfaces, the circle mark represents the dry surfaces, the diamond mark represents the fully hydroxylated surfaces ($\theta = 1$), and the triangle mark represents the half hydroxylated surfaces ($\theta = 0.5$). The red represents the Pt species, and the blue represents the Pd species.

The adsorption energies of Pt and Pd species on $CeO_2(100)$ surfaces vary based on surface conditions and adsorbate configurations (shown in Fig. 5.3b). On dry surfaces, Pt exhibits much stronger adsorption than Pd, with adsorption energies of -5.57 eV for Pt and -3.86 eV for Pd. As the surfaces become partially hydroxylated, the adsorption strengths decrease for both metals, with Pt showing an energy of -4.88 eV and Pd showing -2.55 eV. On fully hydroxylated surfaces, the adsorption energies further decrease, indicating the weakest adsorption, with Pt at -2.50 eV and Pd at -2.03 eV. For metal oxides (MO), on dry surfaces, Pt shows slightly stronger adsorption than Pd, but on partially hydroxylated surfaces, Pd and Pt exhibit smilar adsorption energy (-5.56 eV), and stronger than on dry surfaces. On fully hydroxylated surfaces, Pd exhibits stronger adsorption, with an energy of -3.20 eV compared to Pt's -2.89 eV. For MO_2, on dry and fully hydroxylated surfaces, Pd shows slightly stronger adsorption than Pt, but on partially hydroxylated surfaces, Pt and Pd exhibit stronger adsorption energy. The adsorption

of MO and MO_2 cause surface reconstruction, the adsorption configurations of PtO and PtO_2 are shown in Fig. 5.4. Pd species have similar adsorption configurations. For metal carbonyls, Pt shows stronger adsorption on all surfaces, with adsorption energies of -2.55 eV for Pt and -2.34 eV for Pd on dry surfaces, -4.08 eV for Pt and -3.24 eV for Pd on partially hydroxylated surfaces, and -2.14 eV for Pt and -1.55 eV for Pd on fully hydroxylated surfaces. Finally, for metal hydroxides, Pt consistently shows stronger adsorption across all surface conditions, with the strongest adsorption occurring on partially hydroxylated surfaces (-4.52 eV for Pt and -3.31 eV for Pd), and the weakest adsorption on fully hydroxylated surfaces (-2.22 eV for Pt and -1.65 eV for Pd). For all adsorbate, except the pure metals, the adsorption on the partially hydroxylated surface are the strongest, and on the fully hydroxylated surface are the weakest.

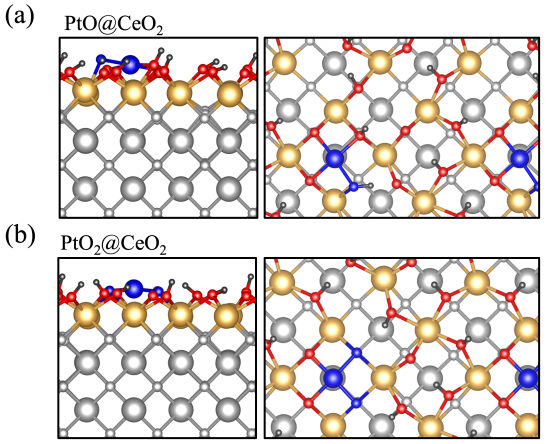

Figure 5.4: Atomic structure of (a) PtO adsorbed on $CeO_2(100)$ $\theta[H_2O] = 1/2$ surfaces. (b) PtO_2 adsorbed on $CeO_2(100)$ $\theta[H_2O] = 1/2$ surfaces H, O, and Ce atoms are shown as small, medium, and large spheres gray and gold, respectively. H atoms are shown in black, while a different color code is used to differentiate between the different layers for Ce (gold, gray) and O (red, gray). The blue spheres represents the adsorbate while the large blue sphere represents Pt, the small sphere represents the H.

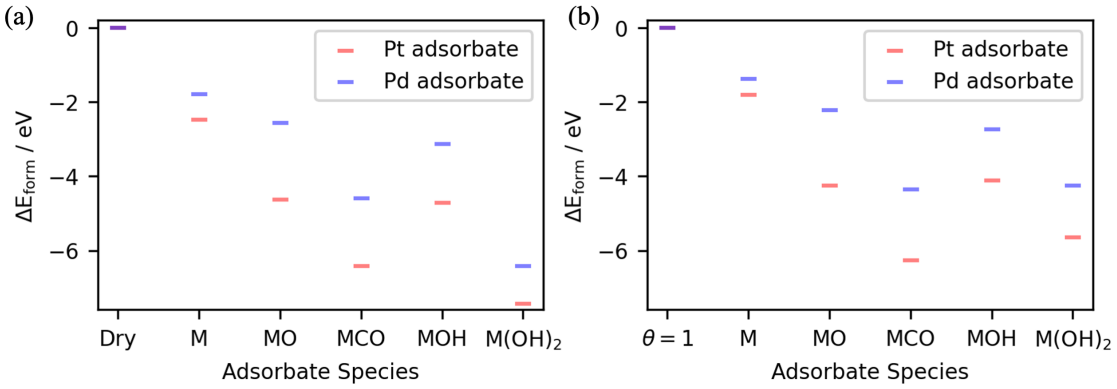

Figure 5.5: Formation energy of the $Al_2O_3(0001)$ adsorption systems referenced to the Pd/Pt gas phase, calculated using Eq.5.7 - 5.12. Adsorption on (a) dry surface and (b) fully hydroxylated surface.

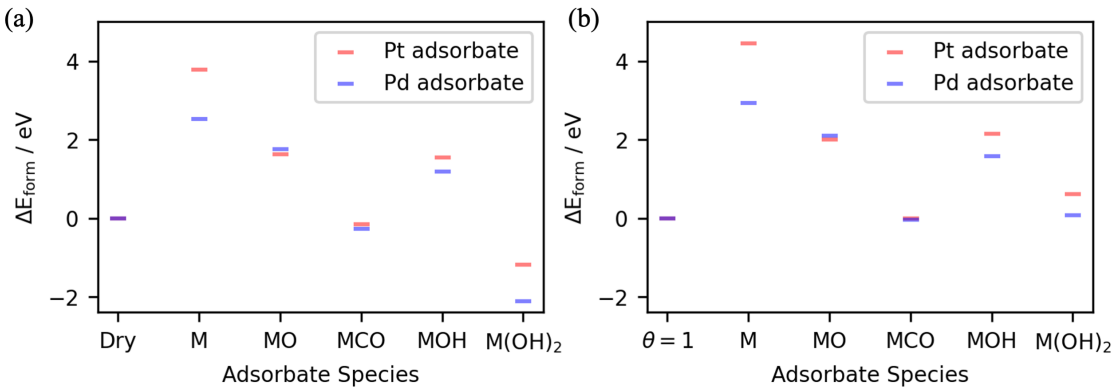

Figure 5.6: Formation energy of the $\alpha-Al_2O_3(0001)$ adsorption systems referenced to the Pd/Pt bulk phase, calculated using Eq.5.7 - 5.12. Adsorption on (a) dry surface and (b) fully hydroxylated surface.

$$\Delta E_{\text{form}}^{\text{M}} = E_{\text{total}} - E_{\text{slab}} - E_{\text{M}}^{\text{bulk/gas}} \tag{5.7}$$

$$\Delta E_{\text{form}}^{\text{MO}} = E_{\text{total}} - E_{\text{slab}} - E_{\text{M}}^{\text{bulk/gas}} - E_{\text{O}_2}/2 \tag{5.8}$$

$$\Delta E_{\text{form}}^{\text{MO}_2} = E_{\text{total}} - E_{\text{slab}} - E_{\text{M}}^{\text{bulk/gas}} - E_{\text{O}_2} \tag{5.9}$$

$$\Delta E_{\text{form}}^{\text{MCO}} = E_{\text{total}} - E_{\text{slab}} - E_{\text{M}}^{\text{bulk/gas}} - E_{\text{CO}} \tag{5.10}$$

$$\Delta E_{\text{form}}^{\text{MOH}} = E_{\text{total}} - E_{\text{slab}} - E_{\text{M}}^{\text{bulk/gas}} - E_{\text{H}_2\text{O}}/2 - E_{\text{O}_2}/4 \tag{5.11}$$

$$\Delta E_{\text{form}}^{\text{M(OH)}_2} = E_{\text{total}} - E_{\text{slab}} - E_{\text{M}}^{\text{bulk/gas}} - E_{\text{H}_2\text{O}} - E_{\text{O}_2}/2 \tag{5.12}$$

Fig. 5.5 illustrate the formation energies (ΔE_{form}) of various Pt and Pd adsorbate species on $\alpha-Al_2O_3(0001)$ surfaces. These energies are calculated relative to the Pt and Pd gas phases by following Eq.5.7 - 5.12. The data are presented for both dry surfaces (Fig. 5.5a) and fully hydroxylated surfaces (Fig. 5.5b). The formation energies for Pt and Pd species on $\alpha-Al_2O_3(0001)$ surfaces reveal distinct trends based on surface condition and adsorbate type. On dry surfaces, Pt species exhibit more negative formation energies across all configurations, with values such as -2.47 eV for metal adsorbates and as low as -7.44 eV for $M(OH)_2$, indicating higher stability compared to Pd species, which have corresponding values of -1.80 eV and -6.43 eV. On fully hydroxylated surfaces, while the formation energies for both Pt and Pd species become less negative, Pt still performs higher stability, with values such as -1.80 eV for metal adsorbates and -5.65 eV for $M(OH)_2$, compared to Pd's -1.38 eV and -4.25 eV. The trends suggest that dry surfaces provide stronger adsorption and higher stability for the adsorbates, particularly for Pt, and that MCO and $M(OH)_2$ configurations exhibit the highest stability. Pt species are generally more stable than Pd species, particularly on dry surfaces. Fully hydroxylated surfaces result in less negative formation energies, indicating reduced stability of the species.

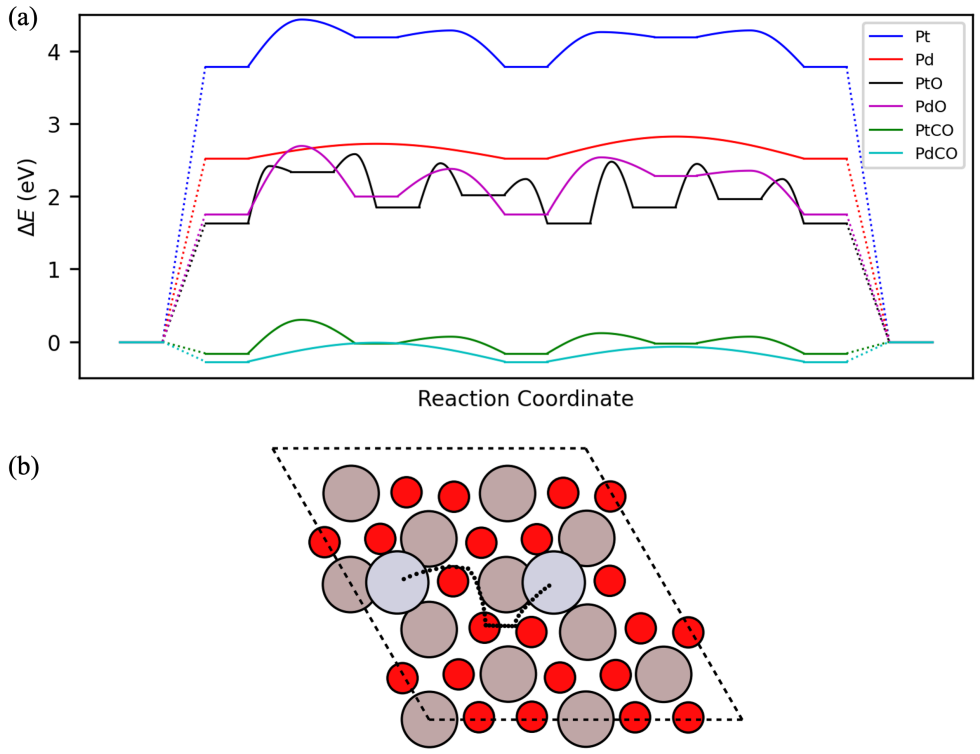

Figure 5.7: (a) The diffusion barriers of different Pd/Pt species on $\alpha-Al_2O_3(0001)$ dry surface. All configurations are referenced by the Pd/Pt bulk phase. (b) The schematic diagram shows the migration path of Pt on a dry surface. The gray and red spheres represent the Al and O, respectively. The two silver spheres represent the initial and the final state of Pt. The black dot depicts the migration pathway for Pt between the initial and final state.

The formation energies of Pt and Pd adsorbates on $\alpha-Al_2O_3(0001)$ surfaces, relative to their respective bulk phases (shown in Fig.5.6), exhibit distinct trends depending on the surface condition and adsorbate species. On dry surfaces, metal adsorbates for Pt and Pd have positive formation energies, with Pt showing a higher value (3.79 eV) compared to Pd (2.52 eV), indicating less favorable formation relative to the bulk. MO also shows positive formation energies for both Pt and Pd, but the values are closer, with Pd being slightly more stable (1.76 eV) compared to Pt (1.63 eV). MCO shows near-neutral formation energies, with both Pt and Pd having slightly negative values, indicating close stability to the bulk phase. MOH also exhibits positive formation energies, with Pt (1.54 eV) being more stable than Pd (1.18 eV). For metal dihydroxides, Pd shows a more negative formation energy (-2.11 eV) compared to Pt (-1.18 eV), indicating that Pd adsorbates in this configuration are more stable relative to their bulk phase.

On fully hydroxylated surfaces, the formation energies generally increase for both metals. Metal adsorbates exhibit even higher positive formation energies, with Pt showing a larger increase to 4.46 eV compared to Pd's 2.94 eV. MO has slightly higher formation energies as well, with Pd now being more stable (2.10 eV) compared to Pt (2.00 eV). MCO shows formation energies close to zero, indicating minimal change from their bulk stability. MOH sees an increase in formation

energies, with Pt showing 2.15 eV compared to Pd's 1.58 eV. Interestingly, metal dihydroxides shift to positive formation energies, with Pt slightly positive (0.61 eV) and Pd close to zero (0.07 eV). These results indicate that while both Pt and Pd adsorbates become less stable relative to their bulk phases when adsorbed on fully hydroxylated surfaces, Pd generally shows a slightly more favorable formation energy profile across different adsorbate species.

Table 5.1.: Diffusion barrier values from Fig. 5.7 and Fig. 5.10, given in eV. E_a^1 denotes the barrier relative to the dry surface, while E_a^2 represents the barrier relative to the state where the adsorbate has already formed.

Surface	α-$Al_2O_3(0001)$				$CeO_2(100)$			
	E_a^1		E_a^2		E_a^1		E_a^2	
Adsorbate	Pt	Pd	Pt	Pd	Pt	Pd	Pt	Pd
Metal	4.43	2.82	0.65	0.30	3.71	2.42	3.03	1.96
MO	2.58	2.69	0.95	0.94	3.10	3.85	1.75	2.27
MCO	0.46	0.26	0.46	0.26	0.29	0.19	0.32	0.70
MOH					4.19	2.36	3.43	1.66

The diffusion barriers of different Pd/Pt species on $\alpha{-}Al_2O_3(0001)$ dry surface are shown in Fig. 5.7, all the diffusion pathway are referenced to the Pd/Pt bulk phase and finishes at the Pd/Pt bulk phase. Pt species exhibit the highest energy barrier, reaching approximately 4.43 eV, indicating that Pt is the least mobile on the surface. Pd species, in contrast, have a maximum barrier of around 2.82 eV, making Pd more mobile than Pt. Among the oxide species, PtO has a peak barrier of 2.58 eV, while PdO shows a slightly lower maximum barrier of 2.38 eV, suggesting that PdO diffuses more easily than PtO. The carbonyl species, PtCO and PdCO, demonstrate the lowest energy barriers. PtCO has a barrier of only 0.46 eV, and PdCO has an even lower barrier of 0.26 eV, indicating that these species are the most mobile on the surface. Overall, Pd and its derivatives (PdO and PdCO) exhibit lower energy barriers compared to their Pt counterparts, suggesting that Pd species are more mobile on the $\alpha{-}Al_2O_3(0001)$ surface, which could influence their catalytic behavior and effectiveness in surface reactions. It is important to note that the barriers during the diffusion itself compared to the first adsorbed species are consistently low, highlighting the significant role of initial adsorption in determining overall barriers. The value of barriers are shown in Table 5.1. When ignoring the initial adsorption, the diffusion barriers for all adsorbed species are below 1.0 eV on $\alpha{-}Al_2O_3(0001)$.

5.2.2. PdPt Migration on $CeO_2(100)$ Surfaces

The formation energies of Pt and Pd adsorbates on $CeO_2(100)$ surfaces, referenced to the Pd/Pt gas phase (shown in Fig. 5.8), show distinct trends based on the surface condition—dry, partially hydroxylated ($\theta = 1/2$), and fully hydroxylated ($\theta = 1$). On the dry surface, Pt adsorbates generally exhibit more negative formation energies compared to Pd adsorbates, indicating greater stability. For instance, metal adsorbates have formation energies of -5.57 eV

for Pt and -3.86 eV for Pd, with similar stability trends seen in metal oxides (MO and MO_2), MCO, and MOH. As the surface becomes partially hydroxylated, the formation energies remain negative except pure metal, and even larger so compared to the dry surface, indicating reduced stability. For example, the formation energy for Pt metal adsorbates is -4.88 eV, compared to -3.56 eV for Pd. The trend continues on the fully hydroxylated surface, where the formation energies are further reduced, with Pt metal adsorbates showing -2.50 eV and Pd showing -2.03 eV. All the species adsorbed less stable on the fully hydroxylated surface compared to both dry and partial hydroxylated surface. Across all surface conditions, Pt adsorbates consistently demonstrate more negative formation energies than Pd adsorbates, indicating that Pt is generally more stable than Pd on $CeO_2(100)$ surfaces. The type of adsorbate also plays a significant role, with metal carbonyl configurations exhibiting some of the most negative formation energies, particularly for Pt, underscoring their higher stability across varying surface hydroxylation states.

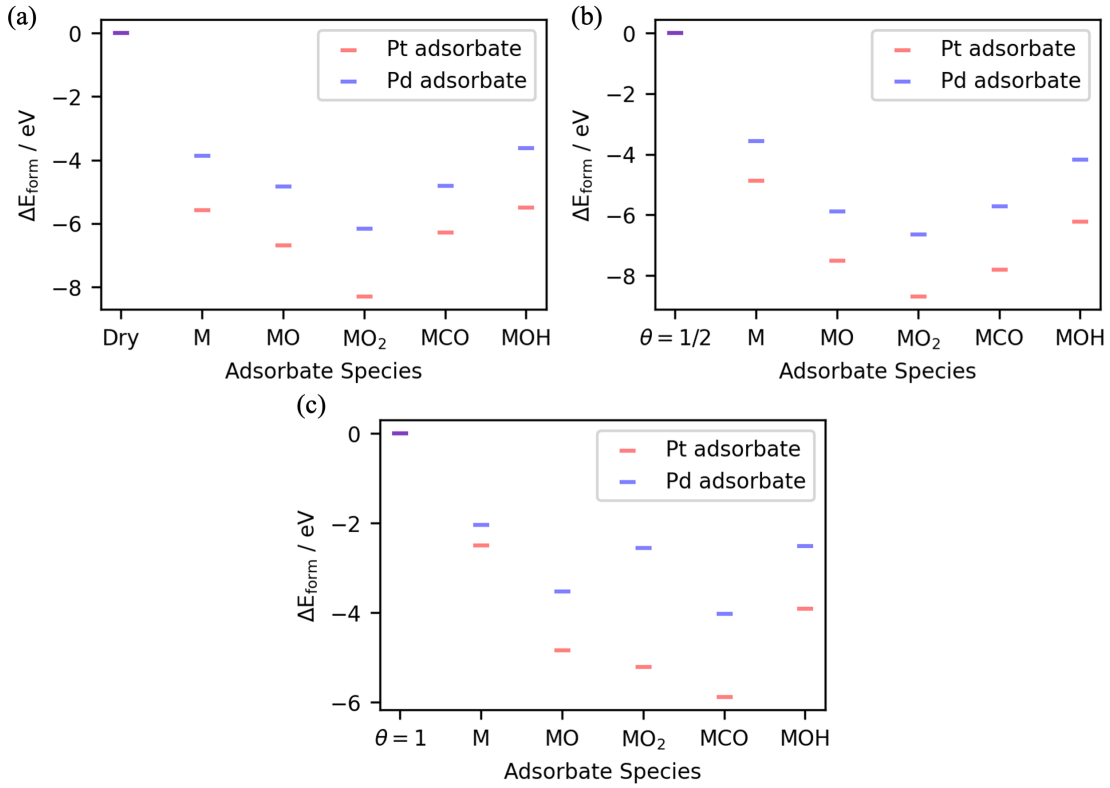

Figure 5.8: Formation energy of the $CeO_2(100)$ adsorption systems referenced to the Pd/Pt gas phase, calculated using Eq.5.7 - 5.12. Adsorption on (a) dry surface and (b) partially hydroxylated surface (c) fully hydroxylated surface.

The formation energies of Pt and Pd adsorbates on $CeO_2(100)$ surfaces, referenced to the bulk phase (shown in Fig. 5.9), vary significantly across different surface conditions—dry, partially hydroxylated ($\theta = 1/2$), and fully hydroxylated ($\theta = 1$). On the dry surface, both Pt and Pd adsorbates generally exhibit low positive formation energies, indicating moderate stability. For instance, metal adsorbates have formation energies of 0.69 eV for Pt and 0.46 eV for Pd.

As the surface becomes partially hydroxylated, the formation energies increase, particularly for metal adsorbates, where Pt shows 1.38 eV and Pd shows 1.77 eV, indicating reduced stability. The formation energies further increase on the fully hydroxylated surface, especially for metal adsorbates, with Pt reaching 3.76 eV and Pd 2.28 eV. Among the adsorbate configurations, MO and MOH exhibit varying stability trends, with formation energies that can be negative or positive depending on the degree of surface hydroxylation. Overall, most Pd adsorbates tend to have slightly lower formation energies compared to Pt adsorbates across the surface conditions, suggesting marginally better stability for Pd in this context. But MO_2 species on all surfaces and MCO on partial hydroxylated surface have opposite results. The analysis underscores that the degree of surface hydroxylation significantly impacts the stability of adsorbates, with fully hydroxylated surfaces leading to the highest formation energies, indicating the lowest stability relative to the bulk phase.

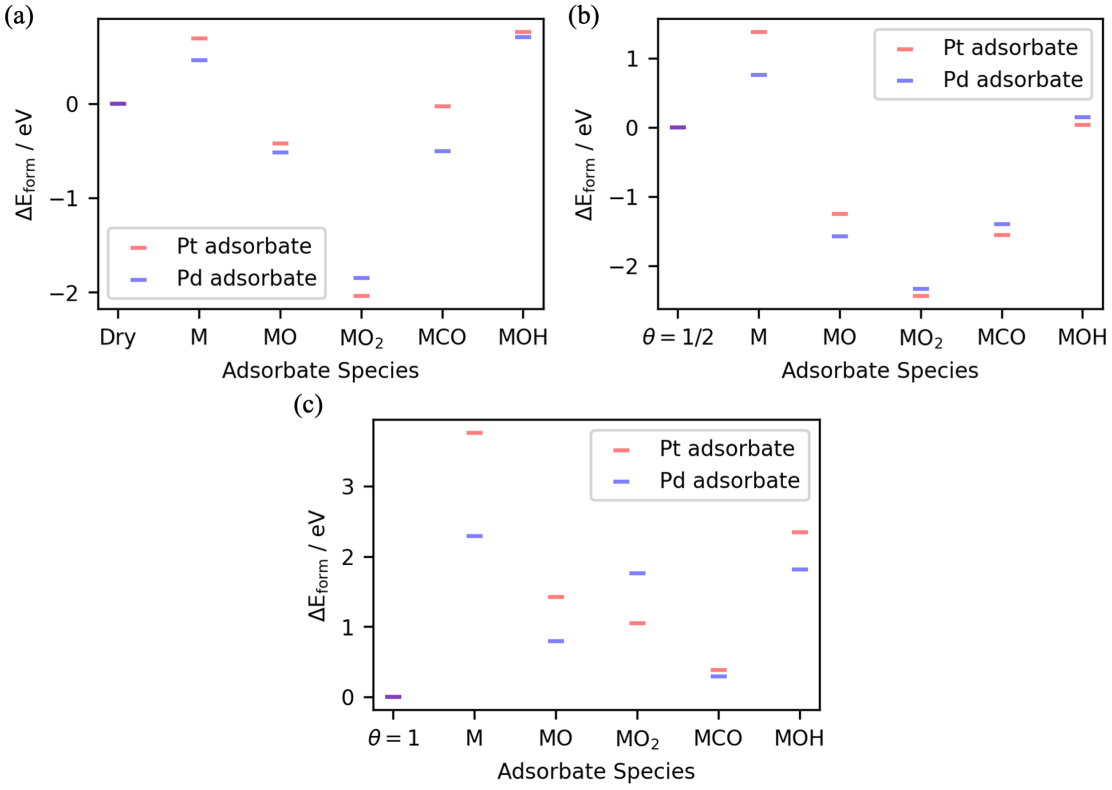

Figure 5.9: Formation energy of the $CeO_2(100)$ adsorption systems referenced to the Pd/Pt bulk phase, calculated using Eq.5.7 - 5.12. Adsorption on (a) dry surface and (b) partial hydroxylated surface (c) fully hydroxylated surface.

The diffusion barriers of different Pd/Pt species on $CeO_2(100)$ dry surface are shown in Fig. 5.10, all the diffusion pathway starts from the Pd/Pt bulk phase and finishes at the Pd/Pt bulk phase. Pt exhibits a relatively high diffusion barrier, with a peak energy of approximately 3.71 eV, suggesting limited mobility on the surface. In contrast, Pd shows a lower maximum barrier of around 2.42 eV, indicating easier diffusion. Among the oxide species, PtO and PdO also demonstrate notable barriers, with PtO reaching 3.10 eV and PdO showing a higher peak

of 3.85 eV, suggesting that PdO is less mobile than PtO on the $CeO_2(100)$ surface. For the carbonyl species, PtCO and PdCO have much lower diffusion barriers, with PtCO peaking at 0.29 eV and PdCO at 0.19 eV, indicating high mobility for these species. Hydroxide species (PtOH and PdOH) exhibit higher diffusion barriers, with PtOH reaching 4.19 eV and PdOH 2.36 eV, suggesting that PtOH is particularly immobile on the surface. Overall, Pd and its derivatives generally show lower energy barriers compared to their Pt counterparts, implying that Pd species are more mobile on the $CeO_2(100)$ surface.

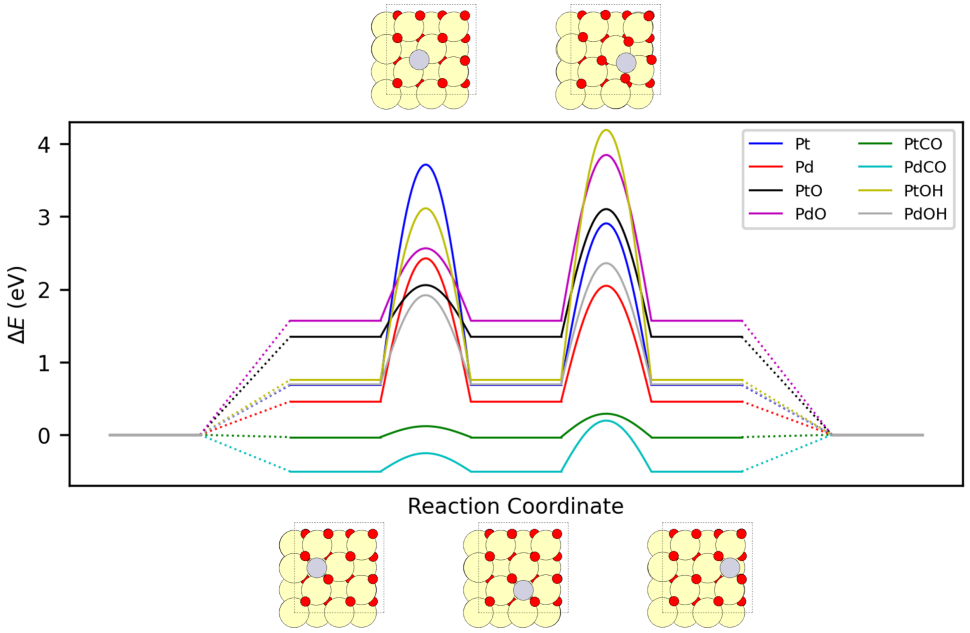

Figure 5.10: The diffusion barriers of different Pd/Pt species on $CeO_2(100)$ dry surface. All configurations are referenced by the Pd/Pt bulk phase. The bottom and top schematics show the migration path of Pt on a dry surface, with the bottom schematic showing the intermediate state and the top schematic showing the transition state.

Fig. 5.11 summarizes the migration barrier for different Pd/Pt species on different surfaces. This shows that Pt species generally have higher migration barriers than Pd species on both surfaces, indicating that Pt species are less mobile. For metal atoms (M), the migration barrier for Pt is significantly higher on both surfaces, with values of 1.61 eV on $\alpha-Al_2O_3(0001)$ and 1.29 eV on $CeO_2(100)$, higher than the migration barrier for Pd. The migration of Pt on $\alpha-Al_2O_3(0001)$ surfaces has a barrier that is 0.72 eV higher compared to its migration on $CeO_2(100)$. Similarly, the migration of Pd on $\alpha-Al_2O_3(0001)$ surfaces has a barrier that is 0.40 eV higher than on $CeO_2(100)$. For MO, the barriers are closer between PtO and PdO (0.11 eV higher) on $\alpha-Al_2O_3(0001)$, but on $CeO_2(100)$, PdO exhibits a 0.74 eV higher barrier compared to PtO. The migration of PtO on $\alpha-Al_2O_3(0001)$ surfaces has a barrier that is 0.52 eV lower compared to its migration on $CeO_2(100)$. Similarly, the migration of PdO on $\alpha-Al_2O_3(0001)$ surfaces has a barrier that is 1.15 eV lower than on $CeO_2(100)$. MCO shows the lowest migration barriers among all species, with both PtCO and PdCO having very low values

on both surfaces. For the barrier on $\alpha-Al_2O_3(0001)$, PtCO is 0.20 eV higher than PdCO. And for $CeO_2(100)$, PtCO is 0.09 eV higher than PdCO. The migration barriers of PtCO and PdCO on $\alpha-Al_2O_3(0001)$ are 0.17 eV and 0.06 eV higher, respectively, compared to their migration on $CeO_2(100)$. For MOH, only data for $CeO_2(100)$ is available, showing a 1.83 eV higher barrier for PtOH than for PdOH.

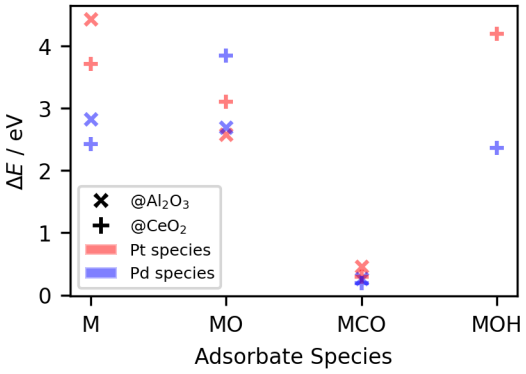

Figure 5.11: The barrier for different Pd/Pt species migration on different surfaces. '×' represents the migration on $\alpha-Al_2O_3(0001)$ dry surfaces, and '+' represents the migration on $CeO_2(100)$ dry surfaces. The red markers represent the Pt species, and the blue markers represent the Pd species.

5.3. Conclusion

Based on the investigation presented in this chapter, the adsorption and migration behaviors of Pt and Pd species on $\alpha-Al_2O_3(0001)$ and $CeO_2(100)$ surfaces were comprehensively analyzed to understand their relative stabilities and mobilities. The results show that Pt species generally exhibit stronger adsorption than Pd species, particularly on dry surfaces. This stronger adsorption indicates that Pt species may have a tendency to form more stable sites on the surface. However, it is important to note that in the context of our study, single Pt and Pd atoms are not considered catalytically active but rather are potential intermediates on the path to deactivation.

Furthermore, Pd species demonstrate lower diffusion barriers compared to Pt species, suggesting that Pd atoms are more mobile on the surface. This increased mobility of Pd could lead to a higher likelihood of aggregation or sintering, contributing to deactivation over time. The findings imply that while Pt species form more stable, adsorbed sites, both Pt and Pd single atoms could migrate and potentially deactivate by absorbing CO. This highlights the importance of managing surface conditions to control the stability and mobility of these species to optimize catalyst performance and minimize deactivation. Additionally, understanding the role of surface hydroxylation is crucial, as fully hydroxylated surfaces tend to reduce the stability of adsorbed species, which could further impact the durability of the catalyst.

6. Surface Segregation of PdPt Alloys

This chapter is based on [**Chen, J.**; Sharapa, D.; Plessow, P. N. Advanced Predictive Modeling of Bimetallic Catalyst Behaviors through Gaussian Process Regression and Monte Carlo Simulations. *in Preparation*].

Recent research has focused on the detailed modeling of CO adsorption on Pd/Pt alloy surfaces, given its relevance to catalytic applications in automotive exhaust treatment and fuel cells. The vibrational properties of adsorbed CO molecules serve as sensitive probes of the local surface environment, providing valuable information on the binding sites and the nature of metal-adsorbate interactions.

Despite significant progress, challenges remain in accurately predicting the behavior of Pd/Pt alloy surfaces under varying conditions. [265] This study aims to address these challenges by combining DFT calculations and Gaussian Process Regression with Monte Carlo simulations to investigate the segregation behavior of Pd/Pt alloy surfaces and the impact of CO adsorption across a range of temperatures and compositions. By incorporating a simulated annealing process, we ensure a thorough exploration of the solution space, enhancing the reliability of our predictions and providing comprehensive insights into the surface phenomena of Pd/Pt alloys.

In order to develop an accurate model for predicting the properties of the PdPt alloy surfaces, it is essential to provide a precise descriptor of the system. This descriptor captures the local atomic environment and serves as the input for the predictive model. In our approach, we use cluster expansion to define these descriptors, which involve contributions from neighboring atoms. The cluster expansion model is a powerful tool for studying metal materials, particularly in the context of predicting and analyzing the properties of alloys and disordered materials. [266–276] The idea of cluster expansion allows us to capture complex interactions by considering both pairwise (doubles) and triplet (triples) configurations of atoms around a central site.

A cluster, in this context, refers to a group of atoms within a specified range around a central atom. It effectively captures the local environment, which plays a critical role in determining the surface formation energy, adsorption properties, and other behaviors of bimetallic alloys. The parameters describing these clusters, such as the number and type of neighboring atoms, are then used to generate the descriptors required for training the model. This approach ensures that the model can account for variations in the atomic configuration and accurately predict surface properties.

6.1. Computational Details

All DFT calculations were performed with the VASP version 5.4.1[225, 257] and the ASE [258] using the BEEF–vdW functional[200, 201] and the PAW method.[224, 259] The lattice constants of the 50%Pd alloy have been optimized in Section 4.1.1 and shown in Fig. 4.1.

To build the training set for slab formation energy, surfaces were modeled with a nine-layer and four-layer slab. The bottom two layers were frozen for four-layer slabs, and all layers were free for nine-layer slabs. The training set contains 650 $4 \times 4 \times 9$ slabs, 500 $2 \times 2 \times 9$ slabs, and 497 $4 \times 4 \times 4$ slabs. The CO adsorption energy and vibrational frequency training set contains 497 $4 \times 4 \times 4$ slabs, with the bottom two layers frozen. One CO molecule was adsorbed on the fcc site for each slab (θ[CO = 1/16]). The vibration calculation setting is the same as Section 4.1.1. The dataset for the adsorbate-adsorbate interaction includes 256 $4 \times 4 \times 4$ slabs, with the bottom two layers frozen. For each slab, the CO coverage θ[CO] = 1/16, 1/8, 3/16, 1/4, 1/2, 3/4, 1 were calculated. All slabs were obtained by repeating the $2 \times 2 \times 4$ cells by 2×2 times.

All the slabs are separated by 28 Å of vacuum to eliminate artificial interactions due to periodic boundary conditions. The expansion of the density includes reciprocal lattice vectors has a norm up to 3/2 times larger than for the wave function, $|\mathbf{G}_{\text{cut}}|$ (PREC=Normal in VASP). The calculations were performed with real-space projectors (LREAL=AUTO) and the self-consistent field (SCF) procedure was converged to a threshold of 10^{-8} eV for the total energy. A 0.01 eV/Å criterion for the maximum forces on individual atoms was used for geometry convergence. Gaussian smearing with a 0.1 eV width was applied.

6.2. Results and Discussion

6.2.1. Model Development

For each atom in the surface slab, its formation energy contribution to the system depends on its corresponding cluster. First, all atoms are placed on an FCC grid with an atomic spacing of $d \approx 2.818$ Å. This cluster consists of atoms neighboring the central atom, with distances less than $2d$ from the central atom. We describe this cluster using the parameters listed in Table 6.1. For each atom in the structure, we count the number of occurrences of each parameter. Therefore, for a $4 \times 4 \times 9$ slab, 144 sets of parameters are generated. A schematic of the clusters that were included in the count is shown in Fig. 6.1.

To parameterize the fcc adsorption site, it is necessary to count the clusters of the three neighboring atoms that make up the site and eliminate duplicates.

6.2.1.1. Model Training through Gaussian Process Regression

The implementation of the GPR to predict the formation energy for a clean surface ($E_{\text{form}}^{\text{clean}}$) involves extra steps. First, reform the descriptors by categorizing neighboring atoms into four distance ranges listed in Table 6.1 (only Single and Pair). Here, we only keep two primary quantities for each geometry: the number of neighboring atoms and the number of neighboring atoms with a different element. These quantities are normalized by predefined factors (shown in Table 6.1 column Bulk) to account for typical neighbor counts within each geometry. The resulting descriptors for each atom thus consist of a set of normalized values that describe the

Table 6.1.: Categorized various types of descriptors based on their geometric configurations in the bulk and surface slab, including Single, Pair(short), Pair($\sqrt{2}$), Pair($\sqrt{3}$), Pair(long). Each geometry category lists specific configurations and their corresponding distance limits or edge compositions. Additionally, the table provides the total count of each descriptor category in different positions: bulk, surface, subsurface, and adsorption site.

Geometry	Distance / Å	Category	Total quantity			
			Bulk	Subsurface	Surface	Adsorption site
Single		Pd	1	1	1	3
		Pt				
Pair(short)	<3.40	Pd-Pd	12	12	9	24
		Pd-Pt				
		Pt-Pt				
Pair($\sqrt{2}$)	3.40-4.43	Pd-Pd	6	6	3	9
		Pd-Pt				
		Pt-Pt				
Pair($\sqrt{3}$)	4.43-5.26	Pd-Pd	24	21	15	45
		Pd-Pt				
		Pt-Pt				
Pair(long)	5.26-5.92	Pd-Pd	12	9	9	27
		Pd-Pt				
		Pt-Pt				
	Side length					
Triangle	Short-Short-Short	Pd-Pd-Pd	24	24	15	37
		Pd-Pd-Pt				
		Pd-Pt-Pt				
		Pt-Pt-Pt				
Triplet($\sqrt{2}$)	Short-$\sqrt{2}$-Short	Pd-Pd-Pd	36	36	18	48
		Pd-Pd-Pt				
		Pd-Pt-Pt				
		Pt-Pt-Pt				
		Pd-Pt-Pd				
		Pt-Pd-Pt				
Triplet($\sqrt{3}$)	Short-$\sqrt{3}$-Short	Pd-Pd-Pd	72	66	42	108
		Pd-Pd-Pt				
		Pd-Pt-Pt				
		Pt-Pt-Pt				
		Pd-Pt-Pd				
		Pt-Pd-Pt				
Triplet(straight)	Short-Short-Long	Pd-Pd-Pd	18	15	12	30
		Pd-Pd-Pt				
		Pd-Pt-Pt				
		Pt-Pt-Pt				
		Pd-Pt-Pd				
		Pt-Pd-Pt				

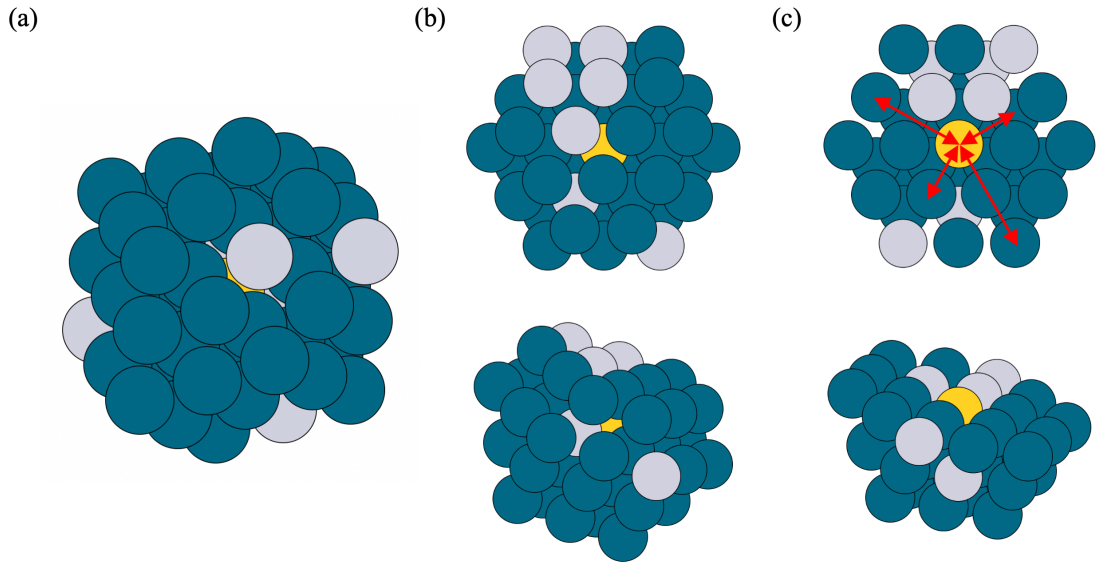

Figure 6.1: The cluster for (a) bulk atoms, (b) subsurface atoms, (c) surface atoms. The red arrows indicate pairs of different lengths. The yellow atom represents the center atom of the cluster.

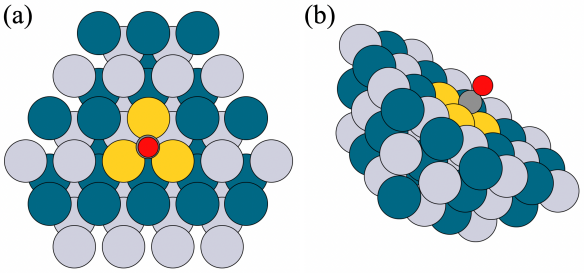

Figure 6.2: The cluster for determining the CO adsorption energy and vibrational frequency. The yellow atoms are the nearest neighbor to the fcc site. (a) Top view, (b) side view.

local atomic environment, including how densely packed the neighbors are and the proportion of different elements of atoms within the specified distance ranges.

Then, the model training steps for $E_{\text{form}}^{\text{clean}}$, adsorption energy ($E_{\text{ads}}^{\theta=1/16}$), and vibrational frequency (ν) are the same. The descriptors are scaled using inverse theta values (θ_d^{-1}) to ensure proper feature scaling. The data is then partitioned into training and testing sets using cross-validation. A sparse GPR approach is employed to handle the computational complexity, where the number of sets of descriptors is reduced to 50 by using a custom reduction function. This function involves computing a kernel matrix and selecting a subset of descriptors that minimize off-diagonal elements in the kernel matrix, ensuring diversity and reducing redundancy. The kernel function used is a sum of RBF kernels (shown as Eq. 6.1), which calculates the similarity between different atomic descriptors. The weights for the GPR model are computed by solving a regularized linear system, which incorporates the kernel matrix and the training target values.

The model parameters, including the mean of the target values, regularization parameter (λ), feature dimensions, θ_d^{-1}, and computed weights, are then saved as the model. This model also includes the reference points (reduced set of descriptors) used in the GPR model.

The Gaussian kernel is defined as:

$$k(x_i, x_j) = \exp\left(-\frac{1}{2}\sum_{d=1}^{D}\theta_d^{-1}(x_i^d - x_j^d)^2\right) \tag{6.1}$$

Here, θ_d^{-1} are the hyperparameters for each feature dimension d.

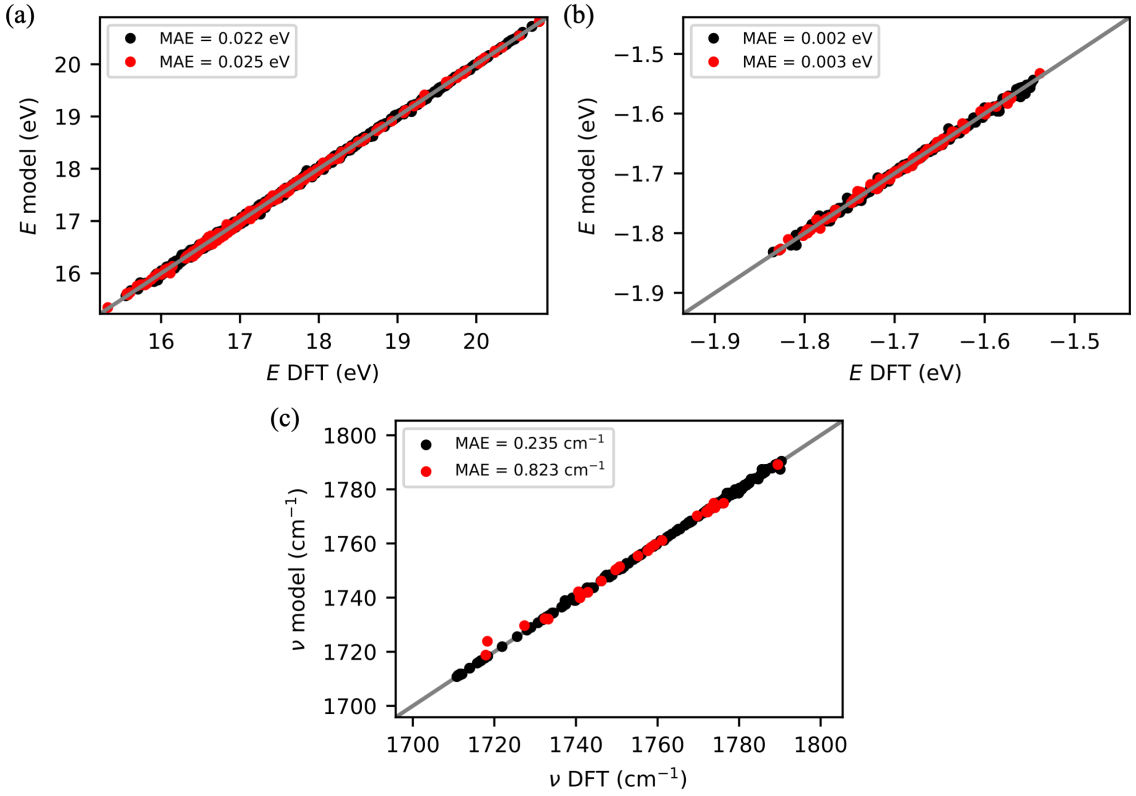

Figure 6.3: The result of GPR model. (a) The formation energy of the slab. (b) The adsorption energy of θ[CO] = 1/16. (c) The vibrational frequency of θ[CO] = 1/16. The black dot represents the training set, and the red dot represents the test set. Only the adsorption at the fcc site is included in the dataset.

Finally, predictions for the test set are made using the trained GPR model, and the performance is evaluated by comparing predicted values with actual target values, visualized through plots of mean absolute errors (shown in Fig. 6.3). The cross-validation results are shown in Fig. E.10-E.12. The preferred adsorption site for CO on Pt(111) is the hollow site within density functional theory, but experimentally, the top site is preferred.[277] While hybrid functionals can sometimes address this issue, they come with significantly higher computational costs, making them impractical for high-throughput studies involving large systems or a broad set of configurations.[201, 278] Since the focus of this chapter is on the development of models and the

verification of their validity, the importance of the accuracy of the DFT calculation results is reduced, as long as DFT can give the right trend for a single type of adsorption site.

6.2.1.2. Adsorbate-Adsorbate Interaction

To predict the adsorbate-adsorbate interaction for CO on a Pd/Pt alloy slab, we use a multi-component energy model. The total energy E is computed as follows:

$$E = E_{\text{clean}}(\mathbf{X}^{\text{atoms}}) + \sum_{i}^{\text{nCO}} E_{\text{ads}}^{\theta=1/16}(\mathbf{X}_i^{\text{site}}) + \sum_{i}^{\text{nCO}} E_{\text{rep}}^{i}(\mathbf{X}_{\text{all}}^{\text{site}}) \tag{6.2}$$

Here, $E_{\text{clean}}(\mathbf{X}^{\text{atoms}})$ represents the energy of the clean alloy slab without any adsorbates. $E_{\text{ads}}^{\theta=1/16}(\mathbf{X}_i^{\text{site}})$ is the adsorption energy of a single CO molecule at a specific site i when the coverage is low ($\theta[\text{CO}] = 1/16$) where $\mathbf{X}_i^{\text{site}}$ represents the set of descriptors for site i.

The interaction between adsorbed CO molecules is captured by the term $E_{\text{rep}}^{i}(\mathbf{X}_{\text{all}}^{\text{site}})$, which includes contributions from repulsive interactions between CO molecules. This term is further decomposed into pairwise interactions as follows:

$$E_{\text{rep}}^{i} = \sum_{j}^{\text{d(ij)=1}} E_{\text{rep1}}^{i}(\mathbf{X}_i^{\text{site}}) + \sum_{j}^{\text{d(ij)=2}} E_{\text{rep2}}^{i}(\mathbf{X}_i^{\text{site}} + \mathbf{X}_j^{\text{site}}) \tag{6.3}$$

In this equation, $E_{\text{rep1}}^{i}(\mathbf{X}_i^{\text{site}})$ describes the nearest-neighbor repulsive interaction between CO molecules, while $E_{\text{rep2}}^{i}(\mathbf{X}_i^{\text{site}} + \mathbf{X}_j^{\text{site}})$ captures the next-nearest-neighbor interaction. The parameters for these repulsive interactions, E_{rep1} and E_{rep2}, are obtained from separate training by solving the least-squares solution to a linear matrix equation.

This method minimizes the sum of the squares of the differences between the observed and predicted values, providing the best-fitting linear relationship between the descriptors and the observed energies. By incorporating these trained interaction terms, we can accurately model

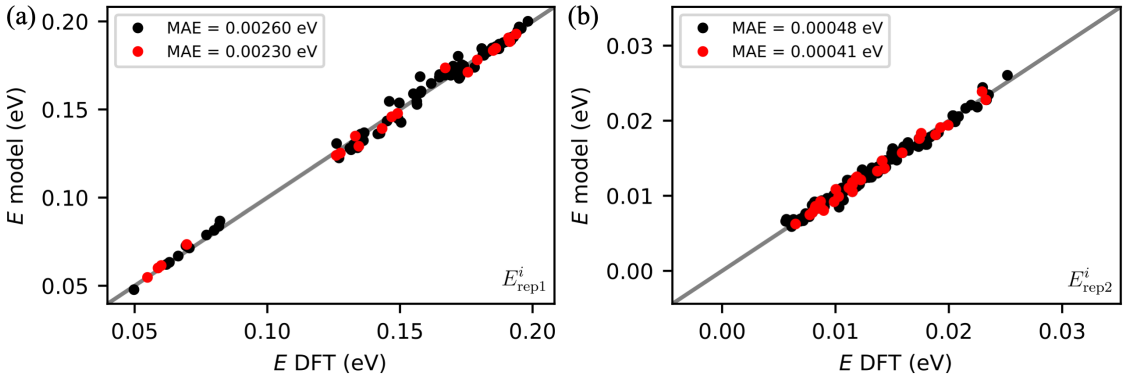

Figure 6.4: The fitting result of (a) E_{rep1} and (b) E_{rep2}. The black dot represents the training set, and the red dot represents the test set.

and predict the behavior of CO adsorption on the Pd/Pt alloy surface, accounting for the complex interactions between adsorbates. The fitting results are shown in Fig. 6.4.

6.2.1.3. Monte Carlo Simulation

In this study, we employed a Monte Carlo simulation utilizing the Metropolis algorithm to investigate the adsorption behavior of CO on a Pd/Pt alloy surface. The simulation was conducted on a $4 \times 4 \times 9$ Pd/Pt alloy slab, where the bottom two layers were fixed to represent the bulk material, leaving 112 unfrozen atoms on the surface that could participate in dynamic processes. Additionally, four potential adsorption sites for CO molecules were considered on the surface.

The simulation encompassed three primary types of stochastic processes:

1. Atom Type Exchange with Flexible Composition: A randomly selected unfrozen atom on the surface changes its elemental type from Pd to Pt or vice versa. This process allows the overall composition of the alloy to vary during the simulation, enabling the exploration of different alloy compositions.
2. Atom Swap with Fixed Composition: Two randomly selected unfrozen atoms swap their elemental types (Pd and Pt). This process keeps the overall composition constant but allows for different atomic arrangements and distributions of Pd and Pt atoms on the surface.
3. Adsorption/Desorption of CO Molecules: A CO molecule is either adsorbed onto or desorbed from a randomly selected adsorption site among the four available on the surface. The simulation considered CO coverages (θ_{CO}) ranging from $\frac{1}{16}$ to $\frac{1}{4}$, corresponding to one to four CO molecules adsorbed on the surface.

One of the aforementioned processes was randomly selected at each simulation iteration based on a uniform probability distribution. For the adsorption event, the energy change ΔE associated with adding a CO molecule to an unoccupied site was calculated. This included the adsorption energy E_{ads} and corrections for vibrational contributions and interactions. For the desorption event, the energy change ΔE associated with removing a CO molecule from an occupied site was calculated similarly.

For an atom exchange with a flexible composition, a single unfrozen atom was randomly selected, and its elemental type was changed from Pd to Pt or vice versa. For an atom swap with a fixed composition, two unfrozen atoms were randomly selected, and their elemental types were swapped. The formation energy E_{form} of the new alloy configuration was calculated. The adsorption energies E_{ads} for any occupied adsorption sites were recalculated, considering the new local atomic environment. The total energy change ΔE was computed as:

$$\Delta E = (E_{\mathrm{form}}^{\mathrm{new}} + \sum E_{\mathrm{ads}}^{\mathrm{new}}) - (E_{\mathrm{form}}^{\mathrm{old}} + \sum E_{\mathrm{ads}}^{\mathrm{old}}) \tag{6.4}$$

The acceptance probability P_{accept} for the adsorption or desorption event was determined using the Metropolis criterion:

$$P_{\text{accept}} = \min(1, \exp(-\frac{\Delta E - \mu_{\text{CO}}}{k_{\text{B}}T})) \tag{6.5}$$

The acceptance probability P_{accept} for the structure optimization was calculated using the Metropolis criterion:

$$P_{\text{accept}} = \min(1, \exp(-\frac{\Delta E}{k_{\text{B}}T})) \tag{6.6}$$

where k_{B} is the Boltzmann constant. The chemical potential of CO (μ_{CO}) was calculated based on the temperature T and CO partial pressure P, using standard thermodynamic relations. E_{form} is the formation energy of the alloy slab without any adsorbed CO molecules. $\sum E_{\text{ads}}$ is the sum of the adsorption energies of all CO molecules currently adsorbed on the surface.

To determine whether the step has been accepted, a random number r in the range (0, 1) was generated. If $r \leq P_{\text{accept}}$, the event was accepted, and the system state was updated accordingly. If $r > P_{\text{accept}}$, the event was rejected, and the system remained in its current state.

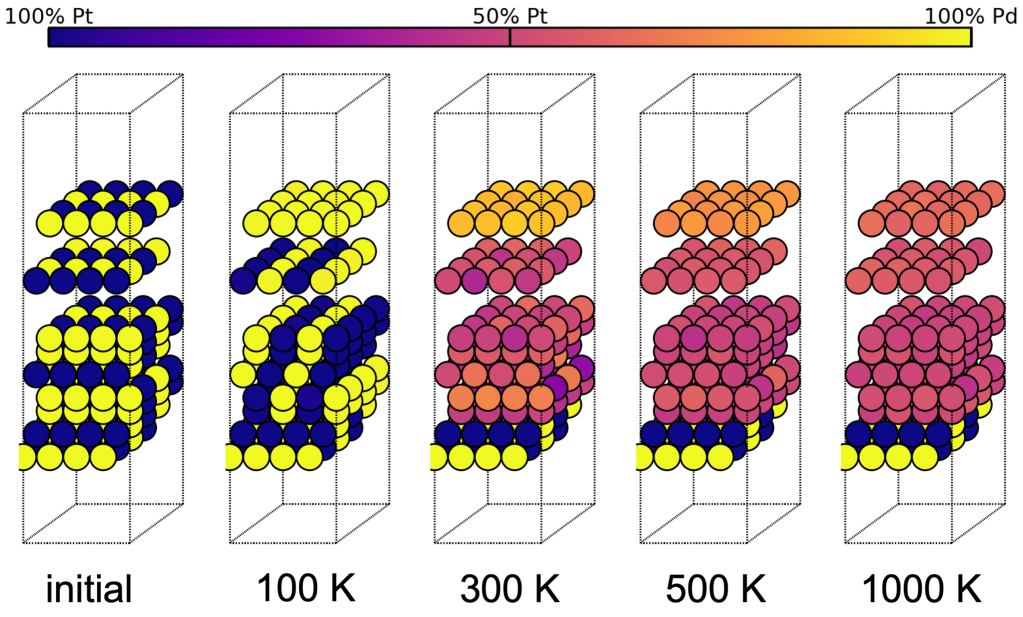

Figure 6.5: Surface Segregation for clean surfaces under different temperatures. The first two layers are lifted from the others for ease of display. The closer the atom is to yellow, the more likely it is to be Pd, and conversely, the closer it is to blue, the more likely it is to be Pt.

The simulated annealing process is employed to optimize the solution by initially permitting extensive exploration of the solution space and subsequently refining the search. This approach commences with a high temperature (1500 K), which increases the likelihood of accepting a diverse range of solutions, including suboptimal ones, thereby allowing the system to avoid local minima. As the temperature decreases, the acceptance probability for less favorable solutions

declines, concentrating the search on the most promising solutions. In this implementation, the initial 60% of the steps are allocated to the annealing phase, which is critical for preventing the system from becoming confined to local minima. By meticulously managing the cooling schedule and the acceptance probability of new solutions, simulated annealing facilitates a comprehensive search for the global minimum, thereby enhancing the overall optimization efficacy of the Monte Carlo simulation.

6.2.2. Surface Segregation in CO Environment

We initially simulated the segregation behavior of a clean surface, starting with a stoichiometry surface of 50% Pd $L1_0$ crystal structure. The composition of the slab was allowed to vary freely, and the structures obtained after Monte Carlo simulation convergence at different temperatures are presented in Fig. 6.5. The results indicate that at low temperatures, such as 100 K, the surface layer will consist entirely of Pd. From the second layer onwards, the structure will transfer from $L1_0$ to $L1_1$ configuration. As the temperature increases, the surface of Pd gradually transforms uniformly into Pt. The lower surface layers progressively lose the $L1_1$ structure, and by 1000 K, the elemental composition of each atom in the subsurface layers becomes completely random. Meanwhile, even at 1000 K, the surface layer still shows a slight preference for Pd.

The variation in the composition of the top four layers with temperature is shown in Fig. 6.6a. Since a 4×4×9 slab has been used for the simulation, each layer include 16 atoms, which

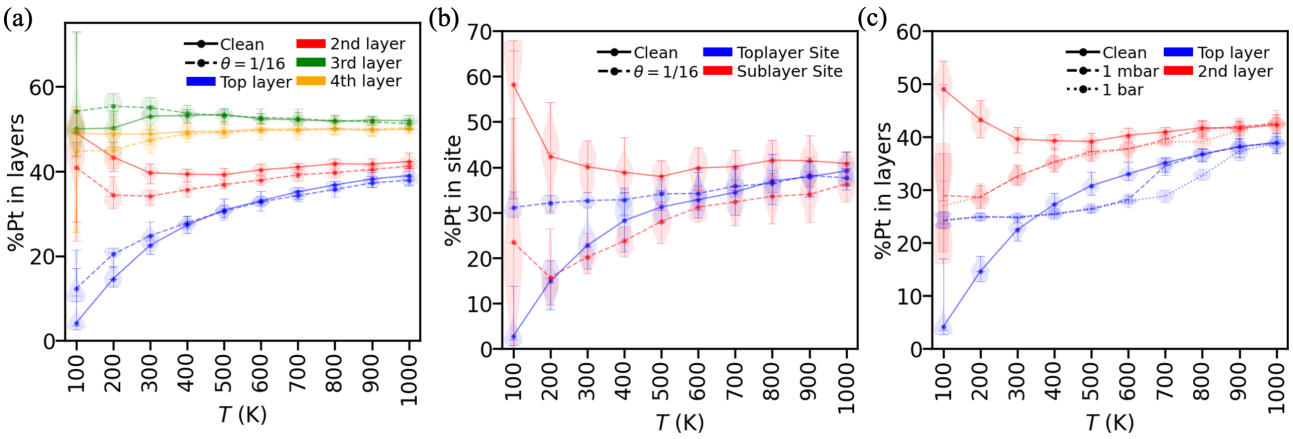

Figure 6.6: The variation in the composition of the top layers with temperature under different conditions, based on the average of 20 simulation results. The violin shows the distribution of these results. The three bars in the violin indicate the maximum value, the median, and the minimum value from top to bottom. (a) The Pt% in the top four layers with and without CO adsorption (θ[CO] = 1/16) if the overall composition of the slab is variable. (b) The Pt% in the three nearest neighbors of CO adsorption sites within the top layer and sublayer (shown as Fig. 4.2) with and without CO adsorption (θ[CO] = 1/16) if the overall composition of the slab is variable. (c) The Pt% in the top two layers with and without CO adsorption-desorption process (θ[CO] from 1/16 to 1/4) under the condition of partial pressure P[CO] = 1 bar or 1 mbar if the overall composition of the slab is variable.

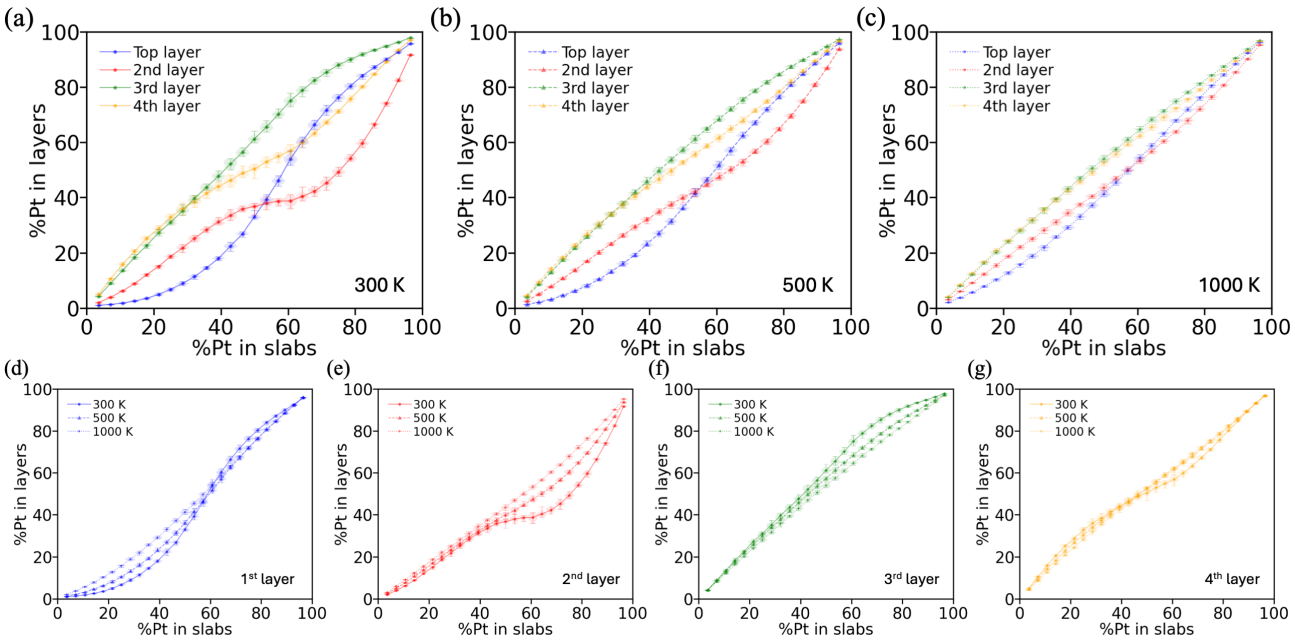

Figure 6.7: Surface segregation for clean surface with fixed overall composition. (a)-(c) Pt% by layer vs. overall Pt% under different temperatures (T = 300, 500, 1000 K). (d)-(g) Compare the change in composition of the same layer at different temperatures.

means each element changes could bring 6.3% variation for the concentration. As Fig. 6.5 shows, the top layer is full of Pd at lower temperatures. As the temperature increases from 100 K to 1000 K, the concentration of Pt will increase from 4.1% to 39.0% while Pt% of the second layer decreases from 49.1% to 42.3%. The composition of deeper layers is not affected by temperature, while Pt% of the third layer is slightly increased from 50.0% to 51.9%, and the fourth layer is slightly increased from 49.0% to 50.0%. If we analyze the distribution of results from the 20 trajectories, the variation is small at temperatures above 300 K. However, at lower temperatures, the results show a large deviation, indicating that the results are not well converged. Particularly at 100 K, where the Pt% in the first layer from one simulation is 17.1%, while the rest of the results are concentrated between 2.7% and 4.1%, with a median of 3.5%. As for the Pt% in the second layer, apart from one value at 28.0%, all other values are close to 50.0%, with the maximum reaching 54.4%. In the third layer, the maximum is 72.9% and the minimum is 43.3%, while the rest of the values are around 49.0%. In the fourth layer, the maximum is 55.3%, the minimum is 25.6%, and the other values are near 50.0%.

Simulations were also conducted with fixed overall slab compositions, ranging from 0% to 100% Pt, at various temperatures (300 K, 500 K, and 1000 K), and the results are presented in Fig. 6.7. Across all temperatures, when the overall Pt fraction is below 50%, Pt preferentially segregates into the deeper layers rather than the top two layers. At 300 K, a sharp increase in Pt concentration in the top layer is observed as the overall Pt fraction rises from 40% to 70%. Only when the overall Pt fraction reaches between 71% and 89% does the Pt concentration in the top layer slightly exceed the overall Pt fraction. Throughout, the Pt concentration in the

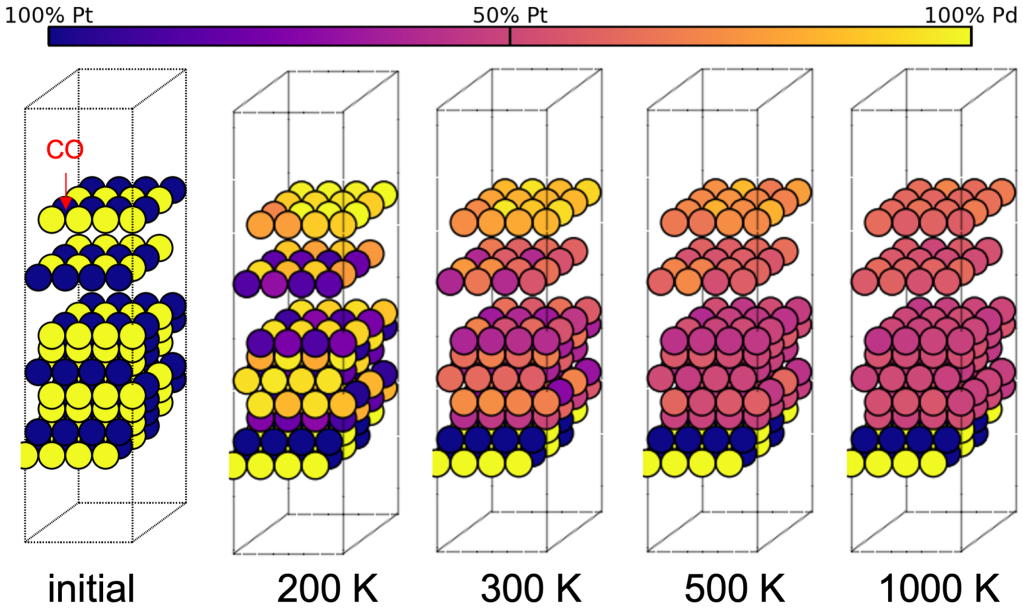

Figure 6.8: Surface Segregation for surfaces with θ[CO] = 1/16 under different temperatures.

second layer remains lower than the overall Pt fraction and shows little growth as the overall Pt fraction increases from 46% to 61%. In contrast, the Pt concentration in the third layer consistently exceeds the overall Pt fraction. When the overall Pt fraction is below 50%, the Pt concentration in the fourth layer is higher than the overall fraction. However, as the overall Pt fraction increases above 50%, the Pt concentration in the fourth layer becomes lower than the overall Pt fraction.

The trends observed at 500 K and 1000 K are similar to those at 300 K, with the key distinction that at higher temperatures, the Pt concentration in the top two layers never exceeds the overall Pt fraction. At 1000 K, the growth rate of Pt concentration in all layers more closely aligns with the growth rate of the overall Pt fraction compared to the behavior at 500 K (shown in Fig. 6.7d-g).

To investigate the effect of CO adsorption, simulations were performed with a fixed CO coverage of θ[CO] = 1/16 (one CO per unit cell) on the fcc site, allowing the overall slab composition to adjust freely. The presence of CO significantly influences surface segregation, as shown in Fig. 6.6a, CO drives Pt into the surface layer at lower temperatures, while the Pt concentration in the second layer remains lower than that of the clean surface but eventually converges to 40%. CO adsorption promotes the introduction of Pt into the top layer at the adsorption site, as shown in Fig. 6.8, disrupting the $L1_1$ structure of the inner layers. As seen in Fig. 6.6b, the adsorption site of CO is more inclined to form the component of Pd_2Pt_1 (33 Pt%). The Pt concentration of the adsorption site increases slowly with increasing temperature, from 31.1% at 100 K to 38.0% at 1000 K. However, the Pt concentration of the corresponding site at the clean surface increases from 2.7% at 100 K to 32.6% at 600 K and finally to 38.6% at 1000 K.

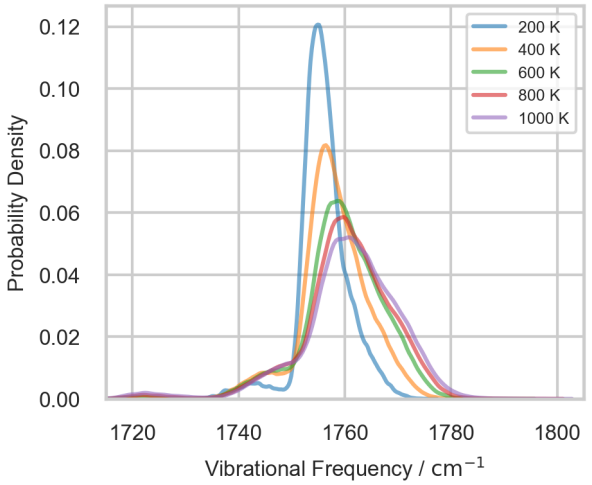

Figure 6.9: Vibration spectrum based on the number of occurrences of specific frequencies in simulations when θ[CO] = 1/16 with variable composition under different temperatures from 200 K to 1000 K.

Meanwhile, the presence of CO also reduces the Pt concentration at the sublayer sites. At 100 K, the site at the clean surface is 57.8% Pt, while when adsorbed with CO, the average is 23.5%. At low temperatures, such as 100 K and 200 K, the composition of the sublayer site exhibits a broad distribution. For the clean surface, at 100 K, the Pt concentration at the top layer sites ranges from a minimum of 33.1% to a maximum of 66.6%, with a median of 65.7% and an average of 57.8%. At 200 K, the distribution becomes approximately normal, with a mean of 43.5%, a median of 43.4%, and upper and lower bounds of 48.4% and 38.3%, respectively. In the presence of CO, the Pt concentration at the sublayer sites exhibits a different distribution at low temperatures. At 100 K, the distribution is close to a normal distribution, with a median and mean of 22.0% and 23.5%, respectively, and a range from 0.1% to 46.6%. At 200 K, the distribution is also close to a normal distribution, with a median and mean of 15.5% and 15.6%, respectively, and a range from 12.0% to 20.5%. As the temperature rises to 1000 K, the Pt concentration of the top layer site converges to around 38%, regardless of the presence of CO, but the sublayer site is 36.1% in the presence of CO and 41.8% on a clean surface.

Then, we simulated the vibrational spectra of adsorbed CO. As a first step, we study again CO with a fixed coverage of θ[CO] = 1/16 with variable composition under different temperatures. The simulated spectra are obtained as histograms based on the vibrational frequencies predicted for individual structures during the Monte Carlo simulation, as shown in Fig. 6.9. The figure depicts the vibrational spectra of CO at various temperatures (200 K, 400 K, 600 K, 800 K, and 1000 K) with a surface coverage (θ[CO]) of 1/16. The x-axis represents the vibrational frequency in cm^{-1}, while the y-axis represents the probability density, indicating how often specific vibrational frequencies occur in the simulations. As the temperature increases from 200 K to 1000 K, the peaks in the vibrational spectra become broader. Additionally, as the

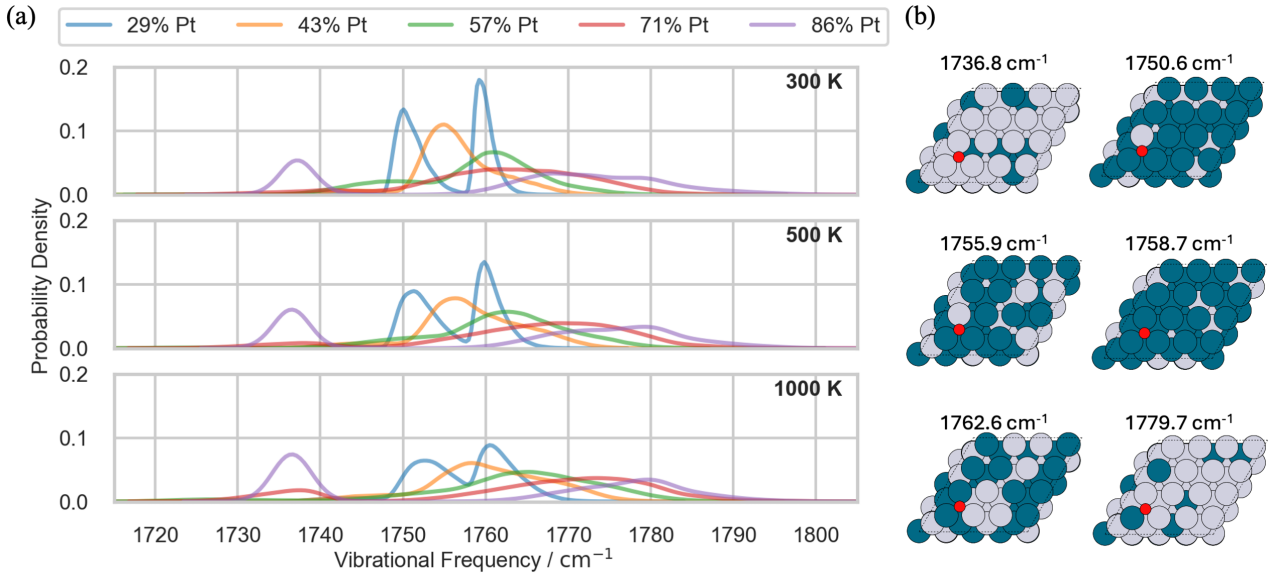

Figure 6.10: (a) Vibration spectrum based on the number of occurrences of specific frequencies in simulations when θ[CO] = 1/16 with fixed composition (from 32% to 88%Pt) under different T = 300, 500, 1000 K. (b) Samples of the structure corresponding to different peaks.

temperature increases, the peak positions shift toward higher frequencies by approximately 10 cm^{-1} due to the increasing Pt concentration in the sublayer site, as shown in Fig. 6.6b. This result is consistent with our observations in Fig. 4.4. The probability density at the peak decreases with increasing temperature. At 200 K, the peak is the sharpest and highest, indicating a high probability density for a specific vibrational frequency. As temperature increases, the peak broadens , suggesting a more dispersed set of vibrational states and a reduced probability for any particular state.

Vibrational spectra were also simulated for θ[CO] = 1/16 and a fixed slab composition (from 29% to 86%Pt). The vibrational spectra (shown in 6.10a) generated by the different compositions differ significantly, with peaks appearing around 1755 cm^{-1} at 43% Pt, around 1736 cm^{-1} at 86% Pt, and flat peaks appearing above 1760 at 45% and 71% Pt. In addition, 86% Pt has a very broad peak at 1780 cm^{-1}, and 57% Pt has a very broad peak between 1760 to 1770 cm^{-1}. It is noteworthy that two close peaks occur at around 1750 and 1760 at cm^{-1} 29% Pt. With increasing temperature, all peaks blue-shift and broaden, except for the 86% Pt peak at around 1736 cm^{-1}, which becomes narrower. It is noteworthy that using a fixed coverage of CO does not account for the actual adsorption and desorption processes. However, our simulation could catch the trend given in Fig. 4.5, the vibrational frequency of hollow site goes through a process of first decreasing and then increasing as as the Pt% grows from 0 to 50.

Fig. 6.10b gives an example of the structures for different peaks. For the structure of 86% Pt, the peak at 1736 cm^{-1} corresponds to the adsorption site Pt_3, and when the adsorption site changes to Pd_1Pt_2, the vibration frequency of CO becomes 1780 cm^{-1}. For the structure of

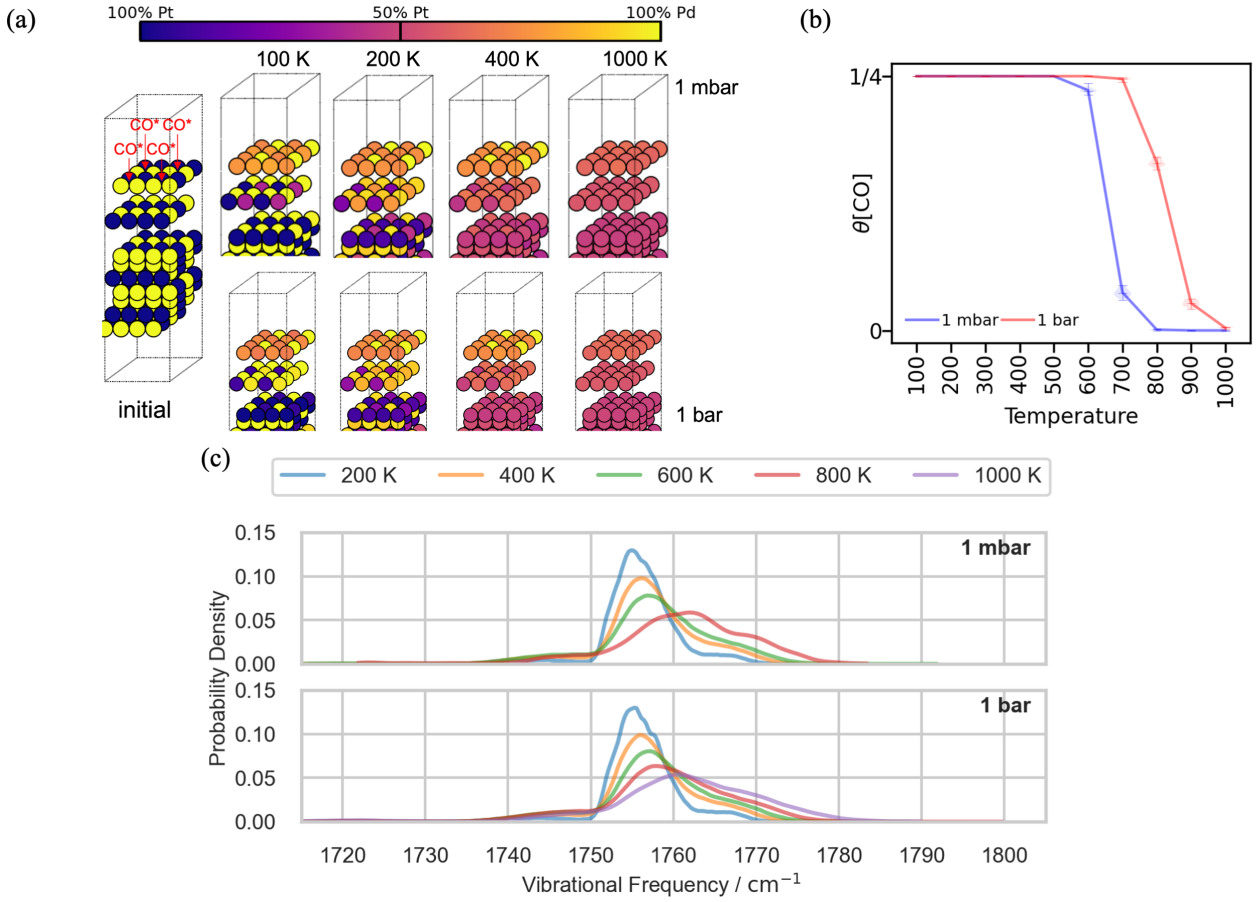

Figure 6.11: (a) Surface segregation for surfaces with free CO adsorption and desorption between θ[CO] = 1/16 and 1/4 under different temperatures with variable composition under different partial pressures (1 mbar and 1 bar). (b) The change in the amount of adsorbed CO on the surfaces with temperature at different pressures. (c) Vibration spectrum based on the number of occurrences of specific frequencies in simulations with free CO adsorption and desorption between θ[CO] = 1/16 and 1/4 with variable composition under different T under different partial pressures (1 mbar and 1 bar).

29% Pt, the two peaks at 1750 and 1759 cm^{-1} correspond to the adsorption sites of Pd_2Pt_1 and Pd_3.

Finally, simulations allowing free CO adsorption and desorption were performed for coverages between θ[CO] = 1/16 and 1/4 under different temperatures with variable composition under different partial pressures of CO. The positions of the four CO adsorption sites and the segregation results are shown in Fig. 6.11a. Surface segregation varies with different CO partial pressures, particularly in the second layer, as illustrated in Fig. 6.6c. At low temperatures, CO tends to achieve higher coverage, resulting in more Pt in the surface layer and more Pd in the second layer. Higher CO partial pressures lead to more Pd in the second layer compared to lower partial pressures. At high temperatures, such as above 800 K, the difference caused by CO partial pressures becomes negligible because CO no longer tends to adsorb on the surface. As shown in Fig. 6.11b, with an increase in temperature, for a partial pressure of 1 mbar, the

amount of CO adsorbed on the surface begins to decrease from 400 K and becomes 0 at 800 K. For a partial pressure of 1 bar, the amount of CO adsorbed on the surface begins to decrease from 600 K and approaches 0 at 1000 K.

6.3. Conclusion

In this study, we employed GPR and Monte Carlo simulations to investigate the segregation behavior of Pd/Pt alloy surfaces and the impact of CO adsorption. DFT calculations were utilized to generate the training set for the GPR model. The training set comprised various slab configurations to ensure a comprehensive representation of the system's behavior.

The core of our methodology involved the application of GPR to predict the formation energy of clean surfaces, the adsorption energy, and the vibrational frequencies of CO on these surfaces. By categorizing neighboring atoms into distinct distance ranges and normalizing these descriptors, we effectively captured the local atomic environments. The GPR model, trained on a diverse dataset, utilized a sparse approach to handle computational complexity, ensuring accurate predictions with reduced redundancy. The kernel function used in the GPR model facilitated the calculation of similarities between different atomic descriptors, leading to precise energy predictions.

The Monte Carlo simulations, incorporating a simulated annealing process, allowed for thorough exploration of the solution space, preventing the system from becoming trapped in local minima and ensuring a comprehensive search for the global minimum. In this implementation, the initial 60% of the steps were allocated to the annealing phase, which was critical for preventing the system from becoming confined to local minima.

Our results demonstrate that the surface layer composition of the Pd/Pt alloy varies significantly with temperature. At low temperatures, the surface layer is predominantly Pd, and the deeper layer is transferred to the $L1_1$ configuration. As temperature increases, the surface layer composition becomes more random, while the lower layers progressively lose their ordered structure. The introduction of CO significantly alters the segregation behavior, promoting Pt presence in the surface layer and disrupting the $L1_1$ structure of inner layers. The vibrational spectra of CO adsorbed on surfaces with varying compositions revealed distinct peaks that shift with temperature and composition, indicating changes in the local environment and adsorption characteristics.

Furthermore, the study explored the effects of CO partial pressures on surface segregation. At lower temperatures, higher CO partial pressures resulted in increased Pt in the surface layer and Pd in the second layer. This effect diminished at higher temperatures, where CO adsorption was less favorable.

Overall, this comprehensive investigation provides valuable insights into the segregation behavior of Pd/Pt alloys and the influence of CO adsorption, with GPR playing a crucial role

in accurately predicting formation energies and adsorption characteristics. The methodologies and findings presented here can inform future studies and applications involving alloy surfaces and adsorbate interactions.

7. Conclusion and Outlook

The conclusion of this dissertation includes the findings from investigations into the stability, structure, and reactivity of hydroxylated α-Al_2O_3 and α-Fe_2O_3(0001) surfaces, as well as the adsorption behavior of CO on Pd/Pt alloy and α-Al_2O_3(0001) surfaces.

Firstly, the studies on α-Al_2O_3 and α-Fe_2O_3(0001) surfaces revealed new insights into their hydroxylated terminations. For α-Al_2O_3(0001), a novel termination featuring isolated $Al(OH)_3$ groups was identified, demonstrating higher stability at elevated temperatures compared to previous models. This stability arises from weakly repulsive interactions between $Al(OH)_3$ groups at low coverages. Similarly, hydroxylated α-Fe_2O_3(0001) surfaces, characterized by isolated $Fe(OH)_3$ groups, were found to be stable at relatively low chemical potentials of water, mirroring the behavior observed for α-Al_2O_3(0001). The study also explored the stability of oxidized and reduced terminations, with reduced surfaces showing stability only at very low chemical potentials of oxygen. The formation and decomposition processes of these hydroxylated surfaces were further investigated. For α-Al_2O_3(0001), local reconstruction via water adsorption and dissociation led to the formation of $Al(OH)_3$ groups and OH-saturated Al-vacancies with modest energy barriers. The kinetics of these processes are significantly influenced by the partial pressure of water. For α-Fe_2O_3(0001), the stability of hydroxylated surfaces remains robust across different computational methodologies, though oxidation and reduction behaviors depend on the chosen value of U in PBE+U calculations.

Further research could focus on expanding this research to explore other metal oxides, such as chromia (Cr_2O_3) and V_2O_3, which would be valuable. These materials, like α-Al_2O_3 and α-Fe_2O_3, are widely used in catalysis and often operate in environments with varying levels of water exposure. Investigating their surfaces under different water conditions could reveal unique hydroxylation behaviors and surface structures, providing a comparative basis for understanding the broader trends in stability and reactivity of transition metal oxides in aqueous environments.

Additionally, the adsorption of CO on Pd, Pt, and Pd/Pt alloy NPs supported on α-Al_2O_3 was studied. The CO adsorption sites varied with NP alloy composition, showing distinct behaviors on pure Pd, Pt, and alloy NPs. CO adsorbed in an on-top configuration on Pt, while on Pd, it mainly adsorbed on bridge and hollow sites. On alloy NPs, both adsorption modes were observed simultaneously, with Pt-rich particles showing lower intensity of Pd adsorption bands, suggesting Pt surface segregation. This was further supported by DFT calculations, which revealed broad IR bands due to varying wavenumbers for different alloy compositions.

Then, a systematic investigation of the α-Al_2O_3(0001) surface using combined experimental and theoretical approaches demonstrated high reactivity and partial hydroxylation under UHV conditions. DFT calculations supported these findings, agreeing with experimental CO vibrational frequencies and binding energies.

Following this, the chapter on the adsorption and migration behaviors of Pt and Pd species on α-$Al_2O_3(0001)$ and $CeO_2(100)$ surfaces provided further insights into the stability and mobility of these species on catalytic supports. The study found that Pt species generally exhibit stronger adsorption and higher stability, particularly on dry surfaces, suggesting their potential for forming durable catalytic sites. In contrast, Pd species showed lower diffusion barriers, indicating greater mobility. These findings underscore the need to balance stability and mobility when designing catalysts and highlight the impact of surface hydroxylation on adsorption energies and stability, offering valuable guidance for optimizing catalytic performance.

Finally, our study on the segregation behavior of Pd/Pt alloy surfaces and the impact of CO adsorption employed DFT calculations, GPR, and Monte Carlo simulations. The findings revealed significant variations in surface layer composition with temperature and CO adsorption, providing valuable insights into the segregation behavior of Pd/Pt alloys and the influence of CO adsorption.

Future research can extend this study by applying the developed model to investigate active sites and deactivation mechanisms of Pt-Pd catalysts under operando conditions at the atomic scale. First, predicting the equilibrium shape of oxide-supported Pt and Pd nanoparticles will help to understand how support interactions and environmental factors influence nanoparticle geometry and stability. Determining these equilibrium shapes under reaction conditions will provide insights into how these particles adapt structurally to maximize catalytic performance. The second step is a theoretical investigation of adsorption energetics and adsorption-induced shape changes. This involves analyzing how adsorbates, such as CO or other intermediates, interact with and reshape the nanoparticles, potentially changing the active sites. Understanding these influences can reveal conditions that optimize catalyst activity that may lead to deactivation. Lastly, modeling sintering kinetics will focus on the dynamics of particle migration and merging under reaction conditions. By simulating the mechanisms of Ostwald ripening and sintering, this step aims to identify factors that promote catalyst deactivation through particle growth and loss of active sites. Such kinetic insights could lead to targeted strategies for inhibiting sintering and extending catalyst lifetimes.

Together, these steps will provide a detailed, atomic-level understanding of how Pt-Pd catalysts behave under operando conditions, offering valuable guidance for designing catalysts with enhanced durability and activity. This research direction will bridge the gap between static catalyst design and dynamic, operando environments, advancing the field of catalyst development.

Overall, this dissertation provides valuable insights into the stability, structure, and reactivity of oxide surfaces and Pd/Pt alloy surfaces, contributing to a deeper understanding of surface phenomena in heterogeneous catalysis. The methodologies and findings presented here offer a robust foundation for future studies and applications involving complex surface interactions in catalytic processes.

References

[1] I. Lefort, J. M. Herreros, and A. Tsolakis, "Reduction of low temperature engine pollutants by understanding the exhaust species interactions in a diesel oxidation catalyst", *Environ. Sci. Technol.* **48**, 2361–2367 (2014).

[2] G. Ertl, H. Knözinger, and J. Weitkamp, *Handbook of Heterogeneous Catalysis*, edited by G. Ertl, H. Knözinger, and J. Weitkamp, Vol. 1-5 (Wiley, 2008), pp. 2274–2345.

[3] A. Cowley, J. Matthey, S. Brown, L. Cole, J. Dickson, M. Fujita, N. Girardot, S. Grant, J. Jiang, R. Raithatha, M. Ryan, M. Underwood, and A. Wang, *PGM market report*, tech. rep. (Johnson Matthey, 2024).

[4] Z. Gao, S. J. Curran, C. S. Daw, and R. M. Wagner, "Light-duty drive cycle simulations of diesel engine-out exhaust properties for an rcci-enabled vehicle", in 8th us natl. combust. meet. 2013, Vol. 3 (2013), pp. 1889–1899.

[5] S. Dey and G. Chandra Dhal, "Controlling carbon monoxide emissions from automobile vehicle exhaust using copper oxide catalysts in a catalytic converter", *Mater. Today Chem.* **17**, 100282 (2020).

[6] M. Betchaku, Y. Nakagawa, M. Tamura, and K. Tomishige, "Reforming of toluene with simulated automobile exhaust gas over hydrotalcite-like-compound-derived Ni catalyst", *Fuel Process. Technol.* **209**, 106545 (2020).

[7] N. Nejar and M. J. Illán-Gómez, "Potassium-copper and potassium-cobalt catalysts supported on alumina for simultaneous NO_x and soot removal from simulated diesel engine exhaust", *Appl. Catal. B Environ.* **70**, 261–268 (2007).

[8] K. F. Kalz, R. Kraehnert, M. Dvoyashkin, R. Dittmeyer, R. Gläser, U. Krewer, K. Reuter, and J. D. Grunwaldt, "Future Challenges in Heterogeneous Catalysis: Understanding Catalysts under Dynamic Reaction Conditions", *ChemCatChem* **9**, 17–29 (2017).

[9] M. A. Newton, "Dynamic adsorbate/reaction induced structural change of supported metal nanoparticles: Heterogeneous catalysis and beyond", *Chem. Soc. Rev.* **37**, 2644–2657 (2008).

[10] R. Schlögl, "Catalysis 4.0", *ChemCatChem* **9**, 533–541 (2017).

[11] A. M. Gänzler, M. Casapu, P. Vernoux, S. Loridant, F. J. Cadete Santos Aires, T. Epicier, B. Betz, R. Hoyer, and J. D. Grunwaldt, "Tuning the Structure of Platinum Particles on Ceria In Situ for Enhancing the Catalytic Performance of Exhaust Gas Catalysts", *Angew. Chemie - Int. Ed.* **56**, 13078–13082 (2017).

[12] M. Cargnello, V. V. Doan-Nguyen, T. R. Gordon, R. E. Diaz, E. A. Stach, R. J. Gorte, P. Fornasiero, and C. B. Murray, "Control of metal nanocrystal size reveals metal-support interface role for ceria catalysts", *Science* **341**, 771–773 (2013).

[13] M. Trueba and S. P. Trasatti, "γ-alumina as a support for catalysts: a review of fundamental aspects", *Eur. J. Inorg. Chem.* **17**, 3393–3403 (2005).

[14] P. Christopher and S. Linic, "Shape- and size-specific chemistry of Ag nanostructures in catalytic ethylene epoxidation", *ChemCatChem* **2**, 78–83 (2010).

[15] M. García-Mota, M. Rieger, and K. Reuter, "*Ab initio* prediction of the equilibrium shape of supported ag nanoparticles on α-al$_2$o$_3$(0001)", *J. Catal.* **321**, 1–6 (2015).

[16] U. Hejral, P. Müller, O. Balmes, D. Pontoni, and A. Stierle, "Tracking the shape-dependent sintering of platinum-rhodium model catalysts under operando conditions", *Nat. Commun.* **7**, 10964 (2016).

[17] R. Molina and G. Poncelet, "α-Alumina-Supported Nickel Catalysts Prepared from Nickel Acetylacetonate: A TPR Study", *J. Catal.* **173**, 257–267 (1998).

[18] G. Poncelet, M. A. Centeno, and R. Molina, "Characterization of reduced α-alumina-supported nickel catalysts by spectroscopic and chemisorption measurements", *Appl. Catal. A Gen.* **288**, 232–242 (2005).

[19] Z. Hou, O. Yokota, T. Tanaka, and T. Yashima, "Characterization of Ca-promoted Ni/α-Al_2O_3 catalyst for CH_4 reforming with CO_2", *Appl. Catal. A Gen.* **253**, 381–387 (2003).

[20] M. Lyubovsky and L. Pfefferle, "Complete methane oxidation over Pd catalyst supported on α-alumina. Influence of temperature and oxygen pressure on the catalyst activity", *Catal. Today* **47**, 29–44 (1999).

[21] F. Pompeo, N. N. Nichio, M. M. Souza, D. V. Cesar, O. A. Ferretti, and M. Schmal, "Study of Ni and Pt catalysts supported on α-Al_2O_3 and ZrO_2 applied in methane reforming with CO_2", *Appl. Catal. A Gen.* **316**, 175–183 (2007).

[22] E. M. Dietze and P. N. Plessow, "Predicting the Strength of Metal-Support Interaction with Computational Descriptors for Adhesion Energies", *J. Phys. Chem. C* **123**, 20443–20450 (2019).

[23] G. Sun, A. N. Alexandrova, and P. Sautet, "Pt_8 cluster on alumina under a pressure of hydrogen: support-dependent reconstruction from first-principles global optimization", *J. Chem. Phys.* **151**, 194703 (2019).

[24] G. Li, B. Zandkarimi, A. C. Cass, T. J. Gorey, B. J. Allen, A. N. Alexandrova, and S. L. Anderson, "Sn-modification of Pt_7/alumina model catalysts: Suppression of carbon deposition and enhanced thermal stability", *J. Chem. Phys.* **152**, 024702 (2020).

[25] T. Xie, B. J. Hare, P. J. Meza-Morales, C. Sievers, and R. B. Getman, "Identification of the Active Sites in the Dehydrogenation of Methanol on Pt/Al_2O_3 Catalysts", *J. Phys. Chem. C* **124**, 19015–19023 (2020).

[26] Z. Lodziana and J. K. Nørskov, "Adsorption of Cu and Pd on α-Al_2O_3(0001) surfaces with different stoichiometries", *J. Chem. Phys.* **115**, 11261 (2001).

[27] I. Milas, B. Hinnemann, and E. A. Carter, "Diffusion of Al, O, Pt, Hf, and Y atoms on α-Al_2O_3(0001): implications for the role of alloying elements in thermal barrier coatings", *J. Mater. Chem.* **21**, 1447–1456 (2011).

[28] B. Hinnemann and E. A. Carter, "Adsorption of Al, O, Hf, Y, Pt, and S Atoms on α-Al_2O_3(0001)", *J. Phys. Chem. C* **111**, 7105–7126 (2007).

[29] N. J. O'Connor, A. S. M. Jonayat, M. J. Janik, and T. P. Senftle, "Interaction trends between single metal atoms and oxide supports identified with density functional theory and statistical learning", *Nat. Catal.* **1**, 531–539 (2018).

[30] L. Zhang, X. Fu, M. Hohage, P. Zeppenfeld, and L. D. Sun, "Growth of pentacene on α-Al_2O_3(0001) studied by in situ optical spectroscopy", *Phys. Rev. Materials* **1**, 043401 (2017).

[31] J. Blomqvist and P. Salo, "First-principles study for the adsorption of segments of BPA-PC on α-Al_2O_3(0001)", *Phys. Rev. B* **84**, 153410 (2011).

[32] J. Feng, W. Zhang, and W. Jiang, "*Ab initio* study of Ag / Al_2O_3 and Au / Al_2O_3 interfaces", *Phys. Rev. B* **72**, 115423 (2005).

[33] J. D. Baran, H. Grönbeck, and A. Hellman, "Mechanism for limiting thickness of thin oxide films on aluminum", *Phys. Rev. Lett.* **112**, 146103 (2014).

[34] M. Koberidze, M. J. Puska, and R. M. Nieminen, "Structural details of Al/Al_2O_3 junctions and their role in the formation of electron tunnel barriers", *Phys. Rev. B* **97**, 195406 (2018).

[35] J. Kang, J. Zhu, C. Curtis, D. Blake, G. Glatzmaier, Y.-H. Kim, and S.-H. Wei, "Atomically abrupt liquid-oxide interface stabilized by self-regulated interfacial defects: The case of Al/Al_2O_3 interfaces", *Phys. Rev. Lett.* **108**, 226105 (2012).

[36] G. Pilania, B. J. Thijsse, R. G. Hoagland, I. Lazić, S. M. Valone, and X.-Y. Liu, "Revisiting the Al/Al_2O_3 Interface: Coherent Interfaces and Misfit Accommodation", *Sci. Rep.* **4**, 4485 (2014).

[37] W. Zhang and J. R. Smith, "Nonstoichiometric interfaces and Al_2O_3 adhesion with Al and Ag", *Phys. Rev. Lett.* **85**, 3225–3228 (2000).

[38] D. J. Siegel, L. G. Hector, and J. B. Adams, "Adhesion, atomic structure, and bonding at the Al(111)/α-Al_2O_3 interface: A first principles study", *Phys. Rev. B* **65**, 085415 (2002).

[39] Q. Zhang, T. Cagin, A. van Duin, W. A. Goddard, Y. Qi, and L. G. Hector, "Adhesion and nonwetting-wetting transition in the Al/α-Al_2O_3 interface", *Phys. Rev. B* **69**, 045423 (2004).

[40] S. H. Oh, Y. Kauffmann, C. Scheu, W. D. Kaplan, and M. Rühle, "Ordered liquid aluminum at the interface with sapphire", *Science* **310**, 661–663 (2005).

[41] I. G. Batirev, A. Alavi, M. W. Finnis, and T. Deutsch, "First-principles calculations of the ideal cleavage energy of bulk Niobium(111)/α-Alumina(0001) interfaces", *Phys. Rev. Lett.* **82**, 1510–1513 (1999).

[42] K. Shimamura, F. Shimojo, R. K. Kalia, A. Nakano, and P. Vashishta, "Bonding and structure of ceramic-ceramic interfaces", *Phys. Rev. Lett.* **111**, 066103 (2013).

[43] K. J. Harmon, K. Letchworth-Weaver, A. P. Gaiduk, F. Giberti, F. Gygi, M. K. Y. Chan, P. Fenter, and G. Galli, "Validating first-principles molecular dynamics calculations of oxide/water interfaces with X-ray reflectivity data", *Phys. Rev. Materials* **4**, 113805 (2020).

[44] Y. R. Koh, J. Shi, B. Wang, R. Hu, H. Ahmad, S. Kerdsongpanya, E. Milosevic, W. A. Doolittle, D. Gall, Z. Tian, S. Graham, and P. E. Hopkins, "Thermal boundary conductance across epitaxial metal/sapphire interfaces", *Phys. Rev. B* **102**, 205304 (2020).

[45] C. Verdozzi, D. R. Jennison, P. A. Schultz, and M. P. Sears, "Sapphire (0001) Surface, Clean and with *d*-Metal Overlayers", *Phys. Rev. Lett.* **82**, 799 (1999).

[46] C. Niu, K. Shepherd, D. Martini, J. Tong, J. A. Kelber, D. R. Jennison, and A. Bogicevic, "Cu interactions with α-Al_2O_3(0001): effects of surface hydroxyl groups versus dehydroxylation by Ar-ion sputtering", *Surf. Sci.* **465**, 163–176 (2000).

[47] R. Lazzari and J. Jupille, "Wetting and interfacial chemistry of metallic films on the hydroxylated α-Al_2O_3(0001) surface", *Phys. Rev. B* **71**, 045409 (2005).

[48] M. Messaykeh, J. Goniakowski, G. Cabailh, J. Jupille, R. Lazzari, P. Lagarde, and N. Trcera, "Chromium adsorption reveals a persistent hydroxylation of vacuum-annealed α-Al_2O_3(0001)", *J. Phys. Chem. C* **123**, 29245–29254 (2019).

[49] H.-L. Thi Le, R. Lazzari, J. Goniakowski, R. Cavallotti, S. Chenot, C. Noguera, J. Jupille, A. Koltsov, and J.-M. Mataigne, "Tuning Adhesion at Metal/Oxide Interfaces by Surface Hydroxylation", *J. Phys. Chem. C* **121**, 11464–11471 (2017).

[50] R. Lazzari and J. Jupille, "Chemical reaction via hydroxyl groups at the titanium/α-Al_2O_3(0001) interface", *Surf. Sci.* **507-510**, 683–687 (2002).

[51] X.-G. Wang, J. R. Smith, and M. Scheffler, "Effect of hydrogen on Al_2O_3/Cu interfacial structure and adhesion", *Phys. Rev. B* **66**, 073411 (2002).

[52] X. G. Wang, J. R. Smith, and M. Scheffler, "Adhesion of Copper and Alumina from First Principles", *J. Am. Ceram. Soc.* **86**, 696–700 (2003).

[53] K. C. Hass, W. F. Schneider, A. Curioni, and W. Andreoni, "The chemistry of water on alumina surfaces: Reaction dynamics from first principles", *Science* **282**, 265–268 (1998).

[54] P. J. Eng, T. P. Trainor, G. E. Brown, G. A. Waychunas, M. Newville, S. R. Sutton, and M. L. Rivers, "Structure of the hydrated α-Al_2O_3 (0001) surface", *Science* **288**, 1029–1033 (2000).

[55] J. A. Kelber, "Alumina surfaces and interfaces under non-ultrahigh vacuum conditions", *Surf. Sci. Rep.* **62**, 271–303 (2007).

[56] C. C. Chang, "LEED studies of the (0001) face of α-Alumina", *J. Appl. Phys.* **39**, 5570–5573 (1968).

[57] T. M. French and G. A. Somorjai, "Composition and surface structure of the (0001) face of α-alumina by low-energy electron diffraction", *J. Phys. Chem.* **74**, 2489–2495 (1970).

[58] G. Renaud, B. Villette, I. Vilfan, and A. Bourret, "Atomic Structure of the $\alpha-Al_2O_3(0001)(\sqrt{31}\times\sqrt{31})R\pm 9°$ Reconstruction", *Phys. Rev. Lett.* **73**, 1825 (1994).

[59] C. Barth and M. Reichling, "Imaging the atomic arrangements on the high-temperature reconstructed α-Al_2O_3(0001) surface", *Nature* **414**, 54–57 (2001).

[60] E. A. A. Jarvis and E. A. Carter, "Metallic Character of the Al_2O_3(0001)-($\sqrt{31}\times\sqrt{31}$)R $\pm$ 9° Surface Reconstruction", *J. Phys. Chem. B* **105**, 4045–4052 (2001).

[61] V. Coustet and J. Jupille, "High-resolution electron-energy-loss spectroscopy of isolated hydroxyl groups on α-Al_2O_3(0001)", *Surf. Sci.* **307–309**, 1161 (1994).

[62] C. E. Nelson, J. W. Elam, M. A. Cameron, M. A. Tolbert, and S. M. George, "Desorption of H_2O from a hydroxylated single-crystal α-Al_2O_3(0001) surface", *Surf. Sci.* **416**, 341–353 (1998).

[63] Q. Fu, T. Wagner, and M. Rühle, "Hydroxylated α-Al_2O_3 (0001) surfaces and metal/α-Al_2O_3 (0001) interfaces", *Surf. Sci.* **600**, 4870–4877 (2006).

[64] J. Ahn and J. W. Rabalais, "Composition and structure of the Al_2O_3{0001}-(1 × 1) surface", *Surf. Sci.* **388**, 121–131 (1997).

[65] J. W. Elam, C. E. Nelson, M. A. Cameron, M. A. Tolbert, and S. M. George, "Adsorption of H_2O on a Single-Crystal α-Al_2O_3(0001) Surface", *J. Phys. Chem. B* **102**, 7008–7015 (1998).

[66] J. Wirth, H. Kirsch, S. Wlosczyk, Y. Tong, P. Saalfrank, and R. K. Campen, "Characterization of water dissociation on α-Al_2O_3 ($1\bar{1}02$): theory and experiment", *Phys. Chem. Chem. Phys.* **18**, 14822–14832 (2016).

[67] T. Kurita, K. Uchida, and A. Oshiyama, "Atomic and electronic structures of α-Al_2O_3 surfaces", *Phys. Rev. B* **82**, 155319 (2010).

[68] T. Becker, A. Birkner, G. Witte, and C. Wöll, "Microstructure of the α-$Al_2O_3(11\bar{2}0)$ surface", *Phys. Rev. B* **65**, 115401 (2002).

[69] S. Aboud, J. Wilcox, and G. E. Brown, "Density functional theory investigation of the interaction of water with α-Al_2O_3 and α-$Fe_2O_3(1\bar{1}02)$ surfaces: Implications for surface reactivity", *Phys. Rev. B* **83**, 125407 (2011).

[70] A. Tougerti, C. Méthivier, S. Cristol, F. Tielens, M. Che, and X. Carrier, "Structure of clean and hydrated α-$Al_2O_3(1\bar{1}02)$ surfaces: implication on surface charge", *Phys. Chem. Chem. Phys.* **13**, 6531–6543 (2011).

[71] S. Heiden, Y. Yue, H. Kirsch, J. Wirth, P. Saalfrank, and R. Kramer Campen, "Water Dissociative Adsorption on α-$Al_2O_3(11\bar{2}0)$ Is Controlled by Surface Site Undercoordination, Density, and Topology", *J. Phys. Chem. C* **122**, 6573–6584 (2018).

[72] R. Wischert, P. Laurent, C. Copéret, F. Delbecq, and P. Sautet, "γ-Alumina: The essential and unexpected role of water for the structure, stability, and reactivity of "defect" sites", *J. Am. Chem. Soc.* **134**, 14430–14449 (2012).

[73] M. Digne, P. Sautet, P. Raybaud, P. Euzen, and H. Toulhoat, "Hydroxyl Groups on γ-Alumina Surfaces: A DFT Study", *J. Catal.* **211**, 1–5 (2002).

[74] M. Digne, P. Sautet, P. Raybaud, P. Euzen, and H. Toulhoat, "Use of DFT to achieve a rational understanding of acid–basic properties of γ-alumina surfaces", *J. Catal.* **226**, 54–68 (2004).

[75] Z. Łodziana, N. Y. Topsøe, and J. K. Nørskov, "A negative surface energy for alumina", *Nat. Mater.* **3**, 289–293 (2004).

[76] X. G. Wang, A. Chaka, and M. Scheffler, "Effect of the environment on α-Al_2O_3 (0001) surface structures", *Phys. Rev. Lett.* **84**, 3650 (2000).

[77] J. V. Lauritsen, M. C. Jensen, K. Venkataramani, B. Hinnemann, S. Helveg, B. S. Clausen, and F. Besenbacher, "Atomic-Scale Structure and Stability of the $\sqrt{31} \times \sqrt{31}R9°$ Surface of $Al_2O_3(0001)$", *Phys. Rev. Lett.* **103**, 076103 (2009).

[78] V. A. Ranea, W. F. Schneider, and I. Carmichael, "DFT characterization of coverage dependent molecular water adsorption modes on α-$Al_2O_3(0001)$", *Surf. Sci.* **602**, 268–275 (2008).

[79] V. A. Ranea, I. Carmichael, and W. F. Schneider, "DFT Investigation of Intermediate Steps in the Hydrolysis of α-$Al_2O_3(0001)$", *J. Phys. Chem. C* **113**, 2149–2158 (2009).

[80] P. Thissen, G. Grundmeier, S. Wippermann, and W. G. Schmidt, "Water adsorption on the α-$Al_2O_3(0001)$ surface", *Phys. Rev. B* **80**, 245403 (2009).

[81] S. Heiden, D. Usvyat, and P. Saalfrank, "Theoretical Surface Science Beyond Gradient-Corrected Density Functional Theory: Water at α-$Al_2O_3(0001)$ as a Case Study", *J. Phys. Chem. C* **123**, 6675–6684 (2019).

[82] J. Wirth and P. Saalfrank, "The Chemistry of Water on α-Alumina: Kinetics and Nuclear Quantum Effects from First Principles", *J. Phys. Chem. C* **116**, 26829–26840 (2012).

[83] H. Kirsch, J. Wirth, Y. Tong, M. Wolf, P. Saalfrank, and R. K. Campen, "Experimental characterization of unimolecular water dissociative adsorption on α-alumina", *J. Phys. Chem. C* **118**, 13623–13630 (2014).

[84] S. Heiden, J. Wirth, R. K. Campen, and P. Saalfrank, "Water Molecular Beam Scattering at α-Al_2O_3(0001): An Ab Initio Molecular Dynamics Study", *J. Phys. Chem. C* **122**, 15494–15504 (2018).

[85] G. Melani, Y. Nagata, R. K. Campen, and P. Saalfrank, "Vibrational spectra of dissociatively adsorbed D_2O on Al-terminated α-Al_2O_3(0001) surfaces from ab initio molecular dynamics", *J. Chem. Phys.* **150**, 244701 (2019).

[86] T. Mullan, L. Maschio, P. Saalfrank, and D. Usvyat, "Reaction barriers on non-conducting surfaces beyond periodic local MP2: Diffusion of hydrogen on $\alpha-Al_2O_3$(0001) as a test case", *J. Chem. Phys.* **139**, 171103 (2022).

[87] G. Melani, Y. Nagata, J. Wirth, and P. Saalfrank, "Vibrational spectroscopy of hydroxylated α-Al_2O_3(0001) surfaces with and without water: An ab initio molecular dynamics study", *J. Chem. Phys.* **149**, 014707 (2018).

[88] G. Melani, Y. Nagata, and P. Saalfrank, "Vibrational energy relaxation of interfacial OH on a water-covered α-Al_2O_3(0001) surface: a non-equilibrium ab initio molecular dynamics study", *Phys. Chem. Chem. Phys.* **23**, 7714–7723 (2021).

[89] G. S. Parkinson, "Iron oxide surfaces", *Surf. Sci. Rep.* **71**, 272–365 (2016).

[90] K. Sivula, F. Le Formal, and M. Grätzel, "Solar water splitting: Progress using hematite (α-Fe_2O_3) photoelectrodes", *ChemSusChem* **4**, 432–449 (2011).

[91] O. Zandi and T. W. Hamann, "The potential versus current state of water splitting with hematite", *Phys. Chem. Chem. Phys.* **17**, 22485–22503 (2015).

[92] H. Wang, T. Chen, H. Liu, W. Li, X. Zou, C. Wang, and M. Li, "Comprehensive Application of Oolitic Hematite for H_2S Removal at High Temperature: Performance and Mechanism", *Energy and Fuels* **33**, 2037–2044 (2019).

[93] M. Albrecht, U. Rodemerck, M. Schneider, M. Bröring, D. Baabe, and E. V. Kondratenko, "Unexpectedly efficient CO_2 hydrogenation to higher hydrocarbons over non-doped Fe_2O_3", *Appl. Catal. B Environ.* **204**, 119–126 (2017).

[94] Q. Yang, V. A. Kondratenko, S. A. Petrov, D. E. Doronkin, E. Saraçi, H. Lund, A. Arinchtein, R. Kraehnert, A. S. Skrypnik, A. A. Matvienko, and E. V. Kondratenko, "Identifying Performance Descriptors in CO_2 Hydrogenation over Iron-Based Catalysts Promoted with Alkali Metals", *Angew. Chemie - Int. Ed.* **61**, e202116517 (2022).

[95] A. S. Skrypnik, S. A. Petrov, V. A. Kondratenko, Q. Yang, H. Lund, A. A. Matvienko, and E. V. Kondratenko, "Descriptors Affecting Methane Selectivity in CO_2 Hydrogenation over Unpromoted Bulk Iron(III)-Based Catalysts", *ACS Catal.* **12**, 11355–11368 (2022).

[96] Q. Yang, V. A. Kondratenko, A. S. Skrypnik, H. Lund, S. Bartling, J. Weiss, A. Brückner, and E. V. Kondratenko, "Understanding of the Fate of α-Fe_2O_3 in CO_2 Hydrogenation through Combined Time-Resolved In Situ Characterization and Microkinetic Analysis", *ACS Catal.* 9064–9077 (2023).

[97] P. Debiagi, R. C. Rocha, A. Scholtissek, J. Janicka, and C. Hasse, "Iron as a sustainable chemical carrier of renewable energy: Analysis of opportunities and challenges for retrofitting coal-fired power plants", *Renew. Sustain. Energy Rev.* **165**, 112579 (2022).

[98] M. L. Ali, Q. Fradet, and U. Riedel, "Kinetic Mechanism Development for the Direct Reduction of Single Hematite Pellets in H_2/CO Atmospheres", *steel Res. Int.* **93**, 2200043 (2022).

[99] A. Barbier, A. Stierle, N. Kasper, M. J. Guittet, and J. Jupille, "Surface termination of hematite at environmental oxygen pressures: Experimental surface phase diagram", *Phys. Rev. B* **75**, 233406 (2007).

[100] X. .-. Wang, W. Weiss, S. K. Shaikhutdinov, M. Ritter, M. Petersen, F. Wagner, R. Schlögl, and M. Scheffler, "The hematite (α-Fe_2O_3) (0001) surface: Evidence for domains of distinct chemistry", *Phys. Rev. Lett.* **81**, 1038–1041 (1998).

[101] A. Kiejna and T. Pabisiak, "Mixed termination of hematite (α-Fe_2O_3)(0001) surface", *J. Phys. Chem. C* **117**, 24339–24344 (2013).

[102] W. Bergermayer, H. Schweiger, and E. Wimmer, "Ab initio thermodynamics of oxide surfaces: O_2 on Fe_2O_3(0001)", *Phys. Rev. B* **69**, 1–12 (2004).

[103] M. T. Nguyen, N. Seriani, and R. Gebauer, "Water adsorption and dissociation on α-Fe_2O_3(0001): PBE+U calculations", *J. Chem. Phys.* **138**, 194709 (2013).

[104] R. Ovcharenko, E. Voloshina, and J. Sauer, "Water adsorption and O-defect formation on Fe_2O_3(0001) surfaces", *Phys. Chem. Chem. Phys.* **18**, 25560–25568 (2016).

[105] T. Pabisiak and A. Kiejna, "Fe adsorption on hematite (α-Fe_2O_3) (0001) and magnetite (Fe_3O_4) (111) surfaces", *J. Chem. Phys.* **141**, 134707 (2014).

[106] T. Stirner, D. Scholz, and J. Sun, "Ab initio simulation of structure and surface energy of low-index surfaces of stoichiometric α-Fe_2O_3", *Surf. Sci.* **671**, 11–16 (2018).

[107] J. Redondo, J. Michalička, F. Kraushofer, G. Franceschi, B. Šmid, N. Kumar, O. Man, M. Blatnik, D. Wrana, B. Mallada, M. Švec, G. S. Parkinson, M. Setvin, M. Riva, U. Diebold, and J. Čechal, "Hematite α-Fe_2O_3(0001) in Top and Side View: Resolving Long-Standing Controversies about Its Surface Structure", *Adv. Mater. Interfaces* **10**, 2300602 (2023).

[108] Y. Yang, H. Ma, J. Zhuang, and X. Wang, "Morphology-controlled synthesis of hematite nanocrystals and their facet effects on gas-sensing properties", *Inorg. Chem.* **50**, 10143–10151 (2011).

[109] X. Huang, X. Hou, X. Zhang, K. M. Rosso, and L. Zhang, "Facet-dependent contaminant removal properties of hematite nanocrystals and their environmental implications", *Environ. Sci. Nano* **5**, 1790–1806 (2018).

[110] Y. Guo, S. J. Clark, and J. Robertson, "Electronic and magnetic properties of Ti_2O_3, Cr_2O_3, and Fe_2O_3 calculated by the screened exchange hybrid density functional", *J. Phys. Condens. Matter* **24**, 325504 (2012).

[111] Z. D. Pozun and G. Henkelman, "Hybrid density functional theory band structure engineering in hematite", *J. Chem. Phys.* **134**, 224706 (2011).

[112] N. J. Mosey and E. A. Carter, "Ab initio evaluation of Coulomb and exchange parameters for DFT + U calculations", *Phys. Rev. B* **76**, 155123 (2007).

[113] A. Rohrbach, J. Hafner, and G. Kresse, "*Ab initio* study of the (0001) surfaces of hematite and chromia: influence of strong electronic correlations", *Phys. Rev. B* **70**, 1–17 (2004).

[114] S. L. Dudarev, A. I. Liechtenstein, M. R. Castell, G. A. D. Briggs, and A. P. Sutton, "Surface states on NiO (100) and the origin of the contrast reversal in atomically resolved scanning tunneling microscope images", *Phys. Rev. B* **56**, 4900 (1997).

[115] S. L. Dudarev, G. A. Botton, S. Y. Savrasov, C. J. Humphreys, and A. P. Sutton, "Electron-energy-loss spectra and the structural stability of nickel oxide: An LSDA + U study", *Phys. Rev. B* **57**, 1505 (1998).

[116] A. I. Liechtenstein, V. I. Anisimov, and J. Zaanen, "Density-functional theory and strong interactions: Orbital ordering in Mott-Hubbard insulators", *Phys. Rev. B* **52**, R5467 (1995).

[117] V. I. Anisimov, F. Aryasetiawan, and A. I. Lichtenstein, "First-principles calculations of the electronic structure and spectra of strongly correlated systems: the LDA + U method", *J. Phys. Condens. Matter* **9**, 767 (1997).

[118] R. B. Wang and A. Hellman, "Initial water adsorption on hematite (α-Fe_2O_3) (0001): A DFT + U study", *J. Chem. Phys.* **148**, 094705 (2018).

[119] M. Lewandowski, I. M. Groot, Z. H. Qin, T. Ossowski, T. Pabisiak, A. Kiejna, A. Pavlovska, S. Shaikhutdinov, H. J. Freund, and E. Bauer, "Nanoscale Patterns on Polar Oxide Surfaces", *Chem. Mater.* **28**, 7433–7443 (2016).

[120] T. Ossowski, T. Pabisiak, A. Kiejna, K. Palotás, and E. Bauer, "Simulation of STM Images of Hematite α-Fe_2O_3(0001) Surfaces: Dependence on Distance and Bias", *J. Phys. Chem. C* **125**, 26711–26717 (2021).

[121] C. Lemire, S. Bertarione, A. Zecchina, D. Scarano, A. Chaka, S. Shaikhutdinov, and H. J. Freund, "Ferryl (Fe=O) termination of the Hematite α-Fe_2O_3(0001) surface", *Phys. Rev. Lett.* **94**, 166101 (2005).

[122] M. Sterrer and H. J. Freund, "Towards realistic surface science models of heterogeneous catalysts: Influence of support hydroxylation and catalyst preparation method", *Catal. Letters* **143**, 375–385 (2013).

[123] S. Yamamoto, T. Kendelewicz, J. T. Newberg, G. Ketteler, D. E. Starr, E. R. Mysak, K. J. Andersson, H. Ogasawara, H. Bluhm, M. Salmeron, G. E. Brown, and A. Nilsson, "Water adsorption on α-Fe_2O_3 (0001) at near ambient conditions", *J. Phys. Chem. C* **114**, 2256–2266 (2010).

[124] L. Schöttner, R. Ovcharenko, A. Nefedov, E. Voloshina, Y. Wang, J. Sauer, and C. Wöll, "Interaction of Water Molecules with the α-Fe_2O_3(0001) Surface: A Combined Experimental and Computational Study", *J. Phys. Chem. C* **123**, 8324–8335 (2019).

[125] S. Yin, X. Ma, and D. E. Ellis, "Initial stages of H2O adsorption and hydroxylation of Fe-terminated α-Fe_2O_3(0001) surface", *Surf. Sci.* **601**, 2426–2437 (2007).

[126] S. M. Souvi, M. Badawi, J. F. Paul, S. Cristol, and L. Cantrel, "A DFT study of the hematite surface state in the presence of H_2, H_2O and O_2", *Surf. Sci.* **610**, 7–15 (2013).

[127] N. J. English, M. Rahman, N. Wadnerkar, and J. M. Macelroy, "Photo-active and dynamical properties of hematite (Fe_2O_3)-water interfaces: An experimental and theoretical study", *Phys. Chem. Chem. Phys.* **16**, 14445–14454 (2014).

[128] G. F. Von Rudorff, R. Jakobsen, K. M. Rosso, and J. Blumberger, "Hematite(001)-liquid water interface from hybrid density functional-based molecular dynamics", *J. Phys. Condens. Matter* **28**, 394001 (2016).

[129] T. P. Trainor, A. M. Chaka, P. J. Eng, M. Newville, G. A. Waychunas, J. G. Catalano, and G. E. Brown, "Structure and reactivity of the hydrated hematite (0001) surface", *Surf. Sci.* **573**, 204–224 (2004).

[130] T. Pabisiak and A. Kiejna, "Incipient adsorption of water and hydroxyl on hematite (0001) surface", *J. Phys. Commun.* **3**, 035023 (2019).

[131] P. Liao, J. A. Keith, and E. A. Carter, "Water oxidation on pure and doped hematite (0001) surfaces: Prediction of Co and Ni as effective dopants for electrocatalysis", *J. Am. Chem. Soc.* **134**, 13296–13309 (2012).

[132] A. Higareda, G. Rosas, R. Pérez, and R. Esparza, "Characterization and Electrocatalytic Features of PtPd and PdPt Bimetallic Nanoparticles for Methanol Electro–oxidation", *ChemNanoMat* **7**, 958–965 (2021).

[133] Y. Liu, M. Chi, V. Mazumder, K. L. More, S. Soled, J. D. Henao, and S. Sun, "Composition-Controlled Synthesis of Bimetallic PdPt Nanoparticles and Their Electro-oxidation of Methanol", *Chem. Mater.* **23**, 4199–4203 (2011).

[134] M. Kaneeda, H. Iizuka, T. Hiratsuka, N. Shinotsuka, and M. Arai, "Improvement of thermal stability of NO oxidation Pt/Al_2O_3 catalyst by addition of Pd", *Appl. Catal., B* **90**, 564–569 (2009).

[135] A. Morlang, U. Neuhausen, K. V. Klementiev, F.-W. Schütze, G. Miehe, H. Fuess, and E. S. Lox, "Bimetallic Pt/Pd diesel oxidation catalysts", *Appl. Catal., B* **60**, 191–199 (2005).

[136] A. Winkler, D. Ferri, and M. Aguirre, "The influence of chemical and thermal aging on the catalytic activity of a monolithic diesel oxidation catalyst", *Appl. Catal., B* **93**, 177–184 (2009).

[137] U. Hejral, P. N. Plessow, D. Franz, M. Shipilin, O. Gutowski, U. Rütt, H. Noei, V. Vonk, and A. Stierle, "Composition-Dependent Alloy Nanoparticle Shape Changes under Reaction Conditions: Kinetic and Thermodynamic Effects", *J. Phys. Chem. C* **128**, 4330–4342 (2024).

[138] J. C. Summers and L. L. Hegedus, "Effects of Platinum and Palladium Impregnation on the Performance and Durability of Automobile Exhaust Oxidizing Catalysts", *J. Catal.* **51**, 185–192 (1978).

[139] A. Russell and W. S. Epling, "Diesel Oxidation Catalysts", *Catal. Rev. Sci. Eng.* **53**, 337–423 (2011).

[140] F. Schüth, "Heterogene Katalyse. Schlüsseltechnologie der chemischen Industrie", *Chem. unserer Zeit* **40**, 92–103 (2006).

[141] H. Unterhalt, G. Rupprechter, and H.-J. Freund, "Vibrational Sum Frequency Spectroscopy on Pd(111) and Supported Pd Nanoparticles: CO Adsorption from Ultrahigh Vacuum to Atmospheric Pressure", *J. Phys. Chem. B* **106**, 356–367 (2002).

[142] Robert G. Greenler, R.K. Brandt, "The origins of multiple bands in the infrared spectra of carbon monoxide adsorbed on metal surfaces", *Colloids Surf., A* **1995**, 19–26 (1995).

[143] A. Schlapka, U. Käsberger, D. Menzel, and P. Jakob, "Vibrational spectroscopy of CO used as a local probe to study the surface morphology of Pt on Ru(001) in the submonolayer regime", *Surf. Sci.* **2002**, 129–135 (2002).

[144] B. E. Hayden and A. M. Bradshaw, "The adsorption of CO on Pt(111) studied by infrared reflection-absorption spectroscopy", *Surf. Sci.* **125**, 787–802 (1983).

[145] M. J. Hossain, M. M. Rahman, and M. Jafar Sharif, "Preference for low-coordination sites by adsorbed CO on small platinum nanoparticles", *Nanoscale Adv.* **2**, 1245–1252 (2020).

[146] K. Wolter, O. Seiferth, J. Libuda, H. Kuhlenbeck, M. Bäumer, and H.-J. Freund, "Infrared study of CO adsorption on alumina supported palladium particles", *Surf. Sci.* **402-404**, 428–432 (1998).

[147] I. V. Yudanov, R. Sahnoun, K. M. Neyman, N. Rösch, J. Hoffmann, S. Schauermann, V. Johánek, H. Unterhalt, G. Rupprechter, J. Libuda, and H.-J. Freund, "CO Adsorption on Pd Nanoparticles: Density Functional and Vibrational Spectroscopy Studies", *J. Phys. Chem. B* **107**, 255–264 (2003).

[148] F. M. Hoffmann, "Infrared Reflection-Absorption Spectroscopy of Adsorbed Molecules", *Surf. Sci. Rep.* **3**, 107–192 (1983).

[149] N. M. Martin, M. van den Bossche, H. Grönbeck, C. Hakanoglu, F. Zhang, T. Li, J. Gustafson, J. F. Weaver, and E. Lundgren, "CO Adsorption on Clean and Oxidized Pd(111)", *J. Phys. Chem. C* **118**, 1118–1128 (2014).

[150] M. Tüshaus, E. Schweizer, P. Hollins, and A. Bradshaw, "Yet another vibrat1onal study of the adsorption system Pt{111}-CO", *J. Electron. Spectrosc. Relat. Phenom.* **44**, 305–316 (1987).

[151] D. M. Haaland, "Infrared Studies of CO Adsorbed on Pt/Al_2O_3: Evidence for CO Bonded in 3-fold Coordination", *Surf. Sci.* **185**, 1–14 (1987).

[152] B. E. Hayden, K. Kretzschmar, A. M. Bradshaw, and R. G. Greenler, "An infrared study of the adsorption of CO on a stepped platinum surface", *Surface Science Letters* **149**, 394–406 (1985).

[153] J. Xu and Y. J. T. Jr., "Terrace width effect on adsorbate vibrations: a comparison of Pt(335) and Pt(112) for chemisorption of CO", *Surf. Sci.* **327**, 193–201 (1995).

[154] S. R. Bare, P. Hofmann, and D. A. King, "Vibrational studies of the surface phases of CO on Pt(110) at 300K", *Surf. Sci.* **144**, 347–369 (1984).

[155] H.-H. Krebs and H. Lüth, "Evidence for two different adsorption sites of CO on Pt(111) from infrared reflection spectroscopy", *App. Phys.* **14**, 337–342 (1977).

[156] R. G. Greenler, K. D. Burch, K. Kretzschmar, R. Klauser, A. M. Bradshaw, and B. E. Hayden, "Stepped single-crystal surfaces as models for small catalyst particles", *Surf. Sci.* **152-153**, 338–345 (1985).

[157] M. J. Kappers and J. H. van der Maas, "Correlation between CO frequency and Pt coordination number. A DRIFT study on supported Pt catalysts", *Catal. Lett.* **10**, 365–373 (1991).

[158] M. Casarin, C. Maccato, and A. Vittadini, "Theoretical study of the chemisorption of CO on $Al_2O_3(0001)$", *Inorg. Chem.* **39**, 5232–5237 (2000).

[159] A. Dianat, J. Zimmermann, N. Seriani, M. Bobeth, W. Pompe, and L. C. Ciacchi, "Ab initio study of element segregation and oxygen adsorption on PtPd and CoCr binary alloy surfaces", *Surf. Sci.* **602**, 876–884 (2008).

[160] L. C. A. van den Oetelaar, O. W. Nooij, S. Oerlemans, A. W. Denier van der Gon, and H. H. Brongersma, "Surface Segregation in Supported Pd-Pt Nanoclusters and Alloys", *J. Phys. Chem. B* **1998**, 3445–3455 (1998).

[161] Poul L. Hansen, Alfons M. Molenbroek, and Andrei V. Ruban, "Alloy Formation and Surface Segregation in Zeolite-Supported PdPt Bimetallic Catalysts", *J. Phys. Chem. B* **1997**, 1861–1868 (1996).

[162] Charles M. Grill, Mary L. McLaughlin, James M. Stevenson, and Richard D. Gonzalez, "Surface Characterization of Supported Pt-Pd Bimetallic Clusters Using Infrared Spectroscopy", *J. Catal.* **1981**, 454–464 (1981).

[163] Y. Wang and C. Wöll, "IR spectroscopic investigations of chemical and photochemical reactions on metal oxides: bridging the materials gap", *Chem. Soc. Rev.* **46**, 1875–1932 (2017).

[164] P. G. Lustemberg, C. Yang, Y. Wang, C. Wöll, and M. V. Ganduglia-Pirovano, "Vibrational frequencies of CO bound to all three low-index cerium oxide surfaces: A consistent theoretical description of vacancy-induced changes using density functional theory", *J. Chem. Phys.* **159**, 34704 (2023).

[165] S. Liu, Y. Li, X. Yu, S. Han, Y. Zhou, Y. Yang, H. Zhang, Z. Jiang, C. Zhu, W. X. Li, C. Wöll, Y. Wang, and W. Shen, "Tuning crystal-phase of bimetallic single-nanoparticle for catalytic hydrogenation", *Nat. Commun.* **13**, 4559 (2022).

[166] F. Maurer, J. Jelic, J. Wang, A. Gänzler, P. Dolcet, C. Wöll, Y. Wang, F. Studt, M. Casapu, and J. D. Grunwaldt, "Tracking the formation, fate and consequence for catalytic activity of Pt single sites on CeO2", *Nat. Catal.* **3**, 824–833 (2020).

[167] A. Chen, X. Yu, Y. Zhou, S. Miao, Y. Li, S. Kuld, J. Sehested, J. Liu, T. Aoki, S. Hong, M. F. Camellone, S. Fabris, J. Ning, C. Jin, C. Yang, A. Nefedov, C. Wöll, Y. Wang, and W. Shen, "Structure of the catalytically active copper–ceria interfacial perimeter", *Nat. Catal.* **2**, 334–341 (2019).

[168] C. Yang, M. Capdevila-Cortada, C. Dong, Y. Zhou, J. Wang, X. Yu, A. Nefedov, S. Heißler, N. López, W. Shen, C. Wöll, and Y. Wang, "Surface Refaceting Mechanism on Cubic Ceria", *J. Phys. Chem. Lett.* **11**, 7925–7931 (2020).

[169] C. Wöll, "Structure and chemical properties of oxide nanoparticles determined by surface-ligand ir spectroscopy", *ACS Catal.* **10**, 168–176 (2020).

[170] Y. Q. Su, J. X. Liu, I. A. Filot, and E. J. Hensen, "Theoretical Study of Ripening Mechanisms of Pd Clusters on Ceria", *Chem. Mater.* **29**, 9456–9462 (2017).

[171] X. Wang, J. A. Van Bokhoven, and D. Palagin, "Ostwald ripening versus single atom trapping: Towards understanding platinum particle sintering", *Phys. Chem. Chem. Phys.* **19**, 30513–30519 (2017).

[172] M. C. Valero, P. Raybaud, and P. Sautet, "Influence of the hydroxylation of γ-Al2O3 surfaces on the stability and diffusion of single Pd atoms: A DFT study", *J. Phys. Chem. B* **110**, 1759–1767 (2006).

[173] J. R. Gomes, F. Illas, N. Cruz Hernández, A. Márquez, and J. F. Sanz, "Interaction of Pd with α-Al_2O_3(0001): A case study of modeling the metal-oxide interface on complex substrates", *Phys. Rev. B* **65**, 125414 (2002).

[174] Z. Łodziana, J. K. Nørskov, and P. Stoltze, "The stability of the hydroxylated (0001) surface of α-Al_2O_3", *J. Chem. Phys.* **118**, 11179 (2003).

[175] Z. W. Seh, J. Kibsgaard, C. F. Dickens, I. Chorkendorff, J. K. Nørskov, and T. F. Jaramillo, "Combining theory and experiment in electrocatalysis: Insights into materials design", *Science* **355**, eaad4998 (2017).

[176] C. Y. Wu, W. J. Wolf, Y. Levartovsky, H. A. Bechtel, M. C. Martin, F. D. Toste, and E. Gross, "High-spatial-resolution mapping of catalytic reactions on single particles", *Nature* **541**, 511–515 (2017).

[177] W. Yuan, B. Zhu, X. Y. Li, T. W. Hansen, Y. Ou, K. Fang, H. Yang, Z. Zhang, J. B. Wagner, Y. Gao, and Y. Wang, "Visualizing H2O molecules reacting at TiO_2 active sites with transmission electron microscopy", *Science* **367**, 428–430 (2020).

[178] W. Yuan, B. Zhu, K. Fang, X. Y. Li, T. W. Hansen, Y. Ou, H. Yang, J. B. Wagner, Y. Gao, Y. Wang, Z. Zhang, T. W. Hansen, and J. B. Wagner, "In situ manipulation of the active Au-TiO_2interface with atomic precision during CO oxidation", *Science* **371**, 517–521 (2021).

[179] D. Jiang, G. Wan, J. Halldin Stenlid, C. E. García-Vargas, J. Zhang, C. Sun, J. Li, F. Abild-Pedersen, C. J. Tassone, and Y. Wang, "Dynamic and reversible transformations of subnanometre-sized palladium on ceria for efficient methane removal", *Nat. Catal.* **6**, 618–627 (2023).

[180] H. Frey, A. Beck, X. Huang, J. A. van Bokhoven, and M. G. Willinger, "Dynamic interplay between metal nanoparticles and oxide support under redox conditions", *Science* **376**, 982–987 (2022).

[181] S. B. Vendelbo, C. F. Elkjær, H. Falsig, I. Puspitasari, P. Dona, L. Mele, B. Morana, B. J. Nelissen, R. Van Rijn, J. F. Creemer, P. J. Kooyman, and S. Helveg, "Visualization of oscillatory behaviour of Pt nanoparticles catalysing CO oxidation", *Nat. Mater.* **13**, 884–890 (2014).

[182] X. Y. Li, P. Ou, X. Duan, L. Ying, J. Meng, B. Zhu, and Y. Gao, "Dynamic Active Sites In Situ Formed in Metal Nanoparticle Reshaping under Reaction Conditions", *JACS Au* **4**, 1892–1900 (2024).

[183] Z. Duan and G. Wang, "Monte Carlo simulation of surface segregation phenomena in extended and nanoparticle surfaces of Pt-Pd alloys", *J. Phys. Condens. Matter* **23**, 475301 (2011).

[184] G. Bozzolo, R. D. Noebe, J. Khalil, and J. Morse, "Atomistic analysis of surface segregation in ni–pd alloys", *Appl. surf. sci.* **219**, Proceedings of Applied surface modeling: Experiment, Theory and Simulations, 149–157 (2003).

[185] S. Helfensteyn, J. Luyten, L. Feyaerts, and C. Creemers, "Modelling surface phenomena in pd-ni alloys", *Appl. surf. sci.* **212-213**, 11th International Conference on Solid Films and Surfaces, 844–849 (2003).

[186] L. V. Pourovskii, I. A. Abrikosov, Y. K. Vekilov, A. V. Ruban, and B. Johansson, "Bulk ordering and surface segregation in $Ni_{50}Pt_{50}$", *Phys. Rev. B* **64**, 035421 (2001).

[187] L. Li, X. Li, Z. Duan, R. J. Meyer, R. Carr, S. Raman, L. Koziol, and G. Henkelman, "Adaptive kinetic Monte Carlo simulations of surface segregation in PdAu nanoparticles", *Nanoscale* **11**, 10524–10535 (2019).

[188] H. Noh, T. B. Flanagan, and Y. Sakamoto, "Hydrogen-induced segregation in PdPt alloys", *J. Alloys Compd.* **231**, 10–14 (1995).

[189] M. Zhao, J. C. Brouwer, W. G. Sloof, and A. J. Böttger, "Surface segregation of Pd–Cu alloy in various gas atmospheres", *Int. J. Hydrogen Energy* **45**, 21567–21572 (2020).

[190] V. L. Deringer, A. P. Bartók, N. Bernstein, D. M. Wilkins, M. Ceriotti, and G. Csányi, "Gaussian Process Regression for Materials and Molecules", *Chem. Rev.* **121**, 10073–10141 (2021).

[191] E. Bélisle, Z. Huang, and A. Gheribi, "Scalable gaussian process regression for prediction of material properties", in Databases theory and applications, edited by H. Wang and M. A. Sharaf (2014), pp. 38–49.

[192] L. Parussini, D. Venturi, P. Perdikaris, and G. E. Karniadakis, "Multi-fidelity Gaussian process regression for prediction of random fields", *J. Comput. Phys.* **336**, 36–50 (2017).

[193] G. Schmitz and O. Christiansen, "Gaussian process regression to accelerate geometry optimizations relying on numerical differentiation", *J. Chem. Phys.* **148**, 241704 (2018).

[194] C. J. Moore, A. J. Chua, C. P. Berry, and J. R. Gair, "Fast methods for training Gaussian processes on large datasets", *R. Soc. Open Sci.* **3**, 160125 (2016).

[195] D. M. Ceperley and B. J. Alder, "Ground State of the Electron Gas by a Stochastic Method", *Phys. Rev. Lett.* **45**, 566 (1980).

[196] A. D. Becke, "Density-functional exchange-energy approximation with correct asymptotic behavior", *Phys. Rev. A* **38**, 3098 (1988).

[197] C. Lee, W. Yang, and R. G. Parr, "Development of the Colle-Salvetti correlation-energy formula into a functional of the electron density", *Phys. Rev. B* **37**, 785 (1988).

[198] J. P. Perdew, J. A. Chevary, S. H. Vosko, K. A. Jackson, M. R. Pederson, D. J. Singh, and C. Fiolhais, "Atoms, molecules, solids, and surfaces: Applications of the generalized gradient approximation for exchange and correlation", *Phys. Rev. B* **46**, 6671 (1992).

[199] J. P. Perdew, K. Burke, and M. Ernzerhof, "Generalized Gradient Approximation Made Simple", *Phys. Rev. Lett.* **77**, 3865 (1996).

[200] J. J. Mortensen, K. Kaasbjerg, S. L. Frederiksen, J. K. Nørskov, J. P. Sethna, and K. W. Jacobsen, "Bayesian error estimation in density-functional theory", *Phys. Rev. Lett.* **95**, 216401 (2005).

[201] J. Wellendorff, K. T. Lundgaard, A. Møgelhøj, V. Petzold, D. D. Landis, J. K. Nørskov, T. Bligaard, and K. W. Jacobsen, "Density functionals for surface science: Exchange-correlation model development with Bayesian error estimation", *Phys. Rev. B* **85**, 235149 (2012).

[202] P. J. Stephens, F. J. Devlin, C. F. Chabalowski, and M. J. Frisch, "Ab Initio calculation of vibrational absorption and circular dichroism spectra using density functional force fields", *J. Phys. Chem.* **98**, 11623–11627 (1994).

[203] J. Heyd, G. E. Scuseria, and M. Ernzerhof, "Hybrid functionals based on a screened Coulomb potential", *J. Chem. Phys.* **118**, 8207–8215 (2003).

[204] J. Heyd and G. E. Scuseria, "Efficient hybrid density functional calculations in solids: Assessment of the Heyd–Scuseria–Ernzerhof screened Coulomb hybrid functional", *J. Chem. Phys.* **121**, 1187–1192 (2004).

[205] J. Heyd, G. E. Scuseria, and M. Ernzerhof, "Erratum: Hybrid functionals based on a screened Coulomb potential (Journal of Chemical Physics (2003) 118 (8207))", *J. Chem. Phys.* **124**, 219906 (2006).

[206] A. V. Krukau, O. A. Vydrov, A. F. Izmaylov, and G. E. Scuseria, "Influence of the exchange screening parameter on the performance of screened hybrid functionals", *J. Chem. Phys.* **125**, 224106 (2006).

[207] A. Tkatchenko and M. Scheffler, "Accurate molecular van der Waals interactions from ground-state electron density and free-atom reference data", *Phys. Rev. Lett.* **102**, 073005 (2009).

[208] A. D. Becke and E. R. Johnson, "Exchange-hole dipole moment and the dispersion interaction revisited", *J. Chem. Phys.* **127**, 154108 (2007).

[209] O. A. Vydrov and T. Van Voorhis, "Nonlocal van der Waals density functional: The simpler the better", *J. Chem. Phys.* **133**, 244103 (2010).

[210] S. Grimme, "Accurate description of van der Waals complexes by density functional theory including empirical corrections", *J. Comput. Chem.* **25**, 1463–1473 (2004).

[211] S. Grimme, "Semiempirical GGA-type density functional constructed with a long-range dispersion correction", *J. Comput. Chem.* **27**, 1787–1799 (2006).

[212] S. Grimme, J. Antony, S. Ehrlich, and H. Krieg, "A consistent and accurate *ab initio* parametrization of density functional dispersion correction (DFT-D) for the 94 elements H-Pu", *J. Chem. Phys.* **132**, 154104 (2010).

[213] E. Caldeweyher, C. Bannwarth, and S. Grimme, "Extension of the D3 dispersion coefficient model", *J. Chem. Phys.* **147**, 34112 (2017).

[214] V. I. Anisimov, J. Zaanen, and O. K. Andersen, "Band theory and Mott insulators: Hubbard U instead of Stoner I", *Phys. Rev. B* **44**, 943 (1991).

[215] H. Jónsson, G. Mills, and K. W. Jacobsen, "Nudged elastic band method for finding minimum energy paths of transitions", in Proceedings of the international conference on classical and quantum dynamics in condensed phase simulations (1998), pp. 385–404.

[216] G. Mills and H. Jónsson, "Quantum and thermal effects in H2 dissociative adsorption: Evaluation of free energy barriers in multidimensional quantum systems", *Phys. Rev. Lett.* **72**, 1124–1127 (1994).

[217] G. Mills, H. Jónsson, and G. K. Schenter, "Reversible work transition state theory: application to dissociative adsorption of hydrogen", *Surf. Sci.* **324**, 305–337 (1995).

[218] G. Henkelman and H. Jónsson, "Improved tangent estimate in the nudged elastic band method for finding minimum energy paths and saddle points", *J. Chem. Phys.* **113**, 9978 (2000).

[219] G. Henkelman and H. Jónsson, "A dimer method for finding saddle points on high dimensional potential surfaces using only first derivatives", *J. Chem. Phys.* **111**, 7010 (1999).

[220] J. Rogal and K. Reuter, *Ab initio atomistic thermodynamics for surfaces: a primer*, tech. rep. EN-AVT-142-02 (Defense Technical Information Center, Fritz-Haber-Institut der Max-Planck-Gesellschaft Faradayweg 4-6 D-14195 Berlin Germany, 2006).

[221] K. Reuter and M. Scheffler, "Composition, structure, and stability of RuO2(110) as a function of oxygen pressure", *Phys. Rev. B* **65**, 035406 (2002).

[222] J. Chen, D. Sharapa, and P. N. Plessow, "Stability and formation of hydroxylated α-Al_2O_3(0001) surfaces at high temperatures", *Phys. Rev. Res.* **4**, 013232 (2022).

[223] J. Chen, D. I. Sharapa, and P. N. Plessow, "Stability of Hydroxylated α-Fe_2O_3(0001) Surfaces", *ACS Omega* **9**, 35449–35457 (2024).

[224] G. Kresse and D. Joubert, "From ultrasoft pseudopotentials to the projector augmented-wave method", *Phys. Rev. B* **59**, 1758 (1999).

[225] G. Kresse and J. Furthmüller, "Efficient iterative schemes for *ab initio* total-energy calculations using a plane-wave basis set", *Phys. Rev. B* **54**, 11169 (1996).

[226] J. Sun, A. Ruzsinszky, and J. P. Perdew, "Strongly Constrained and Appropriately Normed Semilocal Density Functional", *Phys. Rev. Lett.* **115**, 036402 (2015).

[227] A. Rohrbach, J. Hafner, and G. Kresse, "Electronic correlation effects in transition-metal sulfides", *J. Phys. Condens. Matter* **15**, 979–996 (2003).

[228] M. Cococcioni and S. de Gironcoli, "Linear response approach to the calculation of the effective interaction parameters in the LDA+U method", *Phys. Rev. B* **71**, 035105 (2005).

[229] X. Huang, S. K. Ramadugu, and S. E. Mason, "Surface-Specific DFT + U Approach Applied to α-Fe_2O_3(0001)", *J. Phys. Chem. C* **120**, 4919–4930 (2016).

[230] Y. Meng, X. W. Liu, C. F. Huo, W. P. Guo, D. B. Cao, Q. Peng, A. Dearden, X. Gonze, Y. Yang, J. Wang, H. Jiao, Y. Li, and X. D. Wen, "When Density Functional Approximations Meet Iron Oxides", *J. Chem. Theory Comput.* **12**, 5132–5144 (2016).

[231] L. Schöttner, R. Ovcharenko, A. Nefedov, E. Voloshina, Y. Wang, J. Sauer, and C. Wöll, "Interaction of water molecules with the α-Fe2O3(0001) surface: a combined experimental and computational study", *J. Phys. Chem. C* **123**, 8324–8335 (2019).

[232] R. B. Wang and A. Hellman, "Surface terminations of hematite (alpha-fe(2)o(3)) exposed to oxygen, hydrogen, or water: dependence on the density functional theory methodology", *J. Phys. Condens. Matter.* **30**, 275002 (2018).

[233] B. Ruscic and D. H. Bross, *Active thermochemical tables (atct) values based on ver. 1.122 of the thermochemical network*, (2016) `http://ATcT.anl.gov`.

[234] G. Rollmann, A. Rohrbach, P. Entel, and J. Hafner, "First-principles calculation of the structure and magnetic phases of hematite", *Phys. Rev. B* **69**, 1–12 (2004).

[235] L. W. Finger and R. M. Hazen, "Crystal structure and isothermal compression of Fe_2O_3, Cr_2O_3, and V_2O_3 to 50 kbars", *J. Appl. Phys.* **51**, 5362 (1980).

[236] P. N. Plessow, "Efficient Transition State Optimization of Periodic Structures through Automated Relaxed Potential Energy Surface Scans", *J. Chem. Theory Comput.* **14**, 981–990 (2018).

[237] I. Batyrev, A. Alavi, and M. W. Finnis, "*Ab initio* calculations on the al_2o_3(0001) surface", *Faraday Discuss.* **114**, 33–43 (1999).

[238] P. Guénard, G. Renaud, A. Barbier, and M. Gautier-Soyer, "Determination of the α-Al_2O_3(0001) surface relaxation and termination by measurements of crystal truncation rods", *Surf. Rev. Lett.* **5**, 321–324 (1998).

[239] G. Renaud, "Oxide surfaces and metal/oxide interfaces studied by grazing incidence X-ray scattering", *Surf. Sci. Rep.* **32**, 5–90 (1998).

[240] M. Dellostritto and J. Sofo, "Bond Polarizability Model for Sum Frequency Generation at the Al_2O_3(0001)-H_2O Interface", *J. Phys. Chem. A* **121**, 3045–3055 (2017).

[241] P. Huang, T. A. Pham, G. Galli, and E. Schwegler, "Alumina(0001)/Water Interface: Structural Properties and Infrared Spectra from First-Principles Molecular Dynamics Simulations", *J. Phys. Chem. C* **118**, 8944–8951 (2014).

[242] Y. Tong, J. Wirth, H. Kirsch, M. Wolf, P. Saalfrank, and R. K. Campen, "Optically probing Al—O and O—H vibrations to characterize water adsorption and surface reconstruction on α-alumina: An experimental and theoretical study", *J. Chem. Phys.* **142**, 054704 (2015).

[243] A. Sagara, H. Yabe, X. Chen, Y. Onabuta, S. Wang, M.-P. Gaigeot, M. Sprik, and M. Sulpizi, "Oxide/water interfaces: how the surface chemistry modifies interfacial water properties", *J. Phys. Condens. Matter* **24**, 124106 (2012).

[244] P. S. P. Wei and A. W. Smith, "Structure of the (0001) Surface of α-Alumina", *J. Vac. Sci. Technol.* **9**, 1209–1213 (1972).

[245] J. Guo, D. E. Ellis, and D. J. Lam, "Electronic structure and energetics of sapphire (0001) and (11-02) surfaces", *Phys. Rev. B* **45**, 13647–13656 (1992).

[246] E. Wasserman, J. R. Rustad, A. R. Felmy, B. P. Hay, and J. W. Halley, "Ewald methods for polarizable surfaces with application to hydroxylation and hydrogen bonding on the (012) and (001) surfaces of α-Fe_2O_3", *Surf. Sci.* **385**, 217–239 (1997).

[247] M. Lübbe and W. Moritz, "A LEED analysis of the clean surfaces of α-Fe_2O_3(0001) and α-Cr_2O_3(0001) bulk single crystals", *J. Phys. Condens. Matter* **21**, 134010 (2009).

[248] E. Krén, P. Szabó, and G. Konczos, "Neutron diffraction studies on the (1-x) Fe_2O_3 - xRh_2O_3 system", *Phys. Lett.* **19**, 103–104 (1965).

[249] J. M. Coey and G. A. Sawatzky, "A study of hyperfine interactions in the system $(Fe_{1-x}Rh_x)_2O_3$ using the Mossbauer effect (Bonding parameters)", *J. Phys. C Solid State Phys.* **4**, 2386 (1971).

[250] P. Liu, T. Kendelewicz, G. E. Brown, E. J. Nelson, and S. A. Chambers, "Reaction of water vapor with α-Al_2O_3(0001) and α-Fe_2O_3(0001) surfaces: synchrotron X-ray photoemission studies and thermodynamic calculations", *Surf. Sci.* **417**, 53–65 (1998).

[251] R. L. Kurtz and V. E. Henrich, "Surface electronic structure and chemisorption on corundum transition-metal oxides: α- Fe_2O_3", *Phys. Rev. B* **36**, 3413 (1987).

[252] A. Hellman and R. G. Pala, "First-Principles Study of Photoinduced Water-Splitting on Fe_2O_3", *J. Phys. Chem. C* **115**, 12901–12907 (2011).

[253] S. E. Mason, C. R. Iceman, K. S. Tanwar, T. P. Trainor, and A. M. Chaka, "Pb(II) adsorption on isostructural hydrated alumina and hematite (0001) surfaces: A DFT Study", *J. Phys. Chem. C* **113**, 2159–2170 (2009).

[254] T. P. Goumans, A. Wander, W. A. Brown, and C. R. A. Catlow, "Structure and stability of the (001) α-quartz surface", *Phys. Chem. Chem. Phys.* **9**, 2146–2152 (2007).

[255] P. N. Plessow, R. S. Sánchez-Carrera, L. Li, M. Rieger, S. Sauer, A. Schaefer, and F. Abild-Pedersen, "Modeling the Interface of Platinum and α-Quartz(001): Implications for Sintering", *J. Phys. Chem. C* **120**, 10340–10350 (2016).

[256] D. R. Lide, ed., *Crc handbook of chemistry and physics*, 85th ed. (CRC Press, 2004).

[257] G. Kresse and J. Furthmüller, "Efficiency of ab-initio total energy calculations for metals and semiconductors using a plane-wave basis set", *Computational Materials Science* **6**, 15–50 (1996).

[258] A. H. Larsen, J. J. Mortensen, J. Blomqvist, I. E. Castelli, R. Christensen, M. Dułak, J. Friis, M. N. Groves, B. Hammer, C. Hargus, E. D. Hermes, P. C. Jennings, P. B. Jensen, J. Kermode, J. R. Kitchin, E. L. Kolsbjerg, J. Kubal, K. Kaasbjerg, S. Lysgaard, J. B. Maronsson, T. Maxson, T. Olsen, L. Pastewka, A. Peterson, C. Rostgaard, J. Schiøtz, O. Schütt, M. Strange, K. S. Thygesen, T. Vegge, L. Vilhelmsen, M. Walter, Z. Zeng, and K. W. Jacobsen, "The atomic simulation environment—a python library for working with atoms", *Journal of Physics: Condensed Matter* **29**, 273002 (2017).

[259] P. E. Blöchl, "Projector augmented-wave method", *Phys. Rev. B* **50**, 17953–17979 (1994).

[260] G. A. Mekhemer and M. I. Zaki, "Low-temperature IR spectroscopy of CO adsorption on calcined supported CeO_2: probing adsorbed species and adsorbing sites", *Adsorpt. Sci. Technol.* **15**, 377–389 (1997).

[261] D. S. Dolling, J. Chen, J.-C. Schober, M. Creutzburg, A. Jeromin, V. Vonk, D. I. Sharapa, T. F. Keller, P. N. Plessow, H. Noei, and A. Stierle, "Probing Active Sites on Pd/Pt Alloy Nanoparticles by CO Adsorption", *ACS Nano*, `10.1021/acsnano.4c08291` (2024).

[262] A. Trovarelli and J. Llorca, "Ceria Catalysts at Nanoscale: How Do Crystal Shapes Shape Catalysis?", *ACS Catal.* **7**, 4716–4735 (2017).

[263] Z. Yang, Z. Lu, and G. Luo, "First-principles study of the Pt/CeO_2 (111) interface", *Phys. Rev. B* **76**, 075421 (2007).

[264] E. A. Kümmerle and G. Heger, "The Structures of C-$Ce_2O_3+\delta$, Ce_7O_{12}, and $Ce_{11}O_{20}$", *J. Solid State Chem.* **147**, 485–500 (1999).

[265] W. Yu, M. D. Porosoff, and J. G. Chen, "Review of Pt-based bimetallic catalysis: From model surfaces to supported catalysts", *Chem. Rev.* **112**, 5780–5817 (2012).

[266] J. M. Sanchez, "Cluster expansion and the configurational theory of alloys", *Phys. Rev. B* **81**, 224202 (2010).

[267] Q. Wu, B. He, T. Song, J. Gao, and S. Shi, "Cluster expansion method and its application in computational materials science", *Comput. Mater. Sci.* **125**, 243–254 (2016).

[268] M. Y. Lavrentiev, D. Nguyen-Manh, and S. L. Dudarev, "Cluster expansion models for Fe-Cr alloys, the prototype materials for a fusion power plant", *Comput. Mater. Sci.* **49**, S199–S203 (2010).

[269] S. Kadkhodaei and J. A. Muñoz, "Cluster Expansion of Alloy Theory: A Review of Historical Development and Modern Innovations", *JOM 2021 7311* **73**, 3326–3346 (2021).

[270] J. M. Sanchez, "Cluster expansions and the configurational energy of alloys", *Phys. Rev. B* **48**, 14013–14015 (1993).

[271] L. Cao, C. Li, and T. Mueller, "The Use of Cluster Expansions to Predict the Structures and Properties of Surfaces and Nanostructured Materials", *J. Chem. Inf. Model.* **58**, 2401–2413 (2018).

[272] R. Drautz, "Atomic cluster expansion for accurate and transferable interatomic potentials", *Phys. Rev. B* **99**, 14104 (2019).

[273] T. Rehman, M. Jaipal, and A. Chatterjee, "A cluster expansion model for predicting activation barrier of atomic processes", *J. Comput. Phys.* **243**, 244–259 (2013).

[274] L. Semidey-Flecha and D. S. Sholl, "Combining density functional theory and cluster expansion methods to predict H2 permeance through Pd-based binary alloy membranes", *J. Chem. Phys.* **128**, 144701 (2008).

[275] Z. Zhu, Z. Ji, X. Fan, and J. L. Kuo, "Memetic figure selection for cluster expansion in binary alloy systems", in Ieee ssci 2011 - symp. ser. comput. intell. - mc 2011 2011 ieee work. memetic comput. (2011), pp. 15–20.

[276] J. Z. Xie, X. Y. Zhou, and H. Jiang, "Perspective on optimal strategies of building cluster expansion models for configurationally disordered materials", *J. Chem. Phys.* **157**, 200901 (2022).

[277] P. J. Feibelman, B. Hammer, J. K. Norskov, F. Wagner, M. Scheffler, R. Stump, R. Watwe, and J. Dumesic, "The CO/Pt(111) Puzzle†", *J. Phys. Chem. B* **105**, 4018–4025 (2000).

[278] L. Schimka, J. Harl, A. Stroppa, A. Grüneis, M. Marsman, F. Mittendorfer, and G. Kresse, "Accurate surface and adsorption energies from many-body perturbation theory", *Nat. Mater.* **9**, 741–744 (2010).

[279] L. P. Granda-Marulanda, A. Rendón-Calle, S. Builes, F. Illas, M. T. M. Koper, and F. Calle-Vallejo, "A semiempirical method to detect and correct dft-based gas-phase errors and its application in electrocatalysis", *ACS Catal.* **10**, 6900–6907 (2020).

[280] M. E. Harding, J. Vázquez, B. Ruscic, A. K. Wilson, J. Gauss, and J. F. Stanton, "High-accuracy extrapolated ab initio thermochemistry. III. Additional improvements and overview", *J. Chem. Phys.* **128**, 114111 (2008).

[281] D. R. Stull and H. Prophet, *Janaf thermochemical tables*, 2nd (U.S. National Bureau of Standards, Washington, DC, 1971).

Appendix

A. Stability and formation of hydroxylated α-Al_2O_3(0001) surfaces at high temperatures

A.1. Stability of surfaces

Table A.1 lists the stability of all investigated surfaces, which are all shown schematically in Fig. A.1. As an additional test for the stability of the isolated $Al(OH)_3$ groups, an MD simulation was run for the (2×2)-cell with $\theta[Al(OH)_3]$=1/4. Using a reduced k-point sampling (1×1) and a timestep of 0.5 fs, the MD simulation was run for 15,082 steps (7.5 ps) at an average temperature of 1000 K, which was controlled with the Andersen thermostat (collision probability 0.02). Visual inspection of the trajectory showed no reconstruction and optimization of the final structure gave the identical minimum structure, from which the MD was started.

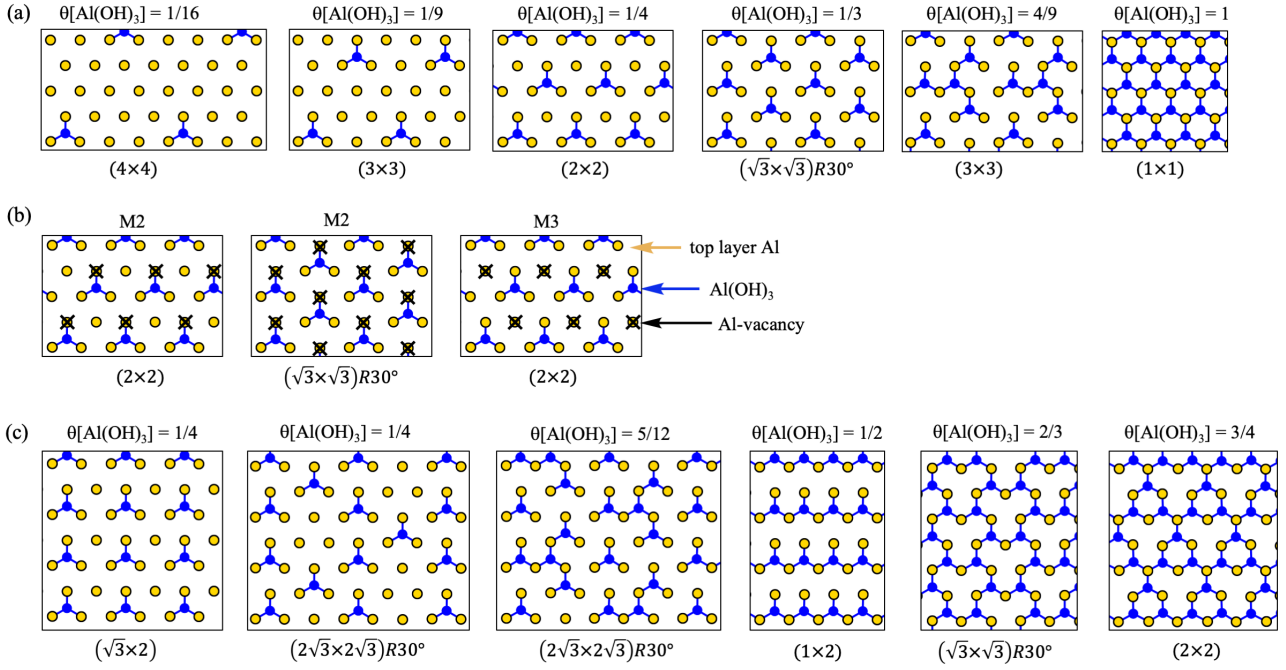

Figure A.1: Schematic representation of all computed structures and specification of the employed unit cell. (a) Structures are also shown in the main text (b) Metastabile structures M2, and M3 as well as an analogous M2 structure with higher concentration of the reconstruction. (c) Additional structures not explicitly discussed in the main text.

Table A.1.: Overview over all computed terminations of the α-Al_2O_3(0001) surface. In addition to the surfaces given in Table 1, which are repeated here, additional investigated surfaces are also listed. The composition is specified in terms of the coverage of H_2O and $Al(OH)_3$ adsorbates relative to the dry surface. The formation energy is given per two OH groups in eV relative to the dry surface and ΔE_{form} is thus equal to the chemical potential μ_{H_2O} at which the surface free energy is identical to that of the stoichiometric surface, see Eq. 1. Additionally, the concentration of hydroxyl groups per surface area, the unit cell and the employed k-point sampling are specified

	coverage (θ)		ΔE_{form} per 2OH (eV)				n(OH)		
Surface	$Al(OH)_3$	H_2O	PBE-D3	BEEF-vDW[a]	SCAN[a]	HSE06[a]	(1/nm^2)	unit cell	k-points
dry/clean	0	0	0	0	0	0	0	[b]	[b]
$\theta[Al(OH)_3]$=1/16	1/16	0	-2.80	-2.75	-2.98	-2.76	0.9	(4×4)	1×1
$\theta[Al(OH)_3]$=1/9	1/9	0	-2.80	-2.75	-2.96	-2.74	1.7	(3×3)	2×2[c]
$\theta[Al(OH)_3]$=1/4	1/4	0	-2.73	-2.70	-2.89	-2.67	3.8	(2×2)	2×2
$\theta[Al(OH)_3]$=1/3	1/3	0	-2.66	-2.66	-2.81	-2.58	5.0	$(\sqrt{3}\times\sqrt{3})R30°$	4×4[c]
$\theta[Al(OH)_3]$=4/9	4/9	0	-2.37	-2.30	-2.51	-2.28	6.7	(3×3)	2×2[c]
$\theta[Al(OH)_3]$=1	1	0	-1.72	-1.44	-1.87	-1.56	15.1	(1×1)	4×4
$\theta[Al(OH)_3]$=1; $\theta[H_2O]$=2	1	2	-1.17	-0.93	-1.21	-0.99	35.3	(1×2)	4×2
M1	0	1	-1.64	-1.57	-1.71	-1.52	10.1	(1×1)	4×4
M2	0	3/4	-1.88	-1.73	-2.00	-1.77	7.6	(2×2)	2×2
M3	0	3/4	-2.15	-2.01	-2.31	-2.04	7.6	(2×2)	2×2
$\theta[Al(OH)_3]$=1/4 (iso)	1/4	0	-2.71	-2.69	-2.87	-2.64	3.8	$(2\sqrt{3}\times2\sqrt{3})R30°$	2×2[c]
$\theta[Al(OH)_3]$=1/4 (iso)	1/4	0	-2.72	-2.69	-2.86	-2.65	3.8	$(\sqrt{3}\times2)$	2×2[c]
$\theta[Al(OH)_3]$=5/12	5/12	0	-2.42	-2.38	-2.57	-2.33	6.3	$(2\sqrt{3}\times2\sqrt{3})R30°$	2×2[c]
$\theta[Al(OH)_3]$=1/2	1/2	0	-2.15	-2.05	-2.31	-2.06	7.6	(1×2)	4×2
$\theta[Al(OH)_3]$=2/3	2/3	0	-1.93	-1.79	-2.05	-1.80	10.1	$(\sqrt{3}\times\sqrt{3})R30°$	4×4[c]
$\theta[Al(OH)_3]$=3/4	3/4	0	-1.88	-1.68	-2.01	-1.74	11.3	(2×2)	2×2
M2	0	1	-1.84	-1.71	-1.96	-1.72	10.1	$(\sqrt{3}\times\sqrt{3})R30°$	4×4[c]

[a] Single point calculation with the PBE-D3 structure. [b] The dry surface serves as the reference and was always computed with the same unit cell and k-point sampling as the hydroxylated surfaces. [c] For HSE06, the k-point sampling in each dimension was reduced by a factor of 2.

$$\gamma = \frac{E^{\text{slab}} - E^{\text{slab}}_{\text{dry}} - \frac{n}{2}E^{\text{bulk}}_{Al_2O_3} - \frac{m}{2}E^{\text{gas}}_{H_2O}}{\frac{m}{2}A} \times A_{1\times1} \quad (1)$$

Here, E^{slab} and $E^{\text{slab}}_{\text{dry}}$ are the energies of the slab models of the considered surface and of the dry surface with identical surface area A, $E^{\text{bulk}}_{Al_2O_3}$ is the energy per formula unit of bulk α-Al_2O_3. The surface area per (1×1) cell is $A_{1\times1} = 19.845$ Å^2. $E^{\text{bulk}}_{Al_2O_3}$ is the energy per bulk formula unit. $E^{\text{gas}}_{H_2O}$ is the energy of wate The stoichiometry coefficients n and m are determined by the amount of additional Al and H atoms on the surface with respect to the dry surface.

A.2. Investigated reaction paths

Figure A.2 shows the structures for the free energy diagram in Fig. 3.11 of the main text and also introduces the labels A1, A2, etc. that are used in Table A.2, where the data shown in Fig. 3.11 is provided. For TS(A1-A2), two transition states are listed in Table A.2, one is catalyzed by an additional water molecule (proton-shuttle). This leads to a dependence of the barrier on the chemical potential of water, as can be seen in Fig. A.2. In the same manner, Fig. A.3 shows the structures for Fig. 3.13, which are labeled C0, C1, etc. C0 refers to a structure with desorbed water, which was not included in Fig. 3.12b. The three minima and two transition states in Fig. 3.12 are labeled consecutively B1, B2, B3 and TS(B1-B2) and TS(B2-B3) in Tables A.2 and A.4. The barrier for water dissociation on the clean surface has been investigated for a few cases, such as the first and fourth water dissociation required to form structure A1 in Fig. A.2 and for the formation of C1. In all of these cases, the barrier was below 0.5 eV, which is in agreement with previous investigations in the literature.

Figure A.4(a) shows the stability of the hydroxylated surfaces for the different investigated density functionals. There is a systematic difference in the stability of the hydroxylated surfaces per hydroxyl group, which increases in the order SCAN < PBE-D3 < BEEF-vdW $\lesssim$ HSE06. Due to the different concentrations of hydroxyl groups on the surface, this leads to a difference in stability that is more pronounced for high values of $\theta[Al(OH)_3]$. This generally shifts the value of μ_{H_2O} at which the transition between different phases occurs to lower values for the stronger binding functionals. Figure A.4(b) shows the stability of additional investigated hydroxylated surfaces with $\frac{1}{3} < \theta[Al(OH)_3] < 1$, which are close in stability to the surface with $\theta[Al(OH)_3]$=4/9.

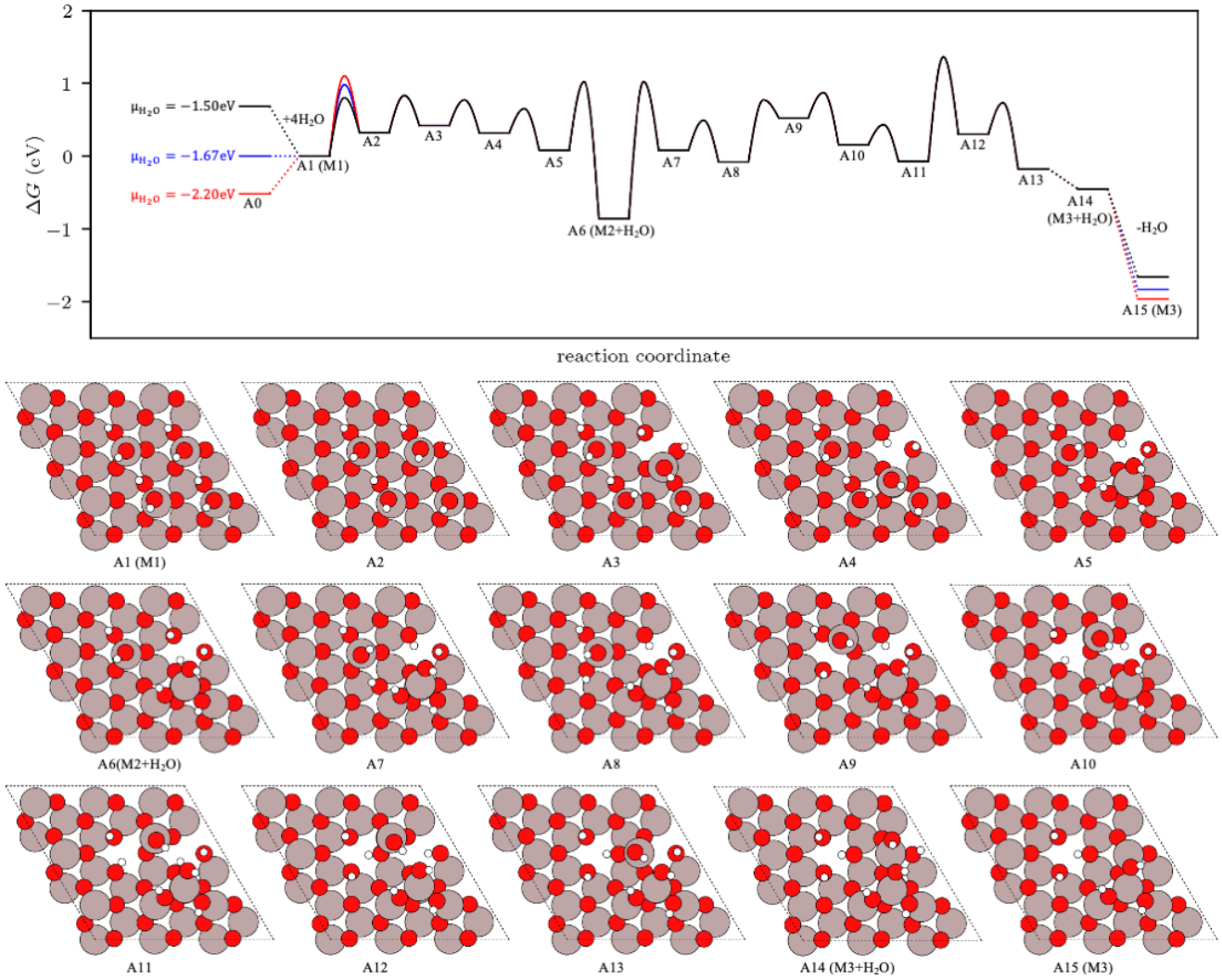

Figure A.2: Detailed description of the reaction pathway shown in Fig. 3.11. The atomic structure of the clean surface (A0) is not depicted. The free energies are listed in Table A.2, total energies in Table A.4.

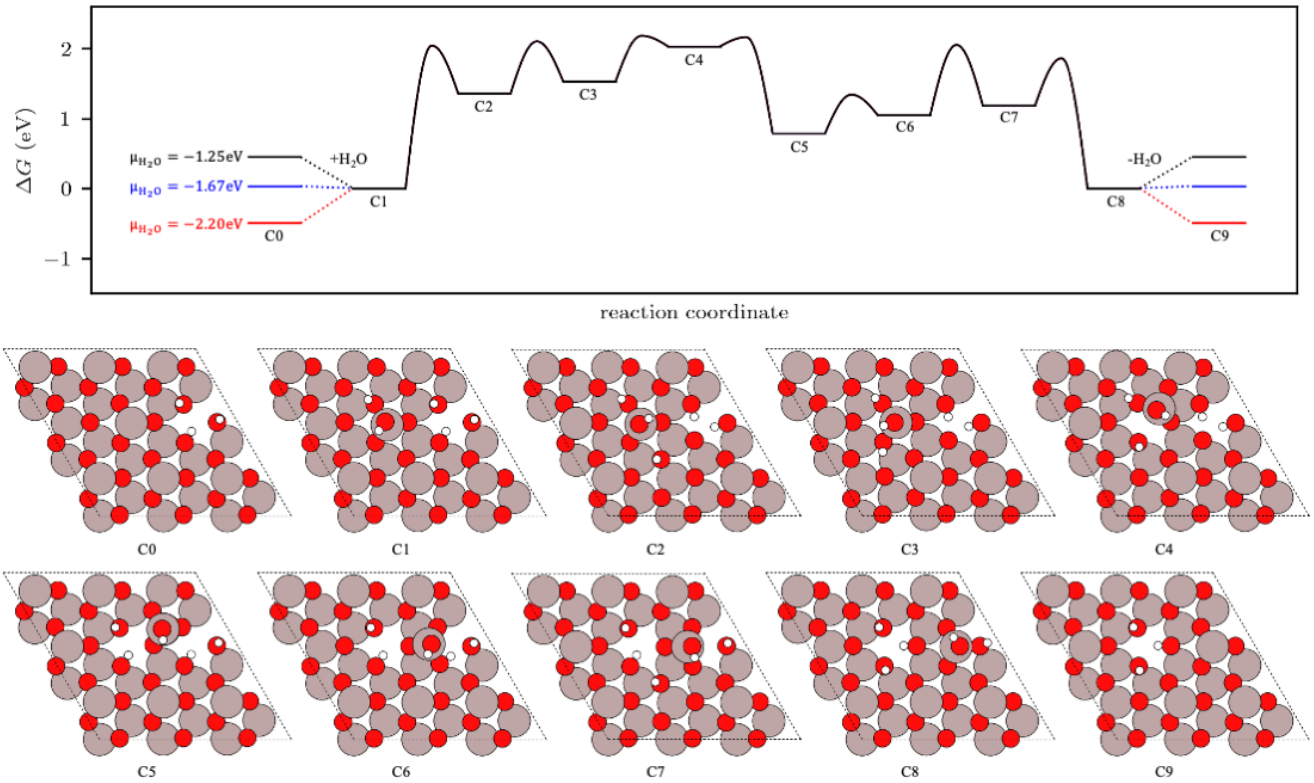

Figure A.3: Detailed description of the reaction pathway is shown in Fig. 3.13. The free energies are listed in Table A.2, and the total energies are listed in Table A.4.

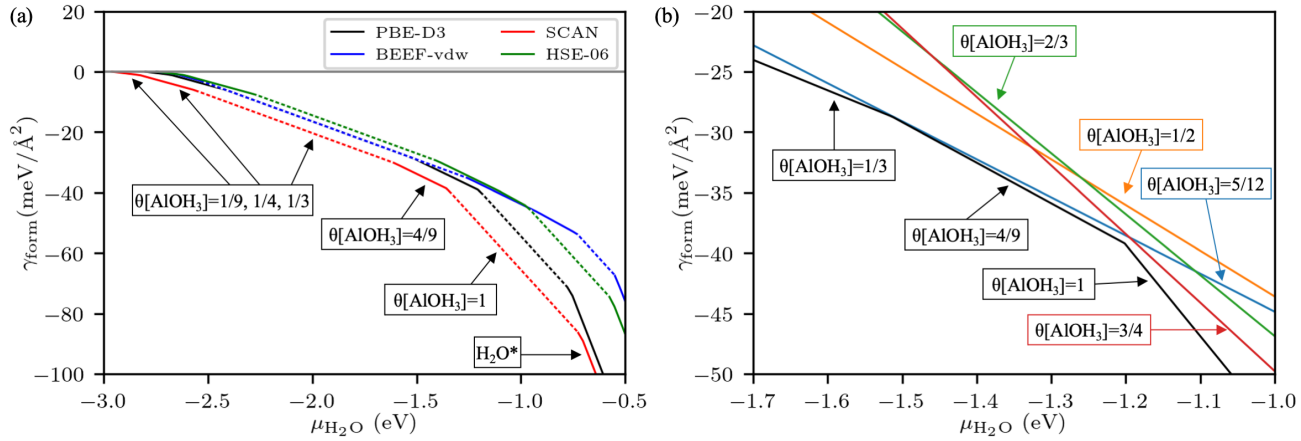

Figure A.4: Additional stability analysis of investigated surfaces. (a) Different functionals. (b) Stability of surfaces $\frac{1}{3} < \theta[\mathrm{Al(OH)_3}] < 1$ with PBE-D3.

Table A.2.: Relative Gibbs free energies (in eV) of minima and transition states shown in Fig. 3.1 at μ_{H_2O} = -1.5 eV, in Fig. 3.12 and in Fig. 3.13 at μ_{H_2O} = -1.25 eV with the labeling introduced in Fig. A.2 and A.3.

Fig. 3.1	ΔG	Fig. 3.1	ΔG	Fig. 3.12	ΔG	Fig. 3.13	ΔG
A0	0.68	TS(A8-A9)	0.77	B1	0.00	C0	0.45
A1	0.00	A9	0.53	TS(B1-B2)	3.22	C1	0.00
TS(A1-A2)	1.35	TS(A9-A10)	0.87	B2	0.78	TS(C1-C2)	2.04
TS(A1-A2)_H_2O	0.80	A10	0.16	TS(B2-B3)	3.22	C2	1.36
A2	0.33	TS(A10-A11)	0.43	B3	0.00	TS(C2-C3)	2.10
TS(A2-A3)	0.83	A11	-0.07			C3	1.53
A3	0.42	TS(A11-A12)	1.36			TS(C3-C4)	2.17
TS(A3-A4)	0.77	A12	0.30			C4	2.03
A4	0.32	TS(A12-A13)	0.73			TS(C4-C5)	2.16
TS(A4-A5)	0.65	A13	-0.17			C5	0.79
A5	0.08	TS(A13-A14)	-0.05			TS(C5-C6)	1.34
TS(A5-A6)	1.02	A14	-0.45			C6	1.05
A6	-0.86	A15	-1.66			TS(C6-C7)	2.05
TS(A6-A7)[b]	1.02					C7	1.09
A7[a]	0.08					TS(C7-C8)	1.86
TS(A7-A8)	0.49					C8	0.00
A8	-0.08					C9	0.45

[a] Identical to A5. [b] Identical to TS(A5-A6).

A.3. Total energies

The computed total energies are listed in Tables A.2 and A.3.

Table A.3.: Computed total energies (in eV) are used to determine the stability of structures.

Structure	Details	PBE-D3	BEEF-vDW[a]	SCAN[a]	HSE06[a]
H_2O	gas	-14.220	-12.810	-15.590	-17.480
$\frac{1}{2}E^{\text{bulk}}_{Al_2O_3}$	bulk	-19.128	-15.251	-25.580	-22.653
dry/clean	(1×1)	-260.652	-207.043	-350.811	-310.174
dry/clean (minus one layer)	(1×1)	-222.396	-176.542	-299.650	-264.868
dry/clean	(1×2)	-521.305	-414.088	-701.620	-620.345
dry/clean	(2×2)	-1042.612	-828.179	-1403.244	-1240.694
dry/clean	(3×3)	-2345.929	-1863.500	-3157.548	-2791.657
dry/clean	(4×4)	-4170.494	-3312.762	-5613.019	-4962.821
dry/clean	$(\sqrt{3}\times\sqrt{3})R30°$	-781.893	-621.055	-1052.359	-930.408
dry/clean	$(2\sqrt{3}\times2\sqrt{3})R30°$	-3127.605	-2484.242	-4209.480	-3720.000
dry/clean	$(\sqrt{3}\times2)$	-1042.571	-828.126	-1403.211	-1240.667
$\theta[Al(OH)_3]$=1/16	(4×4)	-4215.158	-3351.357	-5666.455	-5015.822
$\theta[Al(OH)_3]$=1/9	(3×3)	-2390.589	-1902.092	-3210.957	-2844.641
$\theta[Al(OH)_3]$=1/4	(2×2)	-1087.171	-866.690	-1456.548	-1293.568
$\theta[Al(OH)_3]$=1/3	$(\sqrt{3}\times\sqrt{3})R30°$	-826.339	-659.506	-1105.542	-983.138
$\theta[Al(OH)_3]$=4/9	(3×3)	-2521.994	-2015.194	-3368.482	-3000.798
$\theta[Al(OH)_3]$=1	(1×1)	-303.700	-243.671	-402.579	-361.379
$\theta[Al(OH)_3]$=1; $\theta[H_2O]$=2	(1×2)	-590.822	-479.774	-768.075	-704.307
M1	(1×1)	-276.515	-221.424	-368.119	-329.174
M2	(2×2)	-1090.929	-871.806	-1456.020	-1298.418
M3	(2×2)	-1091.737	-872.648	-1456.945	-1299.249
$\theta[Al(OH)_3]$=1/4 (iso)	$(2\sqrt{3}\times2\sqrt{3})R30°$	-3261.187	-2599.768	-4369.302	-3880.136
$\theta[Al(OH)_3]$=1/4 (iso)	$(\sqrt{3}\times2)$	-1087.107	-866.624	-1456.472	-1293.510
$\theta[Al(OH)_3]$=5/12	$(2\sqrt{3}\times2\sqrt{3})R30°$	-3348.106	-2674.406	-4473.607	-3983.515
$\theta[Al(OH)_3]$=1/2	(1×2)	-564.994	-451.627	-754.053	-672.308
$\theta[Al(OH)_3]$=2/3	$(\sqrt{3}\times\sqrt{3})R30°$	-868.613	-695.363	-1156.461	-1033.530
$\theta[Al(OH)_3]$=3/4	(2×2)	-1019.428	-817.138	-1354.558	-1213.899
M2	$(\sqrt{3}\times\sqrt{3})R30°$	-830.087	-664.622	-1105.022	-987.996

[a] Single point calculation with the PBE-D3 structure.

Table A.4.: Computed total energies (in eV) are used to determine and study reaction pathways, see Figs. A.2, A.3 for labeling.

Fig. 3.11	E	Fig. 3.11	E	Fig. 3.12	E	Fig. 3.13	E
A0	-2345.953	TS(A8-A9)[a]	-2408.760	B1	-2390.614	C0	-2350.805
A1	-2409.531	A9	-2408.999	TS(B1-B2)[b]	-2387.396	C1	-2366.733
TS(A1-A2)[b]	-2408.176	TS(A9-A10)[a]	-2408.663	B2	-2389.831	TS(C1-C2)[a]	-2364.693
TS(A1-A2)_H_2O[b]	-2424.450	A10	-2409.371	TS(B2-B3)[b]	-2387.394	C2	-2365.373
A2	-2409.196	TS(A10-A11)[a]	-2409.101	B3	-2390.614	TS(C2-C3)[b]	-2364.635
TS(A2-A3)[a]	-2408.706	A11	-2409.602			C3	-2365.204
A3	-2409.113	TS(A11-A12)[b]	-2408.167			TS(C3-C4)[b]	-2364.562
TS(A3-A4)[a]	-2408.756	A12	-2409.232			C4	-2364.701
A4	-2409.213	TS(A12-A13)[a]	-2408.801			TS(C4-C5)[b]	-2364.577
TS(A4-A5)[a]	-2408.880	A13	-2409.700			C5	-2365.945
A5	-2409.449	TS(A13-A14)[a]	-2409.580			TS(C5-C6)[a]	-2365.389
TS(A5-A6)[b]	-2408.514	A14	-2409.983			C6	-2365.684
A6	-2410.392	A15	-2395.464			TS(C6-C7)[b]	-2364.685
TS(A6-A7)[b]	-2408.514					C7	-2365.542
A7	-2409.449					TS(C7-C8)[b]	-2364.875
TS(A7-A8)[b]	-2409.042					C8	-2366.733
A8	-2409.607					C9	-2350.805

[a] Transition state estimated from interpolated NEB. [b] Transition state fully optimized.

B. Stability of hydroxylated α-Fe_2O_3(0001) surfaces

B.1. Stability of surfaces

Table B.5 lists the stability of all investigated surfaces, which are all shown schematically in Figures 1.2, 3.3 and 3.6.

Table B.5.: Overview over all computed terminations of the α-Fe_2O_3(0001) surface. The composition is specified in terms of the coverage of H_2O, $Fe(OH)_3$, $Fe(OH)_2$, Fe(OH) and FeO adsorbates relative to the dry surface. The term ΔE_{form} is the formation energy given in eV per (1×1)-unit cell relative to the α-Fe_2O_3(0001) dry surface. $\Delta E^{\text{abs}}_{\text{form}}$ is the absolute formation energy given in eV per unit cell relative to the α-Fe_2O_3(0001) bulk. Additionally, the concentration of hydroxyl groups per surface area, the unit cell and the employed k-point sampling are specified.

	coverage (θ)				n(OH)		
Surface	$Fe(OH)_3$	H_2O	ΔE_{form}	$\Delta E^{\text{abs}}_{\text{form}}$	($1/nm^2$)	unit cell	k-points
θ[$Fe(OH)_3$]=0 (dry/clean)	0	0	0	1.84	0	[a]	[a]
θ[$Fe(OH)_3$]=1/4	1/4	0	-0.83	1.01	3.4	(2×2)	2×2
θ[$Fe(OH)_3$]=1	1	0	-1.89	-0.05	13.6	(1×1)	4×4
θ[H_2O]=1 (Fe_2O_3)	0	1	-1.25	0.59	9.0	(1×1)	4×4
	coverage (θ)				n(OH)		
Surface	$Fe(OH)_2$	H_2O	ΔE_{form}	$\Delta E^{\text{abs}}_{\text{form}}$	($1/nm^2$)	unit cell	k-points
θ[$Fe(OH)_2$]=1/4	1/4	0	-0.32	1.52	2.3	(2×2)	2×2
θ[$Fe(OH)_2$]=1	1	0	-0.42	1.42	9.0	(1×1)	4×4
	coverage (θ)				n(OH)		
Surface	Fe(OH)	H_2O	ΔE_{form}	$\Delta E^{\text{abs}}_{\text{form}}$	($1/nm^2$)	unit cell	k-points
θ[Fe(OH)]=1	1	0	1.48	3.32	4.5	(1×1)	4×4
	coverage (θ)				n(OH)		
Surface	FeO	H_2O	ΔE_{form}	$\Delta E^{\text{abs}}_{\text{form}}$	($1/nm^2$)	unit cell	k-points
θ[FeO]=1	1	0	1.43	3.27	0	(1×1)	4×4

[a] The dry surface serves as the reference and was always computed with the same unit cell and k-point sampling as the hydroxylated surfaces.

B.2. Total rnergies

The computed total energies are listed in Table B.6.

Table B.6.: Computed total energies (in eV) are used to determine the stability of structures.

Structure	Details	total energy (PBE+U)		
H_2O	gas		-14.226	
O_2	gas		-9.866	
CO	gas		-14.780	
		U = 3 eV	U = 4 eV	U = 5 eV
$\frac{1}{2}E^{\text{bulk}}_{Fe_2O_3}$	bulk	-17.844	-17.494	-17.185
θ[$Fe(OH)_3$]=0 (dry/clean)	(1×1)	-317.693	-311.241	-305.517
θ[$Fe(OH)_3$]=0 dry/clean (minus two layer)	(1×1)	-246.311	-241.259	-236.775
θ[$Fe(OH)_3$]=1/4	(2×2)	-1355.554	-1329.275	-1305.957
θ[$Fe(OH)_3$]=1	(1×1)	-399.568	-392.695	-386.602
θ[H_2O]=1	(1×1)	-348.592	-342.198	-336.525
θ[$Fe(OH)_2$]=1/4	(2×2)	-1332.133	-1306.039	-1282.913
θ[$Fe(OH)_2$]=1	(1×1)	-377.445	-370.589	-364.535
θ[FeOH]=1	(1×1)	-354.339	-347.634	-341.731
θ[FeO]=1	(1×1)	-345.402	-338.441	-332.257

B.3. Magnetic moments

Table B.7.: Mean magnetic moments (in μ_B) of the upper half layers from the slabs for the relevant α-Fe_2O_3 surface terminations. The magnetic moment is averaged over all Fe-atoms belonging to the respective layer. The computed magnetic value of the bulk is $\mu = \pm 4.16$

		θ[Fe(OH)$_3$]		
	Dry	$\theta = 1/4$	$\theta = 1$	θ[H$_2$O] = 1
Fe^2_A	–	-4.24	-4.24	–
Fe^1_A	-4.00	-4.07	-4.21	-4.01
Fe^2_B	+4.14	+4.16	+4.16	+4.16
Fe^1_B	+4.17	+4.17	+4.15	+4.16
Fe^2_C	-4.16	-4.15	-4.16	-4.16
Fe^1_C	-4.16	-4.16	-4.16	-4.16
$Fe^2_{A'}$	+4.16	+4.16	+4.16	+4.16
$Fe^1_{A'}$	+4.16	+4.16	+4.16	+4.16
$Fe^2_{B'}$	-4.16	-4.16	-4.16	-4.16
$Fe^1_{B'}$	-4.16	-4.16	-4.16	-4.16

B.4. Transition between hematite and magnetite

The chemical reaction of phase transition from bulk magnetite to bulk hematite can be described as:

$$2Fe_3O_4 + \frac{1}{2}O_2 \rightleftharpoons 3Fe_2O_3 \tag{2}$$

The chemical potential at which the transition from Fe_3O_4 to Fe_2O_3 occurs is calculated by the following equation:

$$\mu_O^{trans} = \frac{3 \times \Delta_f H^{\ominus}_{Fe_2O_3} - 2 \times \Delta_f H^{\ominus}_{Fe_3O_4}}{96.485 \frac{kJ/mol}{eV}} \tag{3}$$

Here, the involved quantities are the standard enthalpy of formation of Fe_2O_3 [256]: $\Delta_f H^{\ominus}_{Fe_2O_3} = -824.2\,kJ/mol$, the standard enthalpy of formation of Fe_3O_4 [256]: $\Delta_f H^{\ominus}_{Fe_4O_4} = -1118.4\,kJ/mol$ Based on the experimental values, we thus obtain the following chemical potential of oxygen where the oxidation of Fe_3O_4 to Fe_2O_3 occurs: $\mu_O^{trans} = -2.44\,eV$

For computed data (PBE+U with U = 3, 4 and 5 eV) [230], the value of μ_O^{trans} is −1.73 , -1.73 and −1.66 eV.

B.5. Dependence of the reaction energies on the oxygen reference

In reactions with O_2 (i.e., molecular oxygen in the gas phase), errors are often encountered in reaction energies computed with approximate density functionals. A common approach to circumvent this is to shift the O_2-reference based on a known reaction energy. For example, using the 'water reference', the O_2 energy can be deduced based on the known reaction energy of water formation (1/2 O_2 + H_2 → H_2O) and the computed energies of H_2 and H_2O. The reference reaction energy can be taken either from experimental values or accurate calculations, which do not differ significantly.

While such an approach may work in some cases, more recent approaches aiming to improve gas phase thermodynamics add corrections to many involved common molecules, not just O_2[279]. In Fig. B.5, we have compiled the errors of common, simple oxidation reactions computed with PBE-D3 and we have added data from the literature[230] for oxidation reactions leading to the formation of iron oxides using PBE-D3 and U=4 eV, as in our work.

Note that for the experimental values of iron oxides we use the 0 K formation enthalpies, while we have used the standard enthalpies in the section above. The transition between hematite and magnetite leads to a difference of about 0.08 eV.

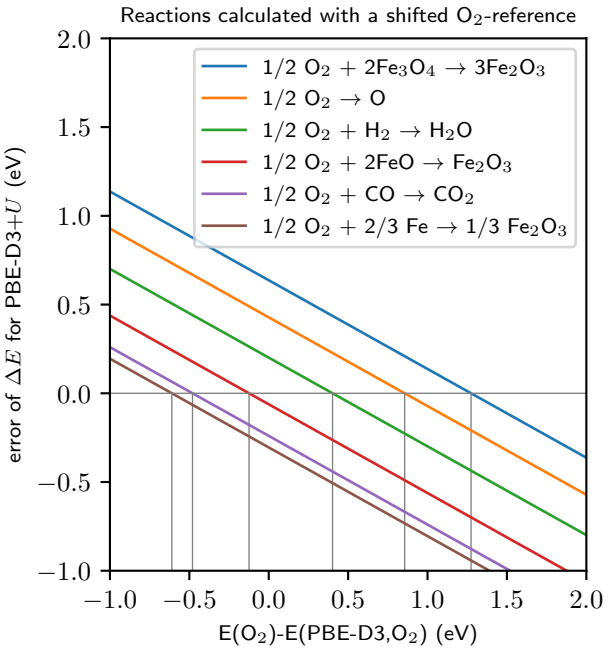

Figure B.5: Error in gas phase reaction energies computed at the PBE-D3 level (this work) and at the PBE-D3+U level (U = 4 eV) taken from the literature[230]. The reaction energies and the reference energies are given in Tables B.8 and B.9.

Table B.8.: Reaction enthalpies in eV at 0 K, computed with PBE-D3 and obtained from experiments.

reaction	PBE-D3+U (U=4)	reference	error
1/2 O_2 + 2Fe_3O_4 → 3Fe_2O_3	-1.725	-2.362	0.637
1/2 O_2 → O	2.987	2.558	0.428
1/2 O_2 + H_2 → H_2O	-2.275	-2.476	0.201
1/2 O_2 + 2FeO → Fe_2O_3	-2.912	-2.850	-0.062
1/2 O_2 + CO → CO_2	-3.135	-2.895	-0.240
1/2 O_2 + 2/3 Fe → 1/3 Fe_2O_3	-3.134	-2.830	-0.305

Table B.9.: Experimental formation enthalpies of molecules at 0 K, highly accurate computed zero point vibrational energies and formation enthalpies of iron oxides from the literature. All energies are given in eV.

	experimental	computed[280]	computed[230]		
Molecule/Atom	Δ_fH(0K)	ZPVE (atomization)	Δ_fH(0K)		
O_2	0[233]	0.099			
H_2	0[233]	0.270			
H_2O	-2.476[233]	0.578			
CO	-1.179[233]	0.135			
CO_2	-4.074[233]	0.316			
O	2.558[233]	0			
H	2.239[233]	0			
			U = 3 eV	U = 4 eV	U = 5 eV
FeO	-2.819[230, 281]		-3.055	-3.245	-3.506
Fe_3O_4	-11.552[230, 281]		-12.284	-13.242	-14.175
Fe_2O_3	-8.489[230, 281]		-8.767	-9.403	-10.002

B.6. Vibrational contributions to Gibbs Free Energy

Table B.10.: Calculated vibrational modes (in cm^{-1}).

θ[$Fe(OH)_3$]=0 (dry/clean)		θ[$Fe(OH)_3$]=1	θ[$Fe(OH)_3$]=1/4	H_2O
Fe_3O_6	$Fe_3O_6 + Fe_2O_3$	$Fe_3O_6 + Fe(OH)_3$	$Fe(OH)_3$	H_2O
75.9	53.0	55.6	141.3	1577.5
77.0	55.0	56.9	146.4	3700.3
107.0	89.8	96.0	148.9	3815.6
148.9	122.6	145.0	202.7	
176.8	146.1	158.6	203.4	
200.5	147.1	163.4	224.7	
201.0	155.5	183.4	340.5	
253.4	203.0	189.9	342.3	
254.0	206.1	202.4	362.1	
280.8	206.4	239.9	398.6	
281.5	247.1	247.4	400.7	
315.7	247.4	256.0	437.1	
316.0	274.8	275.1	508.5	
379.0	274.9	278.0	512.4	
379.9	275.1	283.9	527.9	
382.4	286.5	287.7	768.4	
414.3	287.1	292.7	771.1	
443.2	300.2	299.2	773.1	
443.8	300.4	301.9	3745.9	
477.4	320.8	311.0	3746.2	
508.3	321.1	325.2	3747.2	
508.7	377.7	374.8		
527.4	378.0	382.3		
600.9	379.0	384.9		
665.4	388.9	388.7		
665.8	397.7	401.6		

Continued on next page

Table B.10.: Calculated vibrational modes (in cm^{-1}) (continued)

$\theta[Fe(OH)_3]$=0 (dry/clean)		$\theta[Fe(OH)_3]$=1	$\theta[Fe(OH)_3]$=1/4	H_2O
Fe_3O_6	$Fe_3O_6 + Fe_2O_3$	$Fe_3O_6 + Fe(OH)_3$	$Fe(OH)_3$	H_2O
701.4	398.5	406.8		
	414.0	422.5		
	443.4	449.2		
	444.1	469.9		
	476.9	484.0		
	501.1	507.8		
	501.8	512.8		
	517.3	517.2		
	535.0	525.8		
	545.5	542.0		
	546.6	554.0		
	613.2	556.2		
	616.1	589.8		
	665.6	613.0		
	666.0	619.0		
	701.5	635.4		
		781.9		
		819.8		
		855.4		
		3486.7		
		3696.2		
		3757.3		

B.7. CO and H_2O adsorption on relative surfaces

Adsorption energies of CO and H_2O as probe molecules were computed on the three most relevant surfaces, the known dry surface ($\theta[Fe(OH)_3]$=0), the known fully hydroxylated surface ($\theta[Fe(OH)_3]$=1) and the partially hydroxylated surface ($\theta[Fe(OH)_3]$=1/4) proposed herein.

Adsorption is generally weakest for the fully hydroxylated surface and strongest for the dry surface. For the partially hydroxylated surface (θ[Fe(OH)$_3$]=1/4) it is intermediate. Here some three-fold coordinated surface Fe are still available for binding.

Table B.11.: Computed total energy and adsorption energy (in eV) for one CO/H$_2$O molecule adsorbed on a 2 × 2 slab.

Structure	Adsorbate	E_{ads}	E_{total}
θ[Fe(OH)$_3$]=0 (dry/clean)	CO	-0.612	-1260.371
	H$_2$O	-1.171	-1260.358
θ[Fe(OH)$_3$]=1	CO	-0.200	-1585.783
	H$_2$O	-0.674	-1585.682
θ[Fe(OH)$_3$]=1/4	CO	-0.554	-1344.628
	H$_2$O	-0.990	-1344.491

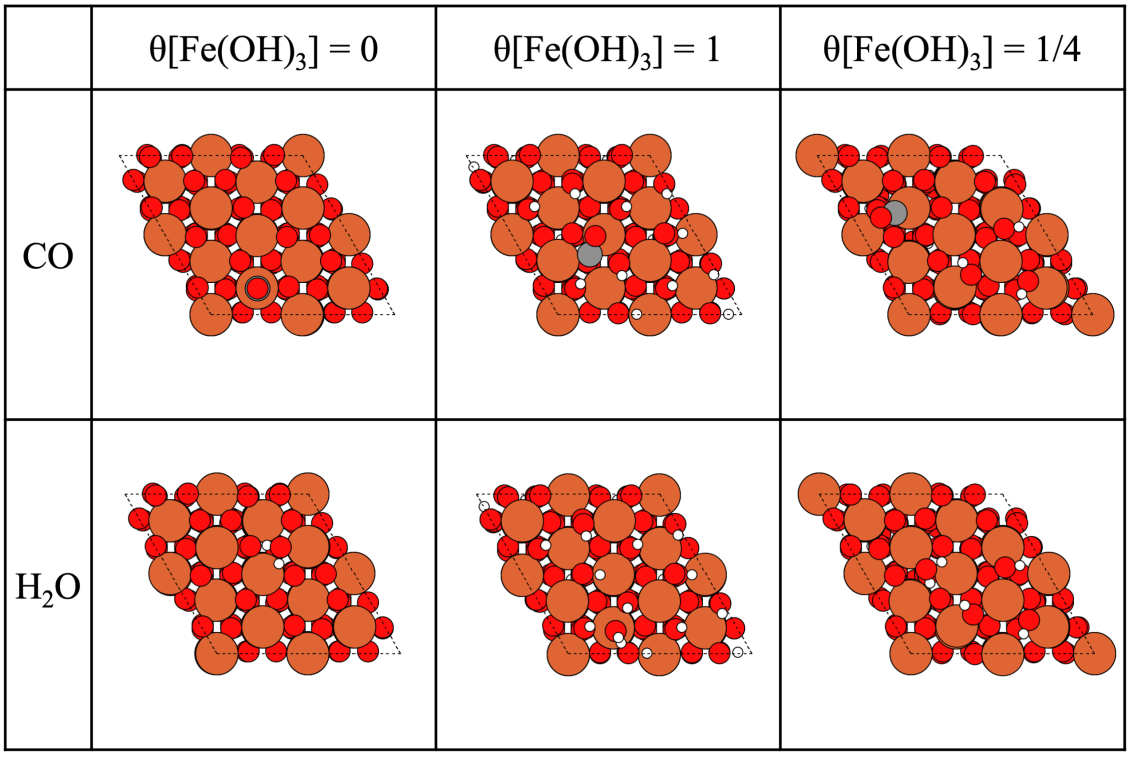

Figure B.6: The configurations of CO/H$_2$O adsorption on the relative surfaces.

C. CO adsorption on Pd/Pt (111) surfaces

C.1. Data

In tables C.12, C.13 the frequencies obtained in this way are reported.

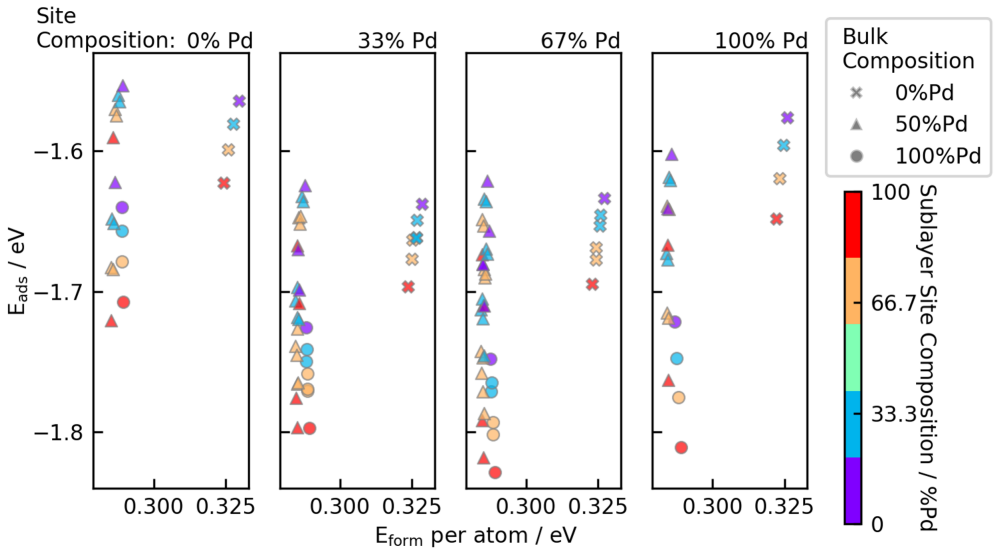

Figure C.7: CO/fcc adsorption energies are shown as a function of the formation energies of slabs. Each panel contains structures with one site composition. The bulk composition is indicated by different symbols, and the composition of the sublayer can be identified from the color of the symbols.

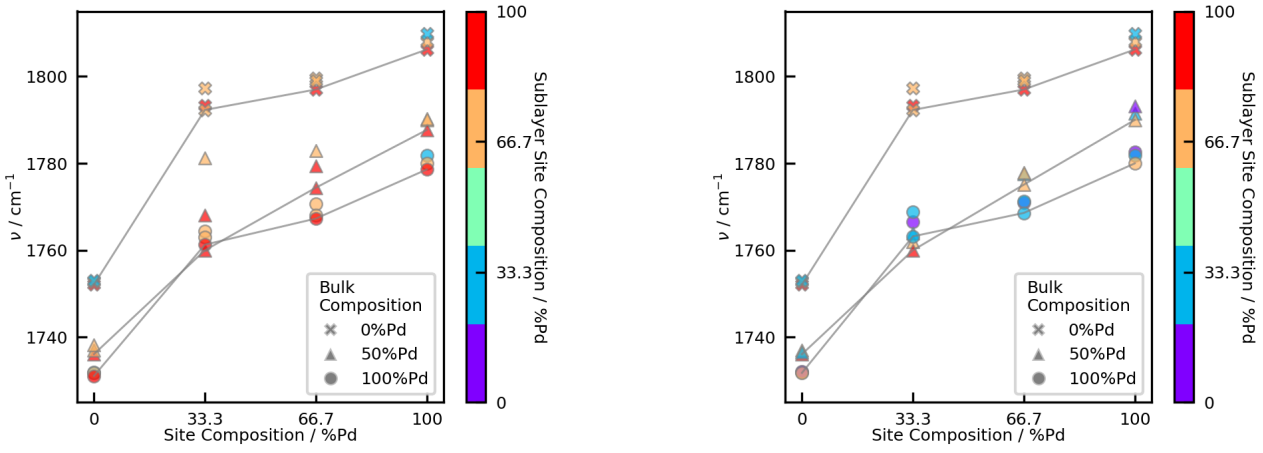

Figure C.8: CO vibrational frequencies at fcc sites in different slabs. The slab of 50% Pd is shown in Fig. 4.4, and the three nearby and closest atoms in the sublayer are variable. Only three data points are shown for each site of each slab type, with (left) the lowest adsorption energy and (right) the lowest formation energy of the clean surface. Different markers indicate various bulk compositions and the x-axis represents the composition of the nearby atoms. The coloration signifies the composition of the three closest in the sublayer.

Table C.12.: Shifted vibrational frequencies (in cm^{-1}) are used in Fig. 4.2 and 4.3. Total energies of the clean slab and adsorption energies are also shown, both are shown in eV. All the $\theta = 1/4$ data are calculated on 2×2×4 slabs and all the $\theta = 1/16$ data are calculated on 4×4×4 slabs.

Slab Composition	E_{total}	Site	Site Composition	ν		E_{ads}	
				θ		θ	
				1/4	1/16	1/4	1/16
100% Pd	-26.560	fcc	Pd_3	1817.6	1776.8	-1.733	-1.818
		hcp	Pd_3	1816.0	1778.9	-1.729	-1.788
		top	Pd	2055.6	2038.6	-1.238	-1.236
75% Pd	-31.395	fcc	Pd_2Pt_1	1813.9	1768.7	-1.700	-1.772
		fcc	Pd_3	1833.4	1794.3	-1.587	-1.686
		hcp	Pd_2Pt_1	1809.5	1769.5	-1.674	-1.726
		hcp	Pd_3	1835.0	1798.8	-1.626	-1.67
		top	Pt	2057.2	2037.1	-1.568	-1.621
50% Pd	-36.071	fcc	Pd_1Pt_2	1811.6	1762.2	-1.647	-1.711
		fcc	Pd_2Pt_1	1831.9	1793.2	-1.569	-1.653
		hcp	Pd_1Pt_2	1823.7	1791.0	-1.585	-1.635
		top	Pt	2057.6	2042.0	-1.504	-1.584
		top	Pd	2068.3	2056.4	-1.088	-1.148
25% Pd	-40.541	fcc	Pd_1Pt_2	1852.5	1794.4	-1.554	-1.652
		fcc	Pt_3	1773.2	1739.0	-1.554	-1.648
		hcp	Pt_3	1770.4	1742.9	-1.525	-1.592
		hcp	Pd_1Pt_2	1834.6	1803.8	-1.543	-1.614
		bridge	PdPt	1901.0	1881.7	-1.447	-1.514
		bridge	Pt_2	1860.9	1838.0	-1.543	-1.617
		top	Pt	2069.5	2054.8	-1.457	-1.559
		top	Pd	2076.3	2065.3	-1.031	-1.081
0% Pd	-44.787	fcc	Pt_3	1782.1	1751.9	-1.449	-1.576
		hcp	Pt_3	1787.5	1762.0	-1.447	-1.539
		bridge	Pt_2	1874.9	1851.1	-1.457	-1.540
		top	Pt	2076.2	2064.7	-1.394	-1.480

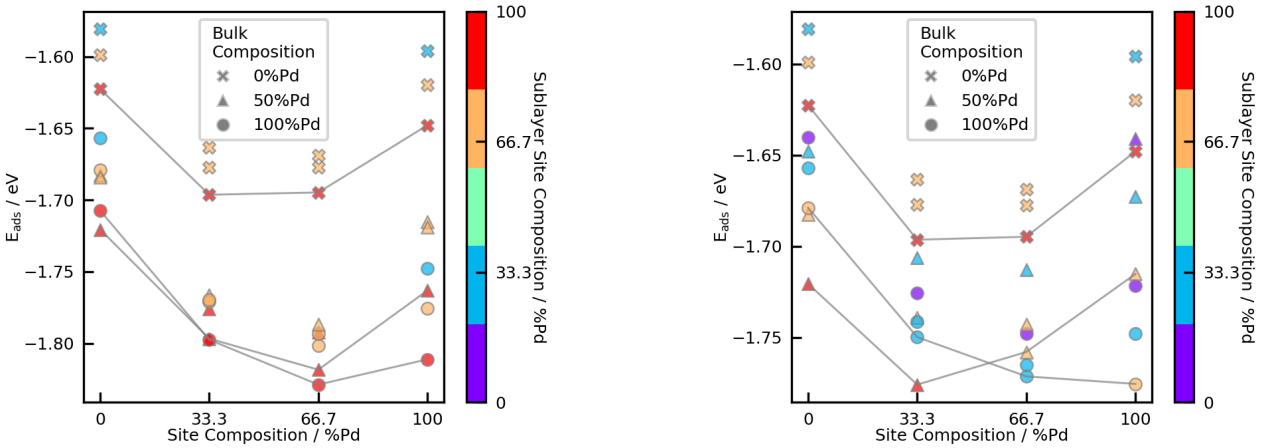

Figure C.9: Adsorption energy of CO at fcc sites in different slabs. The slab of 50% Pd is shown in Fig. 4.4, and the three nearby and closest atoms in the sublayer are variable. Only three data points are shown for each site of each slab type, with (left) the lowest adsorption energy and (right) the lowest formation energy of the clean surface. Different markers indicate various bulk compositions and the x-axis represents the composition of the nearby atoms. The coloration signifies the composition of the three closest in the sublayer.

Table C.13.: Shifted vibrational frequencies (in cm^{-1}) are used in Fig. 4.4, C.7, C.8 and C.9. Total energies and formation energy of the slabs and adsorption energies are also shown, all are shown in eV. All the slabs are 4×4×4.

Bulk Composition	Label	Site Composition	Sublayer Composition	E_{total}	E_{form}	ν	E_{ads}
100% Pd	Pd_{64}	Pd_3	Pd_3	-120.151	18.498	1778.6	-1.811
100% Pd	$Pd_{63}Pt\_1$	Pd_2Pt_1	Pd_3	-121.339	18.508	1767.3	-1.829
100% Pd	$Pd_{63}Pt\_2$	Pd_3	Pd_2Pt_1	-121.351	18.442	1780.0	-1.775
100% Pd	$Pd_{62}Pt_2\_1$	Pd_1Pt_2	Pd_3	-122.484	18.512	1761.3	-1.797
100% Pd	$Pd_{62}Pt_2\_2$	Pd_2Pt_1	Pd_2Pt_1	-122.530	18.462	1768.1	-1.793
100% Pd	$Pd_{62}Pt_2\_3$	Pd_2Pt_1	Pd_2Pt_1	-122.541	18.459	1770.7	-1.802
100% Pd	$Pd_{62}Pt_2\_4$	Pd_3	Pd_1Pt_2	-122.552	18.394	1781.9	-1.748
100% Pd	$Pd_{61}Pt_3\_1$	Pt_3	Pd_3	-123.569	18.516	1731.1	-1.707
100% Pd	$Pd_{61}Pt_3\_2$	Pd_1Pt_2	Pd_2Pt_1	-123.675	18.474	1764.4	-1.771
100% Pd	$Pd_{61}Pt_3\_3$	Pd_2Pt_1	Pd_1Pt_2	-123.715	18.428	1768.6	-1.765
100% Pd	$Pd_{61}Pt_3\_4$	Pd_1Pt_2	Pd_2Pt_1	-123.656	18.481	1757.6	-1.759
100% Pd	$Pd_{61}Pt_3\_5$	Pd_1Pt_2	Pd_2Pt_1	-123.673	18.474	1763.0	-1.770

Bulk Composition	Label	Site Composition	Sublayer Composition	E_{total}	E_{form}	ν	E_{ads}
100% Pd	$Pd_{61}Pt_3$–6	Pd_2Pt_1	Pd_1Pt_2	-123.727	18.422	1771.3	-1.771
100% Pd	$Pd_{61}Pt_3$–7	Pd_3	Pt_3	-123.742	18.357	1782.6	-1.721
100% Pd	$Pd_{60}Pt_4$–1	Pt_3	Pd_2Pt_1	-124.742	18.494	1731.8	-1.679
100% Pd	$Pd_{60}Pt_4$–2	Pd_1Pt_2	Pd_1Pt_2	-124.861	18.447	1768.9	-1.750
100% Pd	$Pd_{60}Pt_4$–3	Pd_1Pt_2	Pd_1Pt_2	-124.842	18.457	1763.2	-1.741
100% Pd	$Pd_{60}Pt_4$–4	Pd_2Pt_1	Pt_3	-124.905	18.401	1771.0	-1.748
100% Pd	$Pd_{59}Pt_5$–1	Pt_3	Pd_1Pt_2	-125.909	18.485	1731.9	-1.657
100% Pd	$Pd_{59}Pt_5$–2	Pd_1Pt_2	Pt_3	-126.018	18.445	1766.5	-1.726
100% Pd	$Pd_{58}Pt_6$	Pt_3	Pt_3	-127.065	18.492	1732.1	-1.640
50% Pd	$Pd_{36}Pt_{28}$	Pd_3	Pd_3	-153.424	18.215	1787.7	-1.763
50% Pd	$Pd_{35}Pt_{29}$–1	Pd_2Pt_1	Pd_3	-154.632	18.216	1774.4	-1.792
50% Pd	$Pd_{35}Pt_{29}$–2	Pd_2Pt_1	Pd_3	-154.629	18.245	1779.4	-1.818
50% Pd	$Pd_{35}Pt_{29}$–3	Pd_3	Pd_2Pt_1	-154.553	18.221	1790.3	-1.719
50% Pd	$Pd_{35}Pt_{29}$–4	Pd_3	Pd_2Pt_1	-154.582	18.189	1790.0	-1.715
50% Pd	$Pd_{34}Pt_{30}$–1	Pd_1Pt_2	Pd_3	-155.791	18.220	1760.0	-1.776
50% Pd	$Pd_{34}Pt_{30}$–2	Pd_2Pt_1	Pd_2Pt_1	-155.750	18.232	1776.3	-1.747
50% Pd	$Pd_{34}Pt_{30}$–3	Pd_2Pt_1	Pd_2Pt_1	-155.791	18.202	1777.9	-1.758
50% Pd	$Pd_{34}Pt_{30}$–4	Pd_2Pt_1	Pd_2Pt_1	-155.784	18.195	1775.1	-1.743
50% Pd	$Pd_{34}Pt_{30}$–5	Pd_1Pt_2	Pd_3	-155.790	18.242	1768.1	-1.797
50% Pd	$Pd_{34}Pt_{30}$–6	Pd_2Pt_1	Pd_2Pt_1	-155.761	18.261	1783.0	-1.787
50% Pd	$Pd_{34}Pt_{30}$–7	Pd_2Pt_1	Pd_2Pt_1	-155.776	18.231	1781.4	-1.771
50% Pd	$Pd_{34}Pt_{30}$–8	Pd_3	Pd_1Pt_2	-155.710	18.203	1792.5	-1.677
50% Pd	$Pd_{34}Pt_{30}$–9	Pd_3	Pd_1Pt_2	-155.735	18.173	1791.5	-1.673
50% Pd	$Pd_{34}Pt_{30}$–10	Pd_3	Pd_3	-155.703	18.199	1799.8	-1.667
50% Pd	$Pd_{33}Pt_{31}$–1	Pt_3	Pd_3	-156.889	18.247	1736.1	-1.721
50% Pd	$Pd_{33}Pt_{31}$–2	Pd_1Pt_2	Pd_2Pt_1	-156.894	18.248	1760.9	-1.727
50% Pd	$Pd_{33}Pt_{31}$–3	Pd_1Pt_2	Pd_2Pt_1	-156.945	18.210	1761.9	-1.739
50% Pd	$Pd_{33}Pt_{31}$–4	Pd_1Pt_2	Pd_2Pt_1	-156.913	18.268	1775.7	-1.765

Bulk Composition	Label	Site Composition	Sublayer Composition	E_{total}	E_{form}	ν	E_{ads}
50% Pd	$Pd_{33}Pt_{31}$–5	Pd_2Pt_1	Pd_1Pt_2	-156.908	18.227	1779.8	-1.719
50% Pd	$Pd_{33}Pt_{31}$–6	Pd_1Pt_2	Pd_2Pt_1	-156.926	18.235	1766.5	-1.745
50% Pd	$Pd_{33}Pt_{31}$–7	Pd_1Pt_2	Pd_2Pt_1	-156.941	18.241	1781.3	-1.766
50% Pd	$Pd_{33}Pt_{31}$–8	Pd_2Pt_1	Pd_1Pt_2	-156.898	18.222	1776.2	-1.705
50% Pd	$Pd_{33}Pt_{31}$–9	Pd_2Pt_1	Pd_1Pt_2	-156.937	18.191	1777.6	-1.713
50% Pd	$Pd_{33}Pt_{31}$–10	Pd_2Pt_1	Pd_1Pt_2	-156.906	18.255	1784.9	-1.746
50% Pd	$Pd_{33}Pt_{31}$–11	Pd_3	Pt_3	-156.859	18.197	1793.2	-1.641
50% Pd	$Pd_{33}Pt_{31}$–12	Pd_2Pt_1	Pd_3	-156.883	18.242	1793.5	-1.710
50% Pd	$Pd_{33}Pt_{31}$–13	Pd_2Pt_1	Pd_3	-156.879	18.210	1792.3	-1.674
50% Pd	$Pd_{33}Pt_{31}$–14	Pd_3	Pd_2Pt_1	-156.861	18.193	1802.5	-1.639
50% Pd	$Pd_{33}Pt_{31}$–15	Pd_3	Pd_2Pt_1	-156.834	18.223	1802.8	-1.641
50% Pd	$Pd_{32}Pt_{32}$–1	Pt_3	Pd_2Pt_1	-157.995	18.284	1738.2	-1.684
50% Pd	$Pd_{32}Pt_{32}$–2	Pt_3	Pd_2Pt_1	-158.026	18.252	1737.0	-1.683
50% Pd	$Pd_{32}Pt_{32}$–3	Pd_1Pt_2	Pd_1Pt_2	-158.043	18.250	1761.4	-1.697
50% Pd	$Pd_{32}Pt_{32}$–4	Pd_1Pt_2	Pd_1Pt_2	-158.091	18.211	1763.9	-1.706
50% Pd	$Pd_{32}Pt_{32}$–5	Pd_1Pt_2	Pd_1Pt_2	-158.068	18.246	1776.1	-1.719
50% Pd	$Pd_{32}Pt_{32}$–6	Pd_2Pt_1	Pt_3	-158.048	18.229	1779.3	-1.681
50% Pd	$Pd_{32}Pt_{32}$–7	Pd_1Pt_2	Pd_1Pt_2	-158.043	18.272	1772.7	-1.720
50% Pd	$Pd_{32}Pt_{32}$–8	Pd_2Pt_1	Pt_3	-158.048	18.228	1779.0	-1.680
50% Pd	$Pd_{32}Pt_{32}$–9	Pd_2Pt_1	Pt_3	-158.042	18.263	1787.0	-1.710
50% Pd	$Pd_{32}Pt_{32}$–10	Pd_1Pt_2	Pd_3	-158.021	18.283	1813.4	-1.708
50% Pd	$Pd_{32}Pt_{32}$–11	Pd_2Pt_1	Pd_2Pt_1	-157.998	18.284	1797.0	-1.687
50% Pd	$Pd_{32}Pt_{32}$–12	Pd_1Pt_2	Pd_3	-158.011	18.252	1788.3	-1.667
50% Pd	$Pd_{32}Pt_{32}$–13	Pd_2Pt_1	Pd_2Pt_1	-158.027	18.252	1795.5	-1.684
50% Pd	$Pd_{32}Pt_{32}$–14	Pd_2Pt_1	Pd_2Pt_1	-158.012	18.273	1798.3	-1.690
50% Pd	$Pd_{32}Pt_{32}$–15	Pd_2Pt_1	Pd_2Pt_1	-158.034	18.210	1794.9	-1.649
50% Pd	$Pd_{32}Pt_{32}$–16	Pd_2Pt_1	Pd_2Pt_1	-157.998	18.250	1795.2	-1.653
50% Pd	$Pd_{32}Pt_{32}$–17	Pd_3	Pd_1Pt_2	-157.985	18.229	1804.5	-1.618

Bulk Composition	Label	Site Composition	Sublayer Composition	E_{total}	E_{form}	ν	E_{ads}
50% Pd	$Pd_{32}Pt_{32}$–18	Pd_3	Pd_1Pt_2	-157.956	18.260	1805.5	-1.621
50% Pd	$Pd_{31}Pt_{33}$–1	Pt_3	Pd_1Pt_2	-159.126	18.300	1738.6	-1.652
50% Pd	$Pd_{31}Pt_{33}$–2	Pt_3	Pd_1Pt_2	-159.155	18.269	1736.5	-1.648
50% Pd	$Pd_{31}Pt_{33}$–3	Pd_1Pt_2	Pt_3	-159.182	18.263	1762.9	-1.670
50% Pd	$Pd_{31}Pt_{33}$–4	Pd_1Pt_2	Pt_3	-159.182	18.292	1785.4	-1.699
50% Pd	$Pd_{31}Pt_{33}$–5	Pt_3	Pd_3	-159.075	18.290	1751.0	-1.590
50% Pd	$Pd_{31}Pt_{33}$–6	Pd_1Pt_2	Pd_2Pt_1	-159.153	18.269	1803.2	-1.647
50% Pd	$Pd_{31}Pt_{33}$–7	Pd_1Pt_2	Pd_2Pt_1	-159.108	18.313	1788.8	-1.646
50% Pd	$Pd_{31}Pt_{33}$–8	Pd_2Pt_1	Pd_1Pt_2	-159.149	18.295	1799.1	-1.669
50% Pd	$Pd_{31}Pt_{33}$–9	Pd_2Pt_1	Pd_1Pt_2	-159.120	18.329	1800.7	-1.673
50% Pd	$Pd_{31}Pt_{33}$–10	Pd_1Pt_2	Pd_2Pt_1	-159.129	18.298	1796.1	-1.652
50% Pd	$Pd_{31}Pt_{33}$–11	Pd_2Pt_1	Pd_1Pt_2	-159.146	18.264	1797.2	-1.634
50% Pd	$Pd_{31}Pt_{33}$–12	Pd_2Pt_1	Pd_1Pt_2	-159.107	18.304	1796.9	-1.636
50% Pd	$Pd_{31}Pt_{33}$–13	Pd_3	Pt_3	-159.098	18.280	1806.7	-1.602
50% Pd	$Pd_{30}Pt_{34}$–1	Pt_3	Pt_3	-160.247	18.330	1737.9	-1.622
50% Pd	$Pd_{30}Pt_{34}$–2	Pt_3	Pd_2Pt_1	-160.197	18.328	1752.1	-1.570
50% Pd	$Pd_{30}Pt_{34}$–3	Pt_3	Pd_2Pt_1	-160.172	18.358	1754.6	-1.575
50% Pd	$Pd_{30}Pt_{34}$–4	Pd_1Pt_2	Pd_1Pt_2	-160.217	18.374	1793.5	-1.636
50% Pd	$Pd_{30}Pt_{34}$–5	Pd_1Pt_2	Pd_1Pt_2	-160.241	18.346	1795.2	-1.632
50% Pd	$Pd_{30}Pt_{34}$–6	Pd_2Pt_1	Pt_3	-160.245	18.367	1802.2	-1.657
50% Pd	$Pd_{30}Pt_{34}$–7	Pd_2Pt_1	Pt_3	-160.245	18.332	1798.3	-1.621
50% Pd	$Pd_{29}Pt_{35}$–1	Pt_3	Pd_1Pt_2	-161.285	18.410	1754.8	-1.560
50% Pd	$Pd_{29}Pt_{35}$–2	Pt_3	Pd_1Pt_2	-161.260	18.440	1756.8	-1.565
50% Pd	$Pd_{29}Pt_{35}$–3	Pd_1Pt_2	Pt_3	-161.340	18.419	1809.7	-1.624
50% Pd	$Pd_{28}Pt_{36}$	Pt_3	Pt_3	-162.360	18.508	1756.8	-1.553
0% Pd	Pd_6Pt_{58}	Pd_3	Pd_3	-186.297	20.624	1806.2	-1.648
0% Pd	Pd_5Pt_{59}–1	Pd_2Pt_1	Pd_3	-187.478	20.670	1797.0	-1.695
0% Pd	Pd_5Pt_{59}–2	Pd_3	Pd_2Pt_1	-187.378	20.694	1808.0	-1.620

Bulk Composition	Label	Site Composition	Sublayer Composition	E_{total}	E_{form}	ν	E_{ads}
0% Pd	Pd_4Pt_{60}–1	Pd_1Pt_2	Pd_3	-188.617	20.712	1793.4	-1.696
0% Pd	Pd_4Pt_{60}–2	Pd_2Pt_1	Pd_2Pt_1	-188.562	20.748	1799.6	-1.677
0% Pd	Pd_4Pt_{60}–3	Pd_2Pt_1	Pd_2Pt_1	-188.549	20.753	1799.0	-1.669
0% Pd	Pd_4Pt_{60}–4	Pd_3	Pd_1Pt_2	-188.456	20.773	1809.8	-1.596
0% Pd	Pd_3Pt_{61}–1	Pt_3	Pd_3	-189.685	20.751	1752.1	-1.623
0% Pd	Pd_3Pt_{61}–2	Pd_1Pt_2	Pd_2Pt_1	-189.687	20.803	1797.3	-1.677
0% Pd	Pd_3Pt_{61}–3	Pd_1Pt_2	Pd_2Pt_1	-189.667	20.809	1792.3	-1.663
0% Pd	Pd_3Pt_{61}–4	Pd_2Pt_1	Pd_1Pt_2	-189.626	20.840	1800.7	-1.653
0% Pd	Pd_3Pt_{61}–5	Pd_2Pt_1	Pd_1Pt_2	-189.612	20.846	1799.2	-1.645
0% Pd	Pd_3Pt_{61}–6	Pd_3	Pt_3	-189.527	20.862	1810.7	-1.576
0% Pd	Pd_2Pt_{62}–1	Pt_3	Pd_2Pt_1	-190.736	20.856	1752.7	-1.599
0% Pd	Pd_2Pt_{62}–2	Pd_1Pt_2	Pd_1Pt_2	-190.752	20.903	1806.8	-1.662
0% Pd	Pd_2Pt_{62}–3	Pd_1Pt_2	Pd_1Pt_2	-190.731	20.911	1794.9	-1.649
0% Pd	Pd_2Pt_{62}–4	Pd_1Pt_2	Pd_1Pt_2	-190.752	20.902	1810.4	-1.662
0% Pd	Pd_2Pt_{62}–5	Pd_2Pt_1	Pt_3	-190.683	20.943	1801.3	-1.633
0% Pd	$PdPt_{63}$–1	Pt_3	Pd_1Pt_2	-191.781	20.973	1753.1	-1.581
0% Pd	$PdPt_{63}$–2	Pd_1Pt_2	Pt_3	-191.788	21.023	1800.5	-1.637
0% Pd	Pt_{64}	Pt_3	Pt_3	-192.817	21.100	1753.5	-1.564

D. CO adsorption on α-Al_2O_3(0001) surfaces

Table D.14.: DFT setting and result of CO adsorption energy (E_{ads} / eV), shifted CO vibrational frequency (ν_{CO} / cm^{-1}), and distances calculated of C-O bond of CO molecule (given in Å)

θ[$Al(OH)_3$]	θ[H_2O]	θ[CO]	Site	E_{ads}	ν_{CO}	$d_{C\text{-}O}$	PREC	NFREE	δ / Å
0	0	1/4	Al	-0.685	47.0	1.138	normal	2	0.01
0	0	1/2	Al	-0.656	29.7	1.1405	accurate	4	0.02
0	0	1/2	Al	-0.655	31.7	1.1405	accurate	2	0.01
0	0	3/4	Al	-0.635	17.8	1.142	normal	2	0.01

θ[Al(OH)$_3$]	θ[H$_2$O]	θ[CO]	Site	E_{ads}	ν_{CO}	$d_{C\text{-}O}$	PREC	NFREE	δ / Å
0	0	3/4	Al	-0.635	19.5	1.142	normal	2	0.01
0	0	1	Al	-0.613	7.3	1.144	normal	2	0.01
0	1/4	1/4	Al	-0.778	58.5	1.137	normal	2	0.01
0	1/4	1/4	H	-0.284	-0.5	1.144	normal	2	0.01
0	1/4	1/2	Al	-0.739	44.4	1.139	accurate	2	0.01
0	1/4	3/4	Al	-0.636	28.5	1.141	accurate	2	0.01
0	1/2	1/4	Al	-0.741	61.8	1.136	normal	2	0.01
0	1/2	1/4	Al	-0.73	60.1	1.137	normal	2	0.01
0	1/2	1/4	Al	-0.761	57.7	1.137	accurate	2	0.01
0	1/2	1/4	Al	-0.74	62.5	1.136	accurate	2	0.01
0	1/2	1/4	H	-0.243	-25.3	1.146	accurate	2	0.01
0	1/2	1/4	H	-0.262	-6	1.144	accurate	2	0.01
0	1/2	1/2	Al	-0.722	44.5	1.139	normal	2	0.01
0	1/2	1/2	Al	-0.656	43.3	1.139	accurate	2	0.01
0	1/2	1/2	Al	-0.653	41.7	1.139	accurate	2	0.01
0	1/2	1/2	H	-0.265	-11.3	1.145	accurate	2	0.01
0	1/2	1/2	H	-0.276	-28.6	1.147	accurate	2	0.01
0	3/4	1/4	Al	-0.716	60.2	1.137	accurate	2	0.01
0	3/4	1/4	H	-0.292	-0.1	1.144	accurate	2	0.01
0	1	1/4	H	-0.369	-2.1	1.144	normal	2	0.01
0	1	1/4	H	-0.329	-18.7	1.145	normal	2	0.01
0	1	1/4	H	-0.335	4.7	1.143	normal	2	0.01
0	1	1/2	H	-0.302	5.9	1.143	normal	2	0.01
0	1	1/2	H	-0.336	-1.1	1.144	normal	2	0.01
0	1	3/4	H	-0.304	5.5	1.143	normal	2	0.01
0	1	1	H	-0.306	6.2	1.143	normal	2	0.01
0	1	1	H	-0.215	-23.2	1.147	normal	2	0.01
1/9	0	1/9	Al	-0.646	30.7	1.14	normal	2	0.01
1/9	0	1/9	Al	-0.629	22	1.141	normal	2	0.01

θ[Al(OH)$_3$]	θ[H$_2$O]	θ[CO]	Site	E_{ads}	ν_{CO}	$d_{C\text{-}O}$	PREC	NFREE	δ / Å
1/9	0	1/9	Al	-0.639	40.3	1.139	normal	2	0.01
1/9	0	1/9	Al	-0.639	39.5	1.139	normal	2	0.01
1/9	0	1/9	H	-0.297	15.7	1.142	normal	2	0.01
1/9	0	2/9	H	-0.296	16	1.142	normal	2	0.01
1/9	0	1/3	H	-0.296	15.2	1.142	normal	2	0.01
1/4	0	1/4	H	-0.411	-0.4	1.144	normal	2	0.01
1/4	0	1/4	H	-0.419	15.5	1.142	normal	2	0.01
1/4	0	1/4	Al	-0.614	-9.1	1.144	normal	2	0.01
1/4	0	1/4	Al	-0.608	-5	1.143	normal	2	0.01
1/4	0	1/4	H	-0.411	2.9	1.143	normal	2	0.01
1/4	0	1/2	H	-0.316	10.5	1.142	accurate	2	0.01
1/4	0	1/2	H	-0.373	0.4	1.1425	normal	2	0.01
1/4	0	3/4	H	-0.344	2.4	1.143	normal	2	0.01
1/4	0	3/4	H	-0.353	11.1	1.142	normal	2	0.01
1	0	1/4	H	-0.212	-15	1.145	normal	2	0.01
1	0	1/4	H	-0.13	5.6	1.143	normal	2	0.01
1	0	1/4	H	-0.235	-27.6	1.146	normal	2	0.01
1	0	1/4	H	-0.208	-24	1.146	normal	2	0.01
1	0	1/2	H	-0.25	-23.8	1.146	normal	2	0.01
1	0	1/2	H	-0.253	-24.4	1.146	normal	2	0.01
1	0	3/4	H	-0.261	-20.2	1.146	normal	2	0.01
1	0	1	H	-0.252	-11.7	1.145	normal	2	0.01
1	0	1	H	-0.269	-18.8	1.145	normal	2	0.01

E. Cross-validation for GPR model

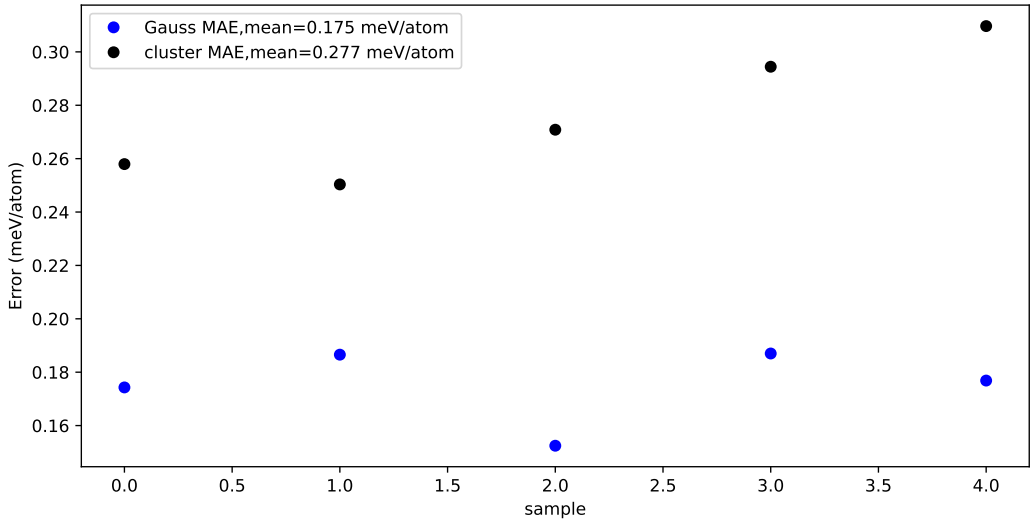

Figure E.10: The mean absolute error of the GPR model for the E_{form} dataset in 5-fold cross-validation. The blue dot shows the result for GPR model, the black dot shows the result for cluster expansion model.

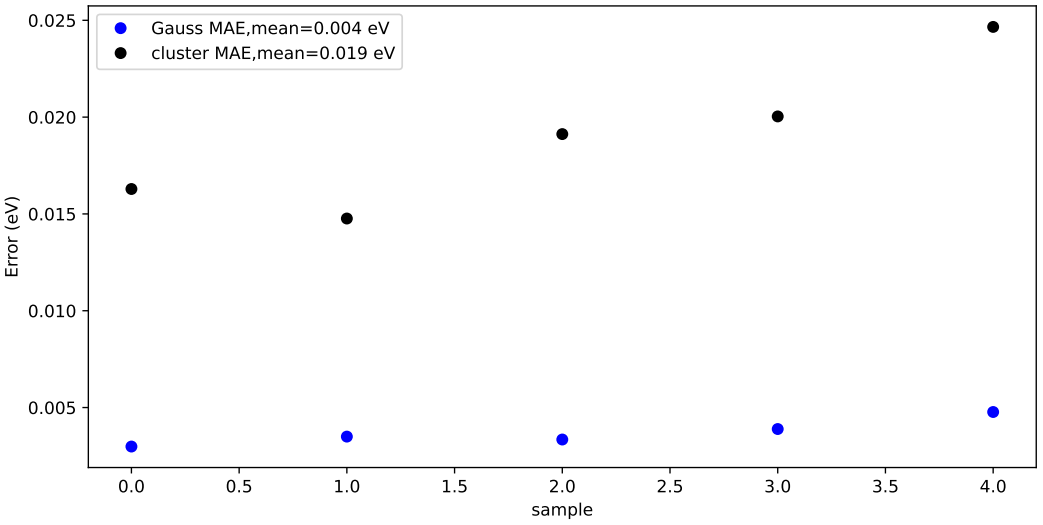

Figure E.11: The mean absolute error of the GPR model for the E_{ads} dataset in 5-fold cross-validation. The blue dot shows the result for GPR model, the black dot shows the result for cluster expansion model.

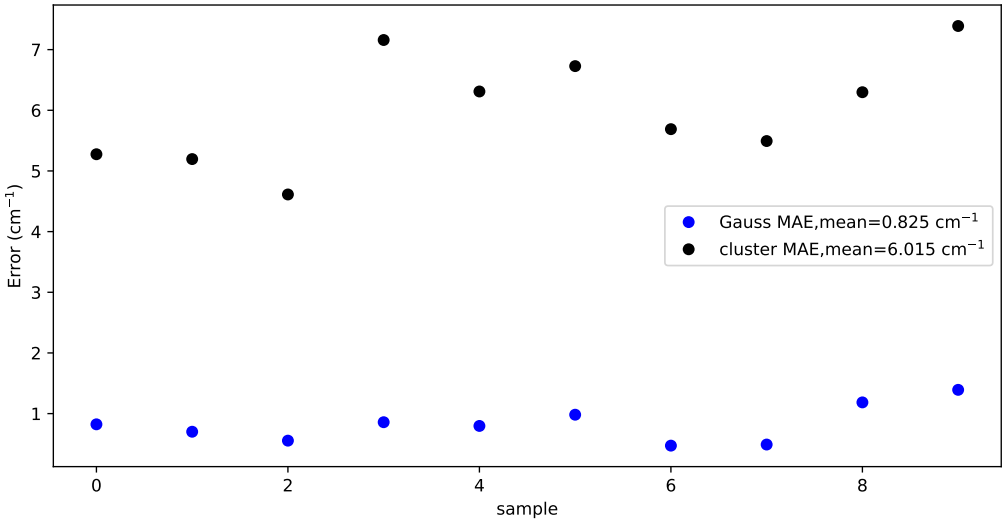

Figure E.12: The mean absolute error of the GPR model for the vibrational frequency dataset in 10-fold cross-validation. The blue dot shows the result for GPR model, the black dot shows the result for cluster expansion model.

List of Abbreviations

BLYP	Becke-Lee-Yang-Parr Functional
CMS	Computational Materials Science
DFT	Density Functional Theory
FT-IRRAS	Fourier Transform Infrared Reflection Absorption Spectroscopy
GGA	Generalized Gradient Approximation
GP	Gaussian Process
GPR	Gaussian Process Regression
HF	Hartree-Fock
IRRAS	Infrared Reflection Absorption Spectroscopy
KRR	Kernel Ridge Regression
LDA	Local Density Approximation
LEED	Low Energy Electron Diffraction
MCMC	Markov Chain Monte Carlo
NEB	Nudged Elastic Band
PAW	Projector-Augmented Wave
PBE	Perdew-Burke-Ernzerhof Functional
PGMs	Platinum Group Metals
PW91	Perdew-Wang Functional
RBF	Radial Basis Function
SI	International System of Units
TFD	Thomas-Fermi-Dirac Approximation
TWC	Three-Way Catalyst
UHV	Ultra-High Vacuum
VASP	Vienna Ab initio Simulation Package
vdW	Van-der-Waals Interaction
XPS	X-Ray Photoelectron Spectroscopy
XRD	X-Ray Diffraction

Acknowledgment

First and foremost, I would like to express my deepest gratitude to my supervisor, Dr. Philipp N. Plessow, for his unwavering support, patience, and constructive guidance throughout my PhD journey. His insights and encouragement were instrumental in shaping my work and keeping me on track during challenging times. I am also grateful to Prof. Dr. Felix Studt, for providing the resources and environment that allowed me to grow as a researcher. Special thanks also go to Dr. Dmytro Sharapa, whose supervision and advice were invaluable.

I extend my heartfelt thanks to my collaborators, Daniel Silvan Dolling, Jan-Christian Schober, Prof. Dr. Andreas Stierle, Siddhi Gojare, Dr. Juana Vazquez, Prof. Dr. Karin Fink, Dr. Chen Shuang, and Dr. Wang Yuemin, for their contributions and insightful discussions that enriched my research. I also want to acknowledge my lab members for their camaraderie and support. In particular, Annika Enß, who kindly proofread my thesis, and Tilman Grüger, who provided help with coding.

I would also like to acknowledge and thank the rest of the group, Dr. Jelena Jelic, Dr. Jonas Amsler, Dr. Zha Shenjun, Dr. Lucas Spiske, Dr. Philipp Huber, Dr. Sarah Bernart, Thanh-Nam Huynh, Claude Coppex, Enrico Sireci, Liana Savintseva, Dr. Mounssef Junior, Bassim, Aleksandr Maliugin, Aleksandr Kramarenko, Dr. Héctor Vicente, and Olgert Dallakyan, for creating a collaborative and motivating atmosphere in the lab.

This research was funded by TrackAct - CRC 1441, supported by the German Research Foundation (DFG). Additional support was provided by GRK 2450, bwunicluster, and JUSTUS 2, bwForCluster. I gratefully acknowledge the state of Baden-Württemberg for their support through bwHPC and the German Research Foundation (DFG) through grant no INST 40/575-1 FUGG (JUSTUS 2 cluster).

After all the aforementioned formal expressions of gratitude, I hereby extend my deepest and most erudite gratitude to the esteemed members of the KCSC football collective, whose limited commendable exhibition of athletic chivalry, though bearing no discernible utility in the exalted realm of academia, has nonetheless engendered a modicum of quotidian felicity, thereby rendering my otherwise intellectually beleaguered existence marginally more tolerable.

I most obsequiously extend my profoundest and most reverential gratitude to the illustrious Feng Yiming, as per her most gracious behest, and furthermore, I am compelled to extol

her indefatigable and perspicacious advocacy—both in the ethereal realm of thought and the ephemeral sphere of discourse—throughout these passing years.

Last but certainly not least, my heart overflows with the deepest gratitude for my beloved parents, Mrs. Wang Yuyu and Prof. Chen Rongshi, and my dearest grandmother, Prof. Pang Huijun. Their unwavering support, boundless love, and endless encouragement have been my anchor and guiding light throughout this journey. Through every challenge and triumph, their faith in me has never wavered, and I can say with certainty that I would not be where I am today without their unconditional love and strength.

List of Publications

1. Dolling, D. S.; **Chen, J.**; Schober, J.-C.; Creutzburg, M.; Jeromin, A.; Vonk, V.; Sharapa, D. I.; Keller, T. F.; Plessow, P. N.; Noei, H.; Stierle, A. Probing Active Sites on Pd/Pt Alloy Nanoparticles by CO Adsorption. *ACS Nano* **2024**. DOI:10.1021/acsnano.4c08291

2. Gojare, S.*; Chen, S.*; **Chen, J.***; Yu, Z.; Quesada, J. V.; Plessow, P. N.; Fink, K.; Wang, Y. Adsorption of CO on α-Al_2O_3(0001): A combined experimental and computational study. *in Preparation* (* indicates equal contribution)

3. **Chen, J.**; Sharapa, D.; Plessow, P. N. Advanced Predictive Modeling of Bimetallic Catalyst Behaviors through Gaussian Process Regression and Monte Carlo Simulations. *in Preparation*

4. **Chen, J.**; Sharapa, D. I.; Plessow, P. N. Stability of hydroxylated α-Fe_2O_3(0001) surfaces. *ACS Omega* **2024**, *9* (33). DOI: 10.1021/acsomega.4c02113

5. **Chen, J.**; Sharapa, D.; Plessow, P. N. Stability and formation of hydroxylated α-Al_2O_3(0001) surfaces at high temperatures. *Phys. Rev. Res.* **2022**, *4* (1). DOI: 10.1103/physrevresearch.4.013232

6. Liu, T.*; Liu, Z.*; **Chen, J.**; Jin, R.; Bai, Y.; Zhou, Y.; Chen, X. Redox-responsive supramolecular micelles for targeted imaging and drug delivery to tumor. *J. Biomed. Nanotechnol.* **2018**, *14* (6). DOI: 10.1166/jbn.2018.2573 (* indicates equal contribution)

7. Liu, J.; Song, Y.; **Chen, J.**; Chen, P.; Shan, D.; Han, E. H. The special role of anodic second phases in the micro-galvanic corrosion of EW75 Mg alloy. *Electrochim. Acta* **2016**, *189*. DOI: 10.1016/j.electacta.2015.12.075

Eidesstattliche Versicherung

Bei dieser Dissertation handelt es sich um meine eigenständig erbrachte Leistung. Ich habe nur die angegebenen Quellen und Hilfsmittel benutzt und mich keiner unzulässigen Hilfe Dritter bedient. Insbesondere habe ich wörtlich oder sinngemäßaus anderen Werken übernommene Inhalte als solche kenntlich gemacht. Ich habe die "Regeln zur Sicherung guter wissenschaftlicher Praxis am Karlsruher Institut für Technologie (KIT)" beachtet. Die Arbeit oder Teile davon habe ich bislang nicht an einer Hochschule des In- oder Auslands als Bestandteil einer Prüfungs- oder Qualifikationsleistung vorgelegt. Die Richtigkeit der vorstehenden Erklärungen bestätige ich. Die Bedeutung der eidesstattlichen Versicherung und die strafrechtlichen Folgen einer unrichtigen oder unvollständigen eidesstattlichen Versicherung sind mir bekannt. Ich versichere an Eides statt, dass ich nach bestem Wissen die reine Wahrheit erklärt und nichts verschwiegen habe.

Karlsruhe, 09.12.2024 _____

M.Sc. Jiachen Chen